1-1-2013

Time-Domain Fiber Loop Ringdown Sensor and Sensor Network

Malik Kaya

Time–domain fiber loop ringdown sensor and sensor network

By

Malik Kaya

A Dissertation
Submitted to the Faculty of
Mississippi State University
in Partial Fulfillment of the Requirements
for the Degree of Doctor of Philosophy
in Applied Physics
in the Department of Physics and Astronomy

Mississippi State, Mississippi

August 2013

Time–domain fiber loop ringdown sensor and sensor network

By

Malik Kaya

Approved:

Chuji Wang Associate Professor Physics and Astronomy (Director of Dissertation)	David L. Monts Professor and Graduate Coordinator Physics and Astronomy (Committee Member)
Hendrik F. Arnoldus Professor Physics and Astronomy (Committee Member)	Matthew J. Berg Assistant Professor Physics and Astronomy (Committee Member)
Robert B. Reese Associate Professor Electrical and Computer Engineering (Committee Member)	Jerome A Gilbert Professor and Interim Dean of the James Worth Bagley College of Engineering

Name: Malik Kaya

Date of Degree: August 17, 2013

Institution: Mississippi State University

Major Field: Applied Physics

Major Professor: Chuji Wang

Title of Study: Time–domain fiber loop ringdown sensor and sensor network

Pages in Study: 223

Candidate for Degree of Doctor of Philosophy

Optical fibers have been mostly used in fiber optic communications, imaging optics, sensing technology, etc. Fiber optic sensors have gained increasing attention for scientific and structural health monitoring (SHM) applications. In this study, fiber loop ringdown (FLRD) sensors were fabricated for scientific, SHM, and sensor networking applications.

FLRD biosensors were fabricated for both bulk refractive index (RI)- and surface RI-based DNA sensing and one type of bacteria sensing. Furthermore, the effect of glucose oxidase (GOD) immobilization at the sensor head on sensor performance was evaluated for both glucose and synthetic urine solutions with glucose concentration between 0.1% and 10%. Detection sensitivities of the glucose sensors were achieved as low as 0.05%.

For chemical sensing, heavy water, ranging from 97% to 10%, and several elemental solutions were monitored by using the FLRD chemical sensors. Bulk index-based FLRD sensing showed that trace elements can be detected in deionized water.

For physical sensing, water and cracking sensors were fabricated and embedded into concrete. A partially-etched single-mode fiber (SMF) was embedded into a concrete bar for water monitoring while a bare SMF without any treatment was directly embedded into another concrete bar for monitoring cracks. Furthermore, detection sensitivities of water and crack sensors were investigated as 10 ml water and 0.5 mm surface crack width, respectively.

Additionally fiber loop ringdown-fiber Bragg grating temperature sensors were developed in the laboratory; two sensor units for water, crack, and temperature sensing were deployed into a concrete cube in a US Department of Energy test bed (Miami, FL). Multi-sensor applications in a real concrete structure were accomplished by testing the six FLRD sensors.

As a final stage, a sensor network was assembled by multiplexing two or three FLRD sensors in series and parallel. Additionally, two FLRD sensors were combined in series and parallel by using a 2×1 micro-electromechanical system optical switch to control sensors individually. For both configurations, contributions of each sensor to two or three coupled signals were simulated theoretically. Results show that numerous FLRD sensors can be connected in different configurations, and a sensor network can be built up for multi-function sensing applications.

DEDICATION

To My Government (Turkiye Cumhuriyeti),

That Believed in Me, Supported Me, and Encouraged Me at Every Step of My PhD Education.

To My Wonderful Parents,

Who Believed in Me and Inspired Me at Every Step of My Life and Nothing Would Be Impossible Without Their Support.

To MyWonderful, Lovely, and Lucky Fiancé

Whose Love, Encouragement, and Support, but Sometimes Problems, Made This Journey More Meaningful and More Gratifying.

ACKNOWLEDGEMENTS

I owe my deepest gratitude to my research advisor, Prof. Chuji Wang, whose teaching, guidance, support and encouragement have helped me to be able to carry on during all this research. His outstanding eternal energy, wisdom, and enthusiasm in research have motivated all his advisees, including me. This dissertation would not have been accomplished without his guidance. In addition to my advisor, I would like to thank the rest of my dissertation committee members, David L. Monts, Henk F. Arnoldus, Matthew J. Berg, and Robert B. Reese for their support and encouragement.

It is a pleasure for me to acknowledge the support and assistance given by David Chevalier from the Department of Biological Science. Also, I would like to express my sincere appreciation to Robert B. Reese in the Department of Electrical and Computer Engineering.

I deeply give thanks to my labmates and all the previous and current group members in our research: Dr. Nimisha Srivastava and Chamini Herath who graduated in 2011 and 2010, respectively, Peeyush Sahay, Haifa Alali, Wei Wu, Zhennan Wang, Che Fuh, Mahesh Ghimire, Marthony Robbins and Diana Hubis. Also, I offer my regards and blessing to all my friends who supported me in any respect during the completion of my study. I would like to express special appreciation to Peeyush Sahay for outstanding collaboration.

I am very thankful to my mother, father, brothers, sister, and fiancé for encouraging and supporting me all the way.

Works in this dissertation are supported by the US National Science Foundation (NSF) through grant CMMI-0927539 and the US Department of Energy Savannah River Nuclear Solutions grant number AC84132N.

TABLE OF CONTENTS

LIST OF TABLES

LIST OF FIGURES

ABBREVIATIONS

AAP: Atomic Absorption Spectroscopy

ASV: Anodic Stripping Voltammetry

BWR: Boiling Water Reactors

Cd: Cadmium

CDM: Coherence Domain Multiplexing

Co: Cobalt

CRDS: Cavity Ringdown Spectroscopy

Cu: Copper

CW: Continuous Wave

DFB: Distributed Feedback

DNA: Deoxyribonucleic Acid

DI: Deionized

dsDNA: Double Strand DNA

DOE: Department of Energy

EF-FLRD: Evanescent Field-Fiber Loop Ringdown

EF: Evanescent Field

FBG: Fiber Bragg Grating

FC/APC: Fiber Connector for Angled Physical Contact

FDM: Frequency Division Multiplexing

Fe: Iron

FOBS: Fiber Optic Biosensor

FOS: Fiber Optic Sensor

FOSN: Fiber Optic Sensor Network

FOSs: Fiber Optic Sensors

FPI: Farby-Perot Interferometric

GOD: Glucose Oxidase

HF: Hydrofluoric

Hg: Mercury

HW: Heavy Water

ICP-MS: Inductively -Coupled Plasma Mass Spectrometry

IR: Infrared

LIF: Laser Induced Fluorescence

LPG: Long Period Grating

MEMS: Micro-electromechanical Systems

Mg: Magnesium

MMF: Multi Mode Fiber

MSU: Mississippi State Universtiy

OTDR: Optical Time Domain Reflectometer

P: Phosphorous

Pb: Lead

PBS: Phosphate-Buffered Saline

PCF: Photonic Crystal Fiber

PDM: Polarization Division Multiplexing

PLL: Poly-L-lysine

PWR: Pressurized Water Reactors

RCS: Reactor Coolant System

RI: Refractive Index

RIs: Refractive Indexes

S/N: Signal-to-Noise

SCW: Surface Crack Width

SHM: Structural Health Monitoring

SMF: Single Mode Fiber

SPR: Surface Plasmon Resonance

ssDNA: Single Strand DNA

T-B: Tris Buffer

TDM: Time Division Multiplexing

TIR: Total Internal Reflection

TXRF: Total-Reflection X-Ray-Fluorescence

UV: Ultra Violet

WDM: Wavelength Division Multiplexing

CHAPTER I

INTRODUCTION

Ab optical fiber is an elastic and transparent material made of silica (glass) or plastic. An optic fiber conveys light as a waveguide [1]. Therefore, optical fibers are mostly used in telecommunications because fiber optic cables can transfer data with low loss and over long distances. Fiber optic cables also have immunity to electromagnetic interference when they are compared to metal wires. Optical fibers have gained increasing attention in sensing technology for over the last 40 years [2]. Fiber optic sensors (FOSs) play an influential role in many applications, such as physical, chemical, biomedical sensing and in different areas, such as health structure monitoring and sensor networking. This study is focused on physical, chemical, and biological applications of fiber loop ringdown (FLRD) sensors and FLRD sensor networks. Chapter I explains FOSs and their advantages, cavity ringdown spectroscopy (CRDS) and FLRD techniques, FLRD sensing mechanisms, and the FLRD system components.

1.1 Fiber Loop Ringdown (FLRD) Sensors

A fiber optic sensor (FOS) system basically consists of a section of optical fiber, a photodetector, a light source, and electronic devices that may include a pulse generator, temperature and current controllers, an oscilloscope, and a computer. Optical fibers transmit light based on the total internal reflection (TIR) principle [3]. The light is guided

through the core of the fiber due to this phenomenon. An optical fiber consists of fiber core which has a smaller refractive index (RI), n_1 and the fiber cladding which has a larger RI, n_2. The cladding RI must always be larger than the core RI for light propagation inside the core with TIR. Whenever light hits the boundary of any two different media which have two different RIs and the incidence angle is bigger than the critical angle, the light will be confined to the first method. This can be explained by Snell's law ($\theta_c = \sin^{-1} [n_2/n_1]$) [4]. The basic principle of a FOS system is to measure electromagnetic energy loss or a light frequency shift due to a sensing event which is to be sensed. The former may be called intensity-domain sensing and the latter is often referred to as frequency-domain sensing technique. FLRD, however, is a new time-domain sensing. In FLRD, a light pulse from a laser source is coupled into a fiber loop. When the light source is shut off rapidly, the coupled light travels many round trips inside the loop. In each round trip, the photodetector receives a small portion of the light through a fiber coupler, and the rest of the light continues to travel inside the loop and experiences internal fiber transmission losses. The signal observed by the detector is a series of spikes whose envelope decays exponentially in time. The decay constant is called the ringdown time and it is the sensing signal of the FLRD technique. As a time-domain sensing technique, FLRD measures ringdown times to sense a parameter or a quantity.

Fundamentally, FOSs can be utilized as intrinsic and extrinsic sensors. In intrinsic sensors, the optical fiber itself is used as a sensor for measurement of quantities after some modifications on the fiber, such as etching and chemical coating. On the other hand, in extrinsic sensors, processing of a light signal is the key factor for detection. After

light leaves the fiber and comes back to the fiber in one of several ways, such as reflection of the light, blocking the light, etc., the signal is processed to measure shift or loss [5, 6]. Figure 1.1 represents the basic working principle of the two types of sensors. Part (a) of the figure shows an illustration of an extrinsic sensor system. A signal comes through the input fiber into the "box", and its feature(s) such as intensity, wavelength, phase, phase angle, etc. change/s inside the box due to outside sensing activity. Later, the signal is sent to the detector or to any equipment to be processed through an output fiber. In part (b) of the figure, an intrinsic sensor system is represented. The signal travels through the fiber core, and one or some of the features change due to sensing activity which occurs directly on the fiber. Five types of intrinsic sensors are available: the first is based on phase-shift or wavelength-shift due to time delay [7-9]. When utilizing a special fiber optic sensor, such as a fiber Bragg grating (FBG) sensor, wavelength or phase-shift can be detected. The Mach-Zehnder interferometer, which has two interferometer arms that detect phase shift of light propagation, is employed for detection of different physical quantities, including pressure, temperature, etc. [10]. The second type is polarimetric sensors which are based on measurement of polarization change. The source must be monochromatic and polarized for a polarimetric sensor. The polarization change is a change of birefringence in the fiber due to the measured physical event [11]. A low-cost polarimetric pressure sensor, based on the coupling between two polarized modes in a standard telecommunication fiber, has been fabricated and operated [12]. The third type of intrinsic sensors measures spackle change in pattern. Projected light from the fiber has a distinctive pattern. For example, vibrations and their parameters are detected by observing output spackle pattern from a multimode optical fiber [13]. The fourth type of

sensors is based on color modulation, which needs two detectors to measure color change of the light. The fifth type of sensors uses microbending to obtain light attenuation. All types of sensors aforementioned need complicated optic and electronic equipment.

In extrinsic fiber optic sensors, a fiber optic cable, generally a multi-mode fiber (MMF), is employed to convey processed light from a sensor to a transmitter. The main advantage of extrinsic sensors is their ability to reach unreachable places, such as aircraft jet engines, to measure temperature [14] or other parameters. Extrinsic sensors are also very good in measuring signals with less noise. The review paper from Yao on fiber-optic extrinsic Fabry-Perot interferometric sensors explains extrinsic sensors working principles very well [15].

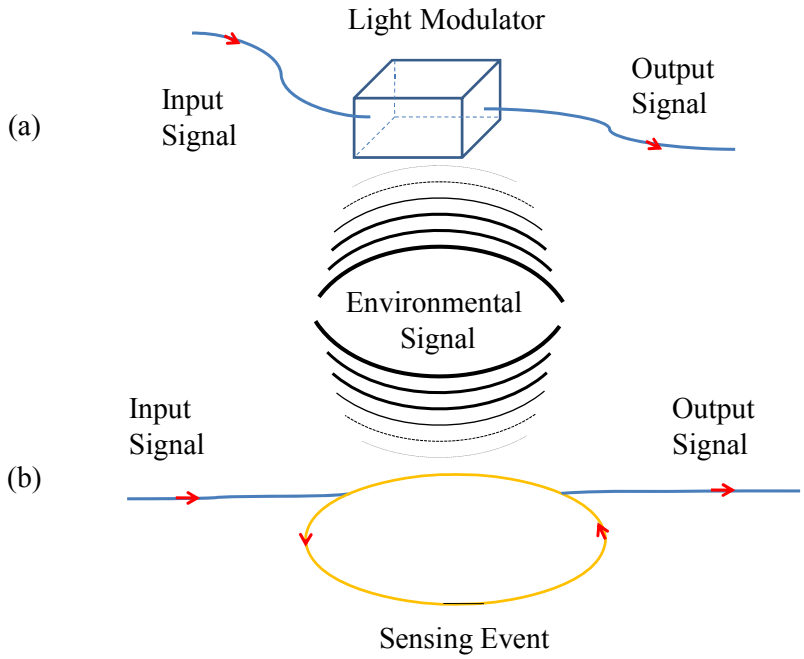

Figure 1.1 Illustration of two types of fiber optic sensors.

(a) Extrinsic sensors; light comes to a "box", is modulated inside the "box" depending on sensing activity, and is sent to a detector, and (b) intrinsic sensors; light travels through the fiber and light intensity is modulated depending on sensing activity.

FOSs have been applied for sensing physical quantities, such as pressure [16-18], force [19], crack [20], temperature [18, 21], acoustics [22], strain [23], humidity [24], etc. FOSs are also applicable for chemical measurements, such as gas analysis [25], concentrations of various elements in liquids [26] (i.e., iron, cobalt, magnesium, etc.), and biomedical applications, such as detection of bacteria, deoxyribonucleic acid (DNA) [27], and glucose in fluids [28]. FOSs can be classified by their applications, such as physical, chemical, and biomedical sensors (biosensors).

The evanescent field-fiber loop ringdown (EF-FLRD) technique [29] is used to measure optical loss in terms of ringdown time, which is based on RI-based measurements. Each medium has a different RI. Therefore, the response of a sensor in terms of ringdown time becomes different whenever the medium around the sensor head changes.

In this study, EF-FLRD sensors made from single-mode fibers (SMF) have been developed to detect several quantities and parameters by applying the evanescent field (EF) sensing mechanism in which optical loss is measured in terms of ringdown time.

1.2 Advantages of Fiber Optic Sensors

Due to their advantages, FOSs have been widely used to sense various quantities such as strain, pressure, temperature, cracks, chemical species, biological cells, small volume of fluids, etc. FOSs offer numerous advantages such as:

- Immunity to electromagnetic interference
- No electrical disturbance for other devices
- No risks of electric sparks because no electrical cable
- Safe in explosive and flammable area since they are electrically insulated

- Small size and light weight
- Common technology base, construction for sensing several quantities (temperature, acoustic, pressure, gas trace, organic molecules, cells, etc.)
- High data transfer capacity at high bandwidth
- No contamination or corrosion because they are chemically passive
- Wide operating temperature range (- 60 ^{o}C to 85 ^{o}C)
- Geometric versatility, configurable in any shape
- High sensitivity and low cost
- Integration capability to setup a sensor network

Although they have many advantages, FOSs are fragile. To use in harsh environments effectively and for long periods of time, FOSs must be chemically coated or covered with a protective material. Due to their fragility, special skills and extra caution are also needed to work on FOSs. Expensive components, such as transmitters and receivers may be needed in some works [30].

1.3 Cavity Ringdown Spectroscopy and Fiber Loop Ringdown Techniques

FLRD is a relatively new sensing technique evolved from the cavity ringdown spectroscopy (CRDS) technique [31]. In FLRD, optical loss of a light pulse inside a fiber loop is measured by the decay time constant of the light intensity. Fundamentally, FLRD measures time in order to detect a quantity. Therefore, FLRD is a time-domain sensing technique. The FLRD technique offers high sensitivity, fast response, and near-real time monitoring due to the multi-pass feature of the light inside the loop.

To understand the FLRD concept in detail, the CRDS technique should be explained first. Figure 1.2 shows a schematic illustration of the CRDS concept. A CRDS

system consists of two highly reflective mirrors (≥99%), a laser source, a photodiode detector, and an oscilloscope. A small portion of a laser pulse, which is sent from the laser source to the first highly reflective mirror, is transferred into the cavity. The cavity is the distance between two face-to-face highly reflective mirrors. The small amount of light travels between the mirrors back and forth, resulting in exponential decay of the light intensity due to loss of the light intensity through each mirror during each round trip. Each small fraction of the light is captured by the photodetector, and the ringdown decay waveform is shown on an oscilloscope. The light intensity inside the cavity follows an exponential decay, and the decay constant, "ringdown time", is given by

$$\tau = \frac{d}{c|lnR|}, \tag{1.1}$$

where d is the cavity length, c is the speed of light, and R is the reflectivity of the mirrors. For high reflective mirrors, R≈1 [32],

$$\tau = \frac{d}{c(1-R)}. \tag{1.2}$$

CRDS has been used for weak absorption measurements, but now has become a mature technique for trace gas analysis and sensing [33].

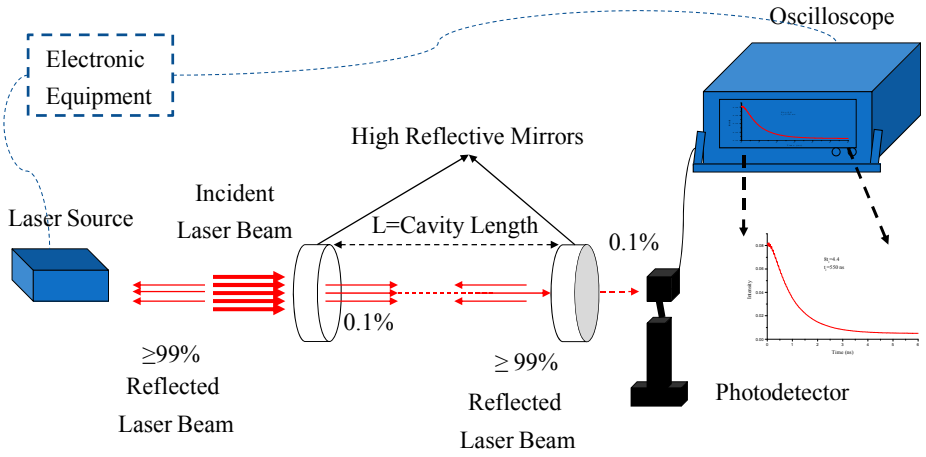

Figure 1.2 Schematic illustration of CRDS concept.

Transferred beam from the second high reflective mirror is collected by the photodetector and sent to an oscilloscope to observe ringdown curve.

The FLRD technique, evolved from the CRDS technique, has become a time-domain sensing technique for fabrication and development of FOS and sensor networks. If a FLRD system and a CRDS system are compared to each other in terms of system equipment similarities, a fiber loop of typically 120 m can be considered as the cavity length, and two couplers are like the high reflective mirrors, as shown in Figure 1.3. When a laser pulse from the laser source is coupled into the fiber loop and the source is shut off rapidly, the pulse travels many round trips inside the fiber loop. In each round trip, its intensity decreases due to the internal optical transmission loss in the loop and optical loss at the sensor head, and the coupling and insertion losses in the couplers. A small fraction of the light is sent to the photodetector during each round trip, and the rest of the light keeps traveling inside the loop, resulting in an exponential decay over time. The photodetector sends signals to the oscilloscope, and the oscilloscope displays a ringdown decay waveform.

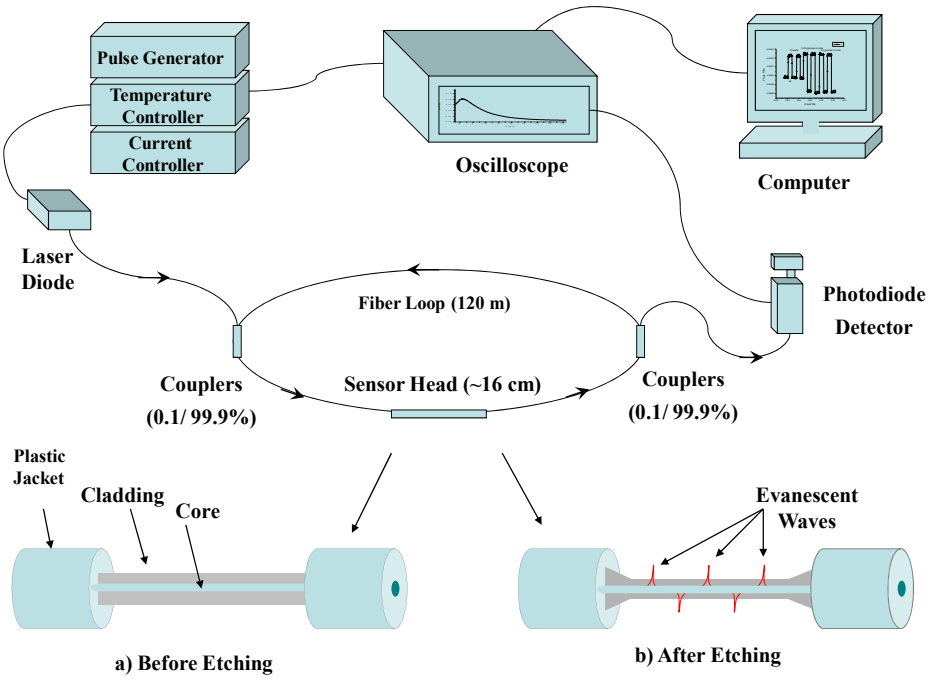

Figure 1.3 Schematic illustration of FLRD system.

Transferred light through the second coupler is collected by the photodetector and sent to the oscilloscope to observe ringdown curve. a) The sensor head before etching in 48% HF solution. b) The sensor head after etched in 48 % HF solution. Small spikes on the sensor head show evanescent waves dispersing from the core to outer medium. Surrounding area of the waves is called "Evanescent Field".

The sensor head is fabricated by etching a small section of the fiber in a 48% hydrofluoric (HF) acid solution for 33-34 min. after plastic jackets have been removed. Two fiber ends are spliced. A detailed explanation of the etching process has been presented elsewhere [34].

For the EF-FLRD principle, after a light pulse is injected into a fiber loop, the light pulse travels inside the fiber loop many round trips. A small fraction of the light pulse is transferred to a photodetector through a fiber coupler during each round trip, and the rest of the light keeps traveling inside the fiber loop, experiencing an internal

transmission loss. The output signal observed by the photodetector can be modeled by [16, 17]

$$\frac{dI}{dt} = -\frac{IAc}{nL}, \tag{1.3}$$

where I is the light intensity at time t where we assume the time equals zero when the light source is shut off and a light pulse is injected into the loop, L is the total length of the fiber loop, c is the speed of light in vacuum, n is the average refractive index of the fiber loop, and A is the total fiber transmission loss of the light in each round trip. The total fiber transmission loss includes the fiber absorption loss, the fiber couplers' insertion loss, and the fiber scattering loss, and A is expressed as

$$\mathrm{A} = \alpha L + E + \gamma, \tag{1.4}$$

where α is the wavelength dependent absorption coefficient for the fiber core material with units of, e.g., cm^{-1}, E is the total insertion loss of the fiber couplers, and γ is the total fiber scattering loss. The solution of Equation (1.3) gives an exponential decay behavior of the light intensity observed by the photodetector;

$$I = I_0 e^{-\frac{c}{nL}At}. \tag{1.5}$$

Equation (1.5) shows that the EF-FLRD technique measures the light intensity decay rate, not the absolute intensity change, ΔI. Therefore, measurement of A is insensitive to incident light intensity, I_0, fluctuations. The time required for I to drop to $1/e$ of I_0 is referred to as the ringdown time, τ_0. Ringdown time is given by

$$\text{(a)} \quad \tau_0 = \frac{nL}{cA} \tag{1.6}$$

(b) $t_r = \frac{nL}{c}$.

$$\tau = \frac{nL}{c(A+B)}. \tag{1.7}$$

The total transmission loss, *A*, is a constant for a given EF-FLRD sensor which may be a pressure, temperature, strain, or crack sensor. Equation (1.6b) defines the round trip time, t_r, of the laser beam inside the loop. The total transmission loss is calculated by the physical parameters of the sensor, such as the fiber absorption loss, the fiber couplers' insertion losses, the refractive index, and the fiber length. Obviously, if the optical loss of the fiber is lower, the decay time constants, τ_0, will be longer. Whenever an external action, such as pressure, strain, or absorption, happens at any section of the sensor head of the fiber loop, an additional optical loss, *B*, will be considered to calculate the new ringdown time, τ, given by Equation (1.7). From Equations (1.6) and (1.7), we have:

$$\left(\frac{1}{\tau} - \frac{1}{\tau_0}\right) = \frac{c}{nL}B. \tag{1.8}$$

Equation (1.8) stands for the principle equation of the EF-FLRD technique, and it implies a change in a sensing activity. Equation (1.8) is obtained by measuring τ_0 which is the ringdown time when there is no sensing activity and τ which is the ringdown time when there is a sensing activity. Equation (1.8) clearly indicates that the activity induced optical loss, *B*, has a linear relationship with the left hand side of Equation (1.8), ($1/\tau - 1/\tau_0$). When only EF-FLRD sensors are considered, *B* is from EF-induced optical loss. Otherwise, *B* will be optical loss due to any FLRD sensing activity, such as bending, gas absorption etc.

The detection sensitivity of EF-FLRD sensors for biological and chemical applications is characterized in the same way by the minimum detectible EF-induced optical loss. On the other hand, the detection sensitivity of the EF-FLRD sensors for physical applications is characterized by determining sensing activities such as bending loss, mechanical deformation, etc. From Equations (1.8) and (1.6b),

$$B = \frac{t_r}{\tau_0}\frac{\Delta\tau}{\tau} = \frac{1}{m}\frac{\Delta\tau}{\tau} \tag{1.9}$$

$$(\Delta\tau = \tau_0 - \tau), \tag{1.10}$$

where t_r is the round trip time and m is the number of round trips. Hence, the minimum detectible optical loss B_{min}, which is defined as the 1σ detection limit, is given by

$$B_{min} = \frac{1}{m}\frac{\sigma_\tau}{\tau}, \tag{1.11}$$

where σ_τ is the 1σ standard deviation of the ringdown time. σ_τ / τ is a value of typical minimum detectible change in light intensity, $\Delta I/I_0$, which can be determined experimentally, and generally is of the order of 10^{-3}. For pressure sensors, B in Equation (1.8) can be expressed as:

$$B = \beta l F, \tag{1.12}$$

where $F=PS$ is an external force on the sensor, S is the interaction area with the sensor, β is the force-induced loss coefficient, and l is the length of the fiber contacts with applied force. Comparing Equation (1.8) and (1.12) gives the ringdown time measurement for pressure sensing:

$$\frac{1}{\tau} - \frac{1}{\tau_0} = kF \tag{1.13}$$

where k is a constant which is $c\beta l/nL$. From Equations (1.4), (1.12), and (1.13), we can calculate ringdown time when an external force is applied on the sensor when A is very small and using first order approximation:

$$\tau = \tau_0 \left(1 - \frac{l}{\alpha L + E} F\right). \tag{1.14}$$

γ is negligible for low scattering loss. Equation (1.14) explains that the measured ringdown time has a linear relation with the applied force [16, 17].

For cracking sensors, a sensor head is made of a section of bare SMF. When a part of the sensor head (SMF) has a stretch of ΔL, a loss of $\alpha \Delta L$ will be created. Therefore, Equation (1.6a) can be modified as

$$\tau = \frac{n(L+\Delta L)}{c(A+a\Delta L)}. \tag{1.15}$$

When stretches are on the order of millimeters, the stretches can be ignorable as compared with the typical 120 m fiber loop length and the resulting optical loss is much smaller than the total optical loss of the fiber loop. Using the first order approximation, we can modify Equation (1.15) as

$$\tau = \tau_0 \left(1 - \frac{\alpha}{A} \Delta L\right). \tag{1.16}$$

Equation (1.16) shows the relationship between stretch length and measured ringdown time [20].

1.4 Sensing Mechanisms

Several different sensing mechanisms have already been demonstrated for various scientific and industrial applications. Chemical coatings or EF scattering and/or

absorption or combined with any optical components, i.e., a long period grating (LPG) or FBG, are utilized for biomedical/biological sensing [27, 28, 34-38]. Various absorption-based sensing mechanisms, such as fluorescence-, direct-, EF absorption-, and capillary electrophoresis-based sensing mechanisms, are employed for fiber optic chemical sensors [39-45]. Thermal expansion-, mechanical deformation-, and interferometric-based sensing are used for fiber optic physical sensors: for instance FBG temperature and strain sensors and Fabry-Perot interferometric (FPI) temperature and pressure sensors [46-51]. All sensing techniques have been studied to improve some or all properties of the FOSs, such as sensitivity, reliability, selectivity, etc.

For intensity based FOSs, detection of signal loss plays the key role. The signal experiences losses under applied force that bends the fiber and causes attenuation of the signal. Another way for signal attenuation is absorption or scattering of the signal from a target. Several sensing mechanisms, such as microbending loss, EF absorption, etc., can generate induced optical loss. One of the intensity-based FOSs is the microbend sensors which are based on the principle that microbends cause an attenuation of the transmitted light [52]. A fiber optic microbend sensor application for strain monitoring has been studied by Luo *et al.* [53]. A section of optical fiber is placed between two plates with a teeth platform to produce microbend losses for strain measurements. Another type of intensity based FOSs is the EF sensors which utilizes light intensity. Propagating light inside the core of the fiber attenuates from the core to the cladding and experiences loss due to refractive index difference of each media, which is called EF scattering. In addition to EF scattering, sensing can be performed by removing cladding from a section of the fiber and using a light source that wavelength of the light can be absorbed by the

chemical to be detected, resulting in a measurement of chemical concentration by change of the light intensity [52]. Sekimoto *et al.* developed an optical-fiber hydrogen sensor which utilizes the absorption change of the EF in the clad region [54].

For wavelength modulation-based FOSs, fluorescence sensors and FBG sensors are the most popular ones. Fluorescence sensors are mostly used in biomedical applications and chemical sensing [55-57], and utilize fluorescent molecules to interact with the target to generate signal [58]. For example, light travels through a fiber to a probe of a fluorescent material. After the fluorescent signal is caught by the fiber, the signal is sent to the demodulator for processing [59]. FBG sensors are commonly used for sensing of physical quantities, such as strain, temperature, etc. [60-62]. The FBG sensing technique detects a wavelength shift. Changing temperature changes the refractive index of the fiber core and the grating period of the FBG sensor head, resulting in a Bragg wavelength shift.

For phase modulated FOSs, the change of a light phase is utilized for detection. The light is separated into two fiber legs: while one leg reaches to the sensing medium, and the light experiences a phase shift in this leg, the other leg stays parallel to the first leg and is separated from the sensing medium. The second leg is also used as a reference. Recombination of the lights will provide interference. The most common interferometers are Mach-Zhender, Michelson, and Fabry-Perot interferometers [5, 63-65].

For polarization modulated FOSs, electric field direction of the light is considered as a polarization state of the light. There are several polarization states, such as linear, circular, and elliptical polarization states. Polarimetric sensors use output polarization states as a detection scheme. Pressure induced polarization coupling has been studied and

temperature desensitization of the sensor output signal is presented based on the principle of polarization-rotated reflection [66]. For biological sensing, EF scattering supplies very accurate and reliable results because the EF scattering technique has high sensitivity and fast response. Besides the EF scattering technique, chemical coating is another effective way to achieve chemical and biological sensing. Coating the sensor head with a chemical makes the sensor more selective and/or more sensitive. For example, when etched SMF was used to sense DNA samples in a solution by the EF sensing technique, the sensor was coated with a chemical to observe the selective response of the sensor to different DNA samples [27].

For chemical sensing, the EF absorption technique has also been used to detect organic compounds in solutions. For example, organic compounds in aqueous solutions are determined by using a quartz glass fiber with a polysiloxane cladding. Absorption of EF by organic species at the interface of the core and the cladding were measured when the EF penetrates into the cladding [67]. In another study, an EF absorption sensing technique in liquid solutions was presented by Su *et al.* [68] by using a microstructured photonic crystal fiber (PCF). They investigated the effects of solution concentration, detection directions, and PCF length on the absorption sensitivity.

For physical sensing, the wavelength shift technique is one of the most used techniques to measure temperature or other physical quantities. Commercially available FBGs are often used to fabricate FGB sensors. The FBG sensing principle is that wavelength shift resulting from a change in temperature is recorded. Besides temperature measurements, mechanical distortion is another physical measurand. A plastic jacket removed-section of SMF is placed into a microbending platform to measure a change in

pressure, force, strain, or stress. For example, conventional microbend sensors are used to detect displacement. The microbending effect has been studied, and the microbending sensitivity has been presented [69]. In another example, the wavelength-dependent optical loss measurement has been presented by monitoring temperature change of FBG-based temperature sensor [70].

1.5 The EF-FLRD System Components

The EF-FLRD system consists of a temperature-controlled continuous wave (CW) diode laser source, two 2×1 fiber couplers, a fused-silica single mode fiber, a photodetector, an oscilloscope, and an electronic control that includes a pulse generator, a temperature controller, and a current controller. In this section, each of the components is explained in detail.

1.5.1 Continuous Wave Diode Laser Source

A pig-tailed distributed feedback (DFB) diode laser is used in the EF-FLRD sensor system as a laser source. DFB diode lasers are single mode diode lasers with a small range of tunability (~2-3 nm). The laser chip has dimensions of 1000 μm × 500 μm × 200 μm (l × w × h). DFB lasers provide a narrow linewidth laser beam with good side mode suppression and have available wavelengths ranging from 760 nm to 2800 nm. The power range varies from 5 mW to 150 mW [71]. The DFB laser used in our studies was purchased from NEL, America Inc. [72]. For example, the center wavelength of one of the laser diodes is 1515 nm and has a tunable range of ±1.5 nm around the central wavelength. Figure 1.4 illustrates the DBF diode laser that has been utilized in this work.

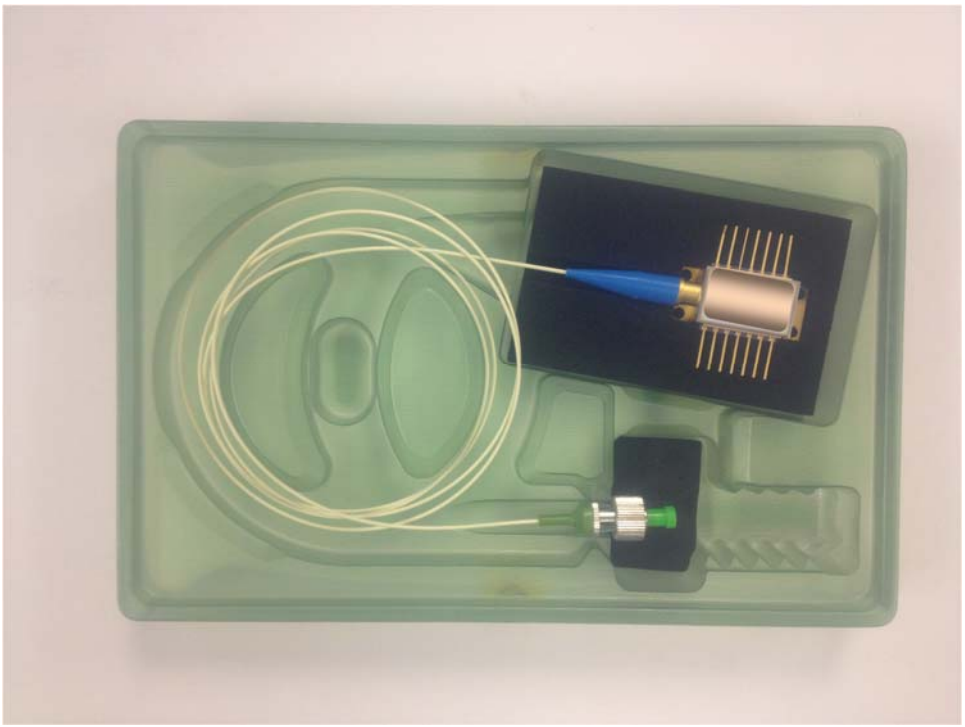

Figure 1.4 Image of pig-tailed temperature-controlled continuous wave diode laser.

1.5.2 Fiber Couplers and Single Mode Fiber

Two identical 2×1 fiber couplers, Opneti Communications Co., were fabricated with a split ratio of 0.1:99.9 in the 2-leg end of the fiber couplers. The couplers used in this study transfer 0.1% and reflect back 99.9% of the incoming laser beam. Each leg of 1 m was connected to the fiber loop of 120 m and has a fiber connector for angled physical contact (FC/APC) fiber connector to connect one to the laser source and the other one to the photodetector. FC/APC stands for fiber connector with an angled polished connector. The SMF, SMF-28e optical fiber, Corning Inc., consists of the core of ~8.2 μm, the cladding of 125 μm, and a plastic jacket of ~245 μm. The operating temperature range of the SMF is - 60 to 85 ^{o}C. Details of the SMF and the couplers can be seen elsewhere [73, 74]. To fabricate a sensor head from the SMF, several tools are needed, such as a stripper,

an optical fiber cleaver, and a single fiber fusion splicer, which are explained in [75]. Figure 1.5 shows the structures of a SMF fiber, a SMF loop with the couplers, and the sensor head fabricated by etching the SMF in a 48% HF solution.

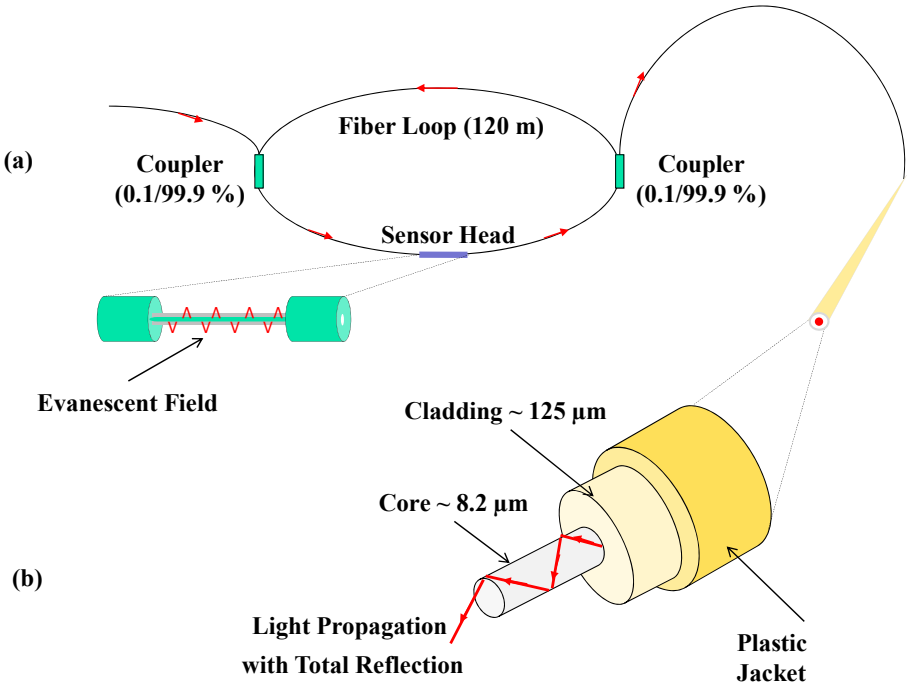

Figure 1.5 Schematic illustration of a SMF loop and structures of SMF.

(a) The SMF loop with two couplers and a sensor head. (b) Light propagation in the core and layers of the SMF: core, cladding, and plastic jacket.

The total optical loss, which includes absorption loss, insertion losses of the fiber connectors, and the couplers' losses, of the fiber loop was estimated to be less than 0.45 dB. The splicing loss estimated by the splicer was between 0.02 and 0.04 dB.

1.5.3 InGaAs Detector

InGaAs photodetectors monitor short-pulsed and weak photosignals. The InGaAs photodetectors used in this study were purchased from Thorlabs. They have a wide

wavelength response range. The wavelength range varies from the ultraviolet (UV) to the mid- infrared (IR) (150 nm to 2.6 μm). In this study, the InGaAs detector model PDA50B (Thorlabs) was used. The photodetector has a detection range of 800 – 1800 nm, low noise, and a wide band range of 0 – 10 V output [76]. The triggering threshold was set at 0.5 V, and the amplification of the detector was setup at 50 dB signal-to-noise ratio with a minimum detectible power of 10 nW.

1.5.4 Oscilloscope

Oscilloscopes are perfect tools to acquire, to display, and to measure waveforms. Oscilloscopes measure voltage as a fuction of time. Oscilloscopes are mostly used for monitoring the precise wave shape of an electrical signal. An oscilloscope, Textronix 410A [77], with a bandwidth of 400 MHz, was employed in this study to monitor signals from the photodetector.

1.5.5 Electronic Control

The electronic control system consists of a pulse generator (Stanford Research Systems (SRS), model DG 535), a temperature controller (ILX Lightwave, model LDX-3220), a current driver (ILX Lightwave, model LDT-5948), and a computer. Ringdown signals detected by the photodetector are applied to trigger the pulse generator to generate a negative square wave of 2.5 V amplitude and 10-100 Hz tunable frequency. This pulsed series is used to drop the laser current to zero. The precision temperature controller controls the temperature of the laser diode for constant room temperature of 25 ^{o}C. Temperature stability of 0.003 ^{o}C ensures the device's performance and very reliable measurements [78]. The laser diode current driver is a high stability and low noise

current source with integrated laser diode protection circuits. Output current range can be tuned from 0 mA to 500 mA [79].

CHAPTER II

BIOLOGICAL SENSORS

Biosensors are optical, chemical, electrical, or mechanical tools with selective detection capability for biological parameters. Fiber optic biosensors (FOBSs) are utilized to measure biological species, such as proteins, cells, DNAs, bacteria, glucose, etc. FOBSs are generally modified with chemical or biological entities to improve their selectivity and sensitivity. A good FOBS has to be both responsive to low concentration of a sample and selective among species based on chemical agents which are normally coated on the surface of the sensor. On account of accuracy, efficiency, low cost, fast response, high sensitivity, and convenience, FOBSs have gained increasing attention and become promising alternatives to traditional techniques for biomolecule measurements. FOBSs have wide application areas, such as detection of biomarkers for medical diagnostics, detection of pathogens and toxins in foods and water, etc. The EF sensing technique is one of the most reliable and sensitive techniques to be used for biosensing.

In this chapter, EF-FLRD sensors are described. The EF-FLRD sensors have been developed to detect biological quantities, such as DNA, bacteria, or glucose in deionized (DI) water and in synthetic urine solutions. Both bulk RI- and surface RI-based DNA sensing and bulk RI-based bacteria sensing are presented. EF-FLRD glucose sensors with and without glucose oxidase (GOD) coatings on the sensor head were tested to investigate the affects of the GOD coatings on the sensors' performance, and the

detection limits of EF-FLRD glucose sensors for standard glucose solutions and for synthetic urine samples were determined.

2.1 FLRD DNA and Bacteria Sensors

FLRD is a new sensing technique which has evolved from the CRDS technique. Even though it was introduced for trace gas detection first [41], application areas of FLRD have been enhanced to include physical, chemical, and biological applications, such as measuring pressure, strain, temperature, refractive index, and microfluids which review studies explain in detail [80, 31]. In the FLRD technique, a time constant is measured as the sensing signal. This gives enhanced sensitivity due to the multi-pass nature of light inside a closed loop. Several sensing mechanisms, such as absorption, microbending, FBG- and LPG-based wavelength shift, and EF absorption and scattering, can be utilized as the sensing platform to fabricate and develop different sensors. By combining EF and FLRD, the EF-FLRD technique has great potential for biosensor development.

A new type of RI-based biosensor using the EF-FLRD sensing scheme is reported in this study. The EF-FLRD sensing technique is used to sense the signal which is a time constant, and the detection sensitivity is enhanced by the multi-pass nature of the ringdown technique. Bulk RI-based and surface RI-based sensing of two different single strand DNAs and one double strand DNA (Integrated DNA Technologies) and one type of bacteria (*Escherichia coli* strain DH5α) are presented for the EF-FLRD sensors that employ a partially-etched single mode fiber as the sensor head. This work reported the first DNA and bacteria sensors using the FLRD technique. Without using any additional optical components, such as FBG or LPG for sensor head fabrication, fabricated and

tested the EF-FLRD biosensors demonstrate lower cost, higher sensitivity, simplified design and configuration, and simplicity when they are compared to their counterparts.

2.1.1 Principle and System Setup of the EF-FLRD Biosensors

As discussed in Section 1.3, the minimum detectible optical loss B_{min} defined as the 1σ detection limit is given by

$$B_{min} = \frac{1}{m}\frac{\sigma_\tau}{\bar{\tau}}, \tag{2.1}$$

where $\bar{\tau}$ and σ_τ are the average ringdown time and the 1σ standard deviation of the ringdown time, respectively. The ringdown baseline noise, which is typically on the order of 10^{-3}, can be calculated by $\sigma_\tau/\bar{\tau}$ and is comparable to the minimum light intensity change ($\Delta I/I_0$) in a conventional intensity-based sensing scheme. Sensitivity of the EF-FLRD sensors can be enhanced by a factor of m which depends on the loop's physical parameters and fabrication design of the loop.

A FLRD system consists of a SMF (SMF 28e, Corning, Inc), two identical 2×1 fiber couplers (Opneti Communication Co.) fabricated with a split ratio of 0.1:99.9 in the 2-leg end of the fiber couplers, a CW diode laser source (NLK1S5AAA, NEL America, Inc), an InGaAs photodetector (Thorlabs, PDA50B), an oscilloscope (Tektronix 410A), and an electronic controller. The cladding and the core diameters of the SMF are 125 μm and 8 μm, respectively. Figure 2.1 shows a schematic illustration of the EF-FLRD biosensor system and setup.

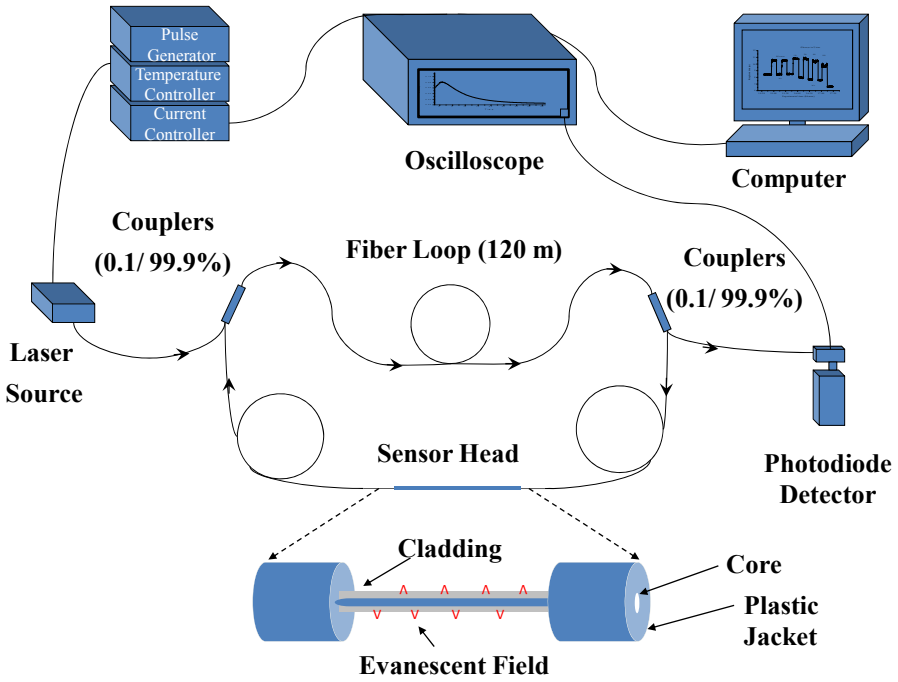

Figure 2.1 Schematic illustration of the EF-FLRD biosensors and side view of the sensor head.

Typical splicing loss was between 0.02 - 0.04 dB in the fabrication step of the sensor head and the total optical loss of the loop, including the absorption loss, fiber connectors' losses, and fiber couplers' losses, was estimated to be <0.45 dB. The length of the fiber loop was 120 m. Generated laser pulses from laser source (1515 nm at 25 ^{o}C) with a 10 Hz pulse rate and a 20 ns pulse width were coupled into the fiber loop through the first 0.1% coupler with an FC/APC connector. The second 0.1% coupler was connected to the photodetector. The amplification of the detector was set at 50 dB signal-to- noise ratio with the minimum detectible power of 10 nW. The laser diode wavelength was precisely tuned to 1515.15 nm with a measurement accuracy of 0.001 nm.

2.1.2 Sensor Head Fabrication Process

Plastic jackets of the two ends of the fiber loop were removed after the loop was cut from somewhere in the middle of the fiber loop and the ends were cleaned with methanol. Lengths of the two ends were arranged, depending on desired sensor head lengths which were in the 9 to 22 cm range in this work. A section of the SMF made by splicing the ends with 0.02 - 0.04 dB estimated splicing loss was etched in 48% HF acid solution for 33 - 34 min. The etching process was continuously monitored in real-time. The etching process was controlled by monitoring the ringdown time in terms of the etched fiber diameter [27].

2.1.3 Response of the Biosensors

The response of the sensor heads to the biological sample solutions was investigated. Three types of DNA samples were used in this study. Sample 1 (S1) and Sample 2 (S2) were 26 base pairs single strand DNAs (ssDNA). The other DNA sample (S3) was a combination of S1 and S2, 26 base pairs double strand DNA (dsDNA).

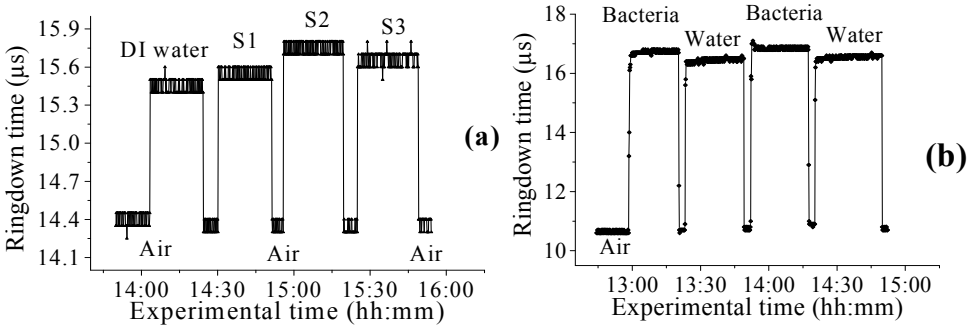

Figure 2.2 Bulk RI-based FLRD sensors for (a) DNA and (b) Bacteria sensing.

Figure 2.2 (a) and (b) show typical responses of the sensor head to different media, such as air, DI water, DNA samples, and bacteria. In Figure 2.2 (a), the response of the EF-FLRD sensors to diluted 30 μM DNA samples in DI water is shown. Another diluted concentration is shown somewhere else [27]. The results show that different DNA solutions with the same concentration have different RIs and the EF-FLRD sensors can distinguish the differences. Figure 2.2 (b) shows the response of the sensor to bacteria and DI water solutions. The sensor can clearly discriminate the two different media, bacteria and DI water. Both figures represented bulk RI-based sensing and showed fast response (<1 s) and good reversibility.

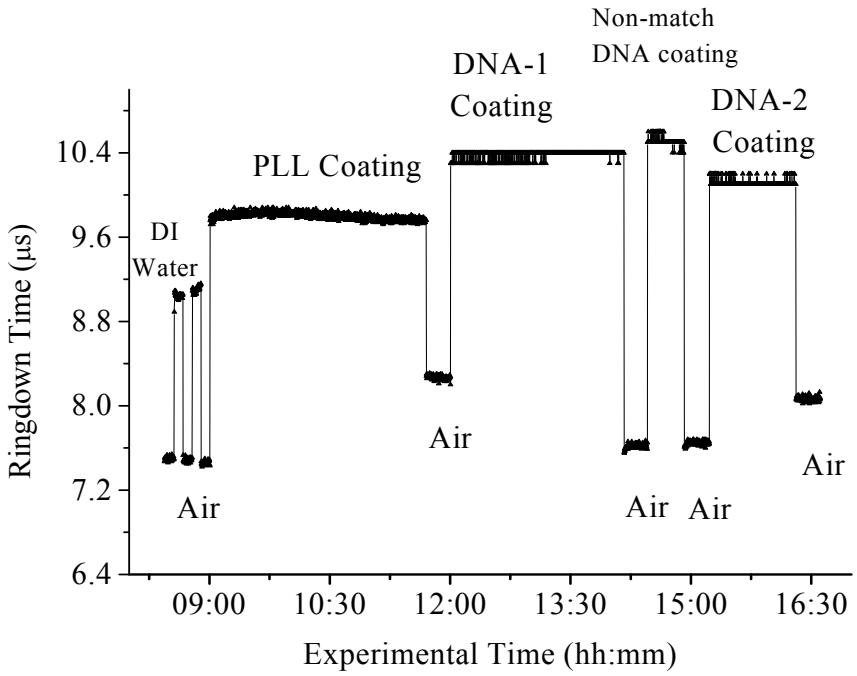

Figure 2.3 Surface RI-based FLRD sensor for label-free DNA sensing.

Using a coating method similar to the technique reported by Jang *et al.* [81] and Chen *et al.* [82], we investigated the feasibility of label-free DNA sensing by the sensor. The partially-etched fiber was first cleaned with phosphate-buffered saline solution (NaH_2PO_4/Na_2HPO_4 *p*H 7.4, 150 mM) (PBS). In order to be effectively coated with poly-L-lysine (PLL) solution (0.1% W/V in water, the molecular weight = 150,000 to 300,000 g/mol), the sensor head was immersed in PLL for 160 min. The sensor head was then cleaned with PBS to remove excess PLL and immersed for 130 min in 20 μm ssDNA S1. Again cleaning with PBS, the sensor head, which was then coated with S1 (the probe DNA), was ready for sensing the matched S2 (the target DNA). The entire coating process was performed at room temperature and the ringdown data was continuously collected throughout the experiment. Since the positively charged NH_3^+ in the PLL chain is binding to the negatively charged DNA, and the probe DNA (S1) selectively binds with the target DNA (S2), the potential label-free DNA sensing should be achievable by the new sensor described in this work. In the experiment, before the sensor head was used to sense the target DNA, the sensor head was immersed in the non-matched DNA S3 with a total concentration 20 μMm (S1 + S2) for 65 min; S3 solution was then removed and the sensor head was cleaned with PBS. Next, the same sensor head was immersed in 20 μM target DNA for 65 min and then cleaned with PBS. Figure 2.3 presents the measured ringdown times in each stage of the coating process, which denote prior-coating (in air), in-PLL-solution, PLL-coated, in-S1 solution, S1-coated, in-S3 solution, S3-coated, in-S2 solution, and S2-coated, respectively. The different coating effects in terms of changes in RI are clearly depicted by the different ringdown times observed.

The sensor head length, diameter of the etched fiber, and the physical parameters can affect the detection sensitivity of the sensor. In this work, a new type of biosensor based on the FLRD technique was presented. Both bulk RI-based and surface RI-based DNA sensing and one type of bacteria sensing are demonstrated. High sensitive, low cost, and near real-time response biosensors were created by using the FLRD technique.

2.1.4 Conclusions

A new type of biosensor based on the FLRD technique has been demonstrated in this work. The bulk RI-based detections of three DNAs and one type of bacteria and the surface RI-based label free detection of DNA are successfully presented. We expect an array of low cost, near-real time response, and high sensitivity fiber optic biosensors using the FLRD technique to be created.

2.2 The EF-FLRD Glucose Sensor

In this work, high sensitive, fast response, and low cost EF-FLRD-based biosensors with sensitivity-enhanced ringdown detection scheme were fabricated and developed. A new FLRD glucose sensor was described. EF attenuation effect due to RI-difference was utilized as the sensing mechanism. Two types of sensor heads were employed; a section of etched single mode fiber and GOD immobilized on partially-etched fiber. The GOD coating effect on the sensor's performance was evaluated. Responses of the sensors to standard glucose solutions and different glucose concentrations in synthetic urine solutions from 0.05% to 10% were studied. The sensor response to different glucose concentrations is non-linear between 1 - 10% and linear between 0.1 - 1%. Finally, the detection limits of the sensors for glucose and synthetic

urine solutions are determined to be 0.075% and 0.05%, respectively. The estimated theoretical detection limit for the EF-FLRD glucose sensor is 0.1%. When this limit is compared to the glucose renal threshold concentration which is 1.6 - 1.7% [83, 84], estimated theoretical detection limit measured in this work is approximately 17 times lower.

2.2.1 Principle of the EF-FLRD Glucose Sensor

After a laser pulse is injected into a fiber loop in a FLRD system, the detector receives an output signal the behavior of which can be modeled by Equation (1.3) which is

$$\frac{dI}{dt} = -\frac{IAc}{nL}, \tag{2.2}$$

where I is the light intensity, L is the total length of the fiber loop, c is the speed of light in vacuum, n is the average refractive index of the fiber loop, and A is the total fiber transmission loss of the light. Behavior of the light intensity detected by the detector is given by the solution of Equation (2.2).

$$I = I_0 e^{-\frac{c}{nL}At}. \tag{2.3}$$

The FLRD technique measures the decay rate of the light intensity, not the absolute intensity change, ΔI. Hence, the total fiber transmission loss, A, measurement is insensitive to incident light intensity fluctuations, I_0. Ringdown times in air and in any solution are given by

$$\tau_0 = \frac{nL}{cA}, \tag{2.4}$$

$$\tau = \frac{nL}{c(A+B)}. \tag{2.5}$$

When the sensor is sensing any quantities, the light pulse in the fiber loop will have an additional optical loss, *B*, which changes the ringdown time in Equation (2.5) and additional optical loss can be calculated from Equations (2.4) and (2.5):

$$B = \frac{nL}{c}\left(\frac{1}{\tau} - \frac{1}{\tau_0}\right). \tag{2.6}$$

If *B* is due to an EF attenuation which is a result of EF absorption, scattering, or both [85] of the transmitted light through the sensor head, Equation (2.6) becomes:

$$B_{EF} = \frac{nL}{c}\left(\frac{1}{\tau} - \frac{1}{\tau_0}\right) = l_e(\gamma_\alpha + \gamma\ ) \tag{2.7}$$

where l_e is the sensor head length, γ_α and γ_β are the light attenuation coefficients due to EF absorption and EF scattering, respectively. If there is no EF absorption, then only the EF scattering effect generates the EF attenuation. Several features of the sensor head affect the EF scattering loss, such as EF penetration dept, the fiber core diameter, and distinctive refractive index of the fiber core and of the cladding. The EF scattering loss for a given EF-FLRD sensor is calculated by the index difference which is $\Delta n = (n_{fibercore} - n_{medium})$; the smaller the index difference, Δn, the longer the ringdown time and therefore, the lower the EF scattering loss [86, 87]. Whenever medium refractive index is equal to the fiber cladding index, the EF attenuation *B* at the sensor head has its minimum value.

In this study, surface index-based and bulk index-based sensing [88] are examined in the development of the sensor heads. First, GOD was immobilized on the surface of

the senor head. Due to reaction between GOD and glucose when the GOD immobilized sensor was immersed into different glucose concentrations, gluconic acid was generated. Therefore, refractive index around the sensor head changed. The chemical reactions are given by [89]:

$$Glucose + O_2 \xrightarrow{GOD} Gluconolactone + H_2O_2, \tag{2.8}$$

$$Gluconolactone + H_2O \longrightarrow Gluconic\ acid. \tag{2.9}$$

Bulk index-based sensing technique is based on immersing the sensor head directly into the solution. The index difference between fiber core and the glucose solution causes the EF attenuation which is determined by observing ringdown time change. In both techniques, the optical loss of the sensor due to the EF attenuation is given by:

$$\Delta B_{EF} = \frac{nL}{c}\left(\frac{1}{\tau^{glcs}} - \frac{1}{{\tau_0}^{air}}\right), \tag{2.10}$$

where ${\tau_0}^{air}$ term represents the ringdown time when the sensor head is in air, τ^{glcs} term represents the ringdown time when the sensor is immersed into any solution which is a glucose solution in Equation (2.10), ΔB_{EF} presents an absolute difference of the EF attenuations when the sensor head is in air and in glucose solution. ΔB_{EF} is negative when the measured ringdown time in glucose is higher than measured ringdown time in air, ${\tau_0}^{air} < \tau^{glcs}$. Equation (2.10) can be modified [29] because each glucose solution has a different refractive index due to different concentration:

$$\Delta B_{EF} = S_0 + S_1 C + S_2 C^2, \tag{2.11}$$

where the *S* terms are constants and *C* is the concentration of the glucose solution (in % or mg/dl) in DI water or in synthetic urine sample. If there is no glucose in solution, ΔB_{EF} shows only the EF attenuation difference of the sensor in air and in DI water or synthetic urine. For low glucose concentrations, the S_2C^2 term in Equation (2.11) can be neglected and thus, ΔB_{EF} and *C* will show linear behavior under the first order approximation. For high glucose concentrations, the S_1C term can be disregarded and the equation will show a nonlinear behavior. Equations (2.10) and (2.11) show the working principle of the studied EF-FLRD glucose sensor. Equation (2.11) is confirmed by determining the EF attenuation versus in high and in low glucose concentrations, 1 - 10% and 0.1 - 1%, respectively.

2.2.2 Response of the EF-FLRD Glucose Sensors in Standard Glucose Solutions and Glucose in Synthetic Urine Solutions

The responses of the EF-FLRD glucose sensors in both standard glucose solutions and different glucose concentrations in synthetic urine solutions were studied in this part. GOD was immobilized on the surface of the sensor head through a stepwise approach [90]. In order to immobilize GOD, the sensor head surface was treated with an ethanol solution of amino linkage aldehyde group, 1% 3-propyl aldehyde, for around 30 min. Then, the modified sensor head was immersed into a 10 µg/ml GOD solution for 1 h at room temperature. A 15 mM Tris buffer (T-B) solution was used for 10 min to remove un-reacted particles on the sensor head. The entire stepwise process was monitored by continuously recording ringdown times. The sensor head with the immobilized GOD were immersed into different concentrations of glucose solutions which were prepared by diluting a standard 10% glucose sample in DI water. Before synthetic urine samples were

prepared by adding 10% glucose solution into synthetic urine samples in different concentrations, synthetic urine samples were heated around 8 second in a microwave up to 37 ^{o}C. The temperature of the urine samples was kept at ~37 ^{o}C during test by using a heating pad which can maintain temperature up to 8 hrs.

2.2.2.1 Glucose Detection in Glucose Solutions

Figure 2.4(a) and (b) show the results of two repeated experiments using two FLRD glucose sensors with GOD coatings on the sensor heads. Each of the graphs shows the sensor's response during the entire process, switching the etched bare sensor head between water and air, treating of the sensor head using 1% aldehyde groups, immobilizing GOD, removing the un-reacted aldehyde groups using a T-B solution, and testing the sensor head in air and different glucose solutions. The graph in Figure 2.4(a) is marked in nine different zones, A-I. For example, zone A shows the sensor's reproducible behavior when the sensor head was exposed to DI water and air. Due to the different index differences, Δn ($n_{fibercore} - n_{medium}$), the sensor read different ringdown times. $\Delta n \approx 1.4491 - 1.0 = 0.4491$ when the sensor head was in air, and $\Delta n \approx 1.4491 - 1.3330 = 0.1161$ when the sensor head was immersed in DI water. The 1.4491, 1.3330, and 1.0 are the refractive indices at 1515 nm of the fiber core, DI water, and air, respectively. The, ≈, denotes that the fiber core in this study was actually an effective fiber core that consisted of the SMF core and the un-etched fiber cladding. The index of the effective fiber core should be slightly different from the index of the SMF core. In the text below, the fiber core at the sensor head is the effective fiber core. The smaller index difference between the fiber core and DI water corresponds to a lower EF attenuation and results in a longer ringdown time, as shown in zone A. In the upper parts of zones B-D,

the sensor read different ringdown times due to different refractive indices of the 1% aldehyde, the GOD, and the T-B solutions. Comparison of the lower parts in zones B-D with the lower parts of zone A shows a noticeable difference in ringdown time. For example, when the sensor head was exposed to air, the lower part of zone C, right after the 1 h immersion in GOD solution, the observed ringdown time was 0.06 μs longer than the recorded ringdown time when the sensor head was exposed to air before the GOD coatings, the lower part of zone A. This ringdown time difference indicated that the sensor head had been effectively modified by the immobilized GOD. In other words, the immobilization of GOD had changed the refractive index of the fiber surface. After a 10 min treatment of the un-reacted aldehyde using the T-B solution, the observed ringdown time dropped after the sensor head was removed from the T-B solution and placed in air. Without knowing the actual indices of the aldehyde groups, T-B solution, and the immobilized GOD layer, the different ringdown times indicated that those chemicals had different indices. Based on the one-σ standard deviation of the recorded ringdown time, which was 0.03 μs at 8.33 μs, the small ringdown time differences resulting from the different treatments, GOD and T-B, were noticeable.

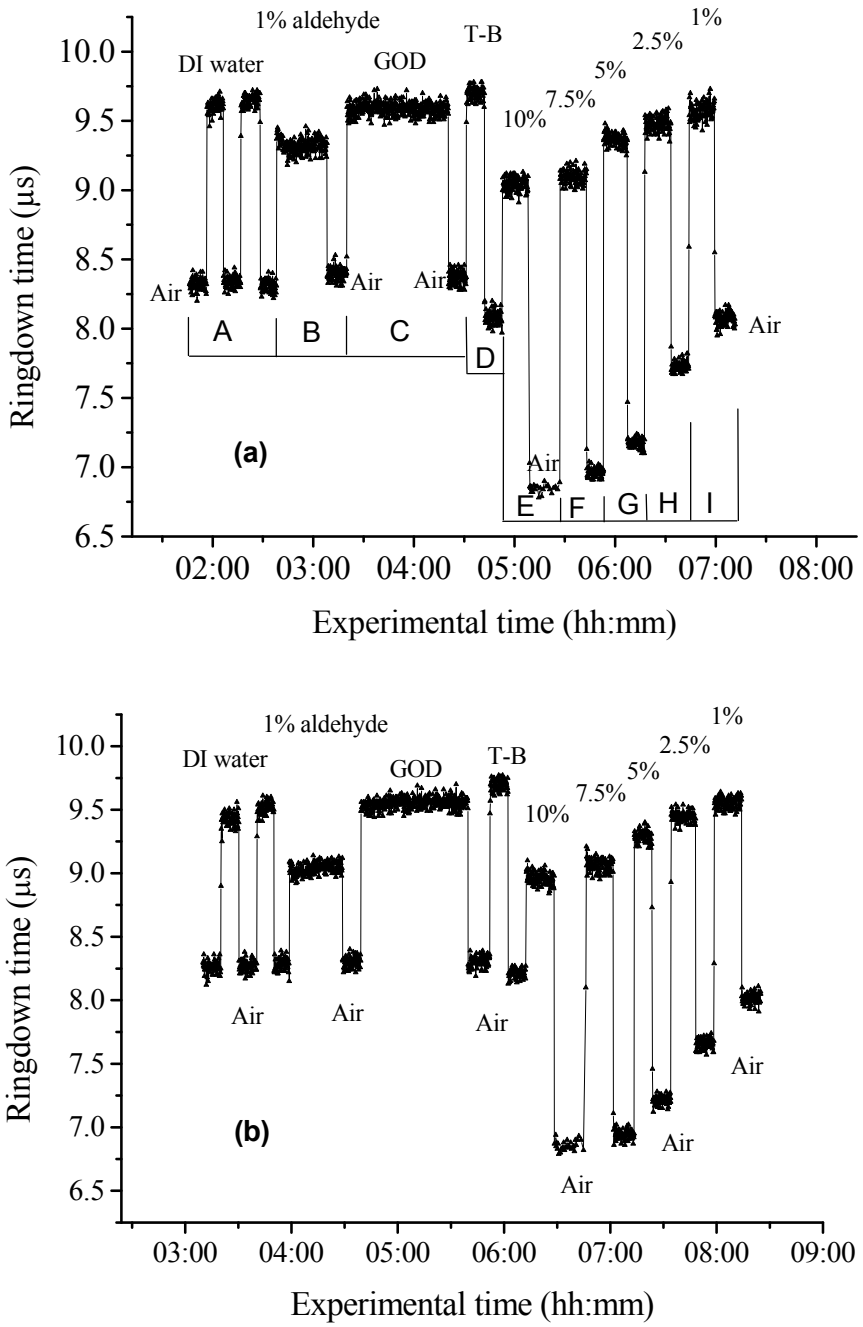

Figure 2.4 Response behavior of two EF-FLRD glucose sensors.

Both sensors had a GOD coated sensor head. Zones A to D: fabrication of the sensor head; zones E-I: the sensor's responses to the glucose solutions with different concentrations. (a) and (b) show the repeated experiments using two glucose sensors.

Zones E-I show the sensor's responses to a change in the external media, such as when the sensor head was immersed in a 10% glucose solution for 12 min and then exposed to air for 12 min as shown by zone E in Figure 2.4(a). Similar testing processes were repeated by exposing the sensor head to both air and different glucose solutions, zones F-I. The sensor read different ringdown times,τ^{glu}, when the sensor head was immersed in different concentrations of glucose solutions. For instance, the observed ringdown time changed from 9.06 μs for the 10% glucose concentration to 9.58 μs for the 1% glucose concentration. One noteworthy point was that the sensor did not read the same ringdown time, τ_0^{air}, when the sensor head was exposed to air right after being removed from different glucose solutions, as shown in the lower parts of zones E-I. Comparison of different pairs of τ^{glu} and τ_0^{air} obtained in each of the cases, E-I, shows that the sensor gave clearly different responses to the different glucose concentrations ranging from 1% to 10%, which correspond to 1g⁄dl to 10 g⁄dl.

Figure 2.4(b) shows the results of the repeated experiment using a second sensor unit. Although the quoted specifications of the two fiber loops were the same, after a series of the lab-based fabrication processes of the sensor heads, such as etching, coating, and splicing, a small difference in the total optical loss between the two loops existed. Therefore, a noticeable difference between the ringdown time baselines, τ_0^{air}, of the two sensors was observed. However, the two sensors' response behavior was reproducible. For example, the response time to a change in the external media and the general trend of the sensor's response to different glucose concentrations were all reproducible. The experimental data were generated when the laser pulse repetition rate was set at 10 Hz. Each data point shown in Figure 2.4 was collected by averaging over 100 ringdown

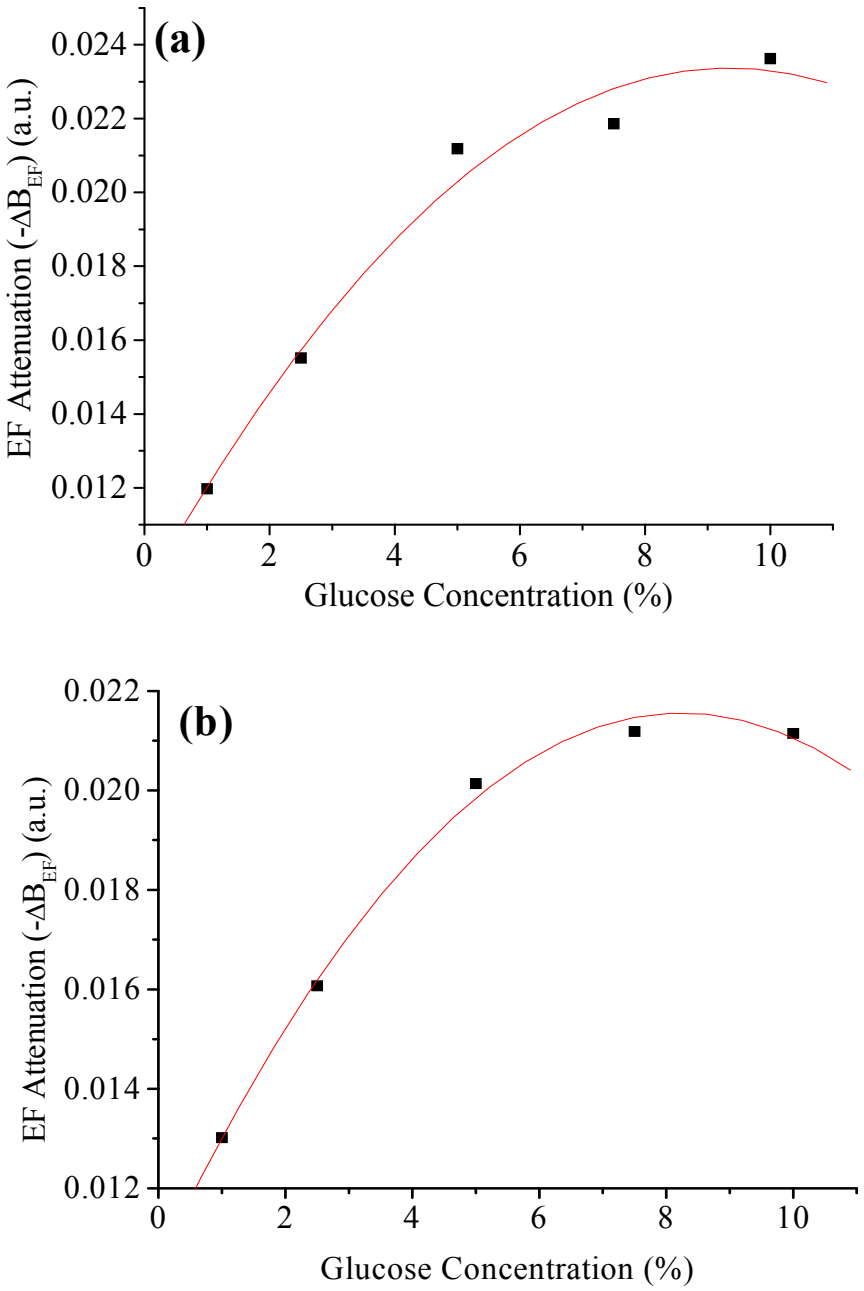

Figure 2.5 The measured EF attenuation difference ΔB_{EF} versus glucose concentration C in glucose solutions.

The dot denotes the experimental data and the line denotes a second order polynomial fitting. (a) The data was from Figure 2.4(a); (b) the data was from Figure 2.4(b). Both sensors showed a non-linear relation between ΔB_{EF} and C in the glucose concentration range of 1% - 10%. The observed trend was consistent with the proposed expression shown in Eq. (2.11).

events, 100 measurements, and the observed time interval between two adjacent data points in Figure 2.4 was 10 s. With this setting, the sensors' response time was ~0.1 s or ~10 Hz.

Figure 2.5(a) and (b) show the curves of the EF attenuation, a.u., versus glucose concentration, %. The y-axis relates to the absolute value of ΔB_{EF} defined in Equation (2.10). ΔB_{EF} was determined by inserting the ringdown time measured in air, τ_0^{air}, and the ringdown time obtained in a solution, τ^{glu}, marked in each zone into Equation (2.10). For instance, in Figure 2.4(a), τ_0^{air} and τ^{glu} in zone E are 6.84 μs and 9.06 μs, respectively and the absolute value of ΔB_{EF} is 0.0236, a.u. The fitted curves in Figure 2.5(a) and (b) show a nonlinear relationship between the EF attenuation and the glucose concentration in the examined range. In Figure 2.5(b) especially, the signal seemed to be saturated in the higher concentration end of the graph. It should be noted that, no glucose samples at concentrations higher than 10% were used in this study. This non-linear relationship is consistent with our proposed expression given in Equation (2.11).

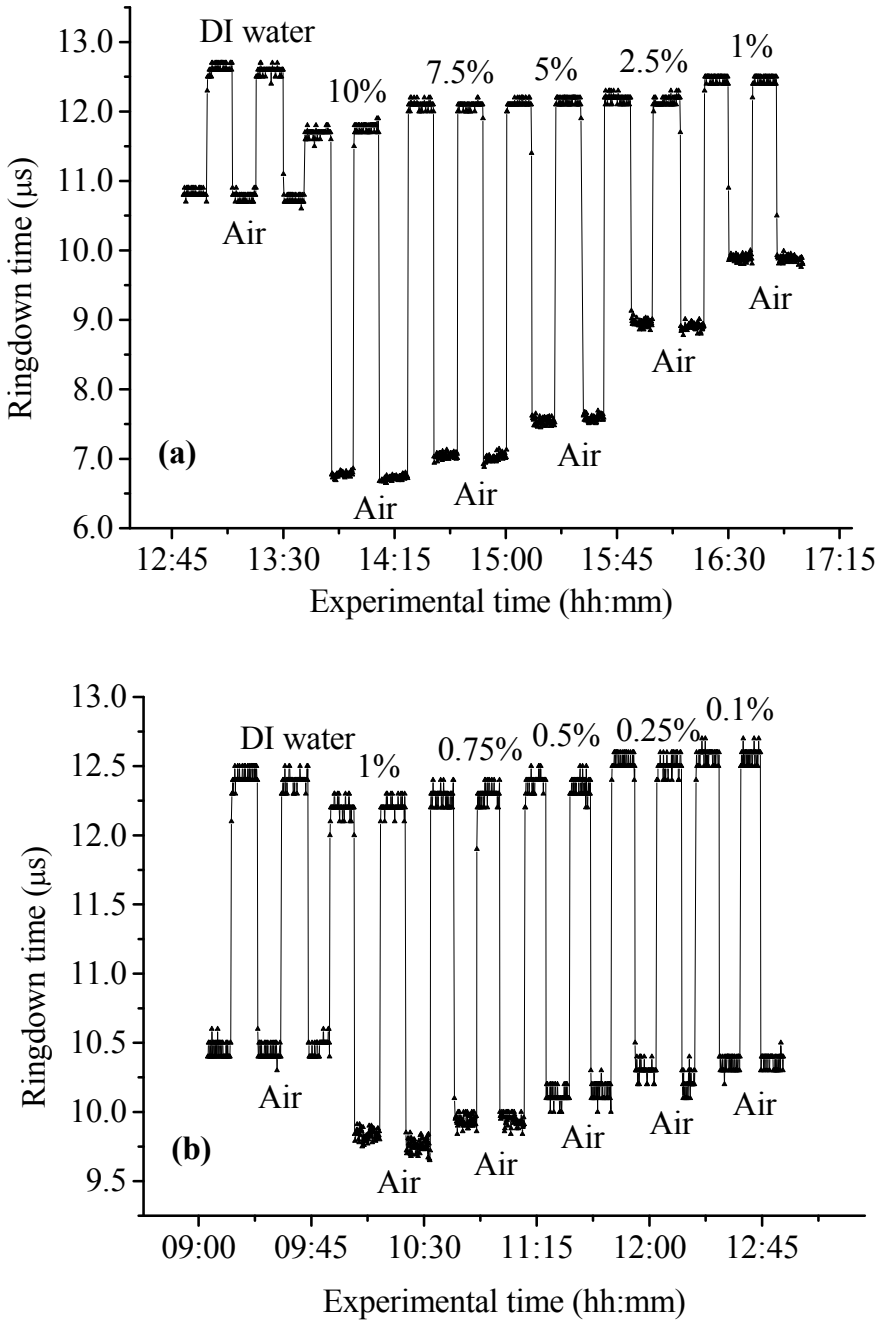

Figure 2.6 Response behaviors of two EF-FLRD glucose sensors, which had no GOD coatings at the sensor heads.

(a) Glucose concentration ranged from 1% to 10%; and (b) glucose concentration ranged from 0.1% to 1%.

In order to compare the effects of the GOD coatings on the performance of the FLRD glucose sensors, two additional FLRD glucose sensors were fabricated using an etched bare SMF as the sensor head, and their responses to different glucose concentrations were also investigated. Figure 2.6(a) and (b) show the responses of these FLRD glucose sensors. Figure 2.6(a) shows the sensor's response when the sensor head was switched between an external medium, DI water or a glucose solution, and air. For each tested medium, DI water or a glucose solution, the sensor was tested twice. In each case, the sensor showed good reproducibility. The sensor's overall behavior was similar to the ones shown in Figure 2.4. For instance, clear differences in the observed ringdown times were observed when the sensor head was immersed in different concentrations of glucose solutions ranging from 1% to 10%. Similarly, the lower parts of the graph showed clear differences in the ringdown baseline,τ_0^{air}, when the sensor head was removed from a glucose solution to air. This behavior was the same as ones observed in the tests with the GOD-coated sensors. The similar response behavior of the sensors with and without the GOD coatings indicates that the different τ_0^{air} observed after the sensor head was removed from different glucose solutions, was not due to the immobilized GOD but rather related to glucose and dependent on the glucose concentration. For example, when the sensor head was removed from a 1% glucose solution and placed in air, the observed ringdown time was clearly different from the observed ringdown time of the sensor head that was placed in air after removal of DI water. One possible explanation for this observed behavior is that when the sensor head was removed from a glucose solution, a very small amount of glucose solution remained on the surface of the sensor head to form a thin film. In the presence of atmospheric oxygen, this glucose film reacted

with the atmospheric oxygen, changing the surface index of the sensor head. The change was even affected by the concentration of the glucose solution. The observed behavior in Figure 2.6(a) was also repeated when the other FLRD glucose sensor, the second sensor without the GOD coatings, was tested with glucose solutions in much lower concentrations, 0.1 - 1% or 100 mg⁄dl - 1 g⁄dl. The results are shown in Figure 2.6(b).

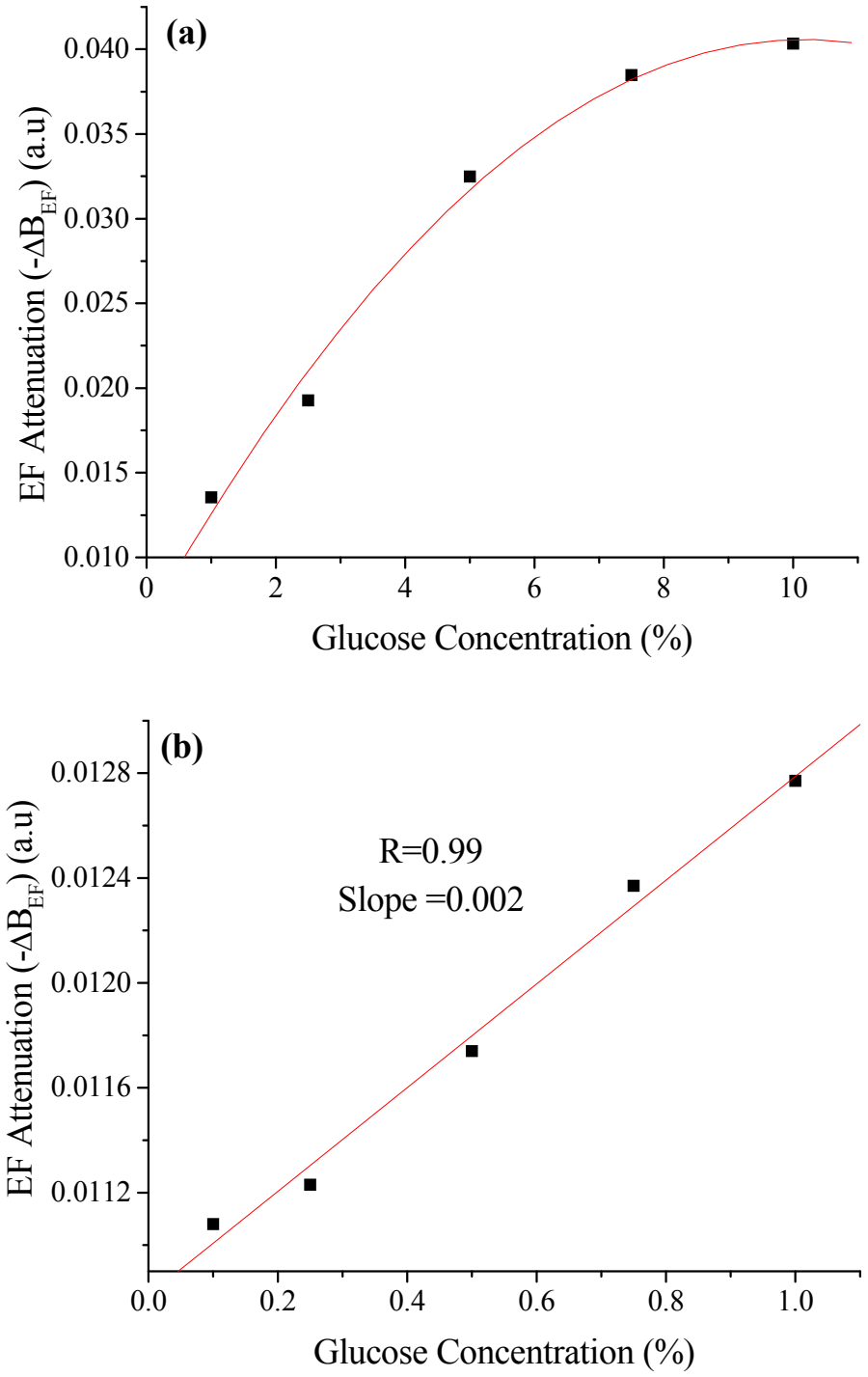

Figure 2.7 The measured EF attenuation difference ΔB_{EF} versus glucose concentration *C* in glucose solutions.

The dot denotes the experimental data and the line denotes the fittings. (a) The data was from Fig. 2.6(a); the sensor showed a non-linear relation between ΔB_{EF} and C in the glucose concentration range of 1% to 10%. (b) The data was from Figure 2.6(b); the sensor showed a linear relation between ΔB_{EF} and C in the glucose concentration range of 0.1% to 1%.

Figure 2.7(a) and (b) show the curves of the measured EF attenuation versus glucose concentration. Similar to the results obtained with the sensors coated with GOD, non-linearity was shown in glucose concentrations ranging from 1% to 10% or from 1 g⁄dl to 10 g⁄dl. However, the experimental data shown in Figure 2.7(b), in which the glucose concentration ranged from 0.1% to 1% gave a good linearity, R = 0.99. This result indicates that the FLRD glucose sensor has a linear response to the glucose concentration when the concentration is lower than 1%. This linear response to the low glucose concentration is consistent with the first order approximation of the expression given in Equation (2.11).

Comparison of the results shown in Figure 2.4 and Figure 2.6 supports that FLRD glucose sensors, both with and without immobilized GOD on the surface of the sensor head, displayed similar performances in terms of reproducibility, response time, and the relationship between EF attenuation and glucose concentration.

2.2.2.2 Glucose Detection in Synthetic Urine Samples

Two additional FLRD glucose sensors were also fabricated for testing with synthetic urines. One of the sensors had a GOD coated sensor head and the other did not have a GOD-coated sensor head. In the experiments, 10% standard glucose solution was added to the synthetic urine to form urine samples with different glucose concentrations ranging from 0.1% to 10%. The sensor with a GOD-coated sensor head was tested with glucose solutions in the concentration range of 0.1% - 1%. The results of the sensor's response are shown in Figure 2.8. Clearly, similar response behavior was observed and the sensor could sense synthetic urine with a glucose concentration as low as 0.1%, 100 mg⁄dl. It should be noticed that the immobilization of GOD on this sensor head skipped

the pre-treatment with 1% aldehyde groups, but it seemed that the GOD was effectively coated. Figure 2.9 shows the curve of the EF attenuation versus urine glucose concentration. The fitted result shows good linearity of the sensor's response in the urine glucose concentration range of 0.1% - 1%. This result further validated the first order approximation of Equation (2.11). Comparison of the results in Figure 2.7 and Figure 2.9 supports the notion that EF-FLRD glucose sensors with and without GOD coatings on the sensor head have a linear response to glucose concentration in the range of 0.1% to 1.0%.

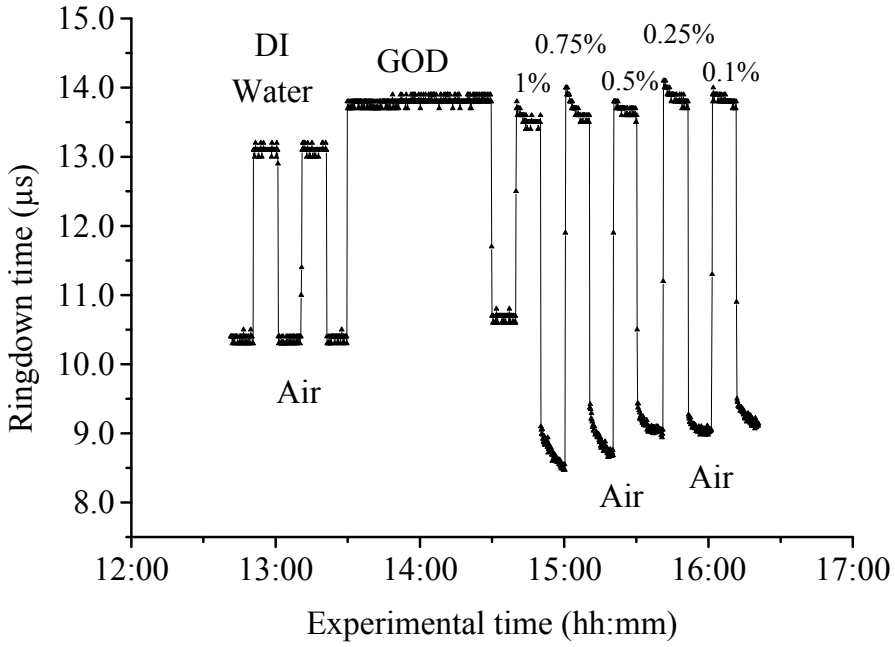

Figure 2.8 Response behavior of an EF-FLRD glucose sensor.

The sensor had GOD coatings at the sensor head. The sensor was tested with the synthetic urine samples in different glucose concentrations ranging from 0.1% to 1%.

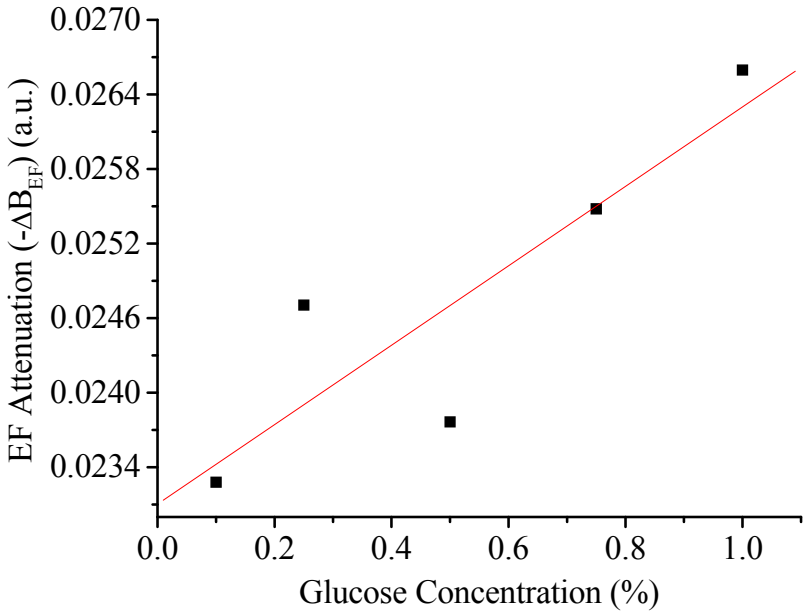

Figure 2.9 Linear response of an EF-FLRD glucose sensor to the synthetic urine samples in different glucose concentrations ranging from 0.1% to 1%. The dot denotes the experimental data and the line denotes a linear fitting.

The other FLRD glucose sensor, which had no GOD coatings at the sensor head, was also tested with synthetic urine with urine-glucose concentrations of 1% to 10%. For each concentration, two tests were conducted and good reproducibility was obtained. The sensor demonstrated (in Figure 2.10) the behavior previously shown by other non-GOD-coated FLRD glucose sensors in glucose solutions. The results in Figure 2.10 also yielded a nonlinear curve of the EF attenuation versus glucose concentration that are similar to the curves shown in Figure 2.5 and Figure 2.7. This result further confirmed that the EF-FLRD glucose sensors gave a non-linear response for 1% to 10% glucose concentrations, as predicted by Equation (2.11).

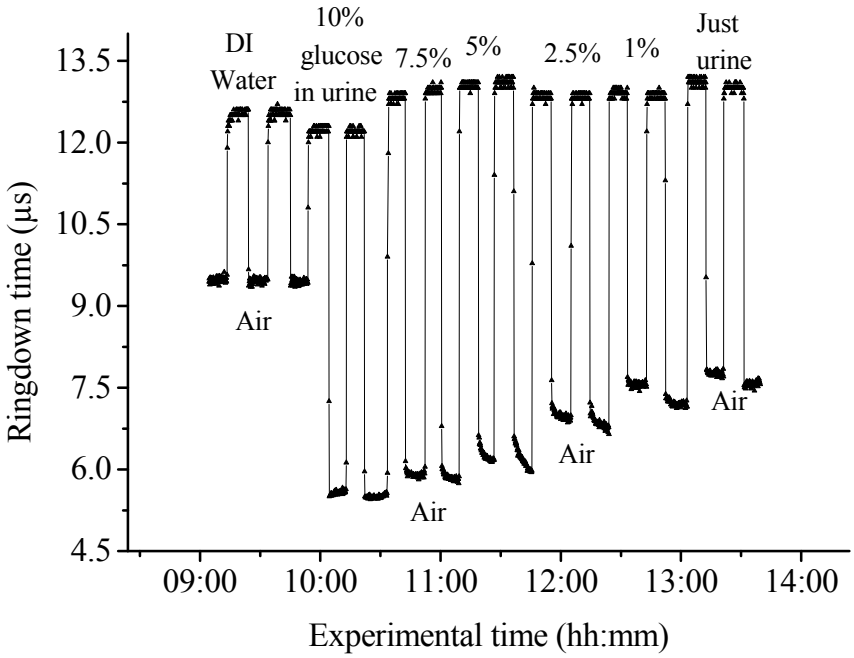

Figure 2.10 Response behavior of an EF-FLRD glucose sensor.

The sensor had no GOD coatings at the sensor head. The sensor was tested with the synthetic urine samples in different glucose concentrations ranging from 1% to 10%.

Comparison of the results shown in Figure 2.8 and Figure 2.10 suggests that FLRD glucose sensors both with and without the GOD coatings on the sensor head gave similar response behaviors when tested in synthetic urine samples in 0.1% to 10% glucose concentrations. Further comparison of the results obtained using the EF-FLRD glucoses sensors with and without GOD coatings suggests that for this particular type of index-based sensors, the GOD coatings on the sensor head were not crucial to their performance.

2.2.2.3 Detection Sensitivity of the EF-FLRD Glucose Sensors

Detection sensitivity of the EF-FLRD glucose sensors was also investigated. Two additional EF-FLRD glucose sensors without GOD coatings at the sensor head were fabricated to investigate the best experimental detection sensitivity in glucose solutions

and in artificial urines. These two sensor heads had an etched fiber length of 22.0 cm. As shown in Figure 2.11, the sensor was first tested in DI water, which showed good reproducibility, before being switched between a 0.075% glucose solution and air. Reproducible ringdown signals were obtained and a difference between the sensor's response to DI water-air and 75 mg⁄dl solution-air was noticeable. The result indicated that the detection sensitivity of this EF-FLRD sensor without GOD coatings was 75 mg⁄dl. The other EF-FLRD glucose sensor was tested in the synthetic urine with a glucose concentration of 50 mg⁄dl, and the results are shown in Figure 2.12. The sensor gave reproducible results and had a fast response, ~0.1 s as well as a detection sensitivity of 50 mg⁄dl.

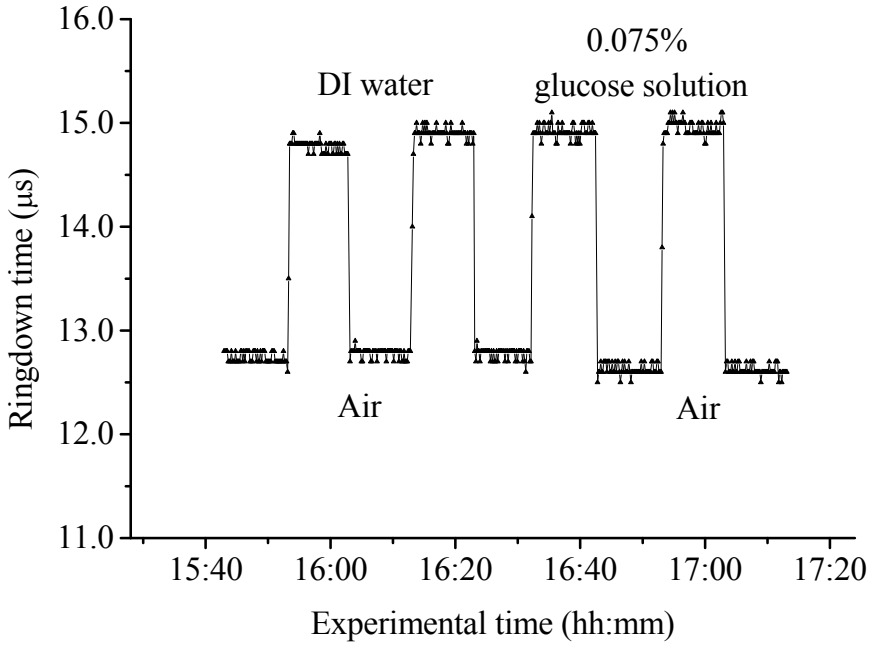

Figure 2.11 Detection sensitivity of an EF-FLRD glucose sensor in a glucose solution with a concentration of 0.075% or 75 mg/dl.

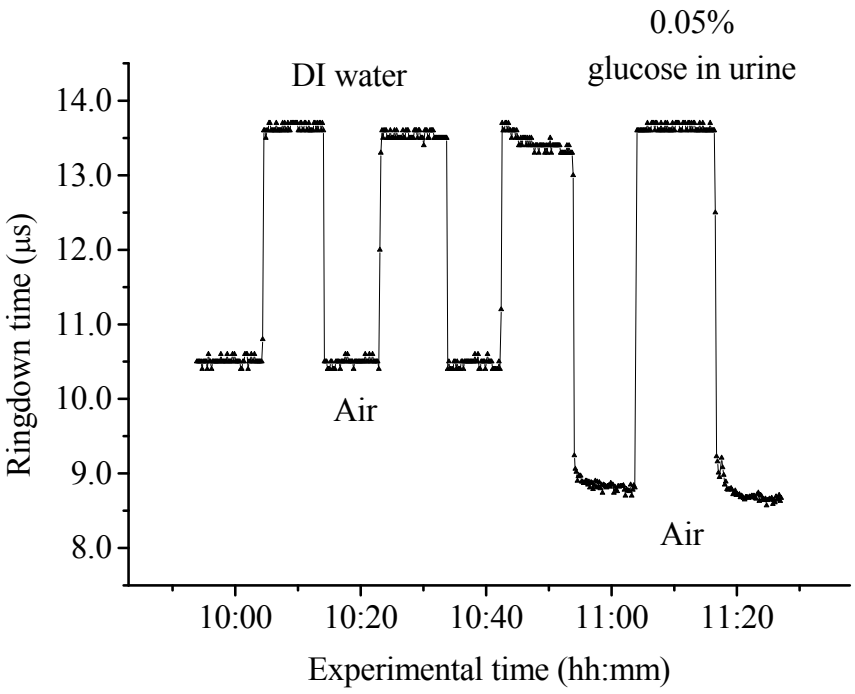

Figure 2.12 Detection sensitivity of an EF-FLRD glucose sensor in a synthetic urine sample with a concentration of 0.05% or 50 mg/dl.

Current fiber optic glucose sensors using different sensing schemes and different sensing mechanisms, including a variety of GOD-based approaches, such as fluorescence [91], fluorescence quenching [92], and sol-gel matrix [93], have achieved a wide range of experimental detection sensitivities, from g/dl to mg/dl. The best experimental detection sensitivities of index-based fiber optic glucose sensors were 10 mg/dl in glucose solution samples and 34 mg/dl in serum based samples reported by Lin *et al.* [90]. Their sensor's response time was less than 3 s. These experimental detection sensitivities can be potentially improved up to 0.1 mg/dl and 0.136 mg/dl in glucose solutions and serum based samples, respectively, if the minimum detectable phase difference is 0.02-degree.

That corresponds to a minimum detectable refractive index unit of approximately 2×10^{-6}, extrapolated from the reported data [90].

A theoretical detection sensitivity of the refractive index difference EF-FLRD glucose sensors can also be estimated. The detection sensitivity of the EF-FLRD sensors can be characterized by the minimum detectable EF attenuation. By using Equations (1.9) and (1.10), the minimum detectable optical loss B_{min}, which is defined as the one-σ detection limit, can be found by:

$$B_{min} = \frac{1}{m}\frac{\sigma_\tau}{\tau}, \tag{2.12}$$

which is Equation 1.12, where σ_τ is the one-σ standard deviation of the ringdown time. σ_τ/τ can be experimentally achieved at 1×10^{-3}, which is a typical level of the minimum detectable change in light intensity, $\Delta I/I_0$, in a conventional intensity-based sensing scheme. For a 120 m long ringdown loop consisting of a standard telecommunications SMF-28e fiber with refractive indices of 1.4491 and 1.4441, respectively, for the fiber core and cladding at 1515.25 nm, the round trip time, t_r, is 580 ns. If the measured ringdown time in the fiber loop is $\tau_0 = 25.0$ μs [27], the number of multiple passes is 43. Thus, based on Equation (2.12), the minimum detectable change in the EF attenuation is:

$$\Delta B_{EF}^{min} = \frac{1}{m}\frac{\sigma_\tau}{\tau} = 2.3 \times 10^{-5}. \tag{2.13}$$

From Figure 2.7(b), for example, we obtain a slope of the curve, S = 2.0×10^{-3} (1/%). Therefore, a detection sensitivity of glucose concentration ΔC_{min} based on the ΔB_{EF}^{min} is determined by:

$$\Delta C_{min} = \frac{\Delta B_{EF}^{min}}{S} = \frac{2.3\times10^{-5}}{2.0\times10^{-3}} \approx 0.01\% = 10\ mg/dl. \tag{2.14}$$

The theoretical detection sensitivity is approximately 17-times lower than the blood glucose renal threshold, which is approximately 170 mg/dl [94]. When the blood glucose exceeds this renal threshold value, the glucose becomes present in human urine. It must be noted that the glucose sensors studied in this work are based on sensing changes in the refractive index. At 20 °C, the refractive index of a glucose solution changes approximately 0.0000225 RIU for every 0.01% change in glucose concentration [95]. When an index-based glucose sensor has a detection sensitivity that is better than 0.01% as estimated in Equation (2.14), the temperature effect on the refractive index of glucose solutions or urine samples must be considered. The temperature coefficient of the refractive index of water at one atmospheric pressure in the temperature range of 10 - 30 °C in the near-infrared spectral region is approximately 0.000085 RIU/°C [96]. This speculation suggests that a temperature control for glucose solutions or urine samples needs to be implemented when an index-based glucose sensor is employed to sense glucose concentrations lower than 0.01% or 10 mg /dl.

2.2.3 Conclusions

The proof-of-the concept of fiber loop ringdown glucose sensors using the refractive index-difference EF attenuation as a sensing mechanism has been investigated. Several EF-FLRD glucose sensors were fabricated with and without the immobilization of GOD on the sensor head. Responses of the sensors to standard glucose solutions and synthetic urines in different glucose concentrations ranging from 0.05% to 10 %, or 50 mg/dl to 10 g/dl, were investigated. The sensors showed linear responses in the lower concentration range, 0.1% - 1%, but non-linear responses for in the higher concentration range, 1% - 10%. The EF-FLRD glucose sensors showed both good reproducibility and

fast responses. Comparisons of the results showed that the sensors with and without GOD coatings in glucose solutions and artificial urine samples indicate that the GOD coatings are not critically important to this kind of index-based glucose sensors' performance. The demonstrated detection sensitivities of the sensors in glucose solutions and synthetic urine samples were 75 mg/dl and 50 mg/dl, respectively. This work has demonstrated simple, low cost, and fast response EF-FLRD glucose sensor, which may be potentially utilized for applications in near-real time glucose monitoring.

2.3 Summary of This Chapter

A new type of biosensor was demonstrated based on the FLRD technique. Several biosensors were fabricated in this work for bulk index-based DNA and bacteria, surface index-based DNA, standard glucose, and glucose in synthetic urine sensing. In the first part of this work, EF-FLRD biosensors were fabricated and tested for DNA and bacteria sensing. Two type ssDNA, one type dsDNA, and one type of bacteria were sensed by using bulk index-based sensing technique. Three types DNAs were also sensed by using surface index-based sensing technique. We anticipate that low cost, near-real time response, and high sensitive fiber optic biosensors can be created by using the FLRD technique.

An EF-FLRD glucose sensor was fabricated as a biosensor in the second part of this work. The proof-of-the-concept of fiber loop ringdown glucose sensors was investigated by using the refractive index-difference EF attenuation as a sensing mechanism. With and without the immobilization of GOD on the sensor head, several EF-FLRD glucose sensors were developed. Responses of the sensors to glucose and synthetic urine solutions in different glucose concentrations were analyzed. Compared

results showed that GOD coating does not have critical importance on the sensor performance for this kind of index-based glucose sensors. Behaviors of the sensors were non-linear for high concentration range, 1.0% - 10%, and linear for low concentration range, 0.1% - 1.0%. Furthermore, detection sensitivities of the sensors for standard glucose and glucose in synthetic urine solutions were demonstrated as 75 mg/dl and 50 mg/dl, or 0.075% and 0.05%, respectively. Estimated theoretical detection sensitivity is approxiametly 17 folds of renal glucose threshold, which is between 160 - 180 mg/dl. The simple, low cost, fast response, and high sensitive EF-FLRD glucose sensors were demonstrated with this work. The sensors may be possibly used for biomedical applications, such as near-real time glucose monitoring.

CHAPTER III

CHEMICAL SENSORS

The first report on fiber loop ringdown spectroscopy was published at the beginning of the 21st century [97]. The first fiber optic amplifier loop for loss measurements was reported by Stewart *et al*. They presented a fiber optic loop with micro-optical gas cell to measure gas phase absorption [41, 97]. Tarsa *et al.* reported a fiber optic resonator for spectroscopic measurements, and absorption of the EF was detected [98]. Brown *et al.* introduced the fiber-loop ring-down method to characterize low-loss process in a fiber optic transmission independent of power fluctuations of the light source [99]. They also detected an absorption spectrum for a small sample volume of an organic dye solution by placing this solution between the fiber ends. The same group improved the FLRD technique by creating a phase-shift measurement [100]. This technique provides low cost and real-time response. All techniques have their merits, but EF-FLRD technique has higher sensitivity, faster response, lower cost, and easier design when it is compared to its counterparts.

In this chapter of the dissertation, EF-FLRD chemical sensors have been described for detection of heavy water (HW) and several trace elements. The detection of HW using the FLRD technique shows potential application in nuclear power plants because HW is used in nuclear facility as a coolant [101]. HW absorbs neutrons from nuclear reaction within a nuclear reactor and reduces the speed of the neutrons to increase

probability of causing nuclear fission for chain reaction. HW is used as a coolant because released neutrons from nuclear reactions will have very high kinetic energy and HW will reduce the high energy to energy which is comparable to thermal energy by aborbing the neutrons. HW is also used as moderator because it provides very efficient momentum transfer. For HW detection, Armani and Vahala employed ultra-high-Q microcavities, which can chemically distinguish similar species [102]. In the experiment, the laser was centered at 1320 nm. The detection limit of HW, which was in regular water, was found as 0.0001% by measuring the quality factor from the transmission spectra. Even though this is a very good and sensitive technique, the fabrication process of microtoroids is costly and time consuming.

Detection of trace elements in DI water is another important study. This is a quite distinctive study because the EF-FLRD sensors have not been utilized before for trace elements' detection in water. There have been several trace element detection experiments using various techniques. For example, the detection of trace elements in pure water was studied by using laser-induced fluorescence (LIF) spectroscopy [103, 104]. Fiber optic LIF-sensors are used for analysis of trace pollutions in water and in soil [105]. They have complicated and costly design when compared to an EF-FLRD chemical sensor system.

In this chapter, the EF-FLRD chemical sensors were tested in different concentrations of D_2O, HW, ranging from 10% to 97% by utilizing the EF sensing technique. The sensors were also tested in solutions with different trace elements, such as magnesium (Mg), iron (Fe), cadmium (Cd), and phosphorus (P). The solutions of the elements had the concentration of 1000 μg/ml. The EF sensing technique used in both

tests was capable of distiguishing a very small change in ringdown times when the sensors were immersed into different solutions. The EF sensing technique provides a high sensitivity and near-real time response (0.1 s).

This chapter consists of four parts. The first part is about the experimental setup. The second part explains the EF sensing technique. The third part shows the testing results of HW with different concentrations in DI water and the behavior of the EF attenuation versus HW concentrations. The last part is about the detection of different trace elements in DI water.

3.1 Experimental Setup

Figure 3.1 shows the experimental setup of EF-FLRD chemical sensors. The setup of the system is the same as the one explained in Chapter II. An electronic control system, an oscilloscope, a photodiode detector, a laser source, a fiber loop, and a computer system formed the EF-FLRD chemical sensor system. After the sensor head was prepared by etching a section of SMF in a 48 % HF solution for ~33 min, the sensor was always tested in DI water. The ringdown time of the sensor head read in DI water was used both as a reference and to show repeatability of the sensor. Later, the sensor was immersed into different concentrations of HW solutions and several elemental solutions. In Figure 3.1, the holder carried an aluminum plate and a plastic ruler. The solutions were filled in the caved ruler of 30 cm length, and this ruler was placed onto the aluminum plate. The holder could be raised up and lowered down manually to arrange sensor height inside the solutions. This was a very important step because the sensor head must neither touch the ruler surface nor be floating in the solutions. The sensor head must be completely immersed into the solutions to get repeatable results.

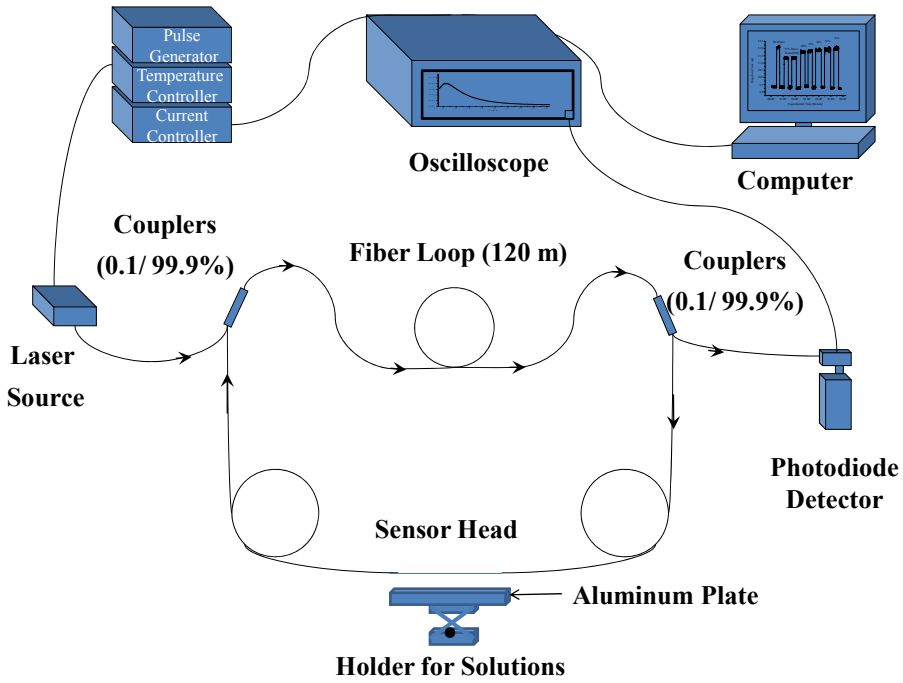

Figure 3.1 Schematic illustration of the EF-FLRD chemical sensor system.

The system consists of a laser source, a fiber loop, a photodiode detector, computer system, an oscilloscope, and an electronic system. A ruler on the aluminum plate holds solutions that sensor head is immersed into.

After the sensor head was fabricated, it was tested in DI water first. The response of the sensor in DI water solution was generally used as a reference. Also, the sensor's repeatability was shown by immersing into DI water twice. Later, the ruler was cleaned and dried after the sensor was taken out from both DI water solution and each elemental solution. Cleaning and drying process protected the sensor head from contamination by each solution. Data collected by oscilloscope was plotted and saved on the computer. Then, the raw data saved in the computer was processed and presented in Sections 3.3 and 3.5.

3.2 The EF Sensing Technique

The EF may occur due to light reflection at the interface of two media which have different refractive indexes. Incoming light from the low refractive index medium to a high refractive index medium will be totally reflected back if the angle is equal or greater than the critical angle. Before the light is reflected, small portion of the light will penetrate into the interface of the two media. This small amount of light will generate a field on the surface, which is called EF. An electronic wave propagates inside the core with TIR. In the sensor head, the light will get through at the interface of the core and the cladding, and more dispersion to the outer medium occurs. This attenuated field is called as “evanescent field” (EF). The EF attenuation is generally an exponential decay. Figure 3.2 shows the EF field and its attenuation to the outer medium. The numbered three points at the interface show different EF attenuations. Number 1 is in the non-etched area of the sensor, and therefore, the EF attenuation to the outer medium is negligible. Numbers 2 and 3 are in the etched part of the section of SMF which is called the sensor head. The EF attenuation is higher in the sensor head because the cladding layer is thinner due to etching. The cladding layer thickness along the sensor head is adjustable by changing the etching time. If d is bigger, the sensor will be less sensitive due to less EF attenuation. On the contrary, if d is smaller, the EF attenuation will be much higher, resulting a significant EF attenuation at the sensor head. The EF intensity is proportional to the penetration depth in the cladding. The EF mechanism and the technique are well-explained in [34].

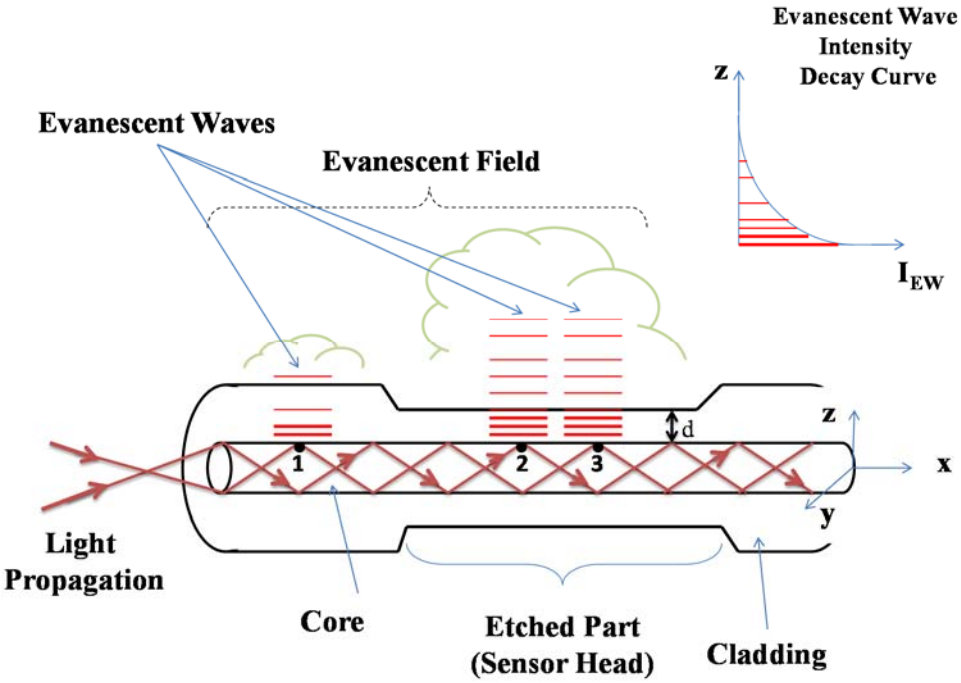

Figure 3.2 Schematic illustration of the EF attenuation in SMF.

Evanescent waves and evanescent fields are shown for both sensor head and un-etched part of the fiber. Also, change of the EF intensity with distance from the core is shown. The EF attenuation is much higher in the sensor head area than in other parts of the fiber.

The sensor head area is the medium where the measurands are placed around because masurands have to be as close as possible to the core to obtain enough sensitivity.

The EF sensing technique is employed in FOS development [106-108]. The EF sensing technique was first utilized by von Lerber and Sigirist [29] to create a high finesse fiber ringdown cavity to examine EF absorption. After that, Tarsa *et al.* [98] used a fiber loop to exhibit detection of the EF absorption of water. Jiang *et al.* reported the detection of the EF absorption of dimethyl sulfoxide solutions in a fiber loop ringdown [109]. The EF sensing technique has been quickly adopted as a very attractive sensing

technique. The EF sensing technique offers high sensitivity, fast response, and good reproducibility.

3.3 Nuclear Power Plants

Most of nuclear power is generated from two kinds of reactors which were developed in the 1950s. The reactors are boiling water reactors (BWRs) and pressurized water reactors (PWRs). In both reactors, heavy water (HW) is an important material because it is used as a coolant. Therefore, HW sensing is highly important in nuclear power plants for environmental safety, economical protection, and safety of human society in case of explosion. EF-FLRD chemical sensors may have been replaced with current detectors or sensors due to their feature merits, such as high sensitivity, fast response, low cost, easy setup, and simple design. Nuclear power plants have so important role in generating energy that around 13% of the world's electricity is generated from nuclear energy [110].

Nuclear power is an alternative power source where nuclear fission of uranium is used to generate heat and hence electricity. The power is produced from controlled nuclear reactions. Generally, commercial power plants use nuclear fission reactions. Nuclear fission occurs when a uranium atom is split into smaller particles, and therefore, an enormous amount of energy is released by the process. Uranium is the fuel for reaction and is radioactive. Therefore, it is unstable even when it is broken down into smaller parts. A uranium atom absorbs a neutron and the reaction starts. After that, the released energy from the reaction is transferred to heat energy while the particles slow down. Later, heat energy is moved through a transfer medium, such as water to turn water into steam. This steam is transferred to a turbine which connected to a generator, and the

generator produces electricity [110, 111]. The working principles of the nuclear power plants to generate electricity are the same for most types of reactors. Continuously released energy from nuclear fission reactions is used to heat water to produce steam. Produced steam is used to drive turbines to generate electricity.

3.3.1 Components of Nuclear Reactors

There are various components of reactors. The components are common for most types of reactors. Figure 3.3 represents components of a nuclear power plant. Most of the components will be explained in the following sections.

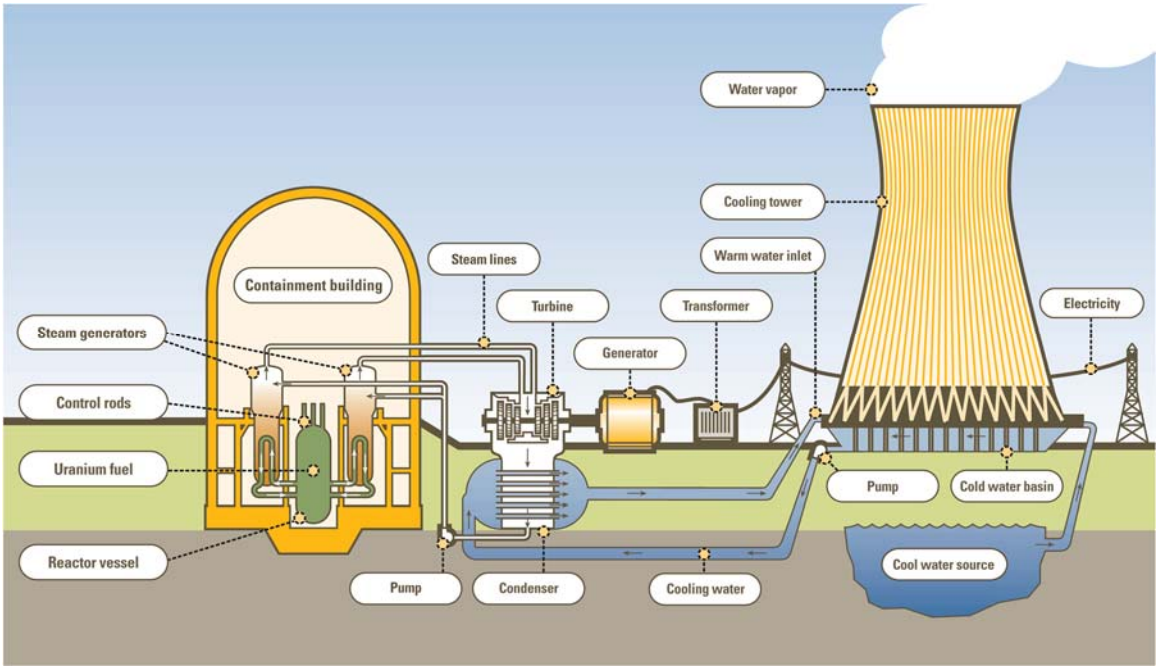

Figure 3.3 Components of a nuclear power plant.

(The picture is from staff.fcps.net).

3.3.1.1 Fuel

Uranium is the basic fuel for nuclear reactors. Uranium pallets are setup in tubes to form fuel rods. The rods are settled down into fuel assemblies in the reactor core. Uranium is split into parts by collision with a neutron. Uranium dissociation is called a fission reaction. For continuity, a neutron source is needed. Released energy from fission reaction is used to heat up water to generate steam.

3.3.1.2 Moderators

Moderators are materials in the core. Moderators are used to slow down the neutrons released from the fission reaction. Therefore, they lead to more fission. Generally heavy water or graphite is used as moderator.

3.3.1.3 Control Rods

Control rods are made from a material which absorbs neutrons, such as cadmium, hafnium, or boron. Control rods are inserted or withdrawn from the core to control the rate of reaction or stop the reaction. Special control rods in some PWRs are employed to support the core for low levels of power.

3.3.1.4 Coolant

Coolant is mostly a fluid which circulates through the core to transfer the heat. In light water reactors, the water moderator is also used as primary coolant. In BWRs, there is secondary coolant circuit. In this circuit, steam is generated from water. HW detection is critically important for a nuclear facility. Therefore, the sensor used for detection should have high sensitivity and fast response. FLRD chemical sensors are very convenient for HW detection due to their high sensitivity and fast response features. HW

will be diminished by time and become functionally inefficient due to absorption of products from nuclear reactions. If immediate care is not taken, nuclear criticality may happen. Therefore, HW detection is exteremely important not only economically, but environmentally as well. FLRD chemical sensors can be utilized for HW detection because of their unique characteristics such as near-real time monitoring, fast response, high sensitivity, and low cost.

3.3.1.5 Pressure Vessels

Pressure vessels are generally made from a strong steel and contain the reactor core and moderator/coolant. It may also be series of tubes holding the fuel. These tubes convey the coolant through the moderator and surround it.

3.3.1.6 Steam Generator

For PWRs, steam generators are parts of the cooling system. Steam generators make steam for turbines by bringing heat from the reactors.

3.3.1.7 Containment

Containment is a structure around the reactor and is associated with steam generators. Containments are designed to protect reactors from outside damage and also to protect the environment from radiation effects. Containments are mostly made from concrete or steel structures.

3.3.2 Types of Nuclear Power Plants

There are two types of reactors: BWRs and PWRs.

3.3.2.1 Boiling Water Reactors

A BWR operates like a fossil fuel generating plant. Boiling water inside the pressure vessel in BWRs produces steam water, which moves upward from the reactor coolant through the core, absorbing heat. When the steam moves to top of the pressure vessel, water particles are removed. The steam is transferred to the turbine generator to turn the turbine [112]. At lower pressure, water in only one circuit boils in the core at around 285 ^{o}C. Steam generated from boiling water passes to the turbines. The turbines must be protected from radiological effects because the water around the core or a reactor is always contaminated with traces of radionuclides. Therefore, water sensing is critically important. EF-FLRD sensors can be utilized in BWRs for precise detection because of fast response and high sensitivity features of the sensors.

A BWR fuel assembly includes 90 - 100 fuel rods, and there are up to 750 assemblies in a reactor core, carrying up to 140 tons of uranium. The secondary control system controls water flow through the core; therefore more steam in the top part decreases moderation. Figure 3.4 represents a BWR system and components.

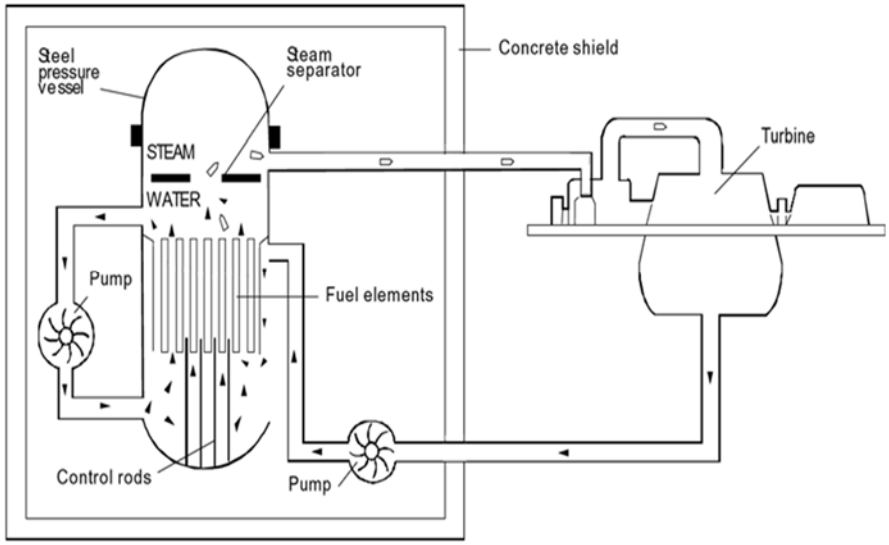

Figure 3.4 Schematic illustration of a boiling water reactor.

(From World Nuclear Association web page)

3.3.2.2 Pressurized Water Reactors

A PWR is the most common type among 230 nuclear power reactors in use for power generation. PWRs use regular water as both coolant and moderator. The design is separated by a primary coolant circuit which flows through the reactor core under high pressure, and a secondary circuit which generates steam to drive the turbine.

A PWR has fuel assemblies with 200 - 300 rods in each and they are arranged vertically in the core. A large reactor has about 150 - 250 fuel assemblies with 80 - 100 tons of uranium. Water has to be kept under 150 times of atmospheric pressure to avoid boiling because water reaches to around 325 ^{o}C in the reactor core. Pressure is produced by steam in a pressuriser as seen in Figure 3.5. Water is also the moderator in the primary coolant circuit. If any significant amount of water boils and turns to steam, the fission reaction will slow down. The EF-FLRD sensors can be employed for continuous and long-time monitoring of water in a PWR system. Changing water amount will affect one

of the safety features. The secondary shutdown system is responsible for adding boron to the primary circuit. The secondary circuit has less pressure, and water boils in the heat exchangers. Generated steam drives the turbine to generate electricity. Then the steam is condensed and returned to the heat exchangers in contact with the primary circuit.

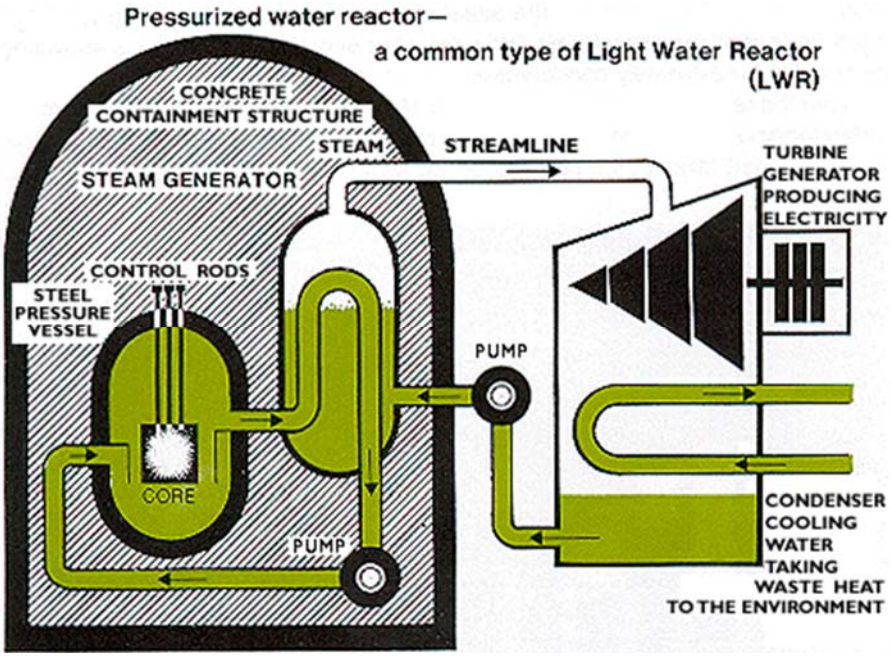

Figure 3.5 Schematic illustration of pressurized water reactor.

(From World Nuclear Association web page)

3.3.3 Coolant System

HW is used as a coolant in heavy water reactors. The coolant should be restricted with the reactor boundary for safety. Even though many precautions have been taken and technological systems have been improved and executed in the reactors, there are still some possible risks for coolant leakage into the environment, such as cracks or corrosion in reactor parts [110]. Therefore, precise HW detection is extremely important. So far, to setup a HW detection system, one should have enough space to setup the system, enough

budget to periodically replace system components, and much time to fabricate the system. On the contrary, the EF sensing technique requires low cost, less time, and a small space to setup.

Improvement of an early detection tool for coolant leakage is extremely important for nuclear safety during normal operation of the reactors. The regularity guidelines strongly suggest for nuclear power plants to use two leak detection systems which have different techniques for very early detection [113]. The reactor coolant system (RCS) leakage, which is important for safety significance, changes depend on the leakage source, leakage rate, and the leakage period of time. Even very small leakage can cause an increase in material deterioration such as corrosion and cracks on the RCS equipments [114].

3.4 Heavy Water Detection

Figure 3.6 shows the response of diluted HW, ranging from 97% to 10%, in DI water. In the first step, the EF-FLRD sensor was tested in air and in DI water. The response of the sensor in the DI water solution was used as a reference to compare with ringdown times of the sensor in HW solutions. Then the sensor was immersed into HW solution of 97% concentration. This step was repeated twice to show repeatability of the sensor for HW response. Average ringdown time was 12.08 μs for the sensor response in DI water. Ringdown time in air before and after DI water test was 9.35 μs. After that the EF-FLRD sensor read ringdown time in HW of 97% concentration as 11.33 μs in both steps. The difference of 0.75 μs between DI water and HW solution shows that DI water and heavy water refractive indexes are different from each other, and that is detectible with the EF-FLRD sensor by using the EF sensing technique. When known refractive

indexes of DI water and HW, 1.3325 and 1.3285 respectively [115], are compared, the difference between refractive indexes is also seen clearly. Later, HW is diluted to 80% by adding DI water, and ringdown time difference from 97% is observed as 0.46 μs. Following diluted concentrations until 10% show differences in terms of observed ringdown times by the EF-FLRD sensor. In 10% HW concentration, ringdown time was 11.99 μs. The difference of 0.09 between initial ringdown time in DI water and the final ringdown time in a 10% HW solution is quite visible in the figure. The baseline stability of the EF-FLRD sensor is 0.36%. The detection limit of the EF-FLRD sensor is 10% HW for our experiment and can be enhanced at least 100 folds, based on our previous work on glucose sensing [27]. The detection limit can be increased by increasing sensor's sensitivity.

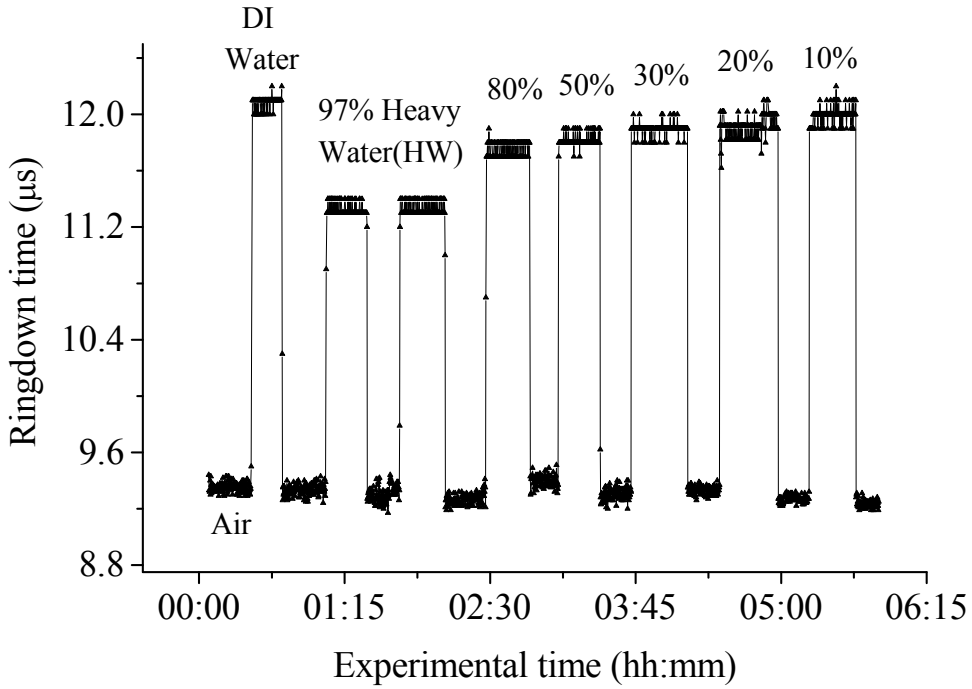

Figure 3.6 Response to different concentrations of Heavy Water.

First, the EF-FLRD sensor was tested in DI water to get a reference data, and then was tested in different concentrations of heavy water solutions.

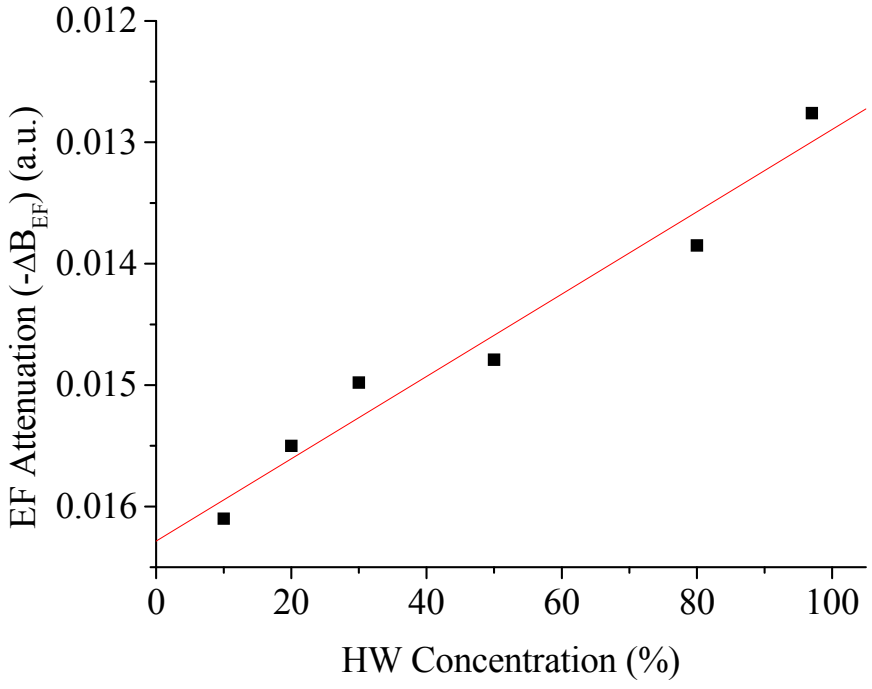

Figure 3.7 The measured EF attenuation difference versus heavy water concentration.

Figure 3.7 shows behavior of the EF attenuation versus HW concentration, %, in DI water. The y-axis is related to the absolute value of ΔB_{EF} defined in Equation (2.10). ΔB_{EF} is calculated by subtracting of inverse ringdown time in air and inverse ringdown time in different concentrations of HW solutions. For example, average ringdown time in 97% HW solution (τ^{HW}) is 11.33 µs, and average ringdown time in air (τ_0^{air}) right after 97% HW solution is 9.27 µs. Calculated absolute value of ΔB_{EF} for 97% HW solution is 0.0127 (a.u.). The fitted curve in the Figure 3.7 shows a linear relationship between the EF attenuation and the HW concentration in the tested range.

3.5 Detection of Different Trace Elements in DI Water

Several elements, such as Mg, Fe, P, and Cd of 1000 µg/ml concentration in 2%-HNO_3/Water, were detected by using the EF-FLRD chemical sensor. Two and three elements were tested in DI water for comparison to both each other and DI water. First, traces of Mg, Fe, and P elemental solutions were tested in DI water after the sensor was immersed into DI water twice. Second, traces of Mg and Fe elements were detected in DI water as a proof of the first test. Third, detection of trace elements, P and Mg, was investigated. Finally, differentation between P and Cd elemental solutions was observed.

Current methods for detections of trace heavy metals in water are atomic absorption spectroscopy (AAS) [116], inductively-coupled plasma mass spectrometry (ICP-MS) [117], total-reflection X-ray fluorescence (TXRF) spectrometry [118], and anodic stripping voltammetry (ASV) [119]. Xie *et al.* developed an ultramicroelectrode arrays sensor to detect trace concentrations of heavy metals in water [120]. They determined trace concentration of heavy metals like Pb and Cd in aqueous solution by using square wave ASV. Wang *et al.* detected heavy metal ions in water by using high-

resolution differential surface plasmon resonance (SPR) with ASV [121]. They demonstrated a quantitative detection of copper (Cu), Pb, and mercury (Hg) ions in water. In another study, Forzani *et al.* detected heavy metal ions in drinking water by using a high-resolution differential SPR sensor [122]. They demonstrated selective detection of Cu^{2+} and Ni^{2+} by coating the sensing surface with peptides NH_2-Gly-Gly-His-COOH and NH_2- $(His)_6$-COOH.

Verma *et al.* developed a fiber optic biosensor for detection of Cd in milk [123]. They achieved the detection limit of 0.1 µg/l by using the biosensor. Prestel *et al.* developed a sensor system for the fluorimetric detection of dissolved heavy metals in ground water and surface water [124]. They also detected different metal ions by using a fiber optic sensor array.

All of these methods obtain good detection limits and a high linear range, but the development of analytical instruments using the aforementioned techniques or methods is costly. Accumulating and processing samples are time-consuming and give possible errors. On the contrary, the EF-FLRD sensors offer high sensitivity, fast response, low cost, and easy system setup. For the element detection experiment, the same FLRD system setup in Figure 1.3 was used.

Figure 3.9 shows detection of three different trace elements, Mg, Fe, and P, in DI water. The samples have a concentration of 1000 µg/ml. Responses to the elemental solutions showed good reproducibility and repeatibility. In Figure 3.9, the EF-FLRD chemical sensor was immersed into the DI water solution twice to show repeatability of the sensor before detection of the trace elements. Afterwards Mg, Fe, and P elements were tested, and differences between the trace elements are clearly presented. The sensor

head was washed off once after detection of each trace element to get rid of contamination. Again, the sensor head was washed off with fresh DI water to make sure there is no containment from the tested element. It is clearly shown in Figure 3.8 that trace detection of each element can be sensed by using the EF-FLRD chemical sensor.

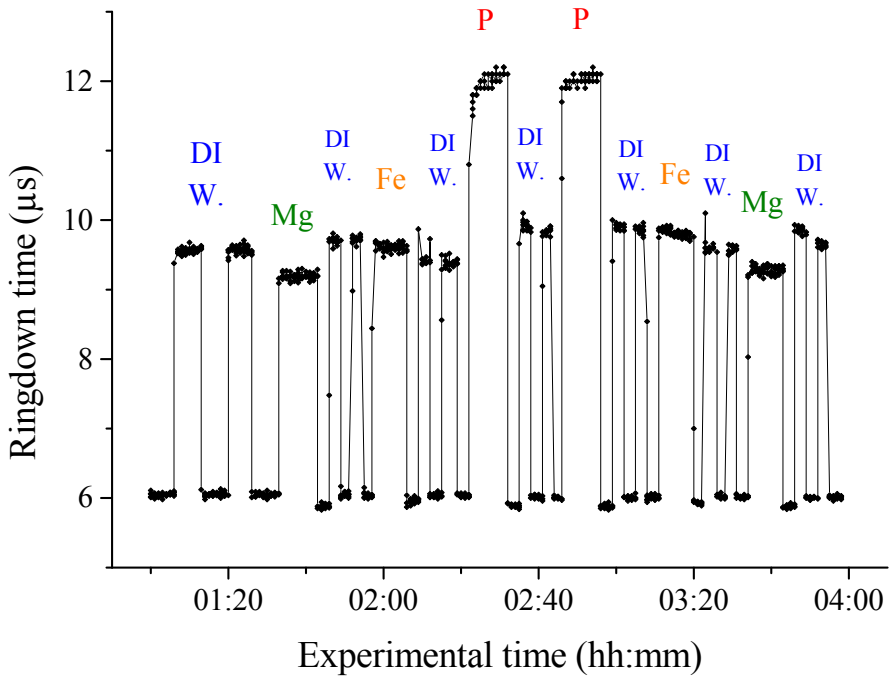

Figure 3.8 Detections of different trace elements, Mg, Fe, and P, in DI water.

Initial DI water test repeated twice shows both the repeatability of the sensor and reference data for a comparison with the sensor's ringdown times with other elemental solutions. The rest of the water steps are to clean sensor head from contamination of each element.

Figure 3.9 shows detection of two of the previously tested trace elements, Mg and Fe, in DI water. The samples have a concentration of 1000 µg/ml. The sensor responded to the elemental solutions reproducibly and repeatably. In Figure 3.9, the EF-FLRD chemical sensor was immersed into DI water solution twice to show repeatability of the sensor before detection of the trace elements. Similar to the previous process, the sensor

head was washed off twice with fresh DI water to get rid of contamination. This data is a proof for Figure 3.8 data that trace detection of Mg and Fe at the same concentration is different from each other.

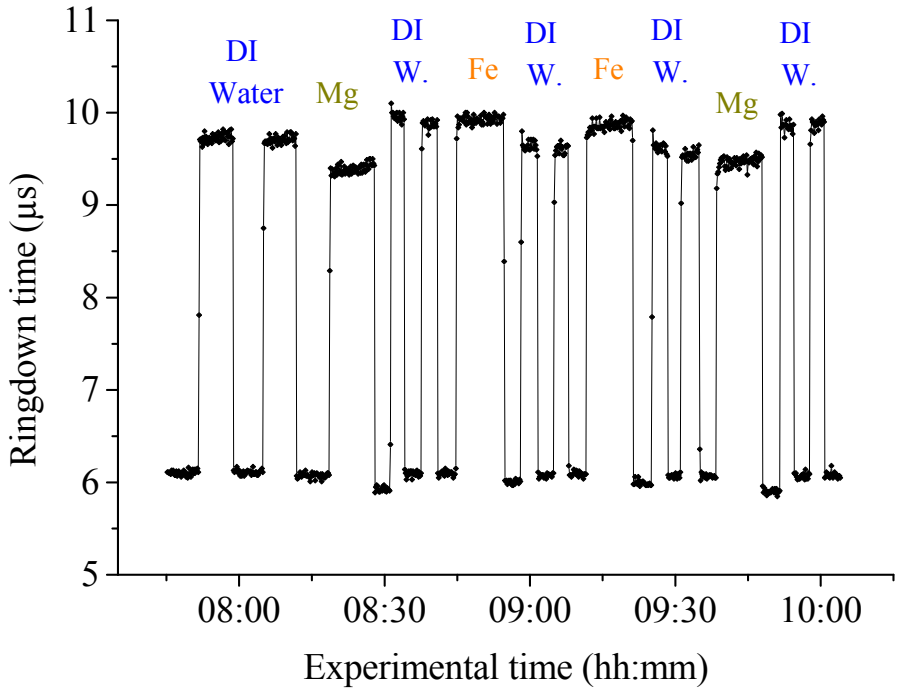

Figure 3.9 Detections of different trace elements, Mg and Fe, in DI water.

When the sensor was in DI water solution, the average ringdown time was 9.72 µs in both steps. After that, the sensor was immersed into Mg solution, and the sensor read the average ringdown time as 9.4 µs. The baseline stability of the sensor which was used in this experiment was 0.4%. The sensor response in terms of ringdown time for Fe solution was 9.92 µs. The EF-FLRD chemical sensor read different ringdown times due to the difference in the refractive indices of each solution. This experiment proved that

the EF-FLRD technique, which is a relatively new sensing technique evolved from the cavity ringdown technique, can be utilized to detect trace elements in DI water.

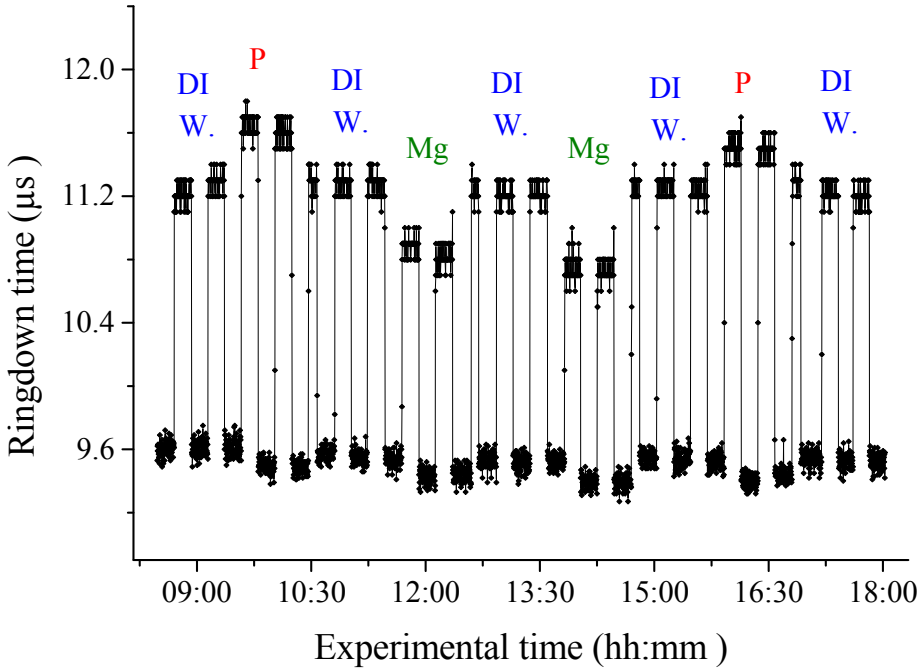

Figure 3.10 Detections of different trace elements, P and Mg, in DI water.

Figure 3.9 shows detection of two different trace elements, P and Mg, in DI water. The samples have a concentration of 1000 µg/ml. Sensor responds to the elemental solutions were measured in terms of ringdown time and showed good reproducibility and repeatability. In Figure 3.9, the EF-FLRD chemical sensor was immersed into the DI water solution twice before testing elements to show repeatability of the sensor. To clean contamination, the sensor head was washed off three time times after each element test.

When the sensor was in DI water solution, the average ringdown time was 11.45 µs in both steps. After that, the sensor was immersed into P solution, and the sensor read

average ringdown time as 11.81 µs. The baseline stability of the sensor which was used in this experiment was 0.3%. The sensor response in terms of ringdown time for Mg solution was 11.05 µs. Responses to Mg elements are different for two experiments because each sensor has different optical losses and sensitivities, resulting in different responses to the same solution. Ringdown time differences between DI water, P, and Mg are due to different refractive indexes of each solution. This experiment showed that the EF-FLRD technique can be used to determine different trace elements in DI water.

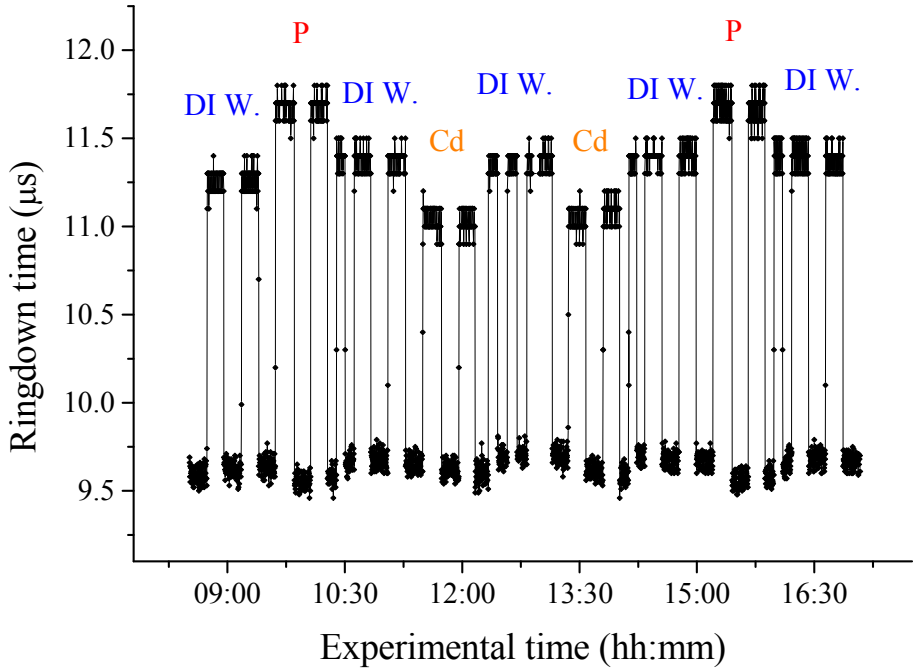

Figure 3.11 Detections of different trace elements, P and Cd, in DI water.

The sensor was tested in DI water twice to show repeatablitiy of the sensor, and then three times after each element test to get rid of contamination.

Figure 3.11 shows detection of two different trace elements, P and Cd, in DI water. The samples have a concentration of 1000 µg/ml. Responses of the sensor to the elemental solutions were observed in terms of ringdown time and showed good

reproducibility and repeatibility. In Figure 3.9, the EF-FLRD chemical sensor was immersed into the DI water solution twice initially before the sensor was tested for trace elements to show repeatability of the sensor. To clean contamination, the sensor head was washed off three time times after each element test. In this experiment, differences of trace elements for P and Cd were presented successfully.

When the sensor was in DI water solution, the average ringdown time was 11.25 μs in both steps. After that, the sensor was immersed into P solution, and the sensor read the average ringdown time as 11.68 μs. The baseline stability of the sensor which was used in this experiment was 0.49%. The sensor response in terms of ringdown time for Cd solution was 11.38 μs. Ringdown time differences between DI water, P, and Cd are due to different refractive indices of each solution. This experiment also showed that the EF-FLRD technique can be employed to determine different trace elements in DI water.

3.6 Conclusions

Several EF-FLRD chemical sensors were developed and tested for detection of HW in different concentrations ranging from 97% - 10% and traces of several chemical elements, such as Fe, Mg, P, and Cd in DI water. Diluting 97% HW in DI water down to 10% changed the refractive index of HW solution in different concentrations. The bulk index-based sensing technique was applied to measure the response of the EF-FLRD sensor to HW solutions in terms of ringdown time. The importance of HW detection is that HW has been used as a coolant in nuclear power plants. Controlling HW change is exteremely important to protect nuclear power plants from explosion, regarding human life and environment protection. Beside HW detection, the EF-FLRD chemical sensors were tested for detection of trace elements in DI water. Each solution has its own

refractive index and had 1000 μg/ml concentration. Accordingly tested elements showed good repeatability and reproducibility. Each experiment was handled precisely and carried out under laboratory conditions. No additional optical components such as OTDR, OSA, etc. were employed. The EF-FRLD chemical sensors utilized in this work were presented repeatable and reproducible responses for trace element detection. Therefore, the EF-FLRD sensors provide low cost, easy design, high sensitivity, and fast response regarding to their counterpars.

CHAPTER IV

PHYSICAL SENSORS

FLRD sensors have also been used for sensing physical quantities with fast response, high sensitivity, and low cost. Wang *et al.* reported development of pressure and force sensors by utilizing the FLRD technique [16, 17]. They used 1 cm long bare SMF as the sensor head. Optical loss in the fiber loop was introduced due to microbending of the fiber. They converted changes in ringdown time to optical losses, resulting in observing the response of the sensor to pressure change. They also introduced FBG-FLRD temperature sensors by using the same FLRD technique [21, 41]. They detected temperature change in FBG due to FBG curve shift by measuring the ringdown time.

The FLRD sensors have been employed widely in structural health monitoring (SHM) to detect moisture and cracks in concrete structures. The first use of FOSs in concrete was suggested by Mendez *et al.* [125]. They reported the use of embedded FOSs in concrete structures for non-destructive measurement of internal stress and strain of concrete as well as for the assessment of structural integrity. Multiplexed grating sensors were installed on a bridge to monitor strain responses of different positions [7].

For crack detection, a novel method for monitoring of fracture critical bridges using distributed fiber optic technology based on stimulated Brillouin scattering was reported by Glisic and Inaudi [126]. The cracks were detected based on change in the

Brillouin frequency of the scattered light in the optical fiber. Sahay *et al.* described for the first time a FLRD concrete crack sensor [20]. They detected manually-produced cracks in concrete bars.

This chapter includes fabrication of water, crack, and temperature sensors and test results of the sensors in concrete bars and concrete structures. Several FLRD water and crack sensors were fabricated and tested under laboratory conditions. The FBG-FLRD temperature sensors were also fabricated and calibrated in the laboratory. Later, two water sensors, two crack sensors, and two temperature sensors were deployed in a concrete cube of dimensions 10 ft × 10 ft × 8 ft at a test site (the US Deparmtne of Energy (DOE) designated test site) in Miami, FL.

4.1 EF-FLRD Water Sensor

4.1.1 Reproducibly Reversible FLRD Water Sensor Embedded in Concrete and Grout for Water Monitoring

Concrete is the most important material in civil engineering. It has unique features, such as lightness, strength, and durability. Even though its durability is high enough to survive for years, concrete structures can be attacked environmentally. This attack causes some damages, such as deterioration and instability of the structures. Moisture is one of the key factors accounting for the deterioration of concrete structures, which leads to the corrosion of structures by dissolving other contaminants inside the structures [127, 128]. On the other hand, water itself is an important ingredient when a concrete structure is being built up and has a critical impact on the structure's lifetime; however, excessive amount of water can cause faster degradation of concrete [129]. Besides the factor of excessive water during the curing process, environmental

phenomena, such as rain, humidity, etc., can also launch the process of degradation of a concrete structure. Water can penetrate inside a concrete structure easily if the structure has a crack. Water transmits damaging ions, such as sulfate, carbonate, chloride, ammonium, etc., which can potentially oxidize the steel structure inside the concrete [130]. In addition, water leaked into structures can freeze and later on may expand inside the concrete. This cycle causes accruing damages, microcracks, and deformation inside the structure [131]. Therefore, detection of water is critically important for retardation of water penetration and early maintenance of concrete structures.

FOSs have been used to monitor concrete structures for over twenty years [132-134]. Advantages and features of FOSs are reviewed in detail in Refs. [24, 132-135]. One of the early studies regarding monitoring of concrete structures was to embed a fiber optic sensor directly in concrete structures and buildings [136]. While early studies were focused on the sensing of strain, corrosion, or deformation of concrete structures using embedded FOS, water and moisture sensing were focused on in later studies. Swart *et al.* reported detecting moisture in concrete via a fiber optic Mach–Zehnder interformeter [137]. The essence of the sensor was based on detecting moisture dependence of shock waves, which were generated in concrete by a spring-loaded gun with stainless steel balls. Another study based on absorption of moisture in concrete was reported by Yeo *et al.* [138]. They used a FBG sensor coated with a moisture sensitive polymer and then embedded the sensor in several concrete samples to detect moisture by measuring the Bragg wavelength shift caused by the expansion of the coated material. The same group reported another study of an FBG-based moisture sensor to test porosity change in different concrete samples when the sensor was exposed to a series of freeze/thaw cycles

[139]. Healy *et al.* fabricated an optical fiber-based moisture sensor by coating a LPG with a moisture-sensitive polymer to observe existence of moisture in building envelopes [140]. They detected moisture based on a refractive index change of the coating materials, resulting from absorption of the moisture. Wavelength of the light, which was propagated in the optical fiber, was a function of refractive indices. Hence, detection of moisture was given by a wavelength shift. Recently Alam *et al.* have studied moisture detection in concrete by using interdigitated near-field sensors [141]. They embedded meander and circular interdigitated sensors in wet concrete samples and detected moisture using interelectrode capacitance as percentage of moisture content in the concrete. More recently, Ghandehari *et al.* have reported a sensing method, in which near infrared electromagnetic radiation was injected into optical fibers to analyze interval structure of the samples [142]. They showed that molecular vibration spectroscopy can supply an effective means for *in situ* measurement of capillary absorption and evaporation in cementitious materials. There have been several other fiber optic water or moisture sensors, which are made from SMF, FBG or other sensing elements [108, 143-148]. However, none of the sensors reported in Refs. [108, 143-148] have been embedded in concrete structures for water or moisture sensing.

The EF-FLRD technique is a very sensitive time-domain sensing technique. EF-FLRD sensors have both the generic features of FOS, such as small size, light weight, and low cost and additional advantages, such as fast response, high sensitivity, and high reversibility. An EF-FLRD sensor head is prepared by etching a section of a SMF loop using a 48% HF acid solution. When a laser pulse travels inside the fiber loop, the light intensity is attenuated after each round trip due to EF absorption and/or scattering loss in

the fiber loop sensor head. If the wavelength of the light is selected to be not absorbed by the medium in the sensor head, the EF loss is generally from EF scattering loss, which is dependent upon RI difference for a given sensor unit. For example, when an EF-FLRD sensor head is exposed to air and water, which have optical indices of 1.0003 and 1.3330 at 1515 nm, respectively, different refractive index differences (Δn) between the fiber core (n_{core} = 1.4491) - air and the fiber core-water have different EF scattering losses that are represented by the sensor in terms of different ringdown times. Detailed description of the EF-FLRD sensors can be read in Refs. [35, 85]. New applications of the EF-FLRD sensor have been reported in a more recent work [27].

The purpose of this study was to monitor water or moisture in concrete mixture by using the EF-FLRD technique, which was achieved by embedding a section of partially etched SMF (the EF-FLRD sensor head) into the concrete mixture made under laboratory conditions. To the best of our knowledge, this technique is for the first time applied for monitoring of water in concrete. Several tests were carried out in different concrete bars where sensors were embedded. Results indicated that when a small amount of water was poured on the concrete and water reached the sensor head, the presence of water and variations in water content in the concrete were detected instantaneously and reversibly by the EF-FLRD sensors.

4.1.2 Experimental Setup

4.1.2.1 The EF-FLRD Sensors

Figure 4.1 illustrates the setup of an EF-FLRD sensor system. A FLRD sensor consists of two major parts: a sensor control system and a sensor unit. The control system consists of a CW diode laser source, a photodiode detector (Thorlabs, PDA50B), and

ringdown electronic control devices. A fiber loop ringdown sensor unit includes a single mode fiber loop connected through two identical 2×1 fiber couplers and a sensor head that was spliced as part of the fiber loop. The same sensor control system can run any FLRD sensor unit through connection and disconnection of a fiber sensor unit to the control system via two single mode fiber FC/APC connectors. Diameters of the fiber cladding and the fiber core of the fiber are 125 m and ~8.2 m, respectively. The two identical 2×1 fiber couplers (Opneti Communication Co.) were fabricated with a split ratio of 0.1:99.9 in the double-leg end of the fiber couplers. The total optical loss of the light in the fiber loop, including absorption loss, fiber connectors' insertion losses, and fiber couplers' losses, was estimated to be <0.45 dB. The typical splicing loss was 0.02 - 0.04 dB and estimated by the splicer. Total length of the fiber loop was 120 m. When a laser beam was coupled into the fiber loop, the photodiode detector observed a ringdown signal, and then this signal was applied to a pulse generator (SRS, model DG 535) to trigger the generator to produce a series of negative square waves. These pulsed square waves were applied to the laser driver to drop laser current to zero rapidly and a series of laser pulses were created from the continuous wave diode laser. For each laser pulse, the photodiode detector observed a series of pulsed spikes generated from each round trip of the laser pulse inside the fiber loop. The ringdown curve was monitored by an oscilloscope (Tektronix, 410A). Details of a typical FLRD sensor loop and its electronic control system can be seen elsewhere [16, 17].

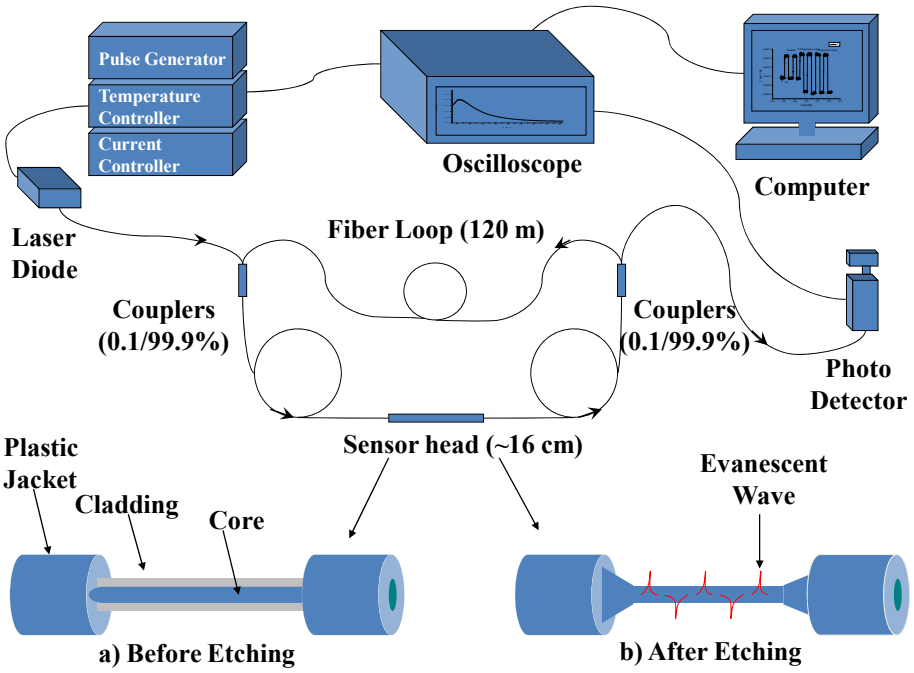

Figure 4.1 Schematic representation of the EF-FLRD sensor system and the EF-FLRD sensor head.

One section of SMF was etched in a 48% HF acid solution for ~34 min after the plastic jacket was removed. Etching process was evaluated in terms of fiber diameter by continuously monitoring ringdown time because etching was radially symmetric [34]. When the EF in the fiber cladding started being disturbed, ringdown time of the laser beam in the loop began to decrease due to the optical loss at the sensor head. The higher optical loss is, the lower ringdown time is. Figure 4.1(a) and (b) illustrates the section of a bare SMF to be etched as the sensor head and the etched fiber sensor head, respectively.

4.1.2.2 The EF-FLRD Sensing Principle

A coupled light pulse travels many round trips inside the fiber loop. Intensity of the light pulse decreases after each round trip because of optical loss, and the photodiode

detector observes different intensity after each round trip. Therefore, the light intensity observed by the detector is molded by [16, 31, 80]

$$\frac{dI}{dt} = -\frac{IAc}{nL} \tag{4.1}$$

where I is the light intensity at time t (time is zero when the light source is injected into the loop), L is the total length of the fiber loop, c is the speed of the light in vacuum, n is the average refractive index of the fiber loop, and A is the total fiber transmission loss of the light per round trip. Behavior of the light intensity is given by solution of Equation (4.1).

$$\mathrm{I} = -\mathrm{I}_0 \mathrm{e}^{-\left(\frac{\mathrm{c}}{\mathrm{nL}}\right)\mathrm{At}} \tag{4.2}$$

The time required for I to decrease to 1/e of I_0 is referred to as the ringdown time, τ_0, and is given by Equation (4.3a).

$$\begin{aligned} &\text{(a)} \quad \tau_0 = \frac{nL}{cA} \\ &\text{(b)} \quad \tau = \frac{\mathrm{nL}}{c(A+B)} \end{aligned} \tag{4.3}$$

The total transmission loss is a constant for a given FLRD sensor, which is determined by the physical parameters of the sensor, such as the fiber absorption loss, the couplers' insertion losses, the refractive index, and the fiber length. When a sensing activity occurs at one section (sensor head) of the fiber loop, the result is an additional optical loss, B, of the light pulse in the fiber loop, which causes a change in the ringdown time, τ, given by Equation (4.3b). From Equations (4.3a) and (4.3b), we have

$$B = \frac{nL}{c}\left(\frac{1}{\tau} - \frac{1}{\tau_0}\right) \tag{4.4}$$

Equation (4.4) indicates that a change in a sensing activity, such as external pressure, deformation, absorption, etc., can be determined by measuring ringdown times with and without the sensing event. For an EF-FLRD water sensor, B denotes the difference in optical loss of the laser beam in the loop between with and without water presence in the concrete. Different water contents affect the optical refractive index of the interface between the surface of the sensor head and its surrounding (the concrete); therefore the change in the index difference changes the EF scattering loss and different ringdown times are read by the sensor [34, 86].

4.1.3 Concrete Samples

Setting of concrete structures is attributed to a transition from liquid phase to a solid phase [149]. Concrete samples were prepared in a rectangular bar-shape so that a sensor head could be straightly laid along the longest axis of symmetry of the bar. Four different concrete bars and four different grout bars were prepared to test eight EF-FLRD sensor units. The concrete bars were made of a ready to-use concrete mix (a mixture of cement and aggregate, Quikrete), all-purpose sand (Quikrete), and water. All mixtures were prepared manually. Therefore, the four concrete bars had different porosity features. Similarly, the grout bars were manually made of tile mortar with polymer (Mapei), all-purpose sand (Quikrete), and water. The four grout bars also had different structure properties. Table 4.1 lists dimensions of the four concrete bars and four grout bars and length of the corresponding sensor head embedded in each of the sensor units (A - H). The estimated weight of each sensor unit is listed in Table 4.1. Setting of each concrete

bar took approximately 48 h in order to be completely hardened. Figure 4.2 shows one of the concrete bars, in which a fiber sensor head was embedded. The sensor unit was ready for test after 48 h curing. The water:cement ratio was 1:4. The water:cement ratio determines permeability and strength of the concrete bars. Higher water:cement ratios result in weaker concrete bars. Aggregates also make concrete bars weaker because aggregates create pores inside concrete structures.

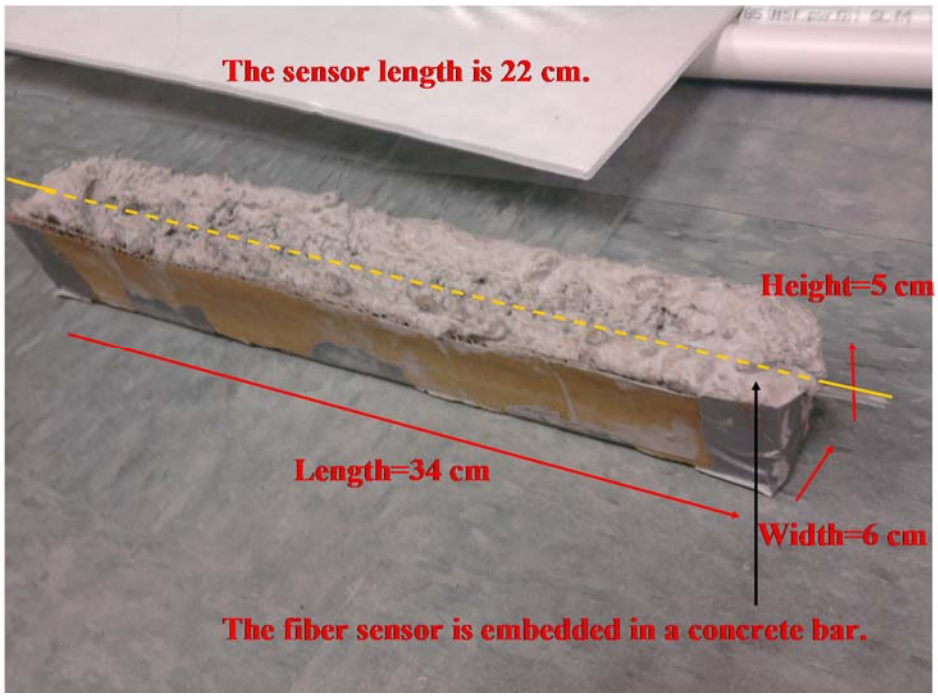

Figure 4.2 A concrete bar with an embedded EF-FLRD water sensor.

Table 4.1 Properties of concrete and grout bars and sensor lengths inside these bars.

Sensor Unit	Estimated Weight of the Bar (kg)	Dimensions (l×w×h) (cm^3)	Sensor Head Length (cm)
A	0.880	22 × 6 × 5	15.0
B	0.890	35 × 5 × 5	16.0
C	0.865	32 × 5 × 4	18.0
D	0.860	30 × 5.5 × 4.5	17.0
E	0.380	31 × 3.5 × 3.5	18.0
F	0.360	30 × 3 × 3.5	17.0
G	0.385	30 × 4.5 × 4.5	18.0
H	0.370	29 × 4.5 × 3.5	17.0

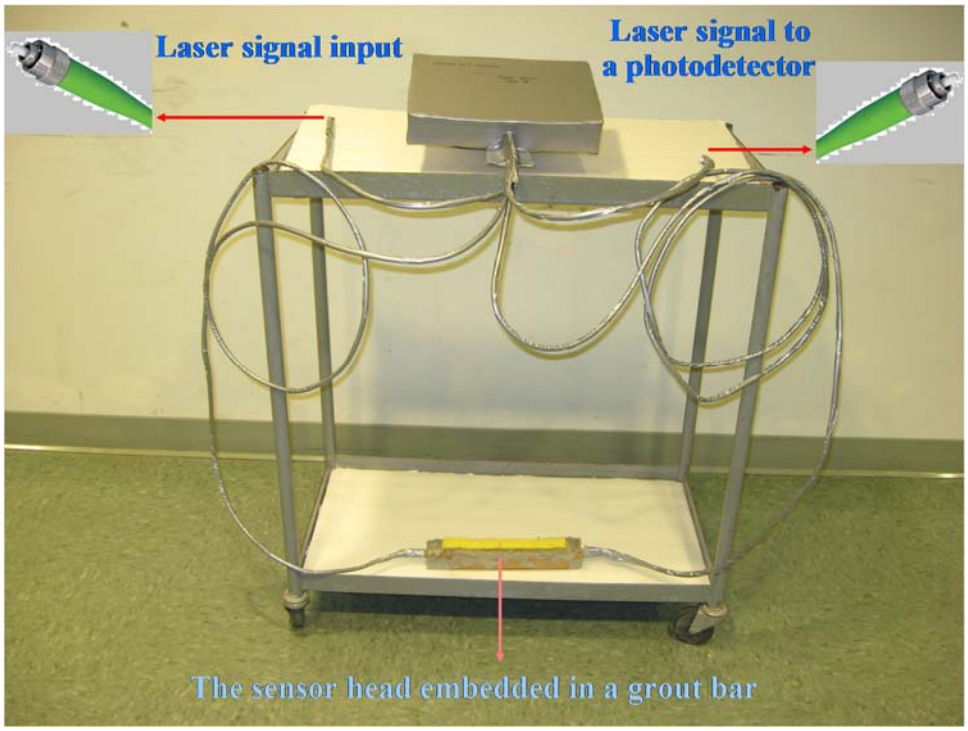

Figure 4.3 An EF-FLRD water sensor unit. The electronics and data acquisition system are not shown in the picture.

After water and cement were mixed together in a ratio of 1:4, half of the carton block, as shown in Figure 4.2, was filled with the mixture. A previously fabricated fiber sensor head was laid down approximately along the axis of the rectangular bar. After that carton block was fully filled with mixture and the concrete bar was left for a 48 h curing process. The porosity generated by the aggregates helps water to leak to the sensor head easily. To protect the fiber from being cut by the sharp edges of the concrete bar, two plastic serum tubes were used to cover the section of the fiber located at each end of the concrete bar. Figure 4.3 shows an EF-FLRD water sensor unit, which was ready for testing. The electronic control portion of the sensor system was not shown in the figure. In the experiments, a small amount of water (10 - 80 ml), depending on different test purposes, was spread onto the surface of the bar and change in ringdown time was monitored.

4.1.4 Results and Discussion

4.1.4.1 Response of the EF-FLRD Water Sensors Embedded in Concrete Samples

Figure 4.4 shows the collected data from four different EF-FLRD water sensors (Units A-D), which were embedded in different concrete bars, as shown in Table 4.1. In Figure 4.4, the data were recorded in different time periods. As concrete properties depend on many factors, such as physical and chemical properties of the cement, the water:cement ratio of the mixture, temperature and time of hydration, the data recorded using different sensor units embedded in different concrete bars might be different from each other. However, the main trend of the data was always same, i.e., ringdown time increased when poured water on the concrete reached the sensor head, and the ringdown time decreased when the water dried out. The other factor is sensitivity of the sensors,

which also determines the detailed features of the data. Different sensors have different sensitivities because of the hand-based fabrication processes of the sensor heads and sensor loops, such as length of the etched fiber in the sensor head, the length of the fiber loop, and total optical loss A were different from each sensor. Fabrication of a sensor head versus its sensitivity was discussed extensively in Ref. [34]. Therefore, each sensor had a different sensitivity. Due to the different properties of the concrete bars and different sensitivities of the EF-FLRD sensors, the four sets of data displayed different features.

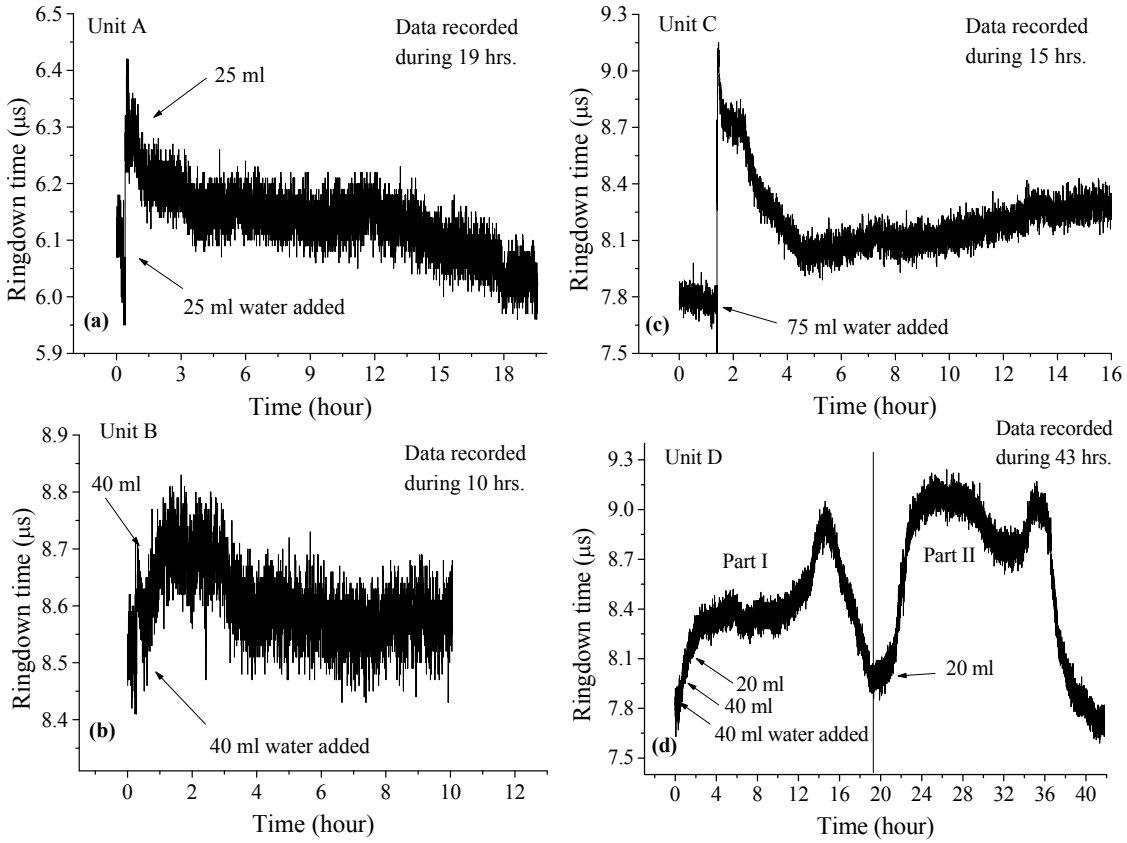

Figure 4.4 Response of four EF-FLRD water sensors embedded in concrete bars to water content.

A - D are different sensor units and their responses are shown in (a) - (d), respectively. The sensors have good reversibility to water content in the concrete.

Figure 4.4(a) shows the data collected for 19 h using sensor Unit A. Twenty minutes after the data collection started, 25 ml water was poured on the surface of the concrete bar. As soon as water reached the sensor head, the sensor sensed water immediately. It was only about 5 min from pouring water onto the surface of the concrete bar to an increase in the observed ringdown time (signal). The 5 min were the water penetration time from the surface of the bar to the sensor head because the response of the EF-FLRD sensor to a change in the medium to be sensed was less than a second [34, 86]. The increase of the ringdown time was due to the fact that refractive index of the

water was higher than the refractive index of the dry concrete [86]. When the small amount of water was completely absorbed by the rest of the concrete and possibly passed through the sensor zone into other parts of the concrete, ringdown time began to decrease slightly due to the small change in the moisture level in the concrete around the sensor head. Another 25 ml of water was poured on the concrete surface. The effect of additional water was that the ringdown time stopped decreasing. At the same time, no significant increase in the ringdown time was observed even after several minutes. The ringdown time was stable for one and half hours and then started decreasing again. During the subsequent 4 h, ringdown time was relatively stable because the moisture level at the sensor head was saturated and hence effectively constant. After another 11 h, curing occurred and ringdown time decreased gradually. The experimental results with Unit A showed that the embedded EF-FLRD sensor was responsive to the water. The addition of the 50 ml of water to the concrete bar in this experiment changed the refractive index of the environment around the sensor head. This change in the refractive index was almost immediately sensed by the sensor, which was demonstrated by an increase in the ringdown time. After approximately 19 h, when the water in that local environment in the concrete dried out, the refractive index around the sensor changed again; that was also picked up by the sensor, exhibiting a successive decrease in the ringdown time. Therefore, in addition to being responsive to the change of water around the sensor head, the sensor was also reversible in terms of change of the ringdown time that reversed back to its baseline.

Another test was conducted using sensor Unit B. As shown in Figure 4.4(b), data were recorded for 10 h, and a total of 80 ml water was used at two different times. After

20 min of data collection, 40 ml water was poured onto the surface of the concrete bar with dimensions of 35 cm × 5 cm × 5 cm. Ringdown time increased immediately. After 1 h, another 40 ml water was poured onto the surface. Ringdown time increased further. After 1 h 6 min, ringdown time became stabilized due to the moisture saturation in the sensor zone. After that, ringdown time started decreasing, indicating the drying process of the concrete. Figure 4.4(c) shows the data collected with sensor Unit C, which was made manually in the same way as Units A and B. Sensor Unit C had dimensions of 32 cm × 4 cm × 5 cm. Data were recorded continuously for 16 h. Ringdown time was recorded for 90 min before 75 ml water was poured. After 2 min, ringdown time increased sharply. This shorter water penetration time, as compared to the 5 min in sensor Unit A, implied that sensor Units C and A had different structure properties while both were made of the same materials. After a short period of time (56 min), the ringdown time started decreasing. The sharp peak shows clear response of the sensor to the change of water content in the location where the sensor was embedded. The sensor had excellent reversibility. Interestingly, after 5 h continuously monitoring, ringdown time became increase in small amplitude. This behavior remains unexplained in this work. The phenomenon could be due to chemical reactions inside the concrete or redistribution of water flow around the sensor head. From the monotonic-trend of the ringdown signal, shown in Figure 4.4(c), it was less likely a noise though this behavior was not observed in other sensor units. Nevertheless, additional experiments need to be carried out to explain this behavior in future study. Especially, effects of physical and chemical properties of the interface between the sensor head and the media on the sensor's sensing behavior is an interesting subject for this particular sensor.

Sensor Unit D was tested continuously for 43 h to study the effect of adding excessive water to the concrete. In addition, this test was designed to investigate the sensor's reproducible reversibility in a complete cycle of dry–wet–dry–wet–dry process. As shown in Figure 4.4(d), the data consist of two distinct parts, as marked in the figure. In Part I, after 40 ml, 40 ml, and 20 ml water were successively poured on the surface of the concrete bar with dimensions of 30 cm × 4.5 cm × 5.5 cm, the ringdown time increased to its peak value of 9.1 μs. The ringdown time curve shows a hysteresis behavior due to the water saturation. After the peak, the decreasing ringdown time indicated the drying out process of the concrete. In order to test the *reproducible reversibility* of the sensor, another 20 ml water was added before the ringdown time dropped completely to the baseline, which was 7.6 μs for this sensor. As expected, ringdown time rapidly increased again and reached the peak value. After a period of 13.4 h, ringdown time decreased and dropped back to the sensor's baseline at 7.6 μs. As shown in part II instead of decreasing monotonically back to the baseline, the ringdown time decrease showed a spike on the slope of the decreasing curve. This phenomenon is speculated to be one (or more) of the various reasons mentioned above for the Unit C. Nevertheless, the results, as shown in Figure 4.4, support that the EF-FLRD water sensors have a fast response and reproducible reversibility when the sensors are embedded in concrete.

4.1.4.2 Response of the EF-FLRD Water Sensors Embedded In Grout Samples

Figure 4.5 shows the results from another three different sensor units (E-G). The sensor units were embedded in grout with a ratio of water:cement:aggregate, 1:5:1. Response of the sensors to the presence of water in the grout was also fast and reversible.

In addition, the three sensors were more sensitive to the same amount of water added because the water:cement ratio in the grout bars was smaller than the ratio of the concrete bars, in which previous sensor units A-D were embedded and tested. Therefore, sensitivities of the sensors were higher due to lower porosity of the grout. The result obtained with sensor Unit E shows a general trend of ringdown time: increasing, steady, and decreasing, which corresponded, respectively, to the presence of water in the sensor, saturation of water content in the sensor zone, and drying out process of the grout. The recorded penetration time of the water from the surface of the grout bar to the sensor location was 5 min. The total monitoring time was 18 h and 70 ml water was poured on the surface of the grout bar. The result shows clearly that the EF-FLRD water sensor is very reversible. Figure 4.5(f) and (g) present the results from testing sensor Units F and G. Both sensors were running for 24 h. 40 ml and 20 ml water were poured onto the surface of the grout bars in each of the sensor units, respectively. In sensor Unit F, 40 ml water was poured after the sensor ran for 60 min, and for sensor Unit G, 20 ml water was poured after the sensor ran for 80 min. In both cases, the sensors read a constant ringdown time when no water was presented in the grout. After water was poured, both sensors read increased ringdown times, followed by gradually decreasing ringdown times. Except differences in the detailed features between two dynamic curves, which were due to different grout structures in the two bars, the response curves show a repeatable water sensing trend. These results demonstrate the repeatability of the sensors' response to water in grout even with different sensor units and different grout properties.

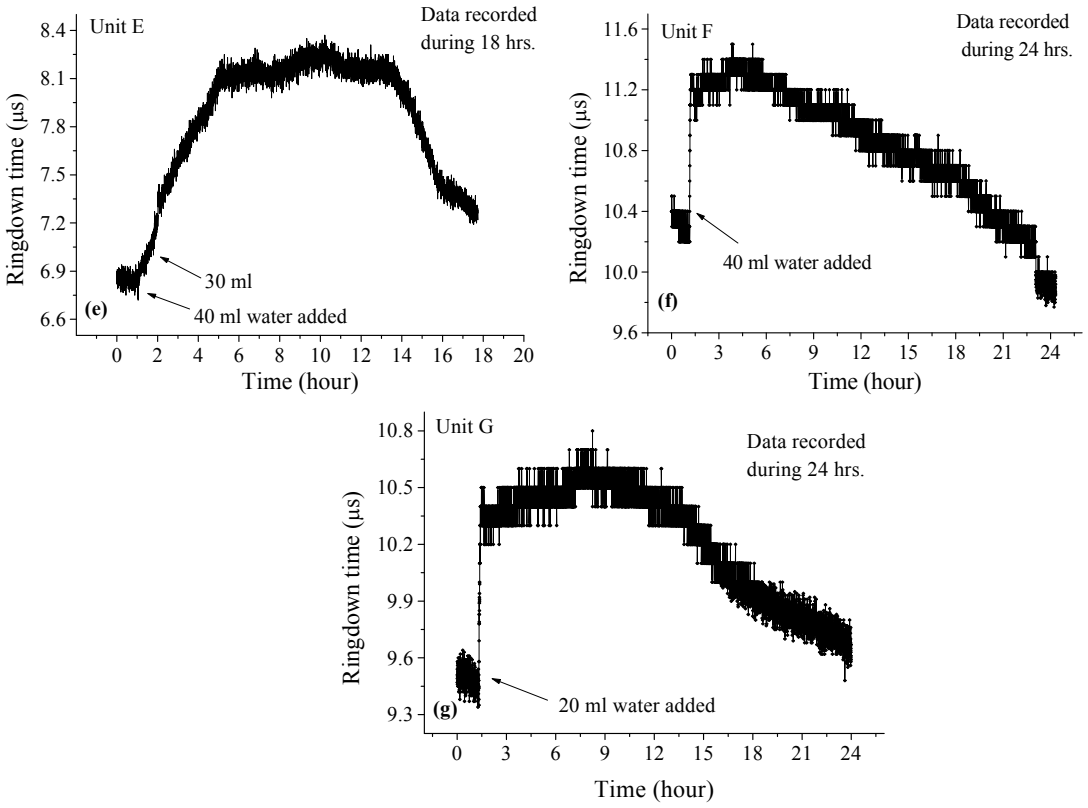

Figure 4.5 Response of three EF-FLRD water sensors embedded in grout bars to water content.

E-G are three different sensor units and their response are shown in (e) - (g), respectively. The sensors have reproducible reversibility to water content in the grout.

4.1.4.3 Detection Sensitivity of the EF-FLRD Water Sensors

Sensitivity of the EF-FLRD water sensor was also analyzed. Here the sensitivity is defined as the minimum detectable water (ml) which makes the sensor responsive when the water is poured onto the surface of a concrete/grout bar. Figure 4.6 illustrates the testing data from sensor Unit H made of the grout. In this test, the sensor was first run for 50 min before water was poured in order to control the baseline stability of the sensor. As shown in the inset, the baseline has a high stability of 0.3%, defined as ringdown baseline noise [16, 34]. This baseline noise was used as a reference to estimate the signal-

to-noise (S/N) ratio to characterize the sensor's detection sensitivity limit. After 2 min, 10 ml water was poured on the surface of the grout bar with dimensions of 29 cm × 3.5 cm × 4.5 cm, ringdown time instantaneously increased from the baseline, 9.5 μs, to the peak value, 13.8 μs. After the peak value, the ringdown decreased gradually, indicating the drying out process of the grout during the following 25 h. This result not only shows the reversibility and fast response of the water sensor, as demonstrated in the previous sensor units, but shows a high water sensitivity of the sensor as well. If estimated by a mass ratio, this 10 ml water sensitivity obtained in this grout bar was only approximately 2.7%. Furthermore, the response of the 10 ml water was 4.3 μs in terms of ringdown time difference. Based on the baseline noise of this sensor, the S/N of the sensor's response to the 10 ml water was 86. This S/N yields a theoretical detection limit of 0.12 ml water for the sensor embedded in grout bar of 370 g. Assuming that this amount of water is homogeneously distributed in the concrete bar, the water sensor becomes a moisture sensor. In terms of the detection sensitivity of a fiber optic sensor embedded in concrete/grout, this is the most sensitive and reversible fiber optic water sensor reported to date. A closer look at the response curve shows a sharp spike located on the slope of the rising curve. This spike was not a noise. It was related to the water permeation dynamics inside the grout. Details of the water interactions with concrete/grout inside the bar remain unknown in this study. However, detection of this single point event suggests that the current water sensor due to its fast response and high reversibility can be used to study the dynamics of water interactions with concrete/grout. This may open an interesting subject of future study.

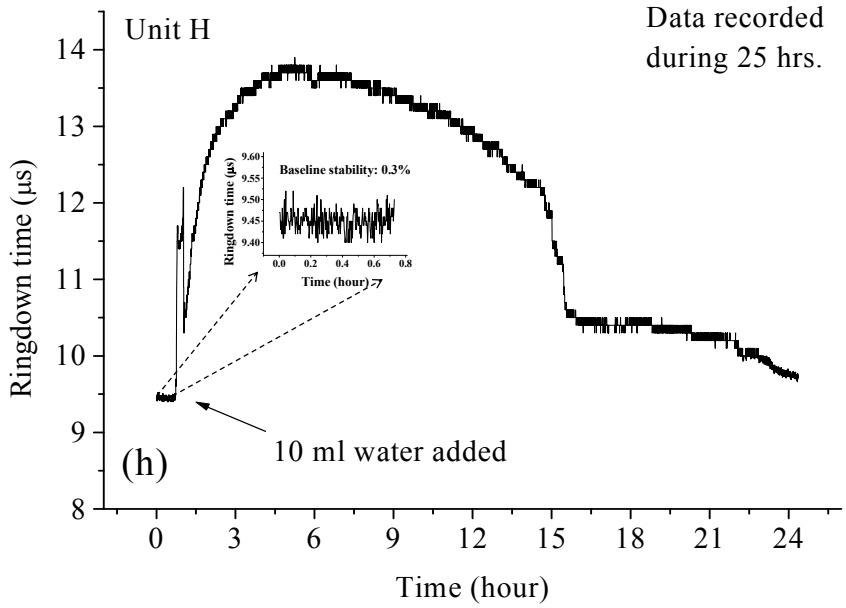

Figure 4.6 High sensitivity of the sensor Unit H embedded in a grout bar.

Table 4.2 Comparison of the embedded EF-FLRD water sensor with other embedded fiber optic water sensors in terms of the sensor type, sensing principle, response time, reversibility, sensitivity, and cost.

Sensor Type	Sensing Principle	Resp. time	Reversibility	Sensitivity	Cost	Ref.
FBG based sensor	Wavelength shift	65 min	Non-reversible	Water-bath	High (FBG, OSA, broadband, light source)	123
Single mode optical fiber	Shock waves propagation	44 hrs	Non-reversible	Water-bath	High (pin photodetector, spring-loaded gun, amplifier)	129
Single mode fiber	Propagation velocity of shock waves	5 km/s	Non-reversible	Water-bath	High (Mach-Zehnder interferometer	131
Polymer coated on FBG	Wavelength shift	240 min	Non-reversible	Water-bath	High (FBG, OSA, broadband light source)	132
Polymer coated on FBG	Wavelength shift	170 min	Non-reversible	Water-bath	High (FBG, OSA, broadband light source)	133
Multimode plastic clad silica fiber	Gravimetric sorptivity	6.7 hrs	Non-reversible	Submerged in water for 5 days	Long fabrication time (~5 weeks)	136
Bare single mode fiber	EF-FLRD ringdown technique	5 min	Reversible	10-80 ml water	Low (single mode fiber, photodiode detector)	This work

4.1.4.4 Comparison of the EF-FLRD Water Sensors Embedded in Concrete Samples with Their Counterparts

Advantages of the EF-FLRD water sensors can be discussed by comparing them with current fiber optic water sensors that have been embedded in concrete for water sensing in the aspects of response time, reversibility, and sensitivity. For example, a polymer coated FBG is based on physical response of the polymer that swells or shrinks

when moisture inside the coated polymer is saturated or evaporated, respectively, resulting in a change in the FBG grating spacing. Polymer coated FBG sensors can be reversible [150]. Reversibility of a polymer coated FBG sensor is restricted by experimental conditions, including environmental temperature. However, no report, even under controlled situations, has demonstrated the reversibility with polymer-based FBG moisture sensors embedded in an actual concrete structure to date. Yeo *et al.* reported measurements of moisture in concrete specimens by using a humidity sensor which was fabricated using a polymer coated FBG as the sensing element [145]. Two humidity sensors were embedded in different locations in a concrete cube and the concrete cube was immersed in a water bath. When the polymer coatings absorbed water, the coated polymer became swollen; the FBG was stressed and a shift in the FBG central wavelength was detected. Another similar study was reported by Yeo *et al.* [139, 151]. A humidity sensor probe was embedded in the concrete to monitor moisture change in the concrete by measuring the FBG's wavelength shift. In both studies, the sensors only read a monotonic trend data, namely, a single step of dry - wet scenario of the concrete. Reversibility of the experiment was not demonstrated. Similar FBG water sensors were also used to study concrete structures with different water:cement ratios in different porosities [138, 139]. In all of these studies the sensors' principle was based on a FBG's wavelength shift, resulting from the swollen polymer-induced stress upon the FBG and the sensors were not reversible; and only dry - wet transition could be monitored. However, in comparison with the tested results reported in this work, one of the advantages of the EF-FLRD water sensor over its counterparts is reversibility, i.e., the same EF-FLRD sensor can be used to monitor successive increasing and decreasing

levels of water in concrete. Table 4.2 shows comparisons of the features of the EF-FLRD water sensors with FBG-water sensors when both types of sensors are embedded in concrete for water sensing. These features include response time, reversibility, sensitivity, and cost. There are numerous types of fiber optic water sensors; however, this comparison is only constrained to the water sensors which have been embedded in concrete. It is worth noticing that another merit of the EF-FLRD water sensor is that it is immune to variations of temperature in the concrete because the temperature coefficient of the bare silica fiber is only 0.5×10^{-6} /°C [17, 152]. This feature is especially important in concrete monitoring, i.e., during the curing period, in which temperature change is drastic.

4.1.5 Conclusions

In this study, novel EF-FLRD water sensors were developed and embedded in concrete and grout bars to monitor water/moisture in the concrete/grout samples. Eight EF-FLRD water sensor units were embedded in four different concrete structures and four different grout structures. The results obtained using the EF-FLRD sensors embedded in the concrete/grout samples show that the presence of water inside the concrete/grout samples can be monitored. This is the first time that water in concrete/grout has been monitored by using the EF-FLRD technique via embedding a bare single mode fiber-based FLRD sensor in concrete and grout with different properties. The results tell differences in properties of the concrete/grout samples, such as porosity and structures of the concrete samples. The recorded data clearly show that this new technique has apparent advantages over current fiber optic water sensors embedded in concrete or grout for water/moisture monitoring; faster response, higher sensitivity,

lower cost, and most importantly, reproducible reversibility. The EF-FLRD sensor is also immune to temperature variations. Additionally, due to its high sensitivity and fast response to the presence of water, the sensor can potentially be utilized for study of chemical and physical dynamics of concrete during the curing period with high temporal and spatial resolution.

4.2 FLRD Crack Sensor

4.2.1 FLRD Sensor for Potential Real-Time Monitoring of Cracks in Concrete Structures: An Exploratory Study

A FLRD crack sensor in concrete structure is reported for the first time. A bare SMF was used to fabricate the sensor head without using any other optical components or any chemical coating, which was driven by a FLRD sensor system. The sensor performance was evaluated on hand-made concrete bars of dimensions 20 cm × 5 cm × 5 cm. Responses of the sensor to cracks which were produced manually were recorded in terms of ringdown times. The sensor demonstrated surface crack width (SCW) detection of 0.5 mm, which leads to a theoretical SCW detection limit of 31 μm. Response of the sensor to a cracking event is near real-time (1.5 s). A large dynamic range of crack detection between a few microns (μm) and a few millimeters (mm) is expected from this sensor. This FLRD crack sensor seems very promising for detection of cracks when embedded in concrete with distinct features, such as simplicity, temperature independence, near real-time response, high SCW detection sensitivity, and a large dynamic range.

Health monitoring of concrete structures, including crack monitoring, is an important requirement in the civil infrastructures [153]. Except natural factors, such as

natural hazards, earthquakes, etc., other factors responsible for cracks in concrete structures are thermal contraction upon drying, ageing, shrinkage due to water imbalance, sub-grade settlements, applied loads, etc. [154]. Cracks may or may not be visible depending on the location. A crack on the surface of a structure is simply detectable, whereas cracks inside a structure may not be obvious at all. Correspondingly, damage severity of cracks to the structure can be different depending on the extent and location of the cracks. For example, a crack width of 0.3 mm is enough to allow water penetration inside concrete blocks which consequently can result in deterioration. Similarly, even a micro-crack at critical points, such as joints, bends, etc., can be highly dangerous and requires immediate care. Therefore, crack monitoring is an essential part of SHM.

There are various non-destructive techniques for crack sensing in concrete structures. For instance, some of the techniques are surface penetrating radar method, impact-echo method, infrared thermography, acoustic emissions, etc. [155-158]. In addition, a new technology named smart aggregate that uses embedded piezoceramic based transducers has also been used to monitor cracks in concrete structures in recent years [159-162]. More details on the conventional techniques involved in crack sensing can be found elsewhere [163, 164]. The first use of fiber optic sensors for SHM is generally credited to Mèndez *et al.* [136]. Compared to the conventional techniques of sensing cracks in concrete structures, techniques based on fiber optic sensing have their own advantages. For example, FOSs have immunity to electromagnetic interferences, good functionality in harsh environments, small footprint, and low-cost [165, 166]. FOSs can be categorized based on sensing mechanism, such as intensiometric sensors, interferometric sensors, FBG sensors, and polarimetric sensors [135]. All aforementioned

sensors have their own merits and limitations. For instance, intensiometric sensors have abilities for long range sensing with the simplest sensing mechanism; whereas interferometric sensors, FBG sensors, and polarimetric sensors are useful in localized sensing, and they involve complex instrumentation [167]. Likewise, on the one hand, light fluctuations affect performance of the intensiometric sensors [168]; temperature fluctuations affect the FBG based sensors, and they require use of additional means to counter the temperature impact [169]. A detailed discussion on different FOS regarding their applications, performances, advantages, limitations, etc., in view of concrete health monitoring can be seen in several excellent reviews [134, 135, 167, 170-175].

Among the previously mentioned FOSs, the intensiometric sensors, which use intensity modulation for measurements, are the simplest one to construct. In principle, the intesiometric sensors can detect damages or cracks at any point in the concrete along the fiber line because they are capable of sensing an event along the whole length of the fiber optic cable. In one of the earliest works involving concrete damage detection using the intensity modulation technique, Rossi and Le Maou [176] conducted experiments with a bare fiber for crack detection in concrete structures. The fiber without its protective coatings was embedded directly in the concrete, and the transmitted signal was monitored. As the crack reached the fiber, the fiber broke, resulting in sudden ceasing of the transmitted signal. Even though it is the simplest, the major limitation of this method is that once the fiber breaks, no further detection can be carried on. Ansari and Navalurkar [177] designed their sensors for crack detection based on the same intensity modulation method yet with a different configuration. The fiber was made in a loop shape such that the fiber crosses the generated crack to increase the sensitivity. The

sensor based on this design is restricted to only small size cracks. Leung *et al.* [178] developed a sensor to monitor flexural cracks in concrete structures. The loss in the back scattered light intensity is related to mechanical deformation. The fiber arrangement which is laid in a zig-zag shape inside the concrete is the key feature of this design. This design increases the sensitivity of the system. The sensor is efficient for monitoring flexural cracks under various types of loads. This technique is simple and sensitive, but only responsive to certain orientations of cracks regarding the orientation of the fiber. Habel *et al.* [179] demonstrated that an intensity-based FOS can be used in a quasi-distributed configuration to measure crack opening widths. Similarly, Lee *et al.* [180] presented that even a low resolution and less sensitive intensity based fiber optic sensor constructed with inexpensive instruments can be useful in the cases where precise measurements of strain or cracks are not required, for example, measurements of hardness.

Usually, an ideal technique should have common desirables for health monitoring of concrete structures including damage detection, a simple sensing mechanism, a long sensing range, low instrumentation cost, high sensitivity, fast response, insensitivity to temperature and light fluctuations, and capability of distributed sensing [181]. In this work, we describe a new FLRD sensor, which potentially meets the aforementioned requirements for crack detection in concrete structures.

The FLRD technique has evolved from the CRDS technique, in which a light pulse is injected into a cavity constructed using two highly reflective mirrors. The coupled light pulse travels back and forth many times before it dies out completely. A small portion of the light energy of the coupled light pulse leaks out of the cavity during

each round trip. The transient profile of this transmitted light intensity exhibits a single exponential decay. The decay rate of the light intensity generates the sensing signal called "ringdown time", from which concentration of a gas inside the cavity can be determined [182-184]. Involving the principle of CRDS, the FLRD technique employs the decreasing rate of the light intensity in a closed fiber loop to determine the ringdown time. The ringdown time changes due to different optical losses of the light pulse traveling inside the fiber loop. The difference in the ringdown time results because of a change in the optical loss, which is related to a sensing event occurred in one section (sensor head) of the fiber loop. The FLRD technique was first demonstrated by Stewart *et al.* [97]. Later many different deviations of FLRD have been reported by different research groups for different applications [16, 17, 31, 80, 99, 185, 186], including pressure, force, and strain sensors using a fiber loop combined with different types of fibers or optical components, such as FBG and long period grating [51, 187-190]. However, to clarify, the FLRD technique has not been explored for crack detection in concrete structures.

Among several FLRD-based sensors, this is the first FLRD-based crack sensor that is fabricated, packaged, and embedded in concrete for testing. Very sensitive and temperature-independent FLRD crack sensors have been developed to monitor cracks in concrete slabs. A bare SMF was used as a sensor head, which detects a sensing event, a cracking event in this case. The sensors were tested in our laboratory with actual concrete bars. Sensors were embedded in a wet concrete slab, so that upon drying out of the concrete, the sensor was integrated with the concrete slab and became one unit. Cracks were produced manually, and resulting responses of the sensors were monitored as a change in the ringdown time. Crack detection sensitivity in terms of SCW of the concrete

slab on the order of tens of microns (μm) was estimated theoretically. Although conventional FOSs, such as FBG, Fabry-Perot sensors, Brillouin based sensors, etc., can have a strain sensitivity as high as 0.1 με [135] or can detect a crack of size as small as sub-millimeters [191], they all utilize complicated instrumentation. Given the simplicity and low instrument cost, the present FLRD crack sensor may represent a new type of crack sensor in SHM.

4.2.2 Sensor Design and Sensing Principle

First, the experimental setup for the FLRD sensors will be described, and then the sensing principle of the technique will be explained.

4.2.2.1 FLRD Sensors

A typical FLRD sensor system for crack detection is illustrated in Figure 4.7. A FLRD sensor system consists of two major sections: a FLRD sensor unit and its control system. The FLRD sensor unit was constructed with a SMF loop (SMF-28e, Corning Inc., Painted Post, NY, USA) that was formed through two identical 2×1 fiber couplers (Opneti Communication Co., Hong Kong); in the middle of the 120 m long fiber loop, one small segment of the bare fiber was used as the sensor head. No modification or special treatment was needed to construct the sensor head; instead the small part of the bare fiber was used as it is for this purpose. The main components of the FLRD sensor control system include a CW diode laser (NTT Electronics, NEL America), laser control electronics, a photodiode detector (PDA50B, Thorlabs, Newton, NJ, USA.), and a ringdown data acquisition portion. The control system used in this work was the same as the one described elsewhere [17, 31]. In general, a FLRD sensor unit can be controlled by

the same sensor control system with different sensing functions. The connection and disconnection of a fiber sensor unit to the control system was readily achieved via two SMF FC/APC connectors.

A SMF has a tensile stress ≥ 100 kspi, a fatigue parameter $N_d = 20$, and diameters of the cladding and core which are 125 μm and ~8.2 μm, respectively. For 120 m fiber loop construction, SMF is used. The split ratio at the two-leg end was 0.1:99.9. The connection of the fiber couplers to the fiber loop is as shown in Figure 4.7. Optical losses of the light in the fiber loop are absorption losses, fiber connectors' insertion losses, and fiber couplers' losses. A total loss optical loss was estimated to be < 0.45 dB for each fiber loop in this study. Ringdown signals were detected by the photodiode detector. A detected signal was fed to a pulse generator to generate a series of negative square waves. These pulsed square waves were applied to the laser driver to drop the laser current to zero rapidly; consequently a series of laser pulses from the continuous wave diode laser were created. A detailed description of a FLRD sensor system can be seen elsewhere [17, 31, 34].

4.2.2.2 FLRD Sensing Principle

A light pulse when coupled into a fiber loop makes many round trips inside the loop. Intensity of the light pulse decreases during each round trip because of the internal optical loss. The photodiode detector observes different intensities of the transmitted light from each round trip. Therefore, the rate of change of the light intensity as observed by the detector can be given as [16],

$$\frac{dI}{dt} = -\frac{IAc}{nL}, \tag{4.5}$$

where I is the light intensity at any arbitrary time t, A is the total fiber transmission loss of the light per round trip; c is the speed of the light. n and L represent the average refractive index and the total length of the fiber loop, respectively. The temporal behavior of the light intensity I can be obtained from Equation (4.6):

$$I = I_0 e^{-\frac{c}{nL}At}. \tag{4.6}$$

The time it takes for the intensity to decrease from I_o to I_o/e is termed as the ringdown time, τ_0, and is given by Equation (4.7a):

$$\begin{aligned} &\text{(a)} \quad \tau_0 = \frac{nL}{cA} \\ &\text{(b)} \quad \tau = \frac{nL}{c(A+B)}. \end{aligned} \tag{4.7}$$

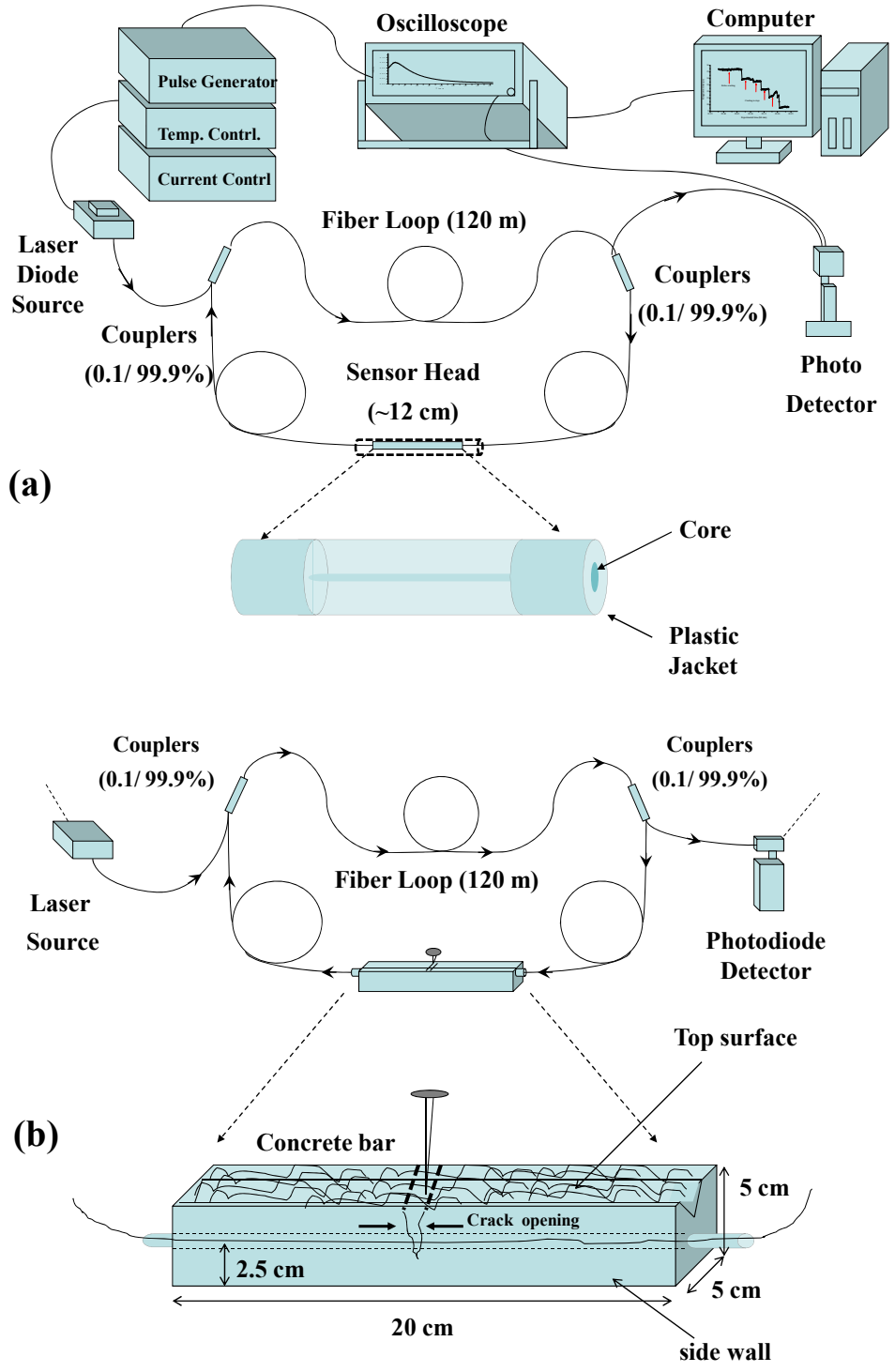

Figure 4.7 FLRD sensor system and configuration

(**a**) Schematic illustration of the FLRD sensor system. (**b**) Sensor configuration for crack sensing in concrete bar.

For a given FLRD sensor, the total transmission loss A depends on the physical parameters of the sensor, such as the fiber absorption loss, the couplers' insertion losses, the refractive index, and the fiber length. A typically remains constant for a given fiber loop. The term B represents the additional optical loss of the light pulse which occurs as a result of a sensing activity at any section of the fiber loop (i.e., sensor head). This causes a change in the ringdown time, τ, given by Equation (4.7b). From Equations (4.7a) and (4.7b), we have:

$$B = \frac{nL}{c}\left(\frac{1}{\tau} - \frac{1}{\tau_0}\right). \tag{4.8}$$

Equation (4.8) shows that an additional optical loss, B, can be determined by measuring the two ringdown times τ and τ_0.Therefore, Equation (4.8) suggests that a change resulting from a sensing activity, such as external pressure, deformation, absorption, etc., can be determined by measuring ringdown times with and without the sensing event. Earlier, FLRD was demonstrated for pressure or force sensing due to micro-bending [16, 17]. In this work, the FLRD technique is further explored to detect cracking events in concrete structures. We first investigated the stretching characteristics of the single mode fiber (elongation in length) to understand the limit of SMF stretching; later, experiments were conducted for crack sensing in concrete bars.

For example, a small part of the fiber in the middle of the fiber loop is stretched by a small length ΔL, if α is the loss per unit stretch length, the total loss due to the stretch ΔL happening in the small part of the fiber loop, can be given as $\alpha\Delta L$. Therefore, Equation (4.7a) is modified to:

$$\tau = \frac{n(L+\Delta L)}{c(A+a\Delta L)}. \tag{4.9}$$

For small stretches, when ΔL is on the order of millimeters against the length of fiber loops of several meters, 120 m in this study, we can surely assume that $L + \Delta L \approx L$; therefore

$$\tau = \frac{nL}{c(A+a\Delta L)} \tag{4.10}$$

If the loss due to the stretching is significantly smaller than the total optical loss in the fiber loop, i.e., $\alpha\Delta L << A$, then,

$$\begin{aligned} &\text{(a)} \quad \tau = \frac{nL}{cA}\left(1 + \frac{\alpha\Delta L}{A}\right)^{-1} \\ &\text{(b)} \quad \tau = \tau_0\left(1 + \frac{\alpha}{A}\Delta L\right) \end{aligned} \tag{4.11}$$

Equation (4.11b) shows a linear relationship between the ringdown time and the stretched length. The ringdown time, τ, is directly proportional to the decrease in the stretched length, ΔL, in the fiber.

Two sets of experiments were conducted to investigate the relation expressed in Equation (4.11). Two points were marked in a small section of the optical fiber in the middle of the loop. One of the marked parts was glued to a fixed mount, and the other marked part was glued to a mount attached to a high precision portable platform with a spatial resolution of ±10 μm. With one mount fixed, the other was moved horizontally to generate a stretch in the fiber. Stretches were produced in steps; the ringdown time, τ, was recorded each time when the stretch length was increased. A graph of τ *versus* ΔL is plotted in Figure 4.8.

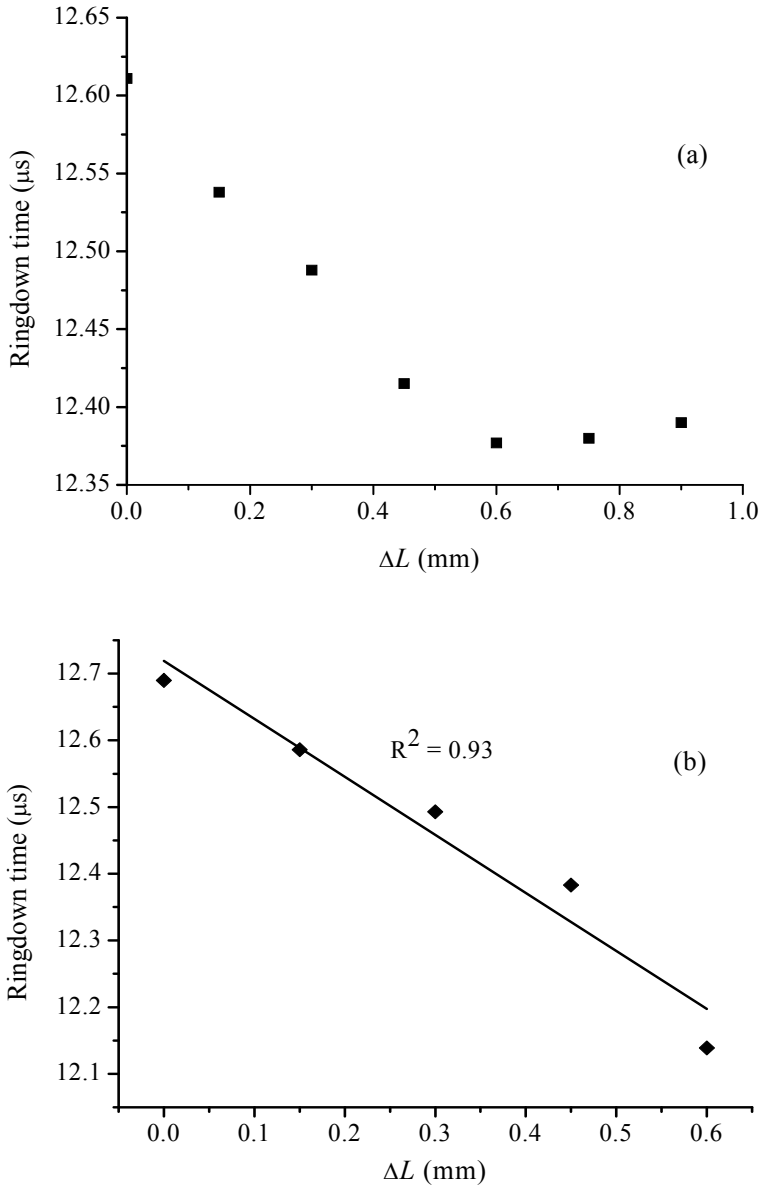

Figure 4.8 Results of stretch experiments

(a) A graph of the ringdown time *versus* the stretched length (ΔL) from the fiber stretch experiment; up to the breaking threshold of the fiber. (**b**) Result from the repeated fiber stretch experiment.

The experiment was conducted with a section of fiber of 8 cm long. The stretches in the fiber were developed in steps. The ringdown time first decreased with increase in the stretched length. A decrease of 0.23 μs in τ was recorded for ΔL = 0.6 mm. Fitting the

experimental curve to a line yielded $R^2 = 0.98$, which showed that the decrease in the ringdown time was fairly linear in this range. However, for $\Delta L > 0.60$ mm, an increase in the ringdown time was noted. The ringdown time, 12.37 μs at $\Delta L = 0.60$ mm, increased to 12.38 and 12.39 μs, at $\Delta L = 0.75$ and 0.90 mm, respectively. The fiber was broken beyond this stretch point. This purposed that the section of 8 cm long SMF had a tolerance level (the breaking point) of 0.9 mm. The experiment was repeated. A similar graph, τ *versus* ΔL, was plotted for this repeated experiment is shown in the Figure 4.8(b). For an increase in the stretched length in the fiber from 0 to 0.6 mm, the ringdown time decreased from 12.69 to 12.13 μs. A linearity of $R^2 = 0.93$ was obtained. The fiber was not stretched further in order to avoid damage or breaking. The part showing non-linear response of the fiber beyond a particular ΔL, 0.6 mm in this case, is ascribed to the fact that in a stretched fiber optic cable, beyond a certain limit of the stretched length in the fiber, the field propagating inside the fiber cable does not remain restricted in the fiber core. The non-linearity arises as a result of coupling differences between the higher order excitations in the cladding part of the fiber optic and the lower order excitations in the fiber core. A similar phenomenon was also reported in an early work [192].

The experimental results confirmed the relationship between τ and ΔL, as derived in Equation (4.11). These stretch characterization results demonstrate that a bare SMF can be utilized to investigate fiber stretch resulting from structure deformation, including cracks. Furthermore, the maximum stretch length can be up to 0.6 mm for a given section of SMF of 8 cm long. If the stretch is completely due to a structure separation on resulting from a crack, the width of crack-gap can also be determined. This is the research hypothesis to be studied in this work.

4.2.2.3 Concrete Samples

Concrete units in the shape of rectangular bar were produced manually by mixing ready-to-use concrete mix (Quikrete, Atlanta, GA, USA) and water with a mix ratio of 3:1. The dimensions of the bars were approximately 20 cm × 5 cm × 5 cm (length × width × height). The wet concrete was poured into a carton box to make up the rectangular mould; later on the carton box was removed after the concrete dried out. While curing and drying out process of a concrete bar, where a section of bare SMF was laid down, the section of the fiber remain embedded inside the concrete bar, making an integrated sensor unit. It is worth mentioning that the section of the fiber optic that was laid down in the concrete was a bare SMF cable without any modification or treatment. However, two elastic rubber tubes were used at the two ends of the concrete bar to protect the fiber from cut by the sharp edges at the corner of the bar. A typical FLRD crack sensor unit is shown in Figure 4.9. The fiber was laid down along the longest symmetry axis of the rectangular bar without stretch. The perpendicular distance from the fiber to the surface of bar is about 2.5 cm. In the similar way, relatively smoother grout bars were produced by adding tile mortar with polymer (Mapei, Deerfield Beach, FL, USA) to the concrete mixture. Both the concrete bars and the grout bars took approximately two days to settle and dry out.

Three sensor units, *units-1*, *2*, and *3*, were fabricated. The *unit-1* was made of ready concrete mix; *unit-2* and *unit-3* were made of concrete and grout mixtures. Each bar unit had one section of bare SMF embedded inside. Approximately 15 cm long fiber cable was extended outside the bar at each end through an elastic rubber tube to shield the fiber from damages. Once the bar dried out, the sections of the fibers extended outside

the bars at the two ends were spliced to a fiber loop to make a complete unit, as shown in Figure 4.9(a). Characteristics of the concrete and grout bars, i.e., *units-1*, *2*, and *3*, are discussed in the following section. One single ringdown loop was utilized to test the three sensor units individually.

4.2.2.4 Sensor Unit

The picture in Figure 4.9(a) shows a FLRD sensor unit constructed for the experiment. The concrete bar was spliced to the fiber loop through the junctions S_1 and S_2, as shown in the figure. A laser pulse was injected into the loop through the FC/APC fiber connector on the input arm of the fiber loop. The output arm of the loop was connected to a photodiode detector. The ringdown decay waveform was monitored by an oscilloscope which was connected to a computer for data processing.

Figure 4.9(b) shows the method of generating cracks in the concrete bars: a nail of 6d size (2 inches) was manually hammered onto the bar. The nail was hammered gently in steps until the crack appeared on the surface of the bar. Crack width on the surface increased slowly during hammering the nail at the same position on the surface of the bar. This crack width on the surface is called surface crack width (SCW). Figure 4.9(c) shows the actual image of a typical surface crack. The crack line is almost normal to the fiber line.

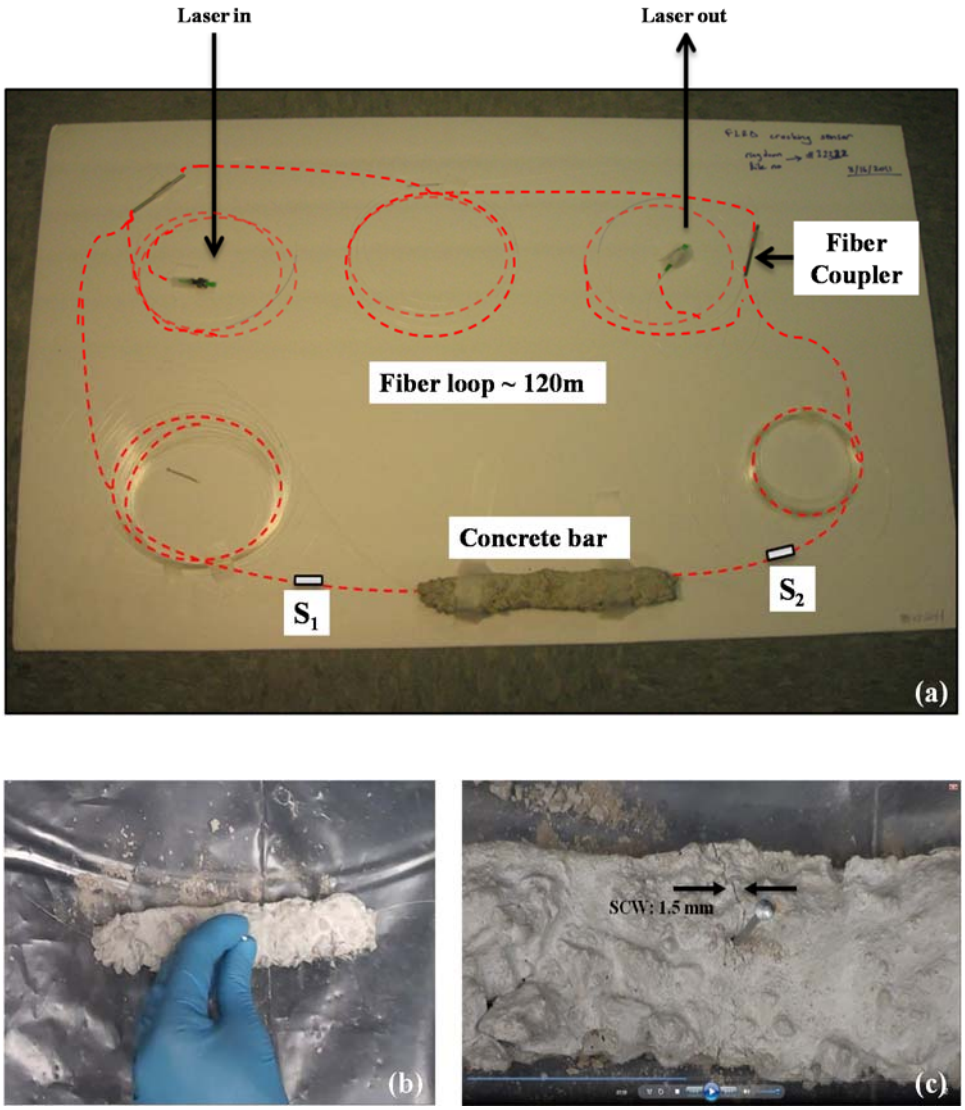

Figure 4.9 A sensor unit and crack experiment

(a) An image of a FLRD crack sensing unit: showing the fiber loop connected to the sensor head (concrete bar). (**b**) An image showing the manual procedures to produce cracks in the concrete bar. (**c**) A typical surface crack as it appears on the top surface of the bar.

In order to check the signal stability, the ringdown baseline stability which is defined as $\sigma/\bar{\tau}$, where σ is the standard deviation, and $\bar{\tau}$ is the base ringdown time, was determined [17]. The baseline stability was calculated as 0.33% by averaging over 100

ringdown events for both the cases, in other word, the fiber loop without a crack sensor head integrated, and the fiber loop with a crack sensor head (the bar units) connected. Figure 4.10 shows a comparison of the baseline stabilities in the two cases. Part *A* in Figure 4.10 displays the collected ringdown data when the sensor with concrete bar was not attached to the loop. The ringdown time (the baseline, τ_0) in this case was ~12.8 μs with a baseline stability of 0.33%. Part *B* represents the ringdown data when the sensor with concrete bar was connected (spliced) to the loop. The ringdown time in this case was 12.4 μs, with the same baseline stability, 0.33%. These results suggested that the signal in the fiber loop was quite stable, and the splicing process (integrating a sensor head into the fiber to form a loop) did not generate additional noise to the sensor's signal. A lower ringdown time when the fiber loop spliced with the concrete bar unit is due to the additional optical losses at two the splicing junctions.

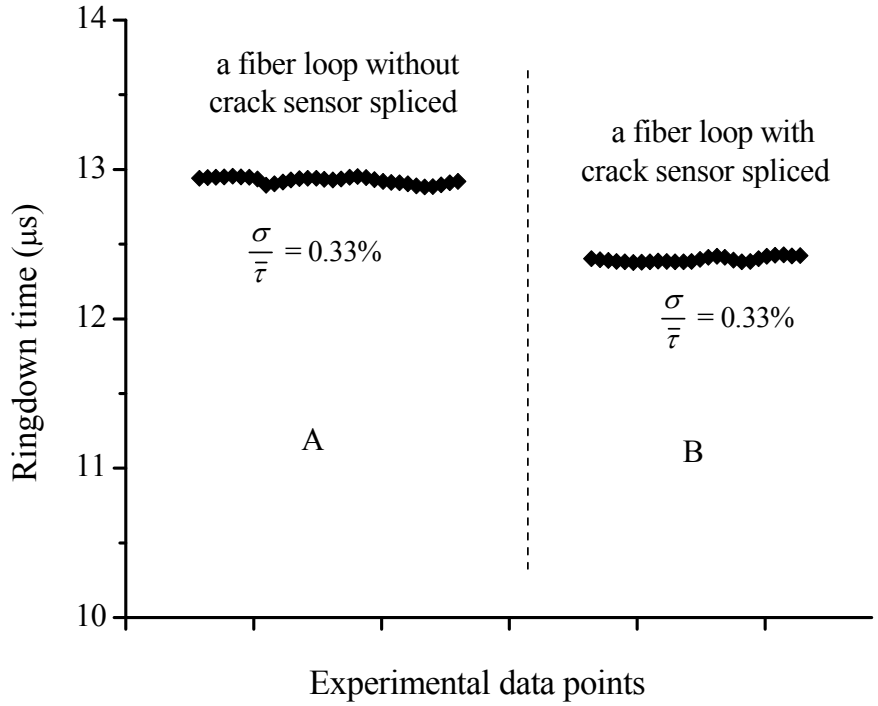

Figure 4.10 Typical sensor baseline stabilities

(**A**) without (**B**) with a sensor head spliced into the fiber loop. Both have the same baseline stability of 0.33% while their baselines are different due to different total losses.

4.2.3 Results and Discussion

4.2.3.1 Response of FLRD Crack Sensor

Figure 4.11 displays the results from tests for the crack sensing. A cracking event created on the bar surface generated a stress on the fiber embedded in the bar; therefore, observed ringdown time decreased due to additional optical loss resulting from fiber stress. The response of the sensor to the cracking event was near real-time (~1.5 s). The ringdown time, τ, averaged over 100 ringdown events, was recorded at different SCW that were produced in steps. In accordance with the sensing principle expressed in Equation (4.11b), decrease in the ringdown time was recorded with increase in SCW.

Experiments were conducted with all of the three units. Results of the experiments are shown in Figure 4.11(a - c), for *units-1*, *2*, and *3*, respectively.

It should be noted that the crack widths which have been plotted in Figure 4.11 in terms of ringdown times are the measured crack widths on the surface of the bars, the SCW. As shown in Figure 4.7(b), the crack first generated on the surface and further propagated down inside the concrete bar by hammering. Sensing of the cracking event was realized by observing a decrease in the ringdown time; thereafter upon every hitting, a proportional decrease in τ was recorded. It would be worth mentioning here that the crack appearing on the surface, viewed either from the top or the side wall, does not necessarily mean that the same amplitude of crack is generated at the location where the fiber is embedded. In this work, there was no particular mechanism or method to estimate the actual crack width at the location of embedded fiber optic. The only physical measureable quantity was SCW. Hence, SCW has been used to plot against the ringdown time in order to analyze the response of the sensor system in crack detection.

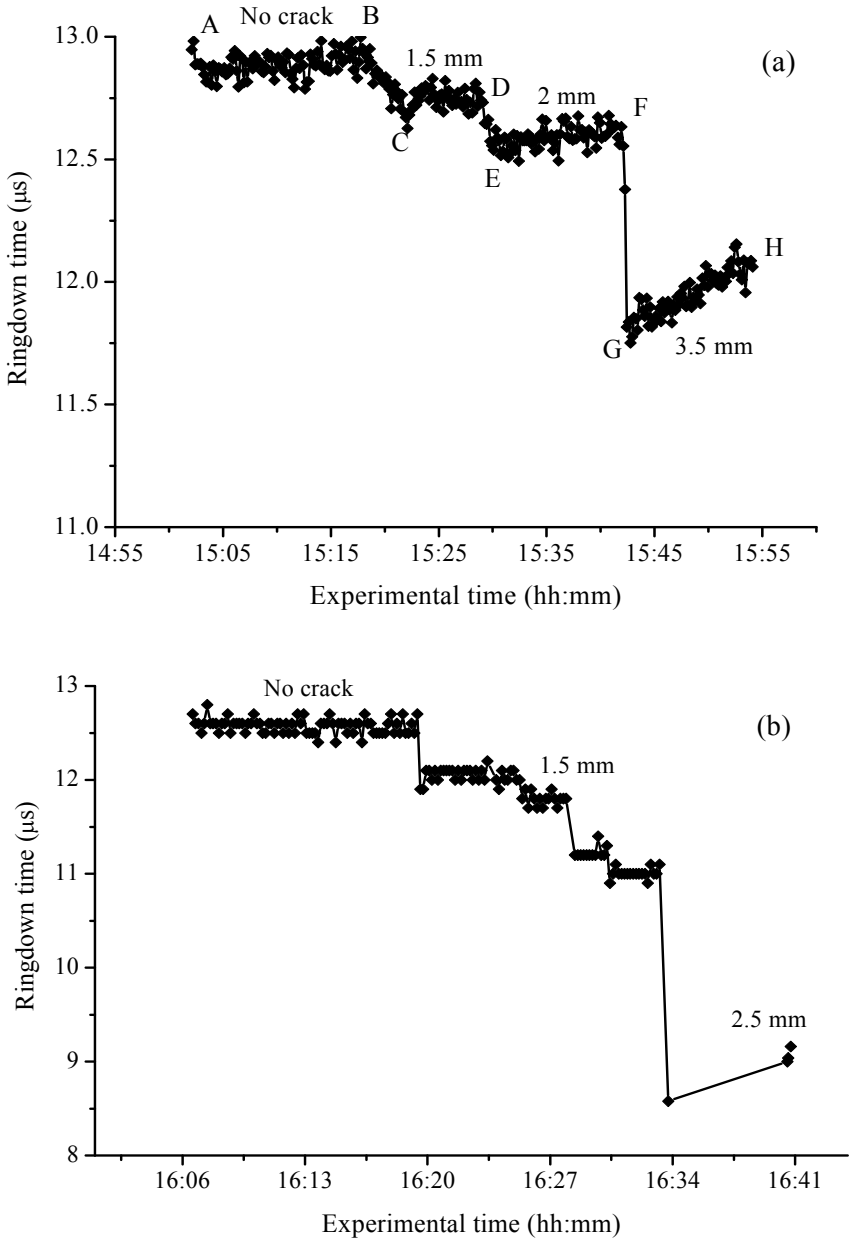

Figure 4.11 Responses of FLRD crack sensors to different surface crack widths.

Figure 4.11(a - c) are the responses of *units-1*, *2*, and *3*, respectively.

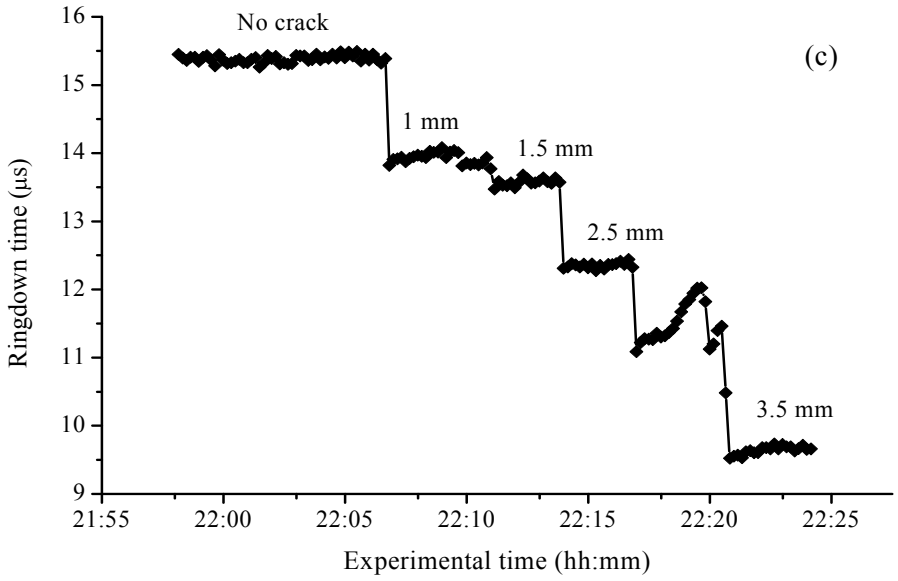

Figure 4.11 (continued)

Due to the heterogeneous distribution of the ingredients in the concrete bar, the propagation of the crack was less uniform inside the bar. Nevertheless, the result shown in Figure 4.11 supports that the fiber embedded inside the concrete did sense the cracking events created on the surface of the concrete bar. Moreover, a step-wise decrease in the ringdown time indicates that an increase cracking effect is happening at the fiber location. Figure 4.11(a) shows the response of the sensor *unit-1* to a set of three SCWs. From point *A* to point *B*, the ringdown times were recorded with the sensor without cracking events created. At point *B*, the nail was started to be hammered gently until an influential change in the ringdown time could be observed on the computer screen. Point *C* was marked when the ringdown time was 12.7 μs. The inclined part from *B* to *C* represents the elapsed time before the first remarkable change in the ringdown time was noticed, which in turn indicated the propagation of the cracking effect that happened from the surface of

the bar to the fiber optic location. The concrete bar at this point of time had developed a few additional surface cracks as well. A SCW of 1.5 mm along the width of the bar was measured at this stage; the data were recorded from the points *C* to *D*. The ringdown time during this time period remained to be approximately 12.7 μs. At point *D*, the bar was hammered again. It resulted in a sharp decrease in ringdown time, reaching the point *E* with τ = 12.5 μs. At the same time, cracks in other directions also extended. The data were recorded for the time period from *E* to *F*, with SCW had increased to 2.0 mm. At point *F*, the bar was hammered once again; there was a big sudden decrease in the ringdown time, reaching τ = 11.8 μs. SCW at this point was 3.5 mm; and the cracks in other directions extended more; and the bar was at the edge of breaking. When the sensor was left for few minutes, the ringdown time slowly increased back to 12 μs. This behavior is speculated to be due to the post-hit relaxation of the fiber inside the bar.

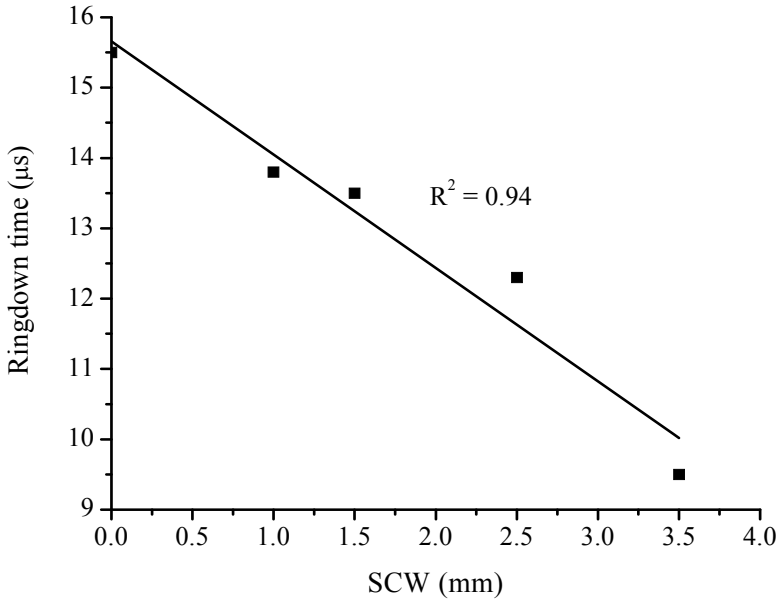

Figure 4.12 Response of the sensor *unit-3* exhibiting a linear relation between the ringdown time and the SCW.

The *unit-1*, made from concrete-mix and water only, was rigid in structure. Generation of uniform cracks in a controlled manner could not be obtained by manually hitting the nail. Therefore, it was desirable to make better concrete bars to handle cracks. Regarding this concern, two additional sensors, *unit-2* and *unit-3*, were fabricated by adding grout mortar-mix (Mapei) to the concrete mixture so that the bars were relatively softer. The compositions of *unit-2* and *unit-3* were mixtures of concrete-mix:grout:water in a ratio of 3:3:2, respectively. Fabrication of new bars by mixing grout additionally allowed production of cracks in a more controlled manner. Experiments were repeated. Figure 4.11(b) shows the response of *unit-2*. A decrease in ringdown time from 12.5 μs to 9.0 μs was recorded in the range of no crack on the surface of the concrete bar and a SCW of 2.5 mm. A sudden decrease in ringdown time, shown by the vertical drop lines in the figure, corresponding to a responding time of 1.5 s, signifies the fast response of the sensor. The ringdown signal remained stable and consistent all time when SCW increased. The results of *unit-3*, recorded in the similar way, are shown in Figure 4.11(c). A SCW up to 3.5 mm was generated, with the sensor responding to an every single cracking event on the surface of the bar. Considerable drops in ringdown time were recorded for each cracking event. Cracks produced in steps with SCW of 1, 1.5, 2.5, and 3.5 mm, resulted in ringdown times of 13.8, 13.5, 12.3, and 9.5 μs, respectively. The larger change in ringdown time for the same change in SCW of 3.5 mm when it is compared to the *unit-1*, indicates that this sensor unit had a better sensitivity. A plot of ringdown time, τ, versus SCW measured for *unit-3* is shown in Figure 4.12. A quantitative relation between the ringdown time and the SCW cannot be predicted beforehand. The linear decrease in ringdown time with increase in the SCW proposes that

the cracking events produced on the surface of the bars generated linearly proportional stresses to the fiber optic embedded inside in the bar. Therefore, we can conclude from the results that a cracking event occurring at the surface of the bar and 2.5 cm above the sensor head can be detected, and the cracking amplitude is reflected by the change in ringdown time. It must be stressed that this type of cracking sensor is better to be utilized for continuous crack monitoring instead of measurement of crack widths inside a concrete structure. A calibration curve, obtained in a computer-simulated and controlled cracking situation, may be useful and helpful for determination of the widths of actual crack-gaps inside the concrete; and this is a subject of future work.

4.2.3.2 Detection Sensitivity of Surface Crack Width

As mentioned before, each of the three sensor units, *unit-1*, *2*, and *3*, responded differently to the cracking events in terms of crack productions. Therefore, in order to analyze the SCW detection sensitivity of the sensors units, the results obtained need to be considered individually.

In the case of *unit-1*, a decrease of 0.2 μs in ringdown time was monitored when the SCW increased from 0 (no crack) to 1.5 mm. However, the next cracking event increased the SCW to 2 mm; an increment of 0.5 mm. The same amount of decrease in ringdown time was recorded, which is 2 μs. This indicated that once the crack on the surface propagated through to the fiber optic position, the sensor exhibited a SCW detection sensitivity of 0.5 mm.

Observations for sensors *unit-2* and *unit-3* were as same as *unit-1*. Experimentally, the difference among the three sensor units was the production of controlled cracks. Unlike in *unit-1*, comparatively controlled cracks were produced in

sensor *units-2* and *3*; both sensor units responded immediately to each cracking event generated on the surface of the bar. A uniform stepwise increase of 0.5 mm in SCW was recorded with each sensor unit, as shown in Figure 4.11(b, c). A substantial decrease in ringdown time in each increasing step of SCW was noted with near real-time response (1.5 s). Conservatively, both sensor units can be considered to be sensitive to a SCW of 0.5 mm or smaller. This estimation is based on the fact that the generation of a SCW smaller than 0.5 mm in each step could not be achieved and controlled in the present experimental situation. However, remarkable changes in ringdown time for a SCW of 0.5 mm in each step, as shown in Figure 4.11(b, c), indicate that the sensor could be theoretically much more sensitive in terms of response to a much smaller SCW. This speculation drives a further consideration of a theoretical detection sensitivity of sensors in terms of a minimum detectable SCW (explained in the following part).

4.2.3.3 Theoretical Detection Sensitivity of the Crack Sensor

The theoretical detection sensitivity of FLRD crack sensors can be estimated by using the baseline stability of the ringdown signals. The baseline stability, $\sigma/\bar{\tau}$, (expressed in %) is construed as the minimum fractional ringdown time that comes from a minimum distinguishable ringdown time, τ, from two separate signals under a given set of experimental conditions. This means that two signals, assume τ_1 and τ_2, can be distinguished only if the difference between them is equal to at least one-σ (the one-σ standard deviation). From Equation (4.11 (b)), we derive:

$$\begin{aligned} &\text{(a)} \quad \Delta\tau = \tau_0 - \tau = \tau_0 \frac{\alpha}{A} \Delta L. \\ &\text{(b)} \quad \Delta\tau = \mathrm{m}\Delta L. \end{aligned} \tag{4.12}$$

The $\Delta\tau$ in Equation (4.12) represents the decrease in the ringdown time, ($\tau_0 > \tau$), with the increase in fiber stretched length ΔL; $m = \tau_0 \frac{\alpha}{A}$, is the slope of the line in the graph of $\Delta\tau$ *versus* ΔL. The slope m is obtained experimentally.

It should be noted that ΔL in Equation (4.12) is the actual stretched length of the fiber, whereas the only physical measurable quantity in this experiment is SCW. However, as discussed earlier, ΔL is proportionally related to SCW; therefore Equation (4.12) must be valid for SCW as well. Therefore, rewriting Equation (4.12) for SCWs, Δd, we have:

$$\Delta\tau = \mathrm{m}\Delta\mathrm{d}. \tag{4.13}$$

Further, from Equation (4.13), it can be derived that:

$$\Delta\mathrm{d}_{\mathrm{min}} = \frac{1}{\mathrm{m}}\Delta\tau_{\mathrm{min}} \tag{4.14}$$

where Δd_{min} is the minimum measurable SCW; $\Delta\tau_{min} = \left(\frac{\sigma}{\bar{\tau}}\right)\tau_0$ is the minimum measurable ringdown time which can be determined with a known baseline stability and a ringdown baseline. A graph between $\Delta\tau$ and Δd, based on the experimental results obtained for the *unit-3*, is plotted in Figure 4.13. The graph shows linearity of $R^2 = 0.94$ and a slope $m = 1.61$.

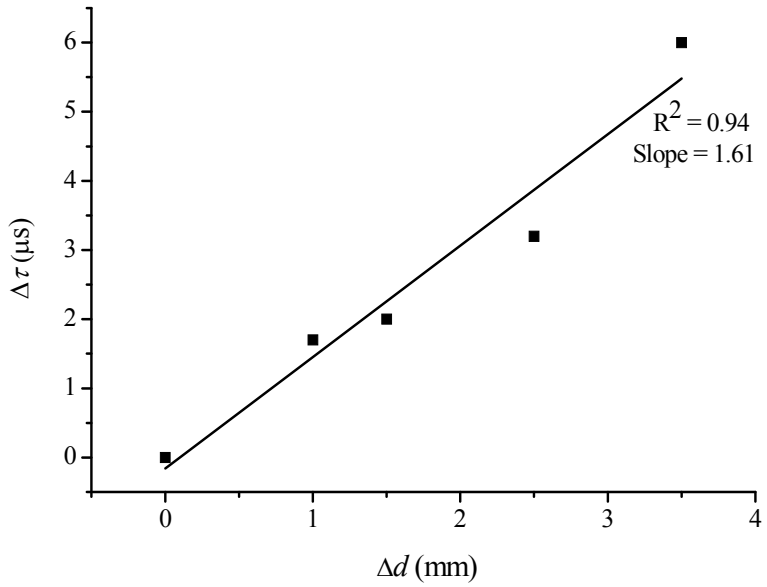

Figure 4.13 A calibration curve of the decreased ringdown time ($\Delta\tau$) *vs.* SCW (Δd), obtained from the sensor *unit-3*.

On the other hand, using the one-σ standard deviation, $\Delta\tau_{min}$ of 0.0511 μs is determined for the baseline stability of 0.33% and the ringdown baseline of 15.50 μs. Consequently, a minimum measurable SCW was determined as Δd_{min} = 31 μm.

This indicates that the presented FLRD crack sensor is theoretically responsive to a surface crack width as small as 31 μm, particularly for sensor *unit-3*. This study suggests that although the actual crack widths at the fiber location may not be determined at this stage, a cracking event happening on the surface of a concrete structure can definitely be monitored by the sensor with a theoretical detection sensitivity of microns. A detailed investigation into the detection sensitivity requires experiments be carried out under controlled conditions.

4.2.3.4 Advantages and Limitations of the FLRD Crack Sensors

The FLRD crack sensor has various unique advantages when compared to its counterparts:

- Simplicity
- Temperature independence
- Near real-time response
- High detection sensitivity and large dynamic range:

4.2.3.4.1 Simplicity

The presented FLRD crack sensors offer simplicity in terms of construction and operation. A bare SMF is directly utilized as a sensor head for the purpose of sensing without using any advanced fiber optic components or chemical coatings. Consequently, the use of SMF offers ease of construction as well as low cost of deployment in concrete structures, unlike other conventional sensors based on FBG, Brillouin scattering, or Fabry–Perot techniques, which include complicated instrumentation procedures and special care in the sensor deployment process [172, 191, 193]. Furthermore, the FLRD crack sensor needs an inexpensive photodiode as the detector, significantly reducing costs in the terminal detection equipment.

4.2.3.4.2 Temperature Independence

The FLRD crack sensor is based on the strain sensing mechanism. Due to the low thermal coefficient, 0.5×10^{-6} °C, of silica fiber [17, 152] and no necessity of other optical components in the sensor head, the FLRD crack sensor is virtually independent of environmental temperature in the range of – 169 to 800 °C [46]. This type of crack sensor

is especially advantageous when temperature variations are an important factor, i.e., in combustion facility, reactors, etc.

4.2.3.4.3 Near Real-Time Response

Fast response of a sensor is always desirable. Near real-time response is another significant feature of the present sensor. The sharp decrease in the ringdown time in Figure 4.11 shows that the response time was 1.5 s. A single measuring time is only 15 ms when 100 measuring event is taken into consideration. In civil structure monitoring applications, this response time has an important socio-economic impact in structure damage mitigation, i.e., in the case of natural disasters.

4.2.3.4.4 High Detection Sensitivity and Large Dynamic Range

The FLRD crack senor in this study has potentially crack detection sensitivity of tens of microns because of the high baseline stability, ~0.33%. As an example, *unit-3* has a detection sensitivity of 31 μm in terms of SCW. On the other hand, crack sensing was successfully carried out for SCW as large as 3.5 mm. Therefore, a large dynamic range of crack detection from tens of microns to a few mm can be expected from this sensor. Since the sensing is successfully accomplished with a bare SMF with simplicity in the construction of sensor, this level of sensitivity and dynamic range for crack detection is still practically appreciable in some applications.

An additional feature of the FLRD crack sensor, which will be explained in the next chapter, is its networking capability. Due to the time-domain sensing scheme of FLRD-based sensing [31], not only the uniform sensing signals, *time*, from multiple FLRD sensor units, but also different sensing functions can be readily multiplexed to

achieve a large scale sensing network. Current FLRD crack sensors have their own limitations. For instance, the FLRD crack sensors can only monitor sensing events, but cannot exactly identify a crack location and measure the crack-width. Following, in order to achieve distributed sensing, multiple sensor heads (units) need to be assembled in a sensor system to detect crack locations as well as time sequence of a series of cracking events when the events occur. All of these problems still remain to be solved.

4.2.4 Conclusions

A new type of FLRD-based sensors for crack detection in concrete structures has been developed. The sensing principle and instrumentation are described. A bare SMF was shown capable of detecting surface cracks with a theoretical detection sensitivity of tens of microns (μm) without any modification and treatment. Performance of the sensors was tested with actual hand-made concrete bars in our laboratory. Responses of the sensors toward manually produced cracks on the surface of concrete bars were recorded. The sensors displayed a fast response (~1.5 s) to the cracking events. In this exploratory study, the SCW was detected with a theoretical detection sensitivity of 31 μm. The sensor responded efficiently to a SCW up to 3.5 mm. Therefore, a large dynamic range of crack detection from microns (μm) to a few millimeters is expected from this sensor. This is the first time that the FLRD technique has been demonstrated for crack detection in actual concrete structures.

4.3 Summary of This Chapter

The EF-FLRD water sensors were fabricated and embedded in concrete and grout bars for monitoring water/moisture inside the structures. The results show that the

existence of water inside the concrete/grout can be monitored by utilizing EF-FLRD sensors embedded in the structures. We demonstrated for the first time that water in concrete/grout can be monitored by employing the EF-FLRD technique. The results showed that each concrete/grout sample had different properties in terms of porosity, structures of the samples, etc. It can be indicated by the recorded data that this new technique has obvious advantages (for instance, low cost, high sensitivity, fast response, and *reproducible reversibility*) over currently available embedded fiber optic water sensors to monitor water/moisture inside concrete or grout structure.

A new type of FLRD-based sensor to detect cracks inside concrete structures was developed. This work demonstrated for the first time FLRD crack sensors embedded in actual concrete structures for crack detection. A SMF was embedded into a concrete bar without any treatment or modification to sense cracks occurring inside the bar. Sensor responses to crack events were recorded in terms of ringdown time. The FLRD based crack sensor showed a fast response (~1.5 s) to crack events. In this work, the SCW was determined with a theoretical detection sensitivity of 31 μm. The response efficiency of the sensor to a SCW was up to 3.5 mm. Therefore, a large dynamic range of crack detection is expected from FLRD crack sensors.

CHAPTER V

SITE TESTING OF MULTI-FUNCTION FLRD SENSORS IN CONCRETE STRUCTURES

In this chapter, application of EF-FLRD sensors in a real structure is presented. Previously explained in detail, water and crack sensors and additionally temperature sensors were fabricated and tested under laboratory conditions and packaged to move to the US Department of Energy (DOE) test site, Miami, FL. Three units for water, crack, and temperature sensors each were fabricated, tested, and packaged for shipment to Miami after many experiments and calibrations were accomplished. Two of them were installed on Panel 5 which had dimensions of 10 ft × 8ft. Panel 5 was deployed into a concrete test cube with dimensions of 10 ft × 10 ft × 8ft. The test cube was filled with wet grout and left for testing installed sensors. Six of the EF-FLRD sensors were successfully installed, deployed, and tested. All of the sensors were tested during installation on the panel, after panels were deployed into the test cube, and before, during, and after grouting process. Later, data were collected remotely from the DOE test site in our laboratory at Mississippi State University (MSU), Starkville, MS.

This chapter includes fabrication and calibration of temperature sensors, installation of all sensors on the panel and deployment process, and remote data collection. Multi-sensor application on a real concrete structure will be fulfilled in this study by fabricating two units each for FLRD water, crack, and temperature sensors and

deploying them into the concrete test cube. We showed that multi-sensor application can be performed with low cost, fast and near real-time response, and high sensitivity.

5.1 FLRD Temperature Sensors

Temperature change was measured by utilizing FLRD-FBG-sensors. Commercially available FBGs were used as the sensing elements at the FLRD-FBG sensor heads. FLRD-FBG temperature sensors were fabrictated by splicing FBG sensor heads to the fiber loops. Later, the temperature calibration was carried out by using a thermocouple to measure the tempearutre at the FLRD-FBG temperature sensor head. In the early steps of temperature sensor fabrication, temperature sensors were placed into two metal plates and soldered to protect the sensor head from concrete leaking inside. Further, the FBG sensor heads were laid down into a copper tube. One side of the copper tube was cut lengthwise to place sensor head inside, then the cave was soldered, and ends of the copper tube were covered to prevent water or concrete leaking inside when the sensor was embedded into a concrete bar. Whenever metal plates or copper tube were heated up, the thermocpule read the temperature change. The FLRD control system read the corresponsing ringdown time. Calibration of the temperature sensors were carried out before the sensor head were placed between metal plates or into the copper tube. The setting of the FLRD-FBG temperature sensor head for calibration and two FLRD-FBG temperature sensor units are shown in Figure 5.1 (a), (b), and (c). Figure 5.1 (a) shows the experimental setting of a FLRD-FBG temperature sensor calibration. The sensor head was immersed into water with ice to cool it down, and into hot water to heat it up. Accordingly by reading temperature on the thermocouple and observing corresponding ringdown time on the FLRD control system, calibration of the temperature sensor was

carried out. The temperature sensor was tested between 10 and 35 °C with this kind of FLRD-FBG temperature sensor, and calibration precision was ±1 °C. To achieve for proposed temperature range of 15 to 45 °C, new FLRD-FBG sensors with a central wavelength at 1567 nm were purchased. Figure 5.1 (b) shows a temperature sensor unit tested under laboratory conditions. The FLRD-FBG temperature sensor head was placed between two thin metal plates with a thickness of 1mm. The edges of the plate were sealed to block penetration of grout into the sensor head when the sensor unit was embedded in the grout. Figure 5.1 (c) shows one of the two identically developed temperature sensors. The sensors were developed by utilizing commercially available FBGs. The FBG sensor head was laid down inside the copper tube. Two arms of the FBG were spliced into a fiber loop, and the arms of the fiber loop were covered by a Teflon tube for protection. Also, the copper tube was soldered for protection against grout leaking inside when the sensor was embedded into the concrete cube.

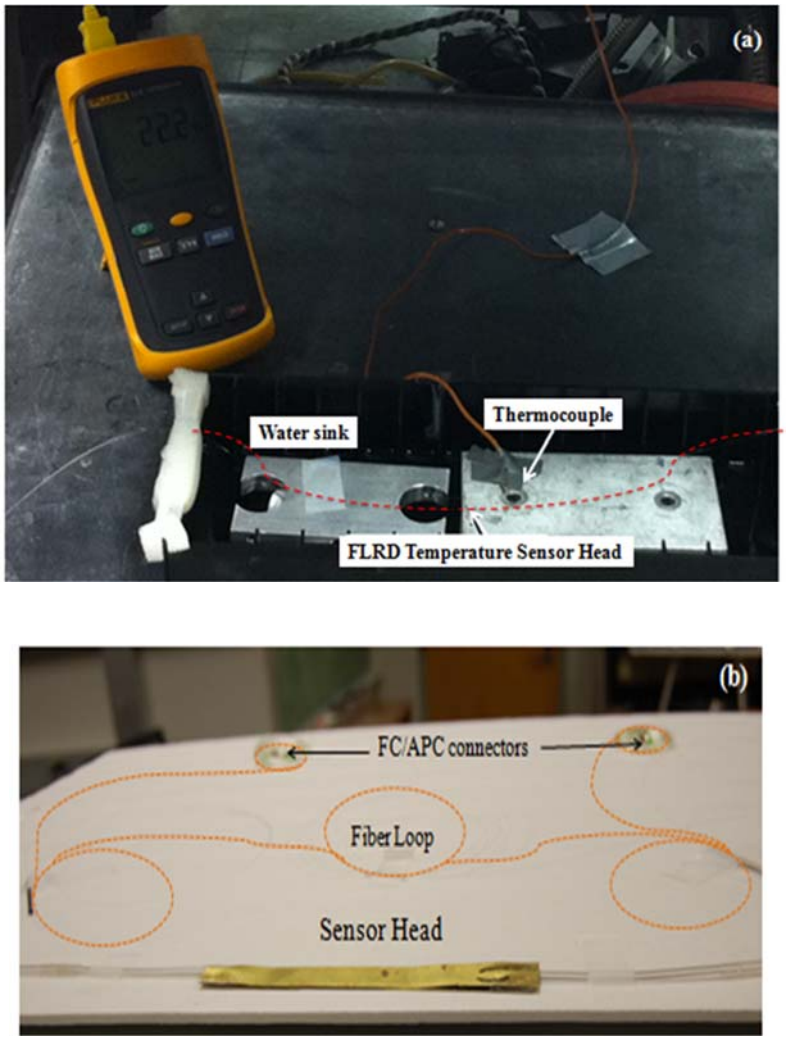

Figure 5.1 FLRD-FBG temperature sensors.

(a) The experimental setting of the FLRD-FBG temperature sensor calibration. (b) A sensor unit, which the sensor head is placed between two metal plates. (c) Another temperature sensor unit, which the sensor head is laid down into a copper tube.

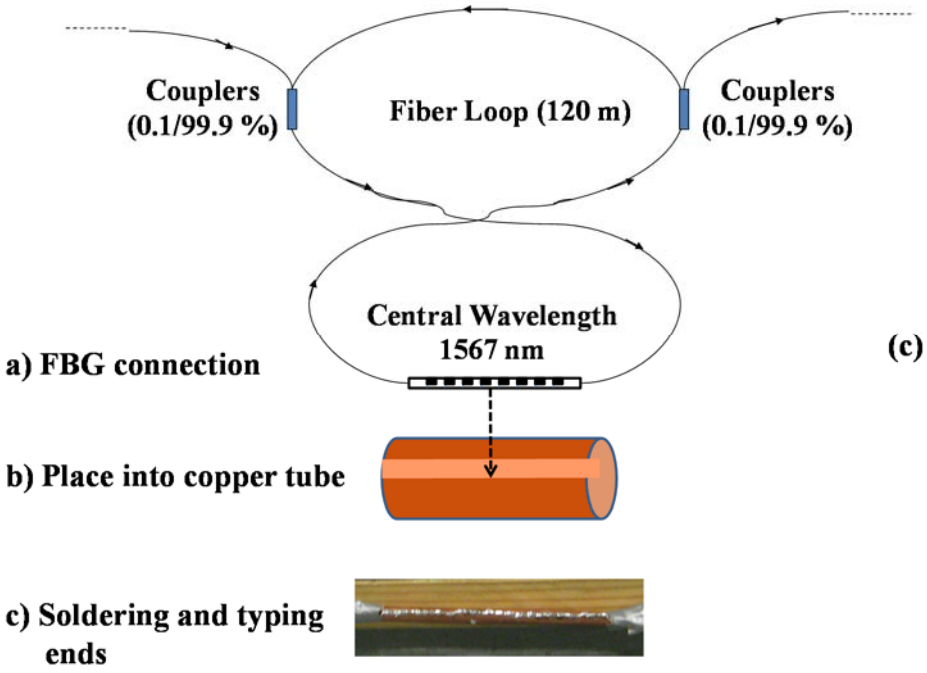

Figure 5.1 (continued)

Figure 5.2 shows the calibration curve of the temperature sensor. Temperature change was recorded in terms of ringdown time.

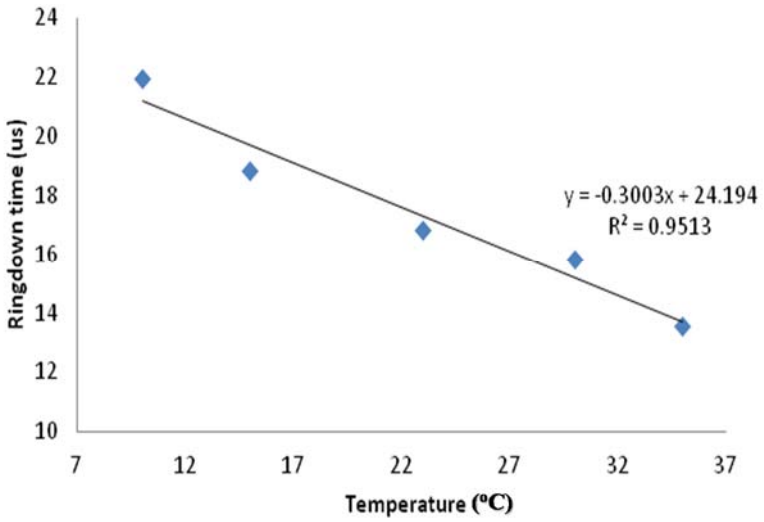

Figure 5.2 The calibration curve of the FLRD-FBG temperature sensor, the curve of the actual temperature (°C) versus ringdown time.

5.2 Installation and Deployment of the Sensors

Three types of FLRD sensors for water, crack, and temperature detections were fabricated. After the sensors were tested under laboratory conditions, they were packaged for installation and testing in the test bed at the DOE site in Miami, FL. Before moving the sensors to in the DOE site in Miami, performances of all six sensors were characterized in detail in terms of sensor severity and units' functionalities. Also, installation of the sensors was planned in detail because the time of installation was limited. Only two sensors from each sensing parameters were installed on Panel 5 as shown in Figure 5.3. In total, six FLRD sensors were installed on Panel 5. Two water and two crack sensors were embedded into concrete/grout bars with dimensions of approximately 30 cm × 5 cm × 5 cm. Two FLRD-FBG temperature sensors were placed into copper tubes with lengths of approximately 12 cm.

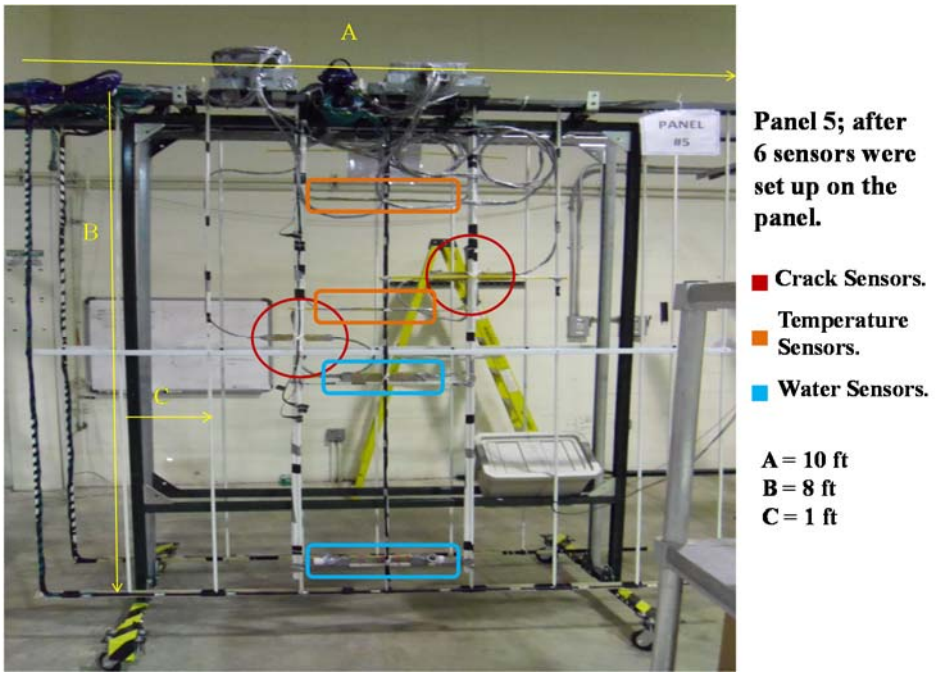

Figure 5.3 The panel FLRD sensors installed on to be embedded into the concrete cube.

When the left top corner of the test cube in the control room side is chosen for origin as shown in Figure 5.7, coordinates of the sensors in the three dimensions are as following: water sensor (bottom) was placed at (5, 4-6, 3.03) and water sensor (top) was installed at (5, 4-6, 1.80). Cracking sensors (bottom) and (top) were placed at (5, 4, 1.54) and (5, 6, 1.15), respectively. Temperature sensors were installed close to the top of Panel 5. Coordinates are (5, 4-6, 1.35) for bottom temperature sensor and (5, 4-6, 0.64) for the top temperature sensor. Y axis shows the sensors were placed between that ranges. All sensors were installed on Panel 5, which makes the x axis 5 ft from the origin. For example, place of water sensor (bottom) is 5 ft on x axis, between 4 and 6 ft on y axis, and 3.03 ft from z axis. Bottom temperature sensor is for the purpose of monitoring

inside temperature change, and the top temperature sensor is for observing surface temperature change of the concrete test cube.

Figure 5.4 shows one of each two sensors on Panel 5. Only one from each of two fabricated water, crack, and temperature sensors is shown in the figure for representation. Water sensor (bottom), crack sensor (top), and temperature sensor (top) are displayed in close-up in the figure. All of the sensors are presented in Figure 5.3 and marked.

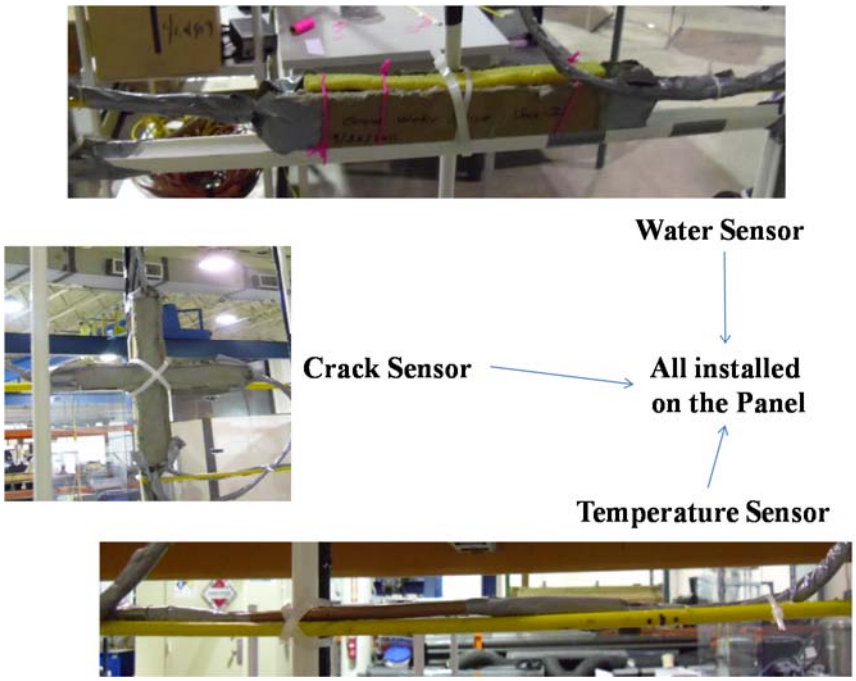

Figure 5.4 Representation of one of each sensor installed on Panel 5.

After sensors were installed on Panel 5, all panels were deployed into the test concrete cube with dimensions of 10 ft × 10 ft × 8ft at in the DOE site in Miami, FL, for real-time monitoring of water/moisture existence, crack events, and temperature changes. Figure 5.5 shows a presentation of the concrete cube after all panels were installed in the

concrete cube. The concrete cube was filled by wet grout after establishment of panels inside, as shown in Figure 5.6.

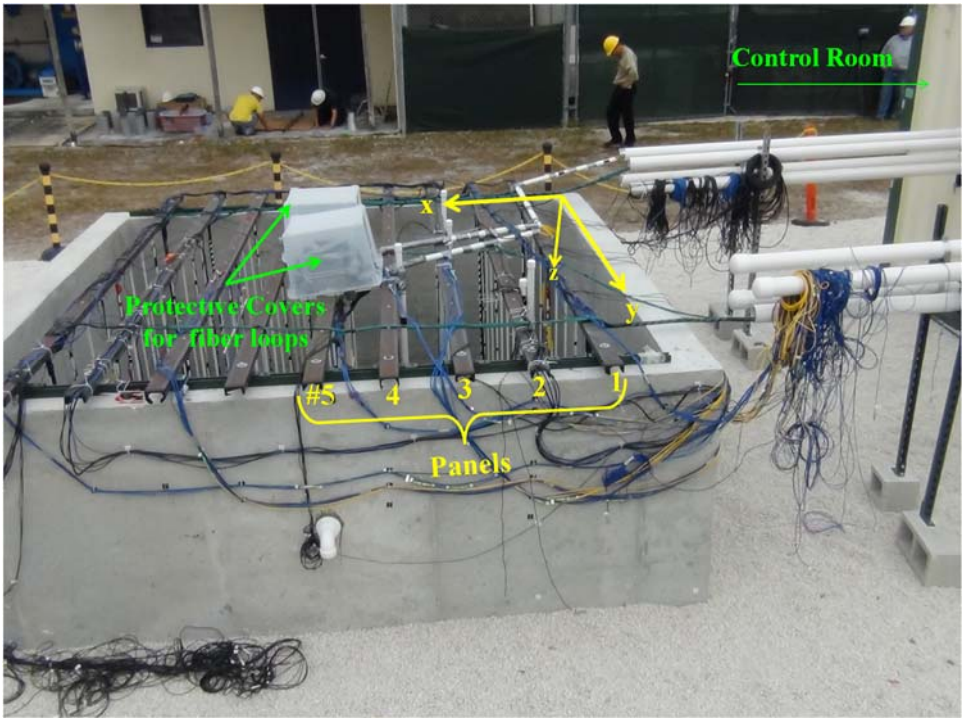

Figure 5.5 The concrete cube after the panels were installed.

Figure 5.6 Concrete pouring into the concrete test cube after panels were deployed.

Figure 5.7 shows the test cube after grout was filled. A removable roof was placed onto the test cube for protection. Rain brings extra water for concrete structure and also affects temperature. Therefore, the portable roof is held close to the cube. Also, the roof protects sensor loops and other extra components of the sensors from damage. Extra parts of the sensors were fixed on top of the panels and covered with plastic boxes. The control room houses computer systems. Each sensor's output and input channels were elongated inside the control room to be connected to the computer manually. Each time one sensor could be monitored.

Figure 5.7 The concrete test cube filled with grout, and ready for testing.

Figure 5.8 The multi-functional portable FLRD control device.

Figure 5.8 shows the portable FLRD control system. The system has a 7-inch screen to display ringdown signals from the FLRD program. The system is remotely controllable by using Ethernet or a wireless network. Only one of the installed sensors can be monitored each time. Manually switching the sensors' connections will provide monitoring of each sensor individually. Test time, from a few hours to a few days, is remotely controllable. Once desired the sensor was connected to the computer at the test site, the sensor could be controlled from the computer at MSU. Figure 5.9 shows the screen of the actual remote computer at the DOE site in Miami, which was logged in from the laboratory at MSU.

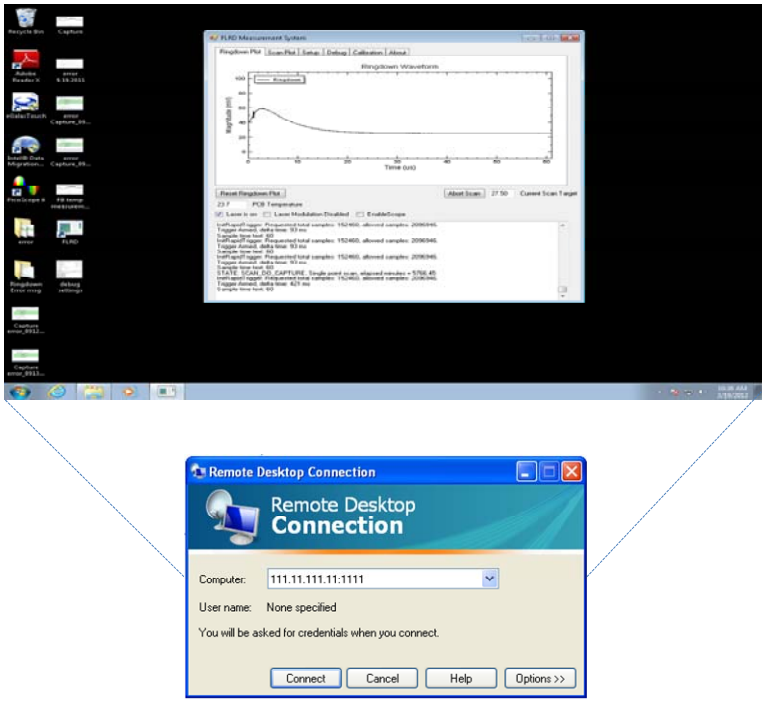

Figure 5.9 Remote login and operation of the FLRD sensor system located at the Test Site Office.

Top: The operation system (in Miami, FL) through remote control at MSU. Bottom: Remote login of the system through the remote desktop.

5.3 Testing of Sensors

5.3.1 FLRD Water Sensors

Figure 5.10 shows the collected data using the FLRD water sensor (bottom). Recording was started after the panels had been installed inside the cube and sensors had been connected to the control system. The water sensor was running before grouting started. The data collection was running till the grouting level reached the second water sensor (top). The gap between two data curves was due to switching and setup of the sensor control connection to the top water sensor. After a while, the bottom water sensor was connected again to observe change in ringdown time.

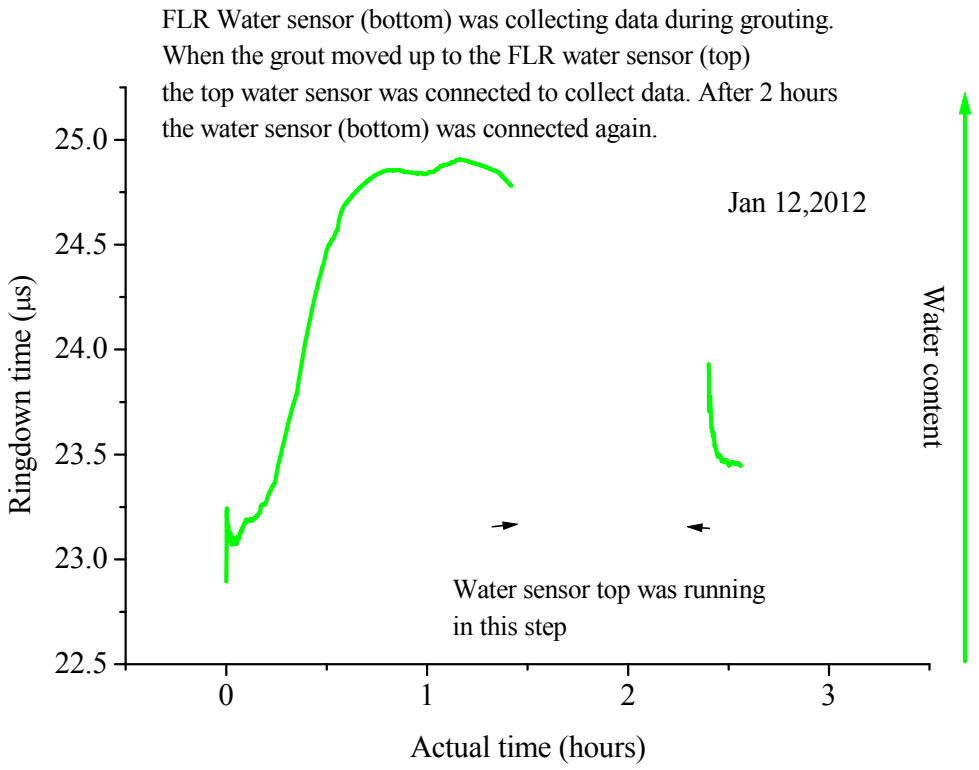

Figure 5.10 The FLRD water sensor (bottom) data collected before, during, and after the grouting.

As shown in Figure 5.10, the starting ringdown time was 23.1 μs before the grouting started. The ringdown time increased to 24.9 μs after the grout covered the sensor completely. The time for the water from the grout to enter the sensor head area was about 50 min. The ringdown time was stable during the subsequent one hour after the ringdown time increased to 24.9 μs, and then the ringdown time started decreasing slightly. In the next period, the top water sensor was connected because the grouting level already covered the bottom water sensor completely. When the top water sensor was connected, the grout was about to cover the grout bar where water (top) sensor was embedded.

Ringdown time showed a linear increase when the grout moved up and covered the sensor head, and the water in the grout began to enter the sensor head. Before the ringdown time from the top water sensor reached the saturated level, the control system was switched again back to the bottom water sensor. Ringdown time gradually decreased to 23.4 μs, as shown in the second part of the data in Figure 5.10. This result indicated that the FLRD water sensor was reversible (assuming water content in the bottom water sensor head began to decrease, i.e., water passed through the bottom sensor). After this point, the temperature sensor was connected to observe temperature change. It is should be noted again that only one sensor was operated each time.

Figure 5.11 shows the data collected from the water sensor (top) during the grouting. The top water sensor operated only for a short period of time because we wanted to keep running the bottom water sensor for most of the testing period to have a complete testing picture of the sensor system. As it can be seen in Figure 5.11, the water sensor (top) was also working functionally.

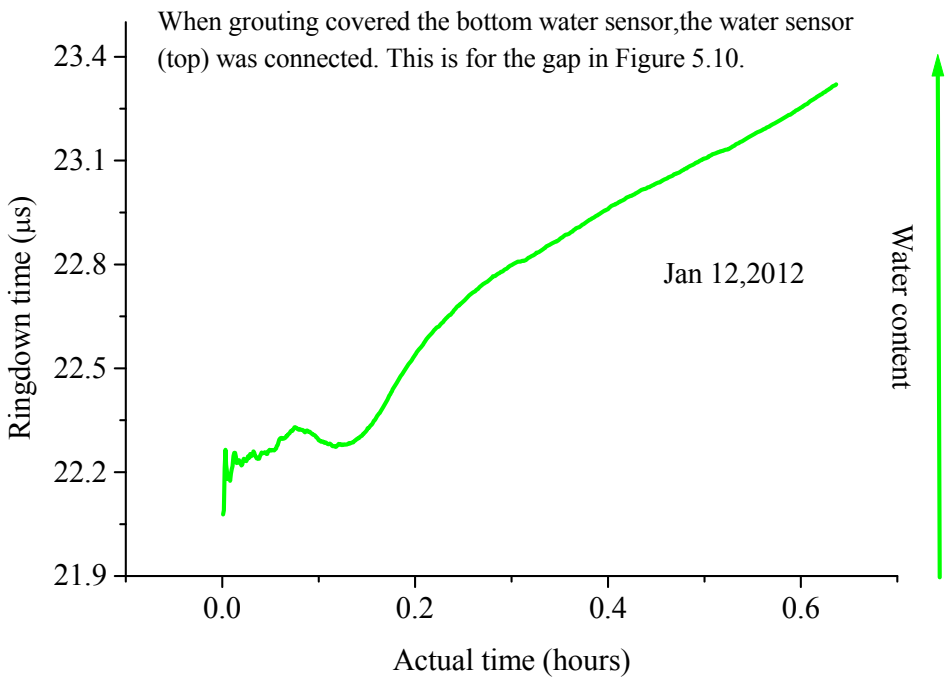

Figure 5.11 The FLRD water sensor (top) data collected during the grouting.

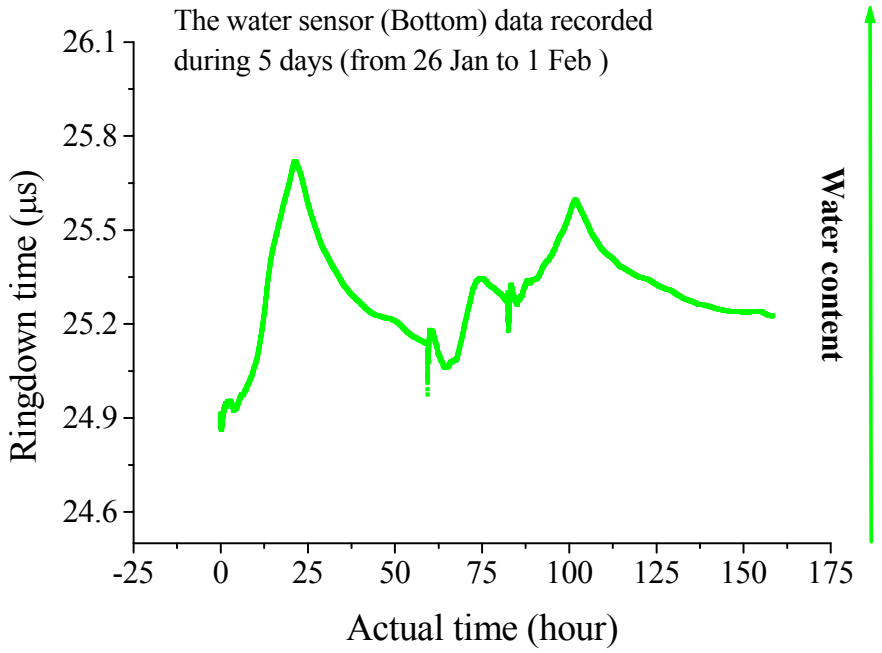

Figure 5.12 The testing data from the FLRD water sensor (bottom) operated remotely during the 5-day period.

The data shows fluctuations of water content around the sensor head in the grout.

Figure 5.12 shows remotely recorded data using the bottom water sensor during the 5-day period between Jan. 26 and Feb. 1, 2012. The total data curve consisted of three parts of data, which were collected for the periods of two days, one day, and two days, respectively; and for each period, the sensor was running continuously. The system was periodically stopped and restarted in order to avoid a possible stop due to excessive data points in a single ringdown data file.

5.3.2 FLRD Crack Sensors

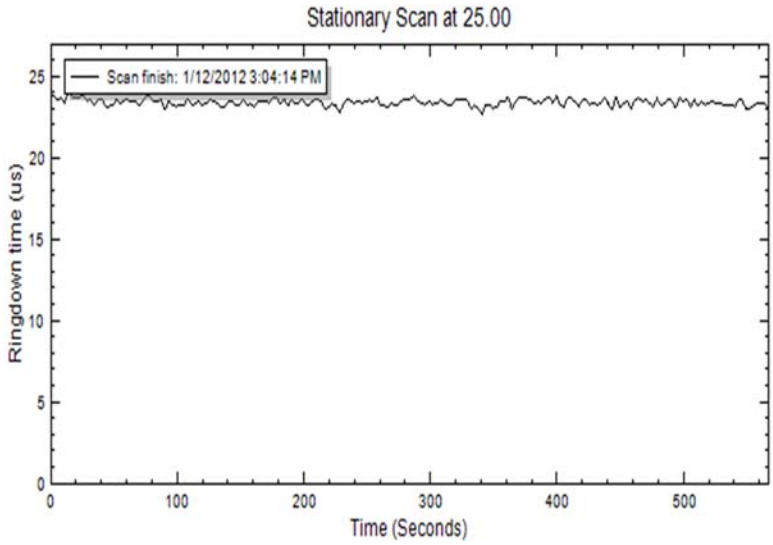

Figure 5.13 Crack sensor (bottom) data recorded after the grouting.

Figure 5.13 shows data collected from the crack sensor (bottom) after the grouting. The purpose of this short-time running was to test whether the crack sensor was damaged or not during the grouting. Especially, there was a blow-out that happened right at the crack sensor location during the grouting because of congestion of the grout inside the injection tube. The result showed that the crack senor was not damaged by the severe

hit and still functional after the grouting. The stabilized ringdown time indicated that no cracking happened during the initial grouting period. Taking a closer look at the ringdown signal shown in Figure 5.13, one would find that the ringdown time had a very small yet noticeable decline trend. This was due to the minimal stress generated by the grout on the sensor head. The grout generated hydrostatic pressure on the sensor when pouring was started.

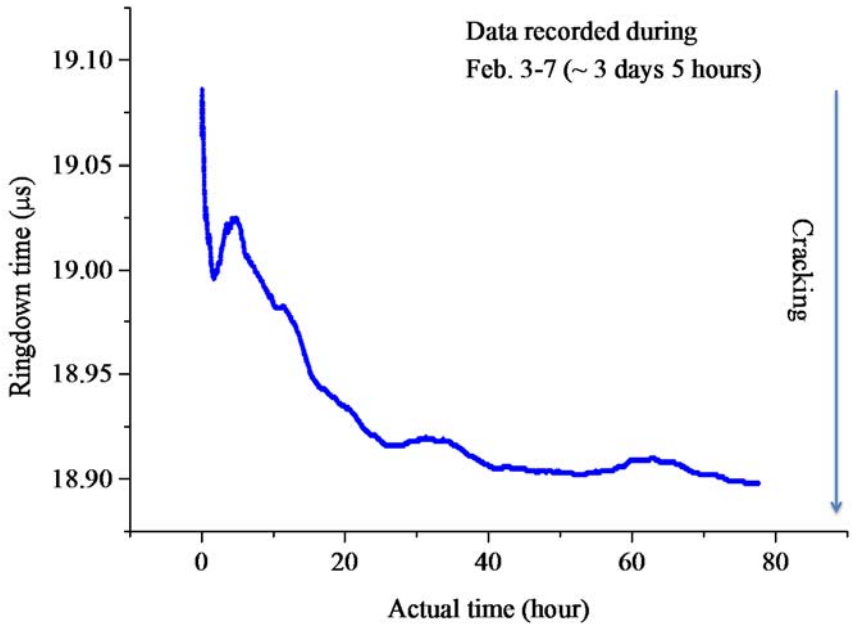

Figure 5.14 Crack sensor (top) data recorded remotely during 3 day and 5 hour.

Figure 5.14 shows ringdown data collected during 3 day and 5 hour period. The significant decrease of ringdown time indicates that there was a potential crack happening inside the grout, as shown in Figure 5.13. However, this prediction needs to be confirmed with other types of crack sensors deployed in the test cube.

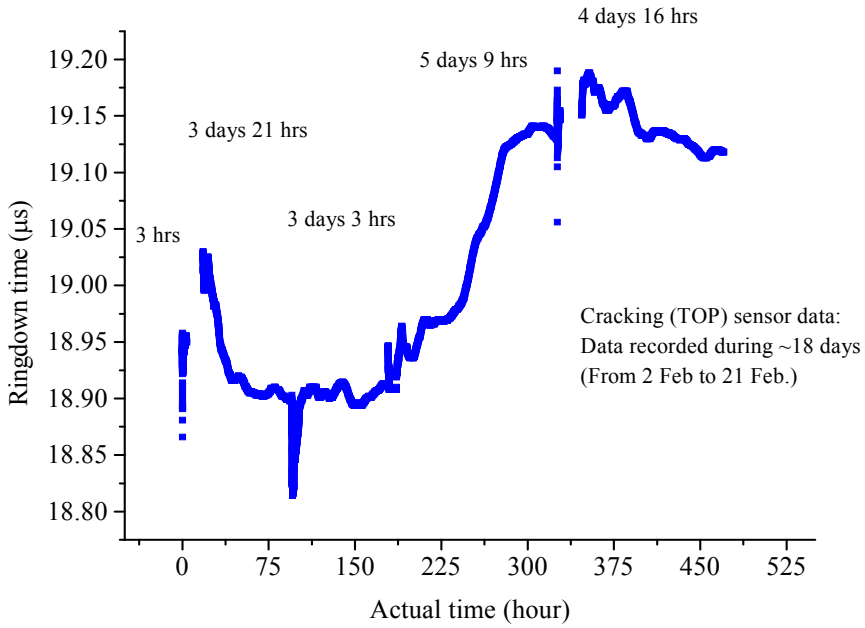

Figure 5.15 Crack sensor (top) data recorded remotely during 18 days.

Figure 5.15 shows the collected data using the top crack sensor during 18 days. Ringdown time was initially 18.85 µs. Decreases and increases in ringdown time show that there was some possible contraction and expansion inside the cube. The crack sensors can be easily affected by any external pressure or stress. Therefore, any change in the grout volume inside the cube could cause variations in the stress or force on the sensors embedded and the ringdown time of the crack sensors would fluctuate. Whenever any cracking happens around the FLRD crack sensors, ringdown time will decrease, depending on the crack size. This behavior has been tested reproducibly in our laboratory at MSU.

The crack sensor (bottom) has also the same trend. The sensor was tested after grouting process went for a short time to test if the sensor was still working or damaged. The sensor had been working efficiently.

5.3.3 FLRD-FBG Temperature Sensors

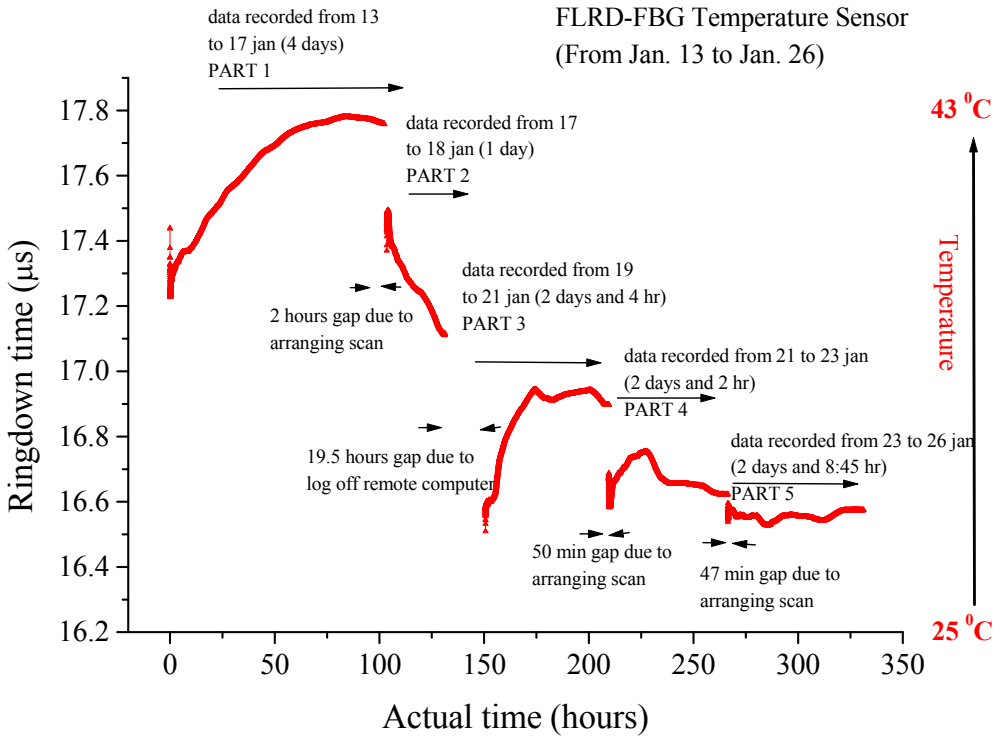

Figure 5.16 The testing data using the FLRD temperature sensor (bottom) recorded remotely during 13 days.

Figure 5.16 demonstrates the data collection using the bottom temperature sensor during a period of ~13 days. The temperature sensor was located at 1.35 ft from the top of the test cube frame. Change in temperature was recorded in terms of ringdown time change and collected data were compared with temperature data from other types of temperature sensors, such as thermal couples from INL (US DOE Idaho National Laboratory). The FLRD-FBG temperature data was in good agreement with those from INL's thermal couples.

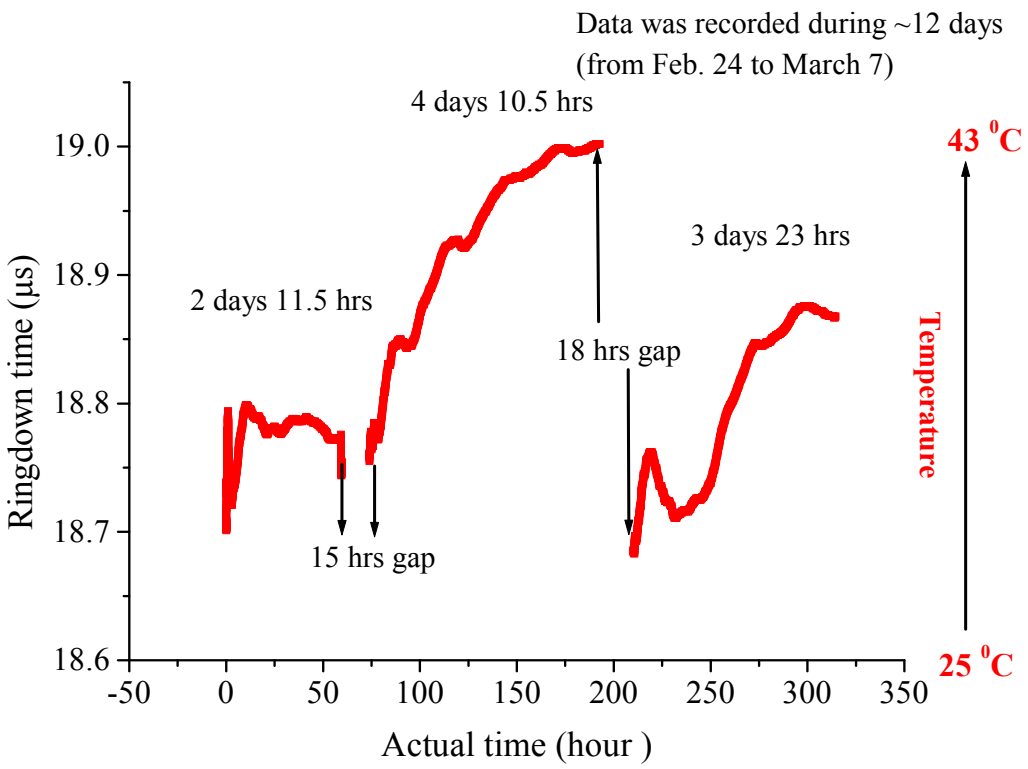

Figure 5.17 The FLRD temperature sensor (top) data recorded remotely during 12 days.

Figure 5.17 shows the collected data from the top temperature sensor during 12 days from Feb. 24 to March 7, 2012. The gaps between the adjacent curves were generated due to the stops of the ringdown software of the control system (It happened occasionally, too, during lab testing and was not debugged in phase I due to the time constraints of the project). The temperature sensor was located at 0.64 ft from the top of the test cube frame. Data was collected periodically and displayed in a single graph, as shown in Figure 5.17 with actual experimental time in the x-axis. Change in the monitored ringdown time with this temperature sensor was faster and more frequent than the one in the bottom temperature sensor because this temperature sensor was located closer to the surface of the cube, 0.64 ft from the surface of the cube, where the grout was

more sensitive to the climate. Exact temperature value can not be measured. Only changes in temperature can be observed.

5.4 Conclusions

Three types of FLRD sensors were designed and developed for the purposes of water, crack, and temperature sensing in concrete structures. The performance of the sensors was first tested with small size concrete bars in our laboratory at MSU, Starkville, MS. The lab experimental results established the idea that the FLRD technique is indeed capable of sensing water, cracks, and temperature in actual concrete structures. Later, all of the sensors were entombed in a test grout cube with dimensions 10 ft × 10 ft × 8 ft at the DOE test site in Miami, FL, for evaluating its performance under real-world scenarios. Sensors are controlled and data are still being collected, remotely in our laboratory. Results from both the experiments, i.e., conducted in the laboratory and from the real-time monitoring in Miami, have been discussed in this work. This work presents for the first time a study of FLRD technology in real-world applications.

CHAPTER VI

FUTURE OF THE FLRD SENSOR NETWORK

FLRD employs an inexpensive telecommunications light source, a photodiode, and a SMF to build up a uniform FOS platform to sense different quantities, such as strain, pressure, temperature, chemical species, refractive index, biological agents, etc. In the FLRD technique, optical loss of a light pulse is measured by the decay time constant of the light pulse. FLRD is a time-domain sensing technique because time is measured in FLRD to detect a quantity. Therefore, FLRD sensors have enhanced sensitivity, near-real time response, and low cost (no use of optical component, such as optical spectral analyzer). There has been an increasing attention to FLRD development, and new applications are being investigated since introduction of FLRD. Discussions on challenging issues in the development of multi-function FOSs or sensor networks using present FLRD sensing schemes can be seen in Ref. [31].

A fiber optic sensor network (FOSN) can be defined as a sensor system employing fiber optic networks installed in a wide area and/or over a long distance, where the optical fiber plays a role either as signal transmission lines or as sensing media. A FOSN is an array of sensors that are embedded either directly into a structure or a solution for detection quantities or close to them. FOSN has significant improvement over counterpart sensor networks providing a wide range of application areas, such as environmental, safety, and security networks [194]. FOSN not only monitor

infrastructures and lifelines, but also are distinguished methods which are a reflection of advantageous characteristics of low transmission loss of the optical fiber [195]. FOSN provides very effective sensing solutions for large range of applications from large scale structures, such as bridges, dams, and other kind of civil structures, to large natural environments [172].

FOSN has three main challenges in spite of advantages: 1) Increasing sensor numbers in a sensor network: The more sensors can be connected to a network, the more data can be collected, but the cost of a system depends on optoelectronic devices. If the optoelectronic unit which is the costly part of a network is shared among sensing points, the cost per sensing element will be reduced [196]. 2) Continuity on the sensor network: When a failure on the network happens, resilience or self-healing is the capability of continuity of the network. This is the main issue for FBG sensor systems [197]. Continuity of monitoring after an accidental damage of the network is critically important for high value systems (such as oil pipelines, power transmissions, etc.), safety (such as nuclear power plants, bridges, dams, etc.), and security (such as airports, banks, etc.) [134, 198-202]. 3) Remote sensing: Lately, remote sensing in FOSN system has received an increasing interest due to monitoring a wide range of parameters and quantities simultaneously in many fields. Remotely controlling and monitoring of structures from a central station located far away from the sensor network field is the idea behind of the remote sensing concept. Being independent of electrical power makes remote sensing of FOSN applications more attractive. Remote sensing provides damage detection as soon as it happens in a network, therefore, intervention to repair the sensor network can be as quick as possible [203, 204].

In this chapter, a sensor network is setup by combining two or three FLRD sensors. Some unique features of the sensor network studied in this chapter are easy setup in both series and parallel configurations, low cost, fast response, real-time monitoring, and high sensitivity. One of the main advantages of a sensor network is that it is able to measure multi-parameters simultaneously. Two configurations of fiber loops' connections for sensor networking are tested. The configurations are in series and in parallel configurations. In both configurations, two or three FLRD sensors were connected and tested successfully. Later, two sensors were connected in both configurations by utilizing a 1×2 micro-electromechanical systems (MEMS) switch and tested individually. Promising results indicate that a FLRD sensor network ensures good repeatability, high sensitivity, fast response, real-time monitoring, low cost, simplified design, and easy configuration.

6.1 Sensor Multiplexing and Techniques

The purpose of any multiplexing technique is to setup a single unit by combining several sensors. Multiplexing can be either in series or in parallel configurations. There are mainly five types of signal multiplexing techniques. They are time division multiplexing (TDM), wavelength division multiplexing (WDM), frequency division multiplexing (FDM), coherence domain multiplexing (CDM), and polarization division multiplexing (PDM). They will be explored in detail in the following sub-chapters.

6.1.1 Time Division Multiplexing

TDM technique is the combination or multiplexing process of two or more signals transferred as a package in one channel. On the contrary, time domain demultiplexing

technique is the splitting process of the coupled signals into individual signals. The TDM technique is generally accommodated by line connection configuration of the sensors. In this technique, the signals require longer times to reach the detector from the last sensor of the connection. TDM can be adapted to all other physical structures by using additional delay lines. For intensity based sensors, the signal reading unit consists of an optical time domain reflectometer (OTDR) [205].

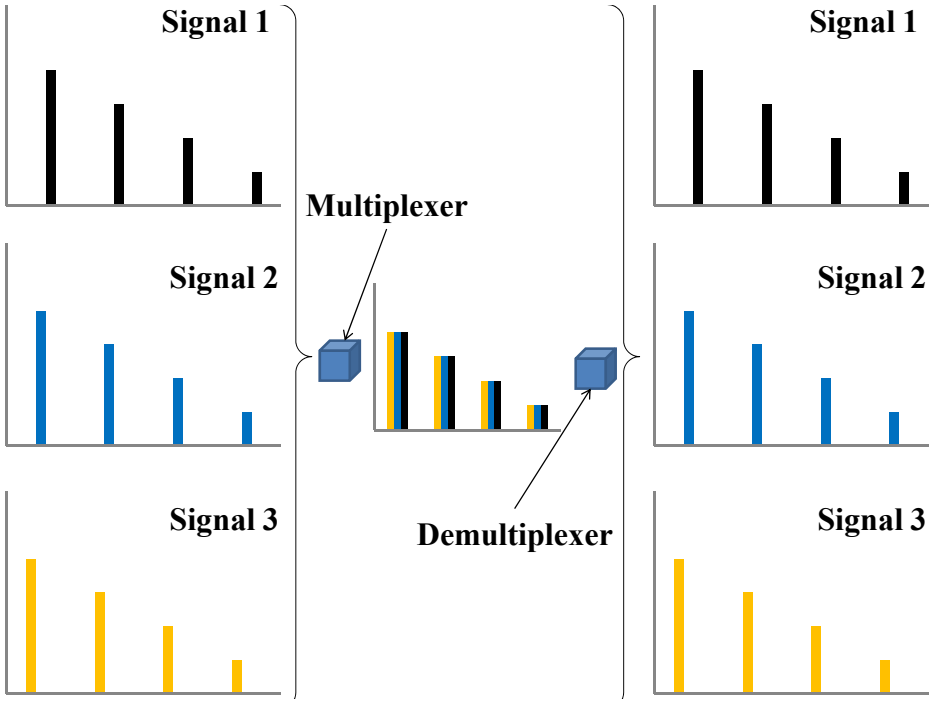

Figure 6.1 Illustration of time domain multiplexing and demultiplexing techniques.

Figure 6.1 shows time domain multiplexing and demultiplexing processes for a sensor network which has three systems. Time delay between the signals determines the location of each system. As shown in Figure 6.1, signals from different sources can be multiplexed into a single channel by a multiplexer, and then this multiplexed signal can

be alternately separated to different sources. Therefore, three signals are successfully transmitted across a single, shared channel. The main reason to use TDM is to minimize cost and to take advantages of huge capacity of the fiber by using existing transmission lines [206].

6.1.2 Wavelength Division Multiplexing

The WDM technique is based on sharing optical bandwidth between several sensors. Therefore, each sensor has a different wavelength range. For WDM technique, FBG is mostly used as the wavelength separation component [60]. The WDM technique combines different wavelength optical signals into a SMF. Figure 6.1 represents how three inputs from three fibers can be multiplexed using multiple wavelengths. In a WDM system, each wavelength is multiplexed and demultiplexed separately with its own transmitter and receiver [207]. Figure 6.2 shows multiplexing and demultiplexing of three different wavelengths. The example given in Figure 6.2 needs three transmitters and three receivers. All wavelengths can be packaged together into a SMF for transmission by utilizing wavelength multiplexer and then received to the receiver separately by using wavelength demultiplexer.

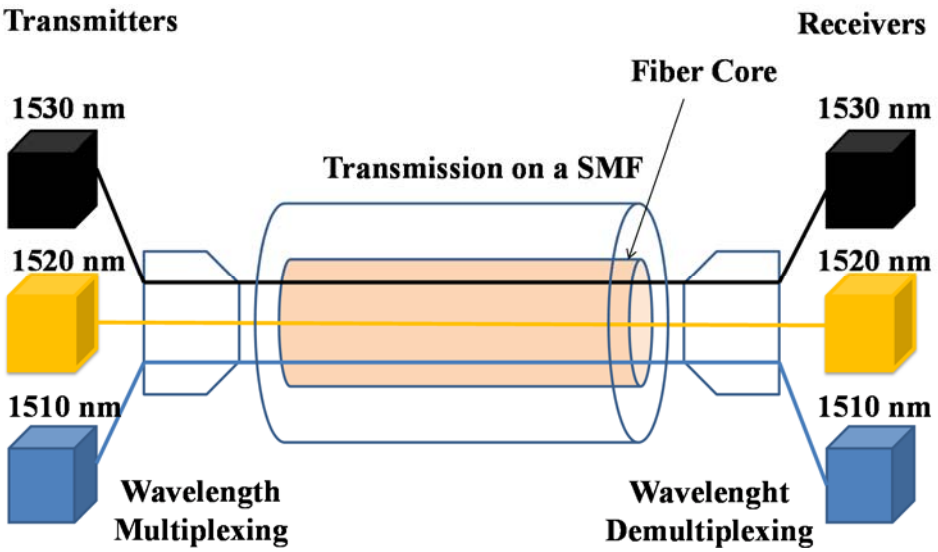

Figure 6.2 Schematic illustration of wavelength multiplexing and demultiplexing technique by using a single mode fiber.

6.1.3 Frequency Division Multiplexing

The FDM technique comprises conducting optical power to each individual sensor and back to corresponding sensor through a path which depends on the designated wavelength for the interrogation of the particular channel [208]. The FDM technique relies on modulation of signals from several sensors at different frequencies. Consequently, the detected signals can be separated electronically. This technique can be applied to structures by employing chirped light source or different unbalanced interferometers [209]. Figure 6.3 shows multiplexing and demultiplexing of three different frequency signals from three sensors. Transmission media can be a SMF. Frequency signals are coupled into the fiber and separated to transmit to a receiver.

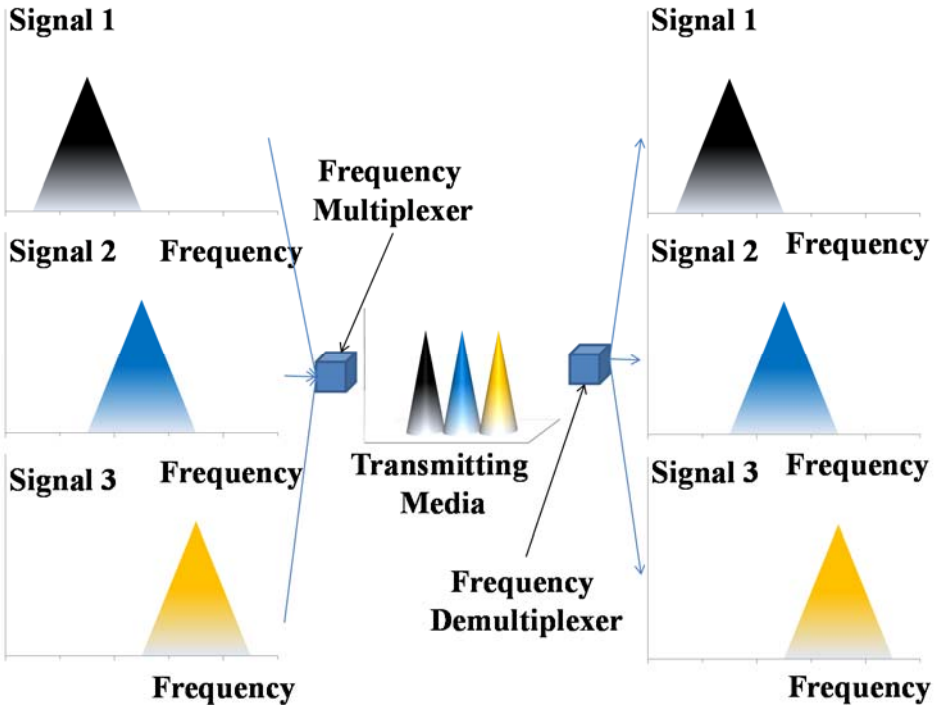

Figure 6.3 Schematic illustration of frequency division multiplexing and demultiplexing technique.

6.1.4 Coherence Domain Multiplexing

The CDM technique can be used in connections of interferometric sensors and can be adjusted to many physical structures. In the CDM technique, a different unbalanced route from two interfering routes is introduced by each sensor [210]. The route unbalance is recompensed separately by the reading unit for each sensor. The key consideration for coherent domain multiplexed sensor network is the necessity to ensure that only the routes intended for interference are coupled closely. This is easy to construct in an extrinsic-reference ladder configuration: the route length of the each sequential sensor should be longer than the previous route [211].

6.1.5 Polarization Division Multiplexing

The PDM technique is one of the key techniques for a high capacity and high performance optical communication system. The PDM technique can double the system efficiency and capacity by carrying independently two data in two orthogonal polarization states [212]. An all-optical regenerator based on a polarization nonlinear loop mirror is purposed [213]. Two polarization tributaries of a PDM signal can be regenerated simultaneously and reassembled automatically with this kind of generator. Configuration and principle can be seen somewhere else in detail [213, 214].

6.2 Experimental Setup

The EF-FLRD sensors were fabricated in the same way as for the construction of the previous biological, chemical, and physical sensors. All FLRD sensors consist of two major parts: a sensor control system and a sensor unit. The control system contains a CW diode laser source, a photodetector (Thorlabs, PDA50B), an oscilloscope (Tektronix, 410A), and electronic control devices, such as current controller, temperature controller, and pulse generator. The sensor unit consisted of a SMF loop which was connected via two identical 2×1 fiber couplers (Opnetic Communication, Co.) and a sensor head. The sensor head was fabricated by etching a part of the fiber in 48% HF solution during ~33 min after the plastic jacket of the fiber was removed and then cleaned with methanol. Fiber core and fiber cladding diameters are ~8.2 μm and 125 μm, respectively. The fiber couplers were produced with a split ratio of 99.9:0.1. The total optical loss of the light in the fiber loop, including fiber connectors' insertion loss, absorption loss, and fiber couplers' losses, was estimated to be < 0.45 dB. The typical estimated loss estimated by the splicer was 0.02 - 0.04 dB. Fiber had 120 m length in total.

When a laser beam was coupled into the fiber loop, the ringdown signal observed by the photodetector was applied to a pulse generator (SRS, DG 535) to trigger the generator to generate a series of negative square waves. These waves were applied to the laser driver to drop laser current to zero quickly, resulting in producing a series of laser pulses from the CW diode laser. A series of pulsed spikes which were generated from each turn of the laser pulse inside the fiber loop was observed by the photodetector. The ringdown time was monitored by an oscilloscope.

Two and three of several fabricated EF-FLRD sensors were connected in series and parallel to setup a sensor network. First, as shown in Figure 6.4, two FLRD sensors were connected in series by using a three-arm fiber loop as a first loop to a two-arm fiber loop as a second loop. Then, three FLRD sensors were combined together subsequently to setup an EF-FLRD sensor network. In this configuration, two three-arm fiber loops were connected via FC/APC fiber connectors. Later, a second three-arm fiber loop was connected to a two-arm fiber loop to complete three units connection in series configuration. Afterwards two FLRD sensors were joined in a series configuration, as explained previously and shown in Figure 6.4, and connected to a 1×2 MEMS optical switch kit to control each sensor individually. Moreover, two and three sensors were connected in a parallel configuration by splitting the laser pulse into two and three equal parts. Ringdown signals from each loop were coupled in a fiber connection cable and the photodetector received the coupled signal through fiber connection cable. Also, two loops were connected to the 1×2 MEMS optical switch kit in a parallel configuration to control each sensor separately. Each configuration, series and parallel, is explained in detail in the following parts of this chapter.

6.3 EF-FLRD Sensor Network: Series Configuration

6.3.1 Two FLRD Sensors in Series Configuration

Figure 6.4 illustrates the design of the FLRD sensor network consisting of two loops in series configuration. Laser pulse from the laser source of intensity I_0 was injected into Loop 1. The first coupler transferred 0.1% of I_0 into a three arms-fiber loop and transmitted 99.9% of I_0 to a two-arm fiber loop as an input light pulse. 0.1% of the 99.9% of I_0 was injected into the second loop through the fiber coupler, and 99.9% of the 99.9% I_0 was reflected back. The reflected portion of the pulse was isolated by a fiber isolator to eliminate superposition of the transferred beam from three-arm fiber loop and the reflected beam from the two-arm fiber loop. Each loop had its own ringdown time because each loop had a different fiber length due to multiple cuts during sensor head fabrication, insertion losses, etc. As shown in Figure 6.4, the loops' outputs were connected by using a fiber optic connection cable which had approximately 50/50 split ratio. A very small portion of light pulses from each loop was coupled into a fiber optic connection cable which was used to combine outputs of the fiber loops, and the photodetector received the signals through the connection cable. A sensor network configuration setup by using three FLRD sensors is presented in Figure 6.4.

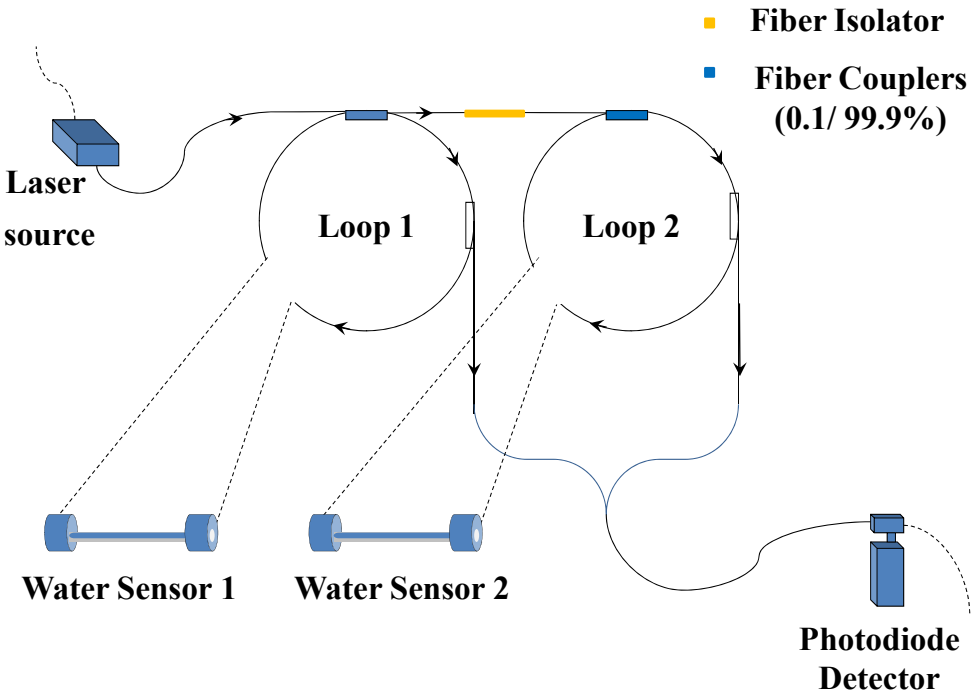

Figure 6.4 Schematic illustration a sensor network in series configuration for two FLRD sensors.

Figure 6.5(a) and (b) show the collected data from two different tests. Several FLRD sensors were fabricated and tested by connecting two sensors in series configuration in each experiment. The connection of the sensors was as shown in Figure 6.4. First, the response of each loop in DI water was recorded in terms of ringdown time; then, the sensors were immersed into DI water in order of Loop 2, Loop 2+1, and Loop 1. As shown in Figure 6.5(a), initially, ringdown time was recorded when both sensors were in air. After that, each sensor was tested in DI water individually. Later, both sensors were immersed into DI water in the aforementioned order. Figure 6.5(b) shows another experiment's result. The experiment was repeated by using the same two units in a slightly different parameter setup. Similarly, both sensors were tested in DI water

individually, afterward; the sensors were plunged to DI water alternately and simultaneously. Both experiment results have the same trend which indicates that a sensor network by using two FLRD sensors in serial configuration can be potentially assembled. A sensor network setup by using FLRD sensors offers high sensitivity, fast response, near-real time monitoring, and low cost.

For two coupled signals, each sensor has different contributions to the coupled signals. Therefore, each sensor's contribution can be estimated by calculating coupling coefficients. Ringdown time values from individual and coupled sensors are given below:

$$\tau_1 = 7.18\ \mu s, \tau_2 = 8.09\ \mu s, and\ \tau_{2+1} = 8.46\ \mu s \tag{6.1}$$

$$\tau_{2+1} = 8.46\ \mu s = a * 7.18\ \mu s + b * 8.09\ \mu s \tag{6.2}$$

$$\tau_1 = 7.11\ \mu s, \tau_2 = 7.84\ \mu s, and\ \tau_{2+1} = 8.29\ \mu s \tag{6.3}$$

$$\tau_{2+1} = 8.29\ \mu s = a * 7.11\ \mu s + b * 7.84\ \mu s \tag{6.4}$$

$$\tau_1 = 7.39\ \mu s, \tau_2 = 8.34\ \mu s, and\ \tau_{2+1} = 8.81\ \mu s \tag{6.5}$$

$$\tau_{2+1} = 8.81\ \mu s = a * 7.39\ \mu s + b * 8.34\ \mu s \tag{6.6}$$

where Equation (6.1) shows averaged ringdown times from Figure 6.7(a), Equation (6.3) shows averaged ringdown times for the data in Figure 6.7(b), and Equation (6.5) shows averaged ringdown times for data in another experiment of two loops connected in series configuration. We can easily find two coefficients a and b from Equations (6.2) and (6.4). From Equation (6.2), we have;

$$\frac{8.29\ \mu s - b * 7.84\ \mu s}{7.11\ \mu s} = a. \tag{6.7}$$

When we plug in a value in Equation (6.4), we can find b value. After plugging Equation (6.7) into Equation (6.4), b value is given as;

$$b = 0.354. \tag{6.8}$$

By plugging b value into Equation (6.2), a value is given as:

$$a = 0.780. \tag{6.9}$$

To prove that a and b values work for any two loop connection in series configuration, we can plug the values in Equation (6.6). It is given as;

$$8.81\ \mu s = 0.780 * 7.39\ \mu s + 0.354 * 8.34\ \mu s \tag{6.10}$$

$$8.81\ \mu s \approx 8.71\ \mu s \tag{6.11}$$

1.13% deviation is expectedly normal because a small number of experiment was considered for the calculation. This simple simulation shows that we can investigate each sensor's contribution to a coupled signal.

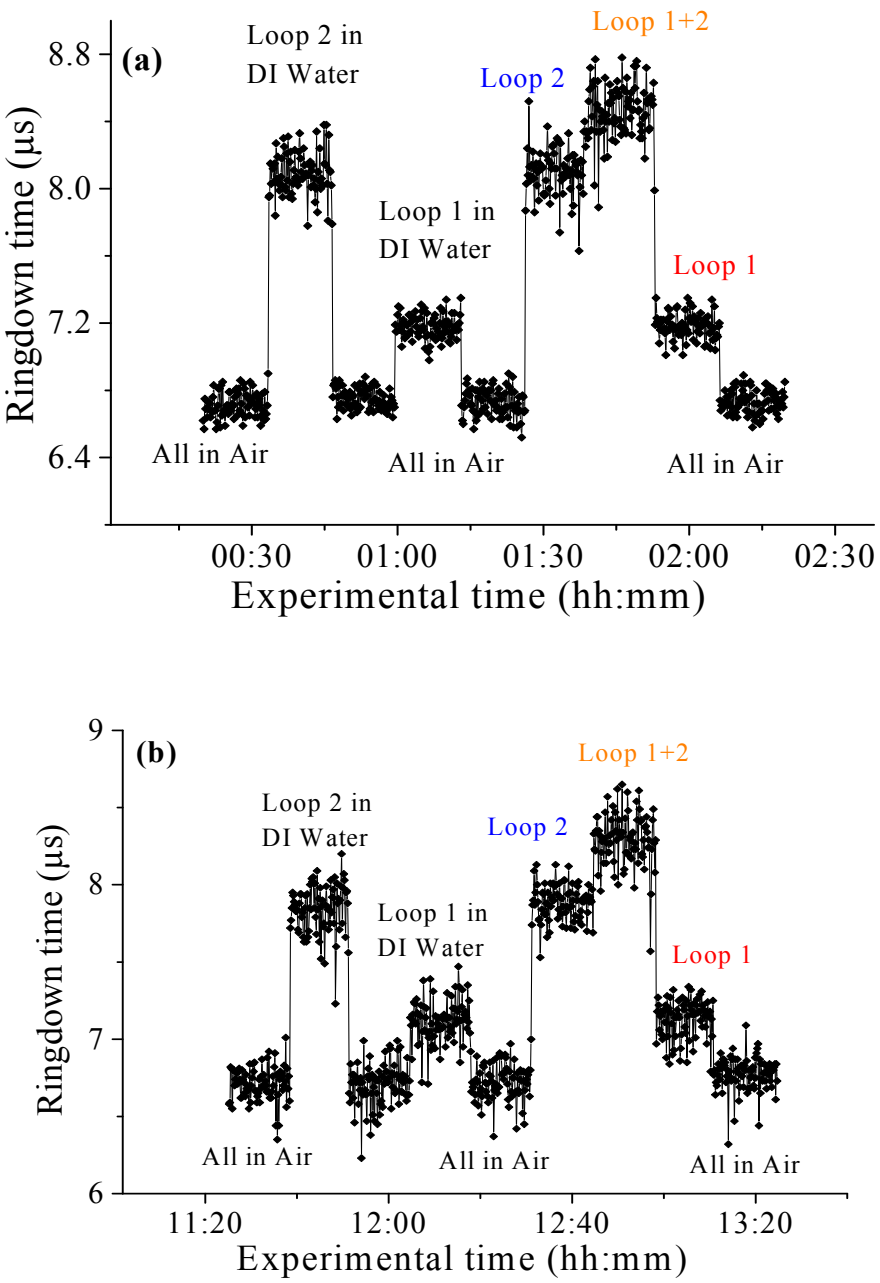

Figure 6.5 Responses of two FLRD sensors connected in serial configuration.

Four different FLRD sensors were fabricated and tested in two different experiments by connecting in serial.

6.3.2 Three FLRD Sensors in Series Configuration

Figure 6.6 represents a design of FLRD sensor network consisting of three loops in series configuration. Two three-arm loops and one two-arm loop were connected to each other through FC/APC fiber connectors. When a laser pulse of intensity I_0 was sent to Loop 1, 0.1% of I_0 was coupled into Loop 1 through the FC/APC fiber coupler. The rest of the beam was transmitted to be used as the input light pulse for Loop 2. The other coupler transferred 0.1% of 99.9% of I_0 into Loop 2 and transmitted the rest of the beam to Loop 3. Approximately 99.8% of initial laser pulse of intensity I_0 was used as input light pulse for Loop 3. Therefore, different amounts of laser pulses traveled inside each loop, resulting in different ringdown times. A very small portion of light pulses from each loop was coupled into a fiber optic connection cable which was used to combine all output channels of the fiber loops, and the photodetector received the signals through the connection cable. A sensor network configuration setup by using three FLRD sensors is illustrated in Figure 6.6.

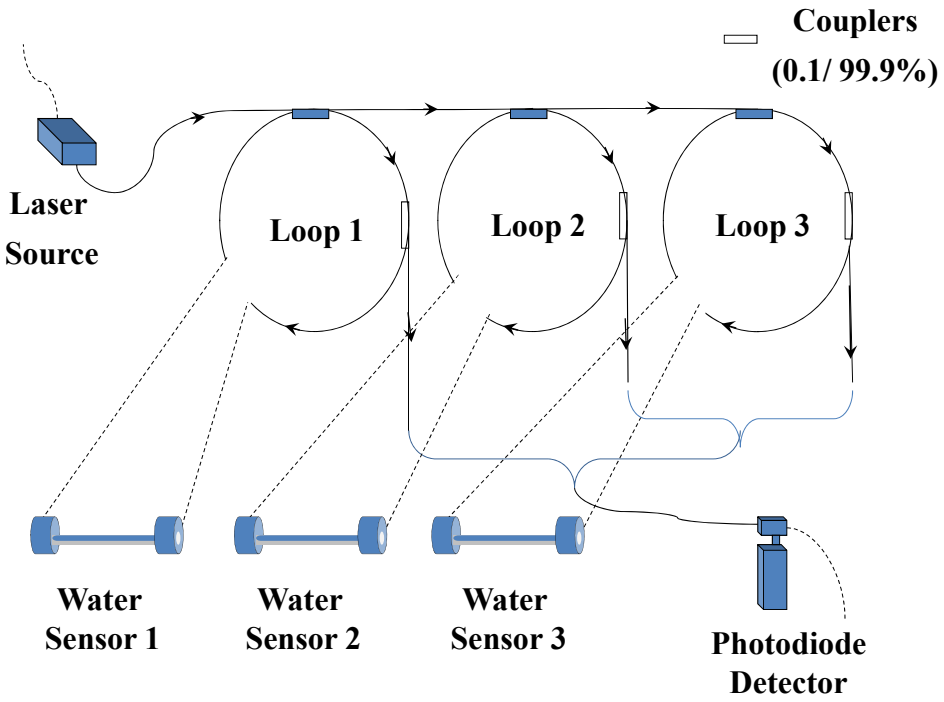

Figure 6.6 Schematic illustration a sensor network in series configuration for three FLRD sensors.

Figure 6.7 shows the response of three serially connected FLRD sensors in air and DI water. First, the sensors were tested individually in DI water to observe each sensor's response in terms of ringdown time. Later, the sensors were immersed into DI water alternately, as a pair, and all together in order of Loop 3, Loop 2, Loop 1, Loop 3, Loop 3+2, Loop 3+2+1, Loop 2+1, and Loop 1, respectively. When Loop 3+2, Loop 2+1, and Loop 3+2+1 were immersed into DI water, two and three coupled signals were received by the photodetector and recorded in terms of ringdown time. For coupled signals in Figure 6.7(a), each sensor had different contributions to the coupled signals. Therefore, each sensor's contribution can be estimated by calculating coefficients by the following;

$$\tau_3 = 7.902\ \mu s, \tau_2 = 8.229\ \mu s, \tau_1 = 8.517\ \mu s \tag{6.12}$$

$$\tau_{3+2} = 8.328\ \mu s, \tau_{3+2+1} = 9.122\ \mu s, \tau_{2+1} = 8.998\ \mu s \tag{6.13}$$

where $\tau_1, \tau_2, and\ \tau_3$ are individual ringdown times of each sensor. τ_{3+2} is coupled ringdown time of Loop 3 and Loop 2. τ_{3+2+1} is coupled ringdown time of three loops. τ_{2+1} is coupled ringdown time of Loop 2 and Loop 1.

$$\tau_{3+2} = 8.328\ \mu s = c * \tau_3 + \mathrm{b} * \tau_2 \tag{6.14}$$

$$\tau_{3+2+1} = 9.122\ \mu s = c * \tau_3 + \mathrm{b} * \tau_2 + \mathrm{a} * \tau_1 \tag{6.15}$$

$$\tau_{2+1} = 8.998\ \mu s = \mathrm{b} * \tau_2 + \mathrm{a} * \tau_1 \tag{6.16}$$

Subtracting Equation (6.16) from Equation (6.15) will gives

$$0.124\ \mu s = \mathrm{c} * 7.902\ \mu s \tag{6.17}$$

$$\mathrm{c} = 0.157. \tag{6.18}$$

Then, plugging c into Equation (6.14) leads us to find the value of b.

$$8.328\ \mu s = 0.157 * 7.902\ \mu s + \mathrm{b} * 8.229\ \mu s \tag{6.19}$$

$$\mathrm{b} = 0.997. \tag{6.20}$$

Finally, plugging b into Equation (6.16) gives the value of a.

$$8.998\ \mu s = 0.997 * 8.229\ \mu s + \mathrm{a} * 8.517\ \mu s \tag{6.21}$$

$$\mathrm{a} = 0.093. \tag{6.22}$$

After the calculations, we obtained 0.093, 0.997, and 0.0157 for a, b, and c, respectively. Similar calculations were applied to three other experiment results to obtain an average of all of the values. The averaged values for $\bar{a}, \bar{b},\ and\ \bar{c}$ are 0.0905, 0.9965, and 0.0212, respectively. The averaged constants were plugged into another experiment result for validation. The experimental result of coupled ringdown time of the three loops

was 8.297 μs. Calculated coupled ringdown time of the three loops was 8.104 μs. For coupled two loops, experimental results of τ_{3+2} and τ_{2+1} were 7.529 μs and 8.055 μs, respectively, and calculated results for τ_{3+2} and τ_{2+1} were 7.415 μs and 7.954 μs, respectively. The existence of the deviation between the experimental and theoretical results is normal because a small number of constants were averaged, and each sensor had different optical losses.

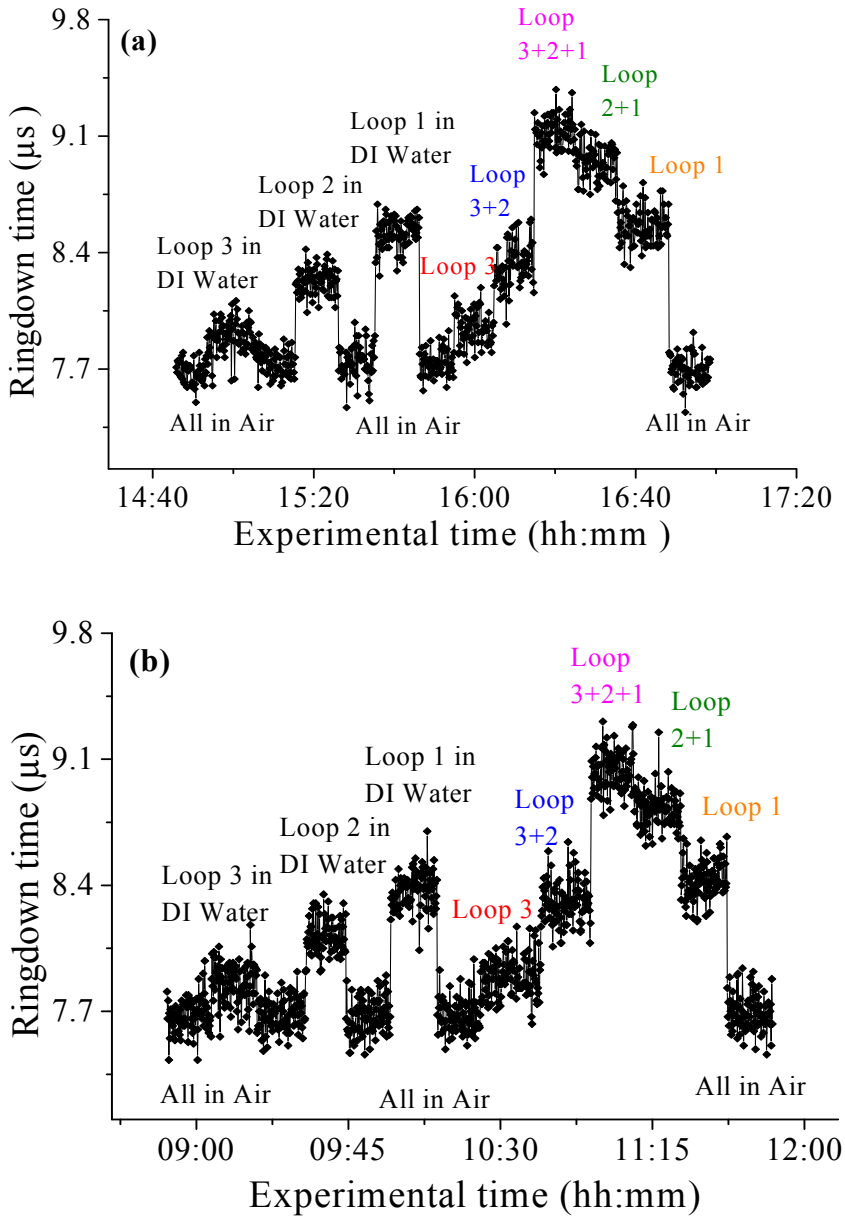

Figure 6.7 Responses of three FLRD sensors connected in serial configuration.

6.3.3 Two FLRD Sensors in Series Configuration by using 1×2 MEMS Optical Switch

6.3.3.1 Optical Switch Kits

Optical switching is one of the most common devices for multiplexing. Sensors can be connected to optical switch kits either in series or in parallel configurations. Optical switch kits can be used in 1×N or 2×N configurations. Optical switch kits in both configurations and with up to 100 channels are commercially available. In this study, a 1×2 MEMS optical switch kit was used to connect two FLRD sensors in both series and in parallel configurations. The 1×2 MEMS optical switch kit is dual-directional. The input channel on the 1×2 MEMS switch can also be used as an output channel. Figure 6.8 shows a 1×2 optical switch kit (Thorlabs) used to setup a sensor network for two FLRD sensors in series and parallel configurations.

As shown in Figure 6.8, the switch kit has three channels. Channel 2 can be used as an input when two FLRD sensors are connected in series configuration and can be used as an output when two FLRD sensors are connected in parallel configuration. Channels 3 and 4 are sensors' connection points. The status indicator shows which loop is active. For instance, if it shows 1, the sensor connected to channel 4 is active. USB port connects the switch kit to the computer. A toggle switch is used to switch channels manually. Power on indicator shows whether the switch kit is on or off.

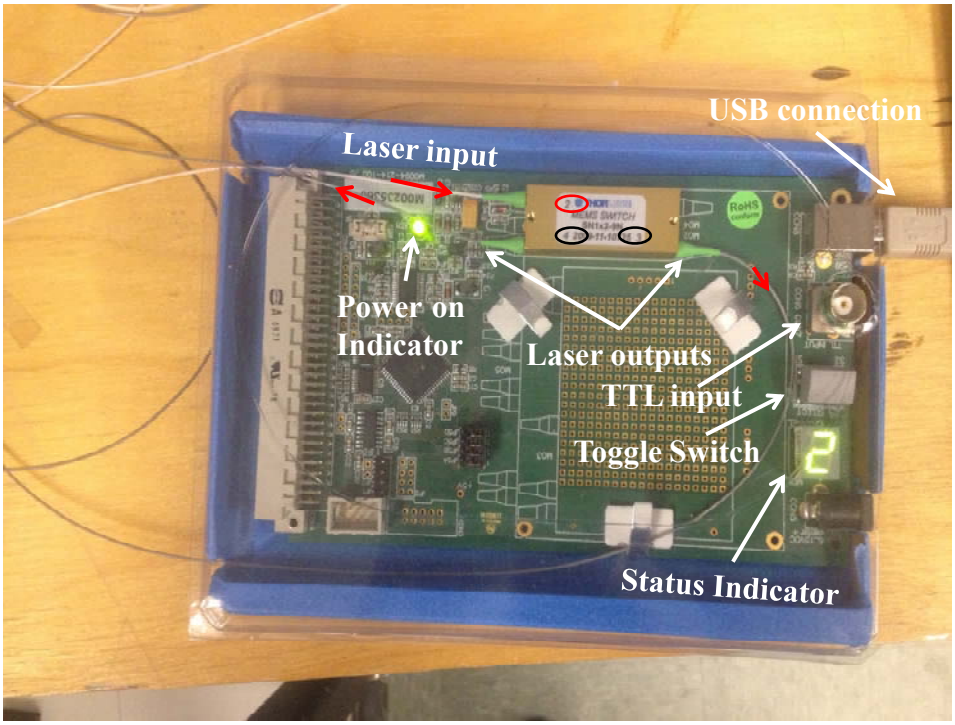

Figure 6.8 1×2 MEMS optical switch kit.

For serial connection of two FLRD sensors, a laser beam from a laser source was injected into the three-arm fiber loop which was joined to the two-arm fiber loop. Outputs of fiber loops were connected to channel 3 and channel 4 of the 1×2 MEMS switch kit. Figure 6.9(a) shows two FLRD sensors connected to the switch kit in a series configuration. When the status indicator showed 1, the signal was received by the photodetector from only the sensor connected to channel 4. When status indicator showed 2, signal was received by the photodetector from only the sensor connected to channel 3. Signals from each loop were sent to the photodetector through channel 2 which was labeled with red circle in Figure 6.8. Received signals by the photodetector were collected by an oscilloscope, and data were recorded in a computer.

For parallel connection of two FLRD sensors, a laser beam from a laser source was injected into the 1×2 MEMS optical switch kit through channel 2 which was labeled with a red circle in Figure 6.8. Channel 2 became the input for two FLRD sensors connected in parallel configuration due to the double-way working feature of 1×2 MEMS optical switch kit. Channels 3 and 4 were used as inputs for two loops connected in parallel configurations. When status indicator showed 1, the sensor connected to channel 4 was active which meant that the laser pulse was injected into only channel 4. When status indicator showed 2, the sensor connected to channel 3 was active which meant that the laser pulse was coupled into the loop connected to channel 3 through channel 3. Loops' outputs were connected to a two-arm fiber optic connection cable in a Y shape which had approximately 50/50 split ratio. After two outputs were combined by the connection cable and became one output, the output was connected to the photodetector to receive the signal by the detector. Received signals were collected in oscilloscope and data were recorded on a computer.

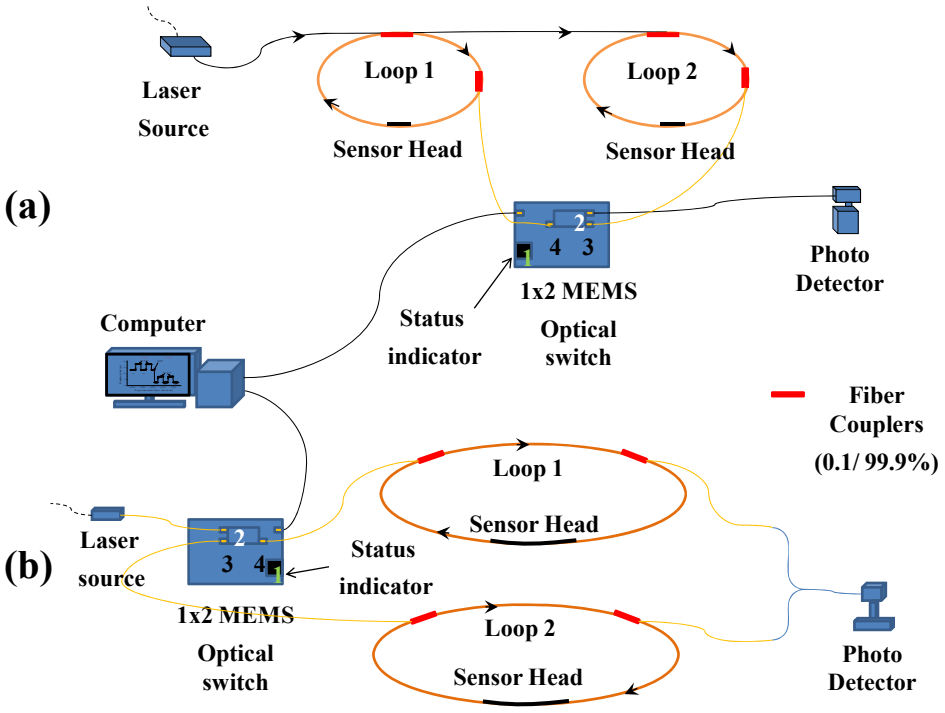

Figure 6.9 Two FLRD sensors connected to a 1×2 MEMS optical switch kit; a) in series configuration, b) in parallel configuration.

Figure 6.10 shows a computer control panel of a 1×2 MEMS optical switch kit. While a sensor network setup in either series connection or parallel connection with two FLRD sensors is running, the switch kit can be controlled easily from the computer by turning on, turning off, or selection of channel 1 or 2 to collect data as shown in Figure 6.10.

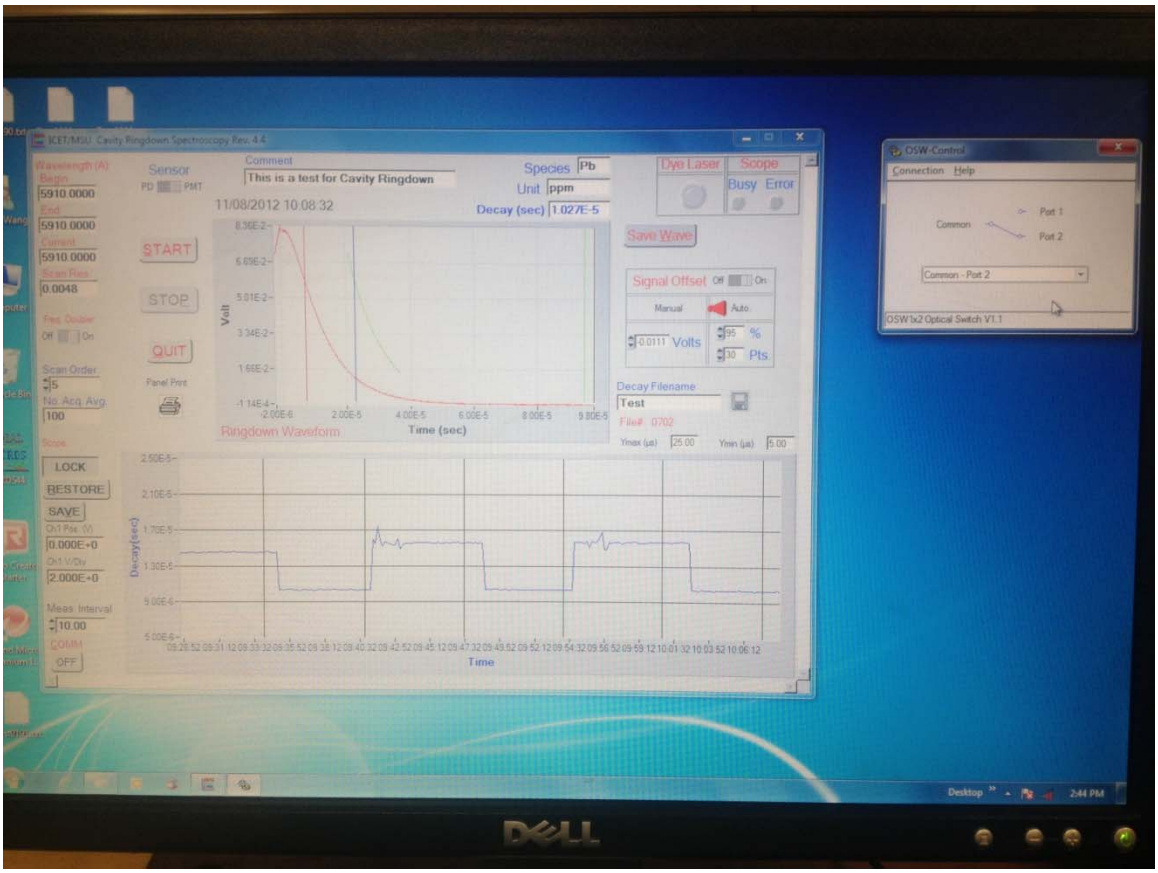

Figure 6.10 MEMS optical switch kit control panel.

Small square on the right of the screen is the control panel for MEMS switch kit, and the big square is a software for FLRD system.

6.3.3.2 Experimental Results

Two FLRD sensors were connected in series by using a 1×2 MEMS optical switch kit. Figure 6.11 shows the response of the sensors when connected to an optical switch kit. Loop 2 was tested in air-DI water cycle first, then, connection was switched to Loop 1. Similarly, Loop 1 was tested in air-DI water cycle. Series configuration of two FLRD sensors was established and tested successfully. Each loop had different ringdown time due to having different sensitivity, different optical and insertion losses, and different fiber lengths. As shown in Figure 6.11, parallel connection of two FLRD

sensors can be controlled individually. A sensor network setup by using two FLRD sensors in parallel configuration provides fast response, high sensitivity, and near-real time monitoring.

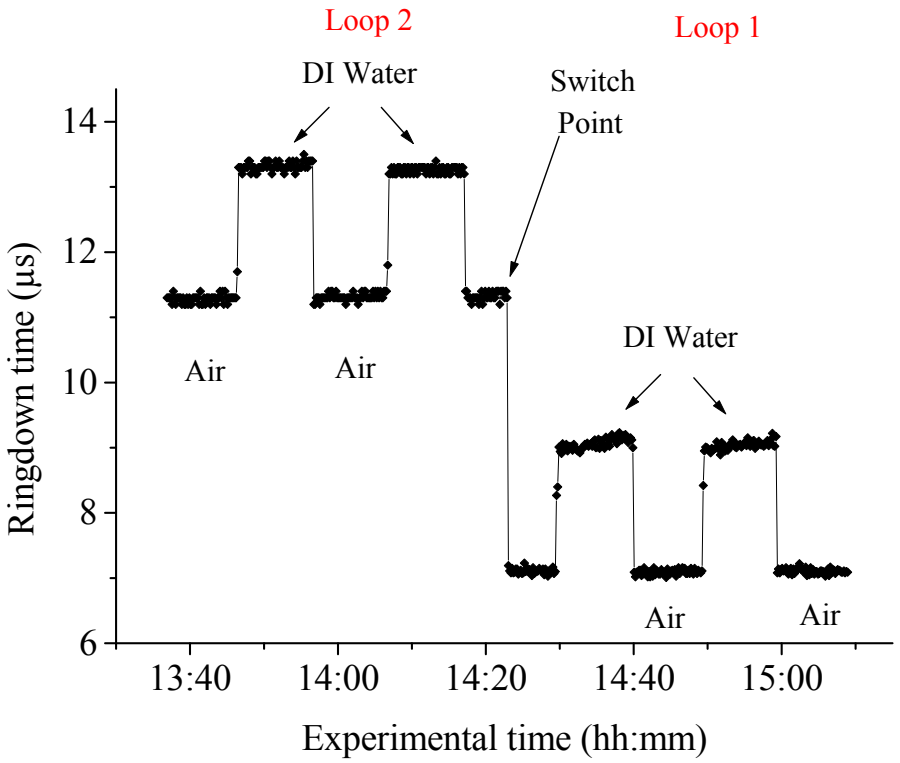

Figure 6.11 Two FLRD sensors connected in series and controlled by using 1×2 MEMS optical switch kit.

6.4 EF-FLRD Sensor Network: Parallel Configuration

6.4.1 Two FLRD Sensors in Parallel Configuration

Figure 6.12 illustrates a design of FLRD sensor network in parallel configuration for identically fabricated two FLRD sensors. A laser pulse from the laser source of intensity I_0 was injected into the loops after the pulse was split into two equal parts. 0.1% of each split pulse was coupled into fiber loops through fiber couplers. The rest of the

beams were reflected back. 0.1% of the 0.1% coupled pulses was transferred to the photodetector from each loop for every lap of the pulses inside the loops. Signals were coupled into a fiber optic connection cable which had 50/50 split ratio. The photodetector received the coupled signal through a connection cable. A sensor network configuration setup by using two FLRD sensors in parallel is presented in Figure 6.12.

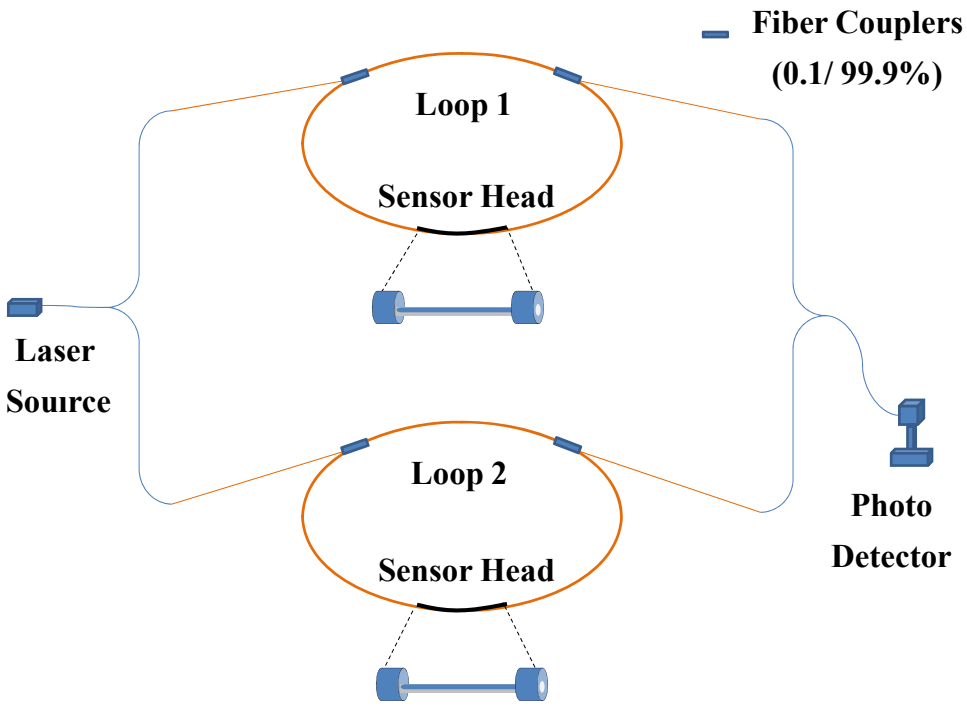

Figure 6.12 Schematic illustration a sensor network in parallel configuration for two FLRD sensors.

Figure 6.13 shows collected data from two different experiments. Several FLRD sensors were fabricated and tested by connecting two in parallel configurations in each experiment. The connection of sensors was as shown in Figure 6.12. The sensors were tested in air and DI water in order of both in air, Loop 2 in DI water, both in DI water,

again Loop 2 in DI water (Loop 1 was exposed to air), and both in air. Coupled signal when both sensors were in DI water was collected by the photodetector through a fiber optic connection cable which had approximately 50/50 split ratio. The experiment was repeated by using the same two units in a different parameter setup, as shown in Figure 6.13(b). Both results had the same trend, and therefore, experiments were repeatable. Results indicate that sensor network using two FLRD sensors in parallel configuration can be potentially assembled. A sensor network setup by using FLRD sensors offers high sensitivity, fast response, near-real time monitoring, and low cost.

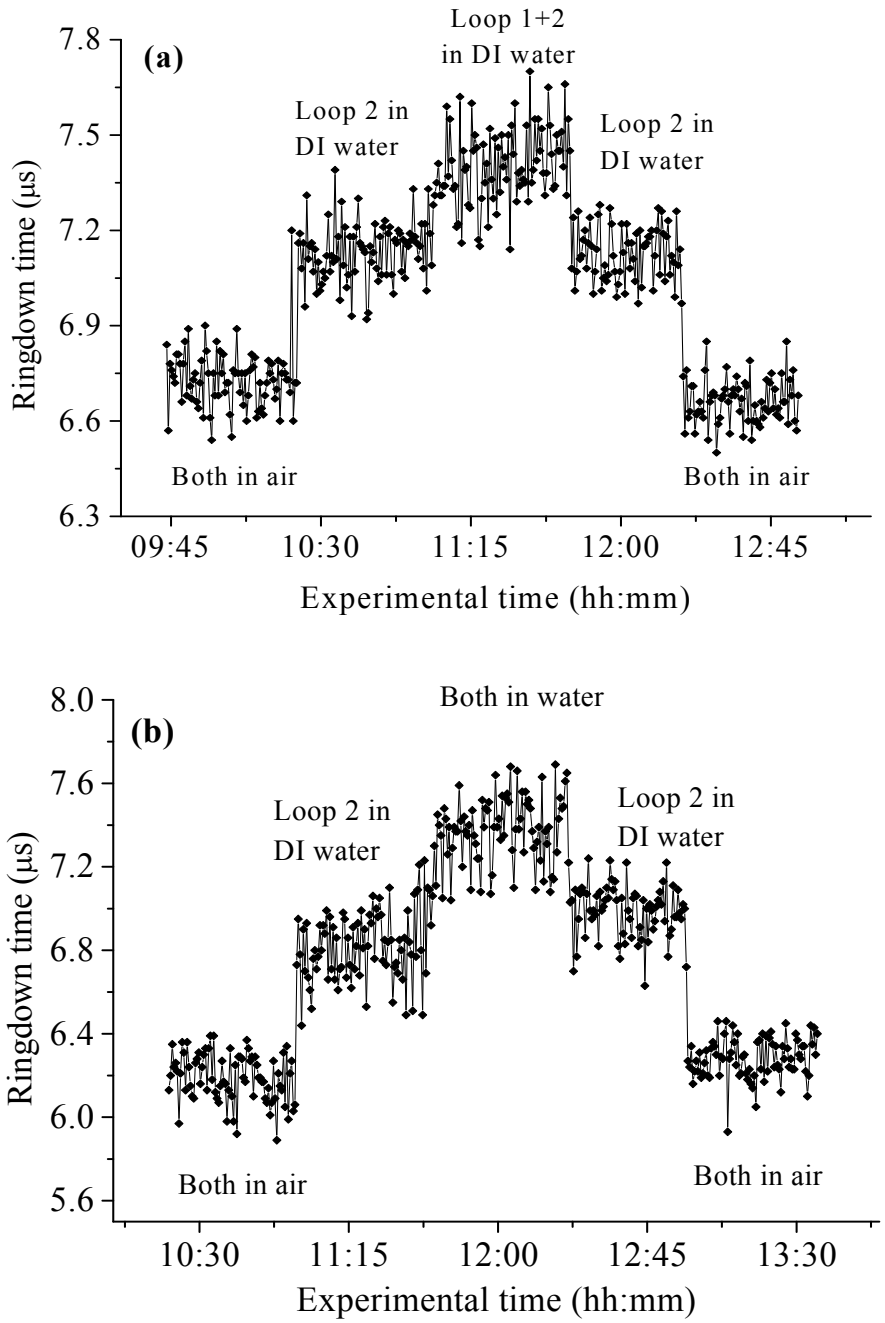

Figure 6.13 Responses of two FLRD sensors connected in parallel configuration.

Four different FLRD sensors were fabricated and tested in two different experiments by connecting in parallel.

6.4.2 Three FLRD Sensors in Parallel Configuration

Figure 6.14 represents a design of FLRD sensor network formed by three identically fabricated FLRD sensors in a parallel configuration. Laser pulses from the laser source of intensity I_0 were coupled into the loops after the pulse was split into three equal parts by a three-arm fiber optic connection cable. 0.1% of each split pulse was injected into the fiber loops through FC/APC fiber couplers. The rest of the beams were reflected back. 0.1% of injected pulses inside the loops was transferred to the photodetector via a second FC/APC fiber coupler in every round of 0.1% pulses inside the loops. Signals were coupled into a fiber optic connection cable. The photodetector received a coupled signal through the connection cable. A sensor network configuration setup by using two FLRD sensors in parallel is presented in Figure 6.14.

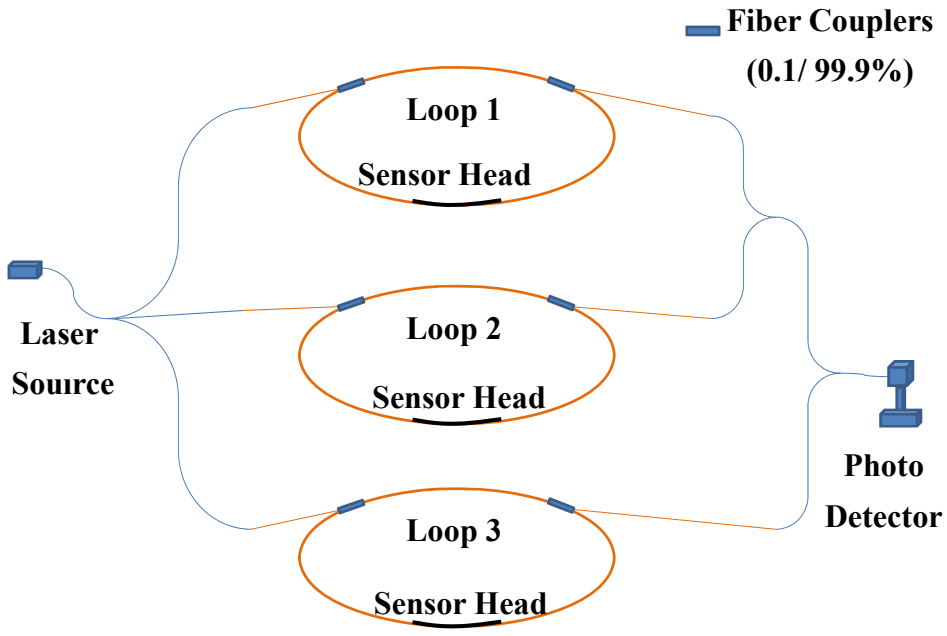

Figure 6.14 Schematic illustration a sensor network in parallel configuration for three FLRD sensors.

Figure 6.15 shows the response of three parallel connected FLRD sensors in air and DI water. First, the sensors were tested individually in DI water to observe each sensor's response. Then, the sensors were immersed into DI water consecutively. Two and three coupled signals were collected by the photodetector and recorded in terms of ringdown time. Ringdown times for coupled signals in Figure 6.15(a) included each relative sensor's contribution. Each sensor's contribution can be evaluated by calculating coefficients by following same concept in Section 6.3.2. After calculation, average values of a, b, and c constants are given by

$$\bar{a} = 0.333,\ \bar{b} = 1.004,\ \bar{c} = 0.107 \tag{6.23}$$

Three different experiments were conducted for calculation. Each coefficient was calculated, and three different values of coefficients were averaged. After that, averaged coefficients were used in another experiment for validation. Theoretical results and experimental results were very close to each other. For example, experimental result of three loops in DI water was 13.832 μs. Calculated result by using averaged coefficients was 13.883 μs. The very small deviation between the experimental and theoretical results is due to different optical losses of each loop, considering small number of constants to be averaged, etc.

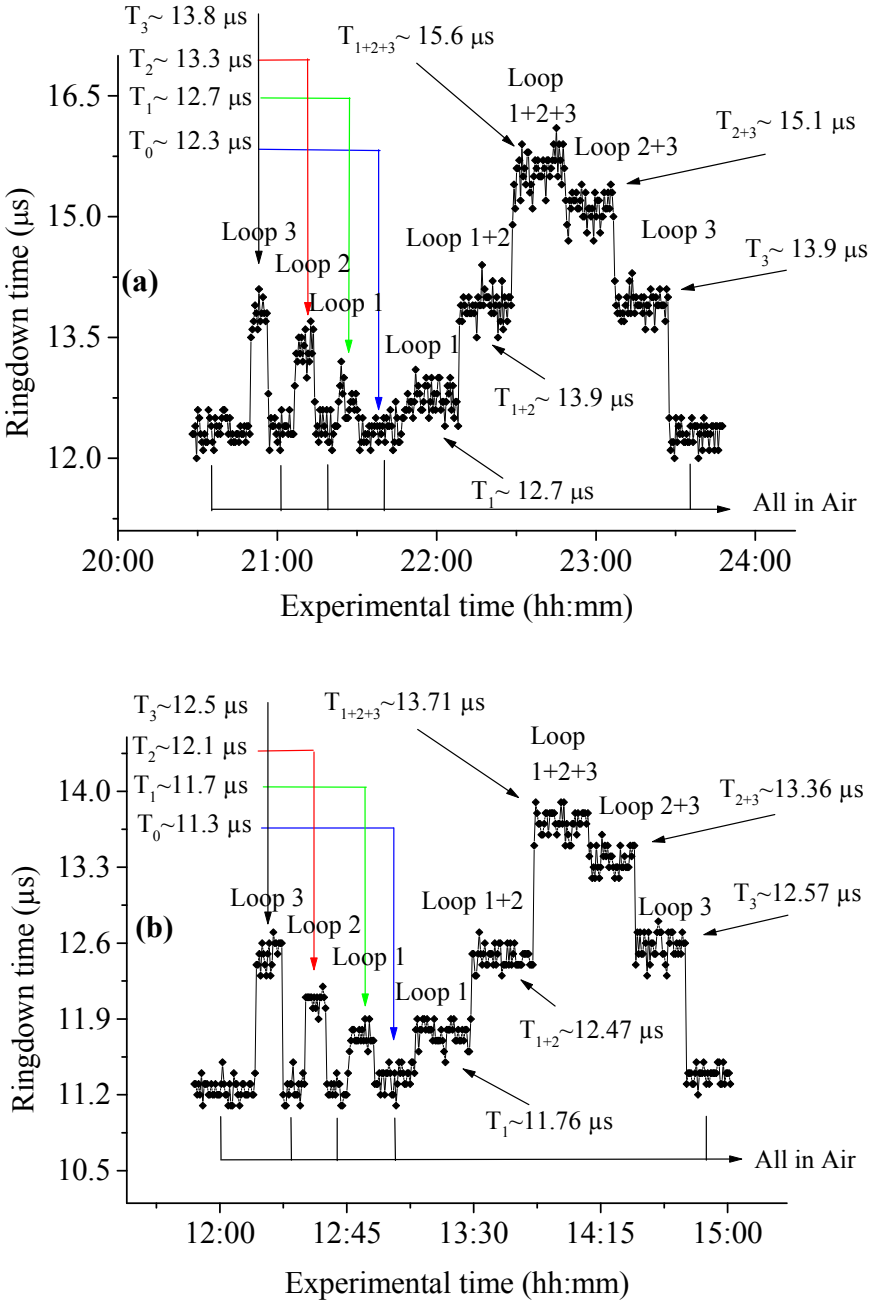

Figure 6.15 Responses of three FLRD sensors connected in parallel configuration.

6.4.3 Two FLRD Sensors in Parallel Configuration by using 1×2 MEMS Optical Switch

Two FLRD sensors were connected in parallel by using a 1×2 MEMS optical switch kit which was explained and shown in Section 6.3.3. Figure 6.16 shows the response of the sensors when the sensors were connected to the optical switch kit. Loop 1 was tested in air-DI water cycle; then, connection was switched to Loop 2. Similarly, Loop 2 was tested in air-DI water cycle. Parallel configuration of two FLRD sensors was established and tested successfully.

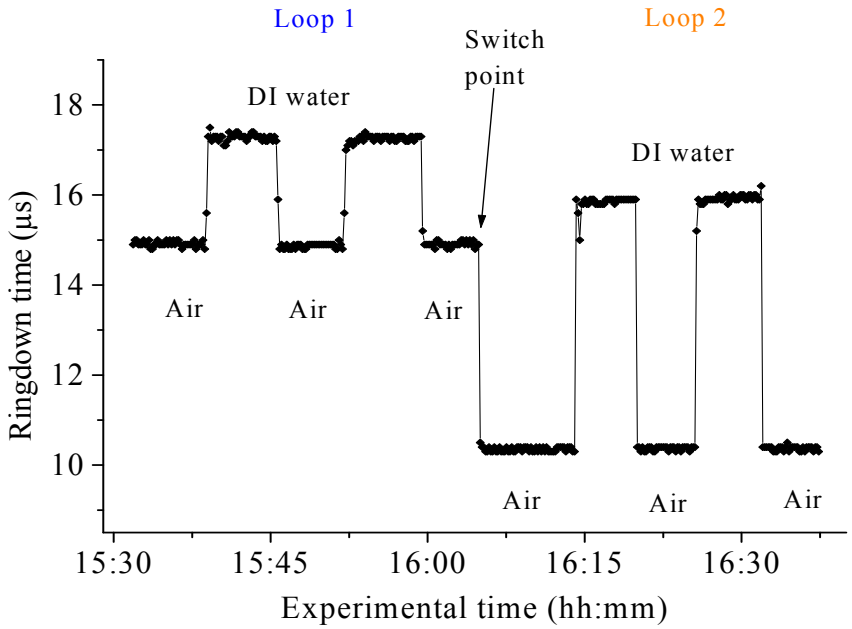

Figure 6.16 Two FLRD sensors connected in parallel and controlled by using a 1×2 MEMS optical switch kit.

6.5 Conclusions

EF-FRLD sensors were assembled in series and parallel configurations to set up a sensor network. First, two FLRD sensors were connected in series configuration and

tested in the laboratory. Repeatable data shows that two parameters can be detected simultaneously. Later, the sensor network was expanded by adding one more FLRD sensor. Three FLRD sensors were combined in series and tested successfully. Likewise, repeatable data were observed. The results suggest that multi-parameters can be detected at the same time by connecting N number of FLRD sensors in series combination. Furthermore, two FLRD sensors were joined in series combination by using a 1×2 MEMS optical switch kit to control each sensor individually. Data from each experiment could be collected individually, not simultaneously. Second, two FLRD sensors were connected in parallel configuration and tested in the laboratory. Repeatability was proven, and data showed that two measurands could be detected simultaneously by using a FLRD sensor network in parallel configuration. Afterwards, the sensor network formed by parallelly connected two FLRD sensors was broadened by adding one more FLRD sensor. Three FLRD sensors were united in series and tested successfully. Like the results of two sensor in parallel configuration, the results of three parallel connected sensors were repeatable as well. We also predict for three parallel connected FLRD sensor network that a multi-functional sensor network can be established for measurement of multi-parameters simultaneously. Additionally, two FLRD sensors connected in parallel configuration by utilizing 1×2 MEMS optical switch kit to manage each sensor individually. Data from each loop can be collected individually, not simultaneously.

We report results from two and three FLRD sensors connected in series and parallel configurations to set up a FLRD sensor network. Results showed good reproducibility and repeatability. We indicate that a sensor network can be established by

connecting two or more FLRD sensors in series and parallel configurations, and multi-functional sensor system can be built up to measure multi-parameters simultaneously.

CHAPTER VII

CONCLUSIONS AND FUTURE WORK

In the present study, we developed biological, chemical, and physical sensors by using FLRD technique and setup a sensor network by combining two or more FLRD sensors in series and parallel configurations. We investigated bulk index- and surface index-based DNA sensing and one type of bacteria by using the FLRD sensing scheme combined with the EF sensing mechanism and a FLRD glucose sensor by using refractive index-difference EF attenuation effect as a sensing mechanism as a biological sensor (biosensor), HW and different trace elements detection in DI water by utilizing EF-FLRD technique as chemical sensor, and monitoring water/moisture and cracks in concrete structure by using the EF-FLRD technique, which was achieved by embedding a section of SMF into the concrete bars made in the laboratory as physical sensor. A section of a SMF was etched to fabricate a sensor head and then embedded into concrete bars for water/moisture monitoring, but the SMF was embedded directly into concrete bars for crack monitoring. Furthermore, sensor network platforms by combining two and three FLRD sensors in series and parallel configurations were developed and tested successfully in this study.

We developed index-based biosensors by utilizing FLRD sensors as biological sensors. We expected an array of EF-FLRD biosensors to be created with a new type of refractive index- and surface index-based biosensors by using an EF-FLRD sensing

scheme. In the sensing scheme, the sensing signal was a time constant, and detection sensitivity was enhanced by the multi-pass nature of the ringdown technique. Many sensing mechanisms could be directly adopted into the uniform sensing platform for the development of distinct sensors. This technique has high potential for biosensor development. Except for one early study based on cancer cell detection, this technique has not been explored before. Without using any additional optical components for sensor head fabrication, our sensor design demonstrated comparable or better performance in terms of cost, design and configuration, and detection sensitivities. Another type of biosensor fabricated and tested in our laboratory was a glucose sensor. In this work, several EF-FLRD sensors were fabricated with and without GOD immobilized on the surface of the sensor head. Effect of GOD immobilization on the sensor's performance was analyzed. Responses of the sensors to standard glucose solutions and synthetic urines in different glucose concentrations, from 50 mg/dl to 10 g/dl, were monitored. Furthermore, the detection sensitivities of the sensors for glucose and synthetic urine solutions were determined as 75 mg/dl and 50 mg/dl, respectively. Estimated theoretical detection sensitivity of the EF-FLRD glucose sensors tested in this study was approximately 17 times lower than the glucose renal threshold concentration which is between 160-180 mg/dl. In this work, we reported results of the sensors' reproducibility, response time, GOD coatings' effect, and detection sensitivities of the FLRD glucose biosensors.

As chemical sensors, several EF-FLRD sensors for HW and trace elements in DI water were developed. HW is critically important for nuclear power plants because it is used as a coolant. HW was tested in the range of 97-10% in our laboratory. The

concentration of HW was changed by adding DI water into it. Another test for chemical sensing was based on detecting of trace elements in DI water, such as Fe, Mg, Cd, and P. Chemical elements having 1000 μg/ml concentrations were detected by directly immersing FLRD sensors into the solutions, which was bulk index-based sensing technique. Without utilizing any expensive optical devices, i.e., OSA, or components such as FBG or LPG, fabricated FLRD chemical sensors showed high sensitivity and fast response for HW and trace element detection in DI water.

Monitoring water/moisture and crack in concrete structures were very good examples for application of physical sensors in the real world. My first study on application of FLRD sensors on real structures was focused on monitoring water or moisture in concrete structures. The FLRD water sensors with sensor heads were embedded into hand-made concrete bars. The presence of water around the sensor head in concrete was detected instantaneously and reversibly by the EF-FLRD sensors when a small amount of water was leaked into the concrete. In this study, it is presented for the first time application of EF-FLRD technique in real structures (concrete) for water monitoring. My second study was monitoring cracks on the surface and inside a concrete structure. Contrary to water sensors, the FLRD crack sensor head was fabricated using bare SMF. Fabricated and packaged FRLD crack sensors were embedded in concrete bars for testing. Manually produced cracks by hammering a nail on the bars were monitored, and responses of the sensors to the cracks were recorded as a change in the ringdown times. By this study, the first time FLRD-based crack sensors were fabricated, packaged, and embedded in real structures (concrete bars) for testing. The FLRD crack sensors may symbolize a new type of crack sensor for SHM.

At the final stage of this study, a sensor network by assembling two or more FLRD sensors in series or parallel configurations was developed. First, two FLRD sensors were connected consecutively to setup a series configuration, and a laser pulse was injected into the first loop. Signals from each loop were coupled in a fiber optic connection cable to convey to a photodetector. The same process was used for three sensor connection in series as well. Second, two FLRD sensors were multiplexed in a parallel configuration, and equally split laser pulses were injected into the loops. Signals from each loop were coupled in a fiber optic connection cable to transfer to a photodetector. The same process was used for three sensor connection in parallel as well. All data for two and three sensor connections in series and parallel were presented and discussed in CHAPTER VI. For three-coupled signals in series and parallel configurations, contributions of each sensor to the coupled signal were calculated. In addition, two FLRD sensors were connected in series and parallel configurations to 1×2 MEMS optical switch kit to control each sensor individually. Promising results indicated that a large number of FLRD sensors could be connected in series or parallel configurations for the purpose of sensing multi-parameters simultaneously.

This study investigated several applications of a new type of sensing technique called the FLRD technique. The FLRD technique was carried out on biomedical, chemical, and physics applications in the present study. This study can be useful for design, application, and proof-of-the-concept of the FLRD sensors associated with the EF sensing mechanism. Moreover, this study also demonstrates that fast response and high sensitive EF-FLRD technique can be a powerful diagnostic tool for biomedical, chemical, and physical applications when it is combined with FLRD sensors.

7.1 FUTURE RESEARCH DIRECTIONS

The presented research is focused on several applications of FLRD sensors for detection, measurement, or monitoring of various quantities. Each individual application has distinctive qualification for specific purposes. A sensor network is highly advantageous and practical to monitor any system in detail. For instance, setting up a sensor network on a bridge to control its durability, which several features of the bridge must be considered, such as pressure on the columns, temperature of the structure, strain on the ropes, etc., is much advantageous over setting up several sensor systems for each purpose. Combination and use with maximum efficiency of several EF-FLRD sensors in one unit with low cost are the most challenging step in sensor networking. Even though a sensor has a high sensitivity when it is not connected to a sensor network, sensitivity of the network will decrease after uniting sensors in series or parallel configurations. Increasing optical loss due to increase in connection points causes a decrease in sensitivity of the network.

After minimizing each obstruction in a sensor network, developing sensor networks for biomedical, chemical, and physical applications will be the main objective in future works. For example, a sensor network for monitoring blood sugar level, heart rate, body temperature, cholesterol, etc. in a human body can be developed and utilized in medical applications. Another example, a sensor network to monitor corrosion, crack, temperature, and pressure, of a nuclear containment building and cooling tower in a nuclear power plants can be developed and used effectively.

Aforementioned sensors in this dissertation can be combined in series and parallel configurations to perform sensing multiparameters simultaneously. There is no limit to

the number of the sensors to be integrated in a sensor network theoretically. It seems that multi-functional sensor networks will be dominant in many areas such as scientific applications, auto industries, health monitoring, etc.

7.2 FUTURE APPLICATIONS

A FLRD sensor network can be configured and experiments can be performed on biomedical applications. For instance, simultaneous detection of several diseases can be possible. Similarly, a FLRD sensor network can be installed on any construction, such as bridges, buildings, etc., for simultaneous monitoring of corrosion, cracking, temperature change, and pressure. Simultaneous monitoring of multi-parameter is extremely advantegous in terms of low cost, less space, and early maintenance.

REFERENCES

1. I. Chabay, “Optical waveguides”, Anal. Chem., 54, 1071 - 1088 (1982).

2. B. Culshaw and A. Kersey, “Fiber-optic sensing: A historical perspective”, J. Lightw. Technol., 26, 1064 - 1078 (2008).

3. K. Thyagarajan and A. K. Ghatak, Fiber Optic Essentials, Wiley-Interscience, John Wiley&Sons, Inc., Hoboken, New Jersey, 2007, pp. 10 - 15, Retrieved 1 May 2012.

4. R. A. Shelby, D. R. Smith, and S. Schultz, “Experimental verification of a negative index of refraction”, Science, 292, 77 - 79 (2001).

5. Fiber optic sensors: An introduction for engineers and scientists, E. Udd and W. B. Spillman Jr., John Wiley & Sons, Inc., Hoboken, New Jersey (2011).

6. P. M. Tracey, “Intrinsic fiber–optic sensors”, IEEE Sensors, 27, 96 - 98 (1991).

7. H. J. Patrick, G. M. Williams, A. D. Kersey, J. R. Pedrezzani, and A. M. Vendsarkar, “Hybrid fiber Bragg grating/long period fiber grating sensor for strain/temperature discrimination”, IEEE Photon. Technol. Lett., 8, 1223 - 1225 (1996).

8. J. Mandal, Y. Shen, S. Pal, T. Sun, K. T. V. Grattan, and A. T. Augousti, “Bragg grating tuned fiber laser system for measurement of wide range temperature and strain”, Opt. Commun., 244, 111 - 121 (2005).

9. Y. J. Rao, “Recent progress in applications of in-fibre Bragg grating sensors”, Opt. Lasers Eng., 31, 297 - 324 (1999).

10. L. Li, L. Xia, Z. Xia, and D. Liu, “All-fiber Mach-Zenhder interferometer for sensing applications”, Opt. Exp., 20, 11109 - 11120 (2012).

11. S. Lecler and P. Meyreuis, Intirnsic optical fiber sensor, 2012. Fiber optic sensors, M. Yasin (Ed.), ISBN: 978-953-307-922-6, InTech, Available from: http://www.intechopen.com/books/fiber-opticsensors/intrinsic-optical-fiber-sensor

12. G. C. Constantin, G. Perrone, S. Abrate, and N. N. Puscas, “Fabrication and characterization of low-cost polarimetric fiber-optic pressure sensor”, J. Optoelec. Adv. Mat., 8, 1635 - 1638 (2006).

13. I. Lujo, P. Klokoc, T. Komljenovic, M. Bosiljevac, and Z. Sipus, “Fiber–optic vibration sensor based on multimode fiber”, Radioengineering, 17, 93 - 97 (2008).

14. M. Palmer, High frequency temperature sensors for high temperature turbine monitoring, Luna Innovations Inc., 2006, pp: 1-7. Available online at: https://docs.google.com/viewer?a=v&q=cache:aPFlLA6TWtQJ:www.virtualacquisitionshowcase.com/document/1230/briefing+&hl=en&gl=us&pid=bl&srcid=ADGEESgy711CIqQEy44wsz_UckkhXTXGvQrDBA4aguAfnqcPoWfrNgVb_stpGB_Lub6BGJvu1x2GTIl2brExB6xjaA4kb7RpsNXJZsvtdp1E0XltMJnjpLvezutNCNrbY7WQ9MsXRvZq&sig=AHIEtbTqZiNMIdPuTR3aR5fZUYGMDN2bbA

15. Y. J. Rao, “Recent progress in fiber–optic extrinsic Fabry–Perot interferometric sensors”, Opt. Fiber Technol. 12, 227 - 237 (2006).

16. C. Wang and S. T. Scherrer, “Fiber ringdown pressure sensors”, Opt. Lett., 29, 352 - 354 (2004).

17. C. Wang and S. T. Scherrer, “Fiber loop ringdown for physical sensor development: pressure sensor”, Appl. Opt., 43, 6458 - 6464 (2004).

18. G. B. Hocker, “Fiber-optic sensing of pressure and temperature”, Appl. Opt., 18, 1445 - 1449 (1979).

19. I. Iordachita, Z. Sun, M. Balicki, J. U. Kang, S. J. Phee, J. Handa, P. Gehlbach, and R. Taylor, “A sub-milimetric, 0.25 mN resolution fully integrated fiber optic force-sensing tool for retinal microsurgery”, Int. J. CARS, 4, 383 - 390 (2009).

20. P. Sahay, M. Kaya, and C. Wang, “Fiber loop ringdown sensor for potential real-time monitoring of cracks in concrete structures: An exploratory study”, Sensors, 13, 39 - 57 (2013).

21. C. Wang, “Fiber ringdown temperature sensors”, Opt. Eng. 44, 030503/1 - 2 (2005).

22. J. A. Bucaro, E. F. Carome, and H. D. Darby, “Fiber optic acoustic sensor”, J. Acoust. Soc. Am., 67, 1854 - 1854 (1980).

23. A. D. Kersey, T. A. Berkoff, and W. W. Morey, “Fiber-optic Bragg grating strain sensor with drift-compensated high-resolution interferometric wavelength-shift detection”, Opt. Lett., 18, 72 - 74 (1993).

24. T. L. Yeo, T. Sun, and K. T. V. Grattan, “Fiber–optic sensor technologies for humidity and moisture measurement”, Sens. Actuat. A: Phys., 144, 280 - 295 (2008).

25. U. Willer, D. Scheel, I. Kostjucenko, C. Bohling, W. Schade, and E. Faber, "Fiber–optic evanescent–field laser sensors for in–situ gas diagnostic", Spect. Acta Part A: Mol. Biomol. Spect., 58, 2427 - 2432 (2002).

26. P. Raatikainen, I. Kassamakov, R. Kakanakov, and M. Luukkala, "Fiber-optic liquid level sensor", Sens. Actuat. A: Phys., 58, 93 - 97 (1997).

27. C. Herath, C. Wang, M. Kaya, and D. Chevalier, "Fiber loop ringdown DNA and bacteria sensors", J. Biomed. Opt., 16, 050501/1 - 3 (2011).

28. C. Wang, M. Kaya, and C. Wang, "Evanescent field-fiber loop ringdown glucose sensor", J. Biomed. Opt., 17, 037004/1 - 10 (2012).

29. T. V. Lerber and M. W. Sigrist, "Cavity–ring–down principle for fiber–optic resonators: Experimental realization of bending loss and evanescent–field sensing", Appl. Opt., 41, 3567 - 3575 (2002).

30. M. Y. Frankel and R. D. Esman, "True time-delay fiber-optic control of an ultra wide-band array transmitted receiver with multibeam capability", IEEE T. Microw. Theory, 43, 2387 - 2394 (1995).

31. C. Wang, "Fiber loop ringdown – a time–domain sensing technique for multi–function fiber optic sensor platforms: Current status and design perspectives", Sensors, 9, 7595 - 7621 (2009).

32. C. Wang and P. Sahay, "Breath analysis using laser spectroscopic techniques: Breath biomarkers, spectral fingerprints and detection limits", Sensors, 9, 8230 - 8262 (2009).

33. C. Wang, N. Srivastava, B. A. Jones, and R. B. Reese, "A novel multiple species ringdown spectrometer for in situ measurements of methane, carbon dioxide, and carbon isotope", Appl. Phys. B, 92, 259 - 270 (2008).

34. C. Wang and C. Herath, "Fabrication and characterization of fiber loop ringdown evanescent field sensors", Meas. Sci. Technol., 21, 085205/1 - 10 (2010).

35. C. Stamm, R. Dangel, and W. Lukosz, "Biosensing with the integrated-optical difference interferometer: dual-wavelength operation", Opt. Commun., 153, 347 - 359 (1998).

36. H. J. Know, S. C. Pieper, and K. A. Kang, "Fiber optic immunosensors for cardiovasculor disease diagnosis: quantification of protein C, Factor V Leiden, and Cardiac Troponin T in plasma", Adv. Exp. Med. Biol., 510**,** 115 - 119 (2003).

37. L. Van der Sneppen, F. Ariese, C. Gooijer, and W. Ubachs, "Liquid-phase and evanescent-wave ring-down spectroscopy in analytical chemistry", Annu. Rev. Anal Chem., 2, 13 - 35 (2009).

38. E. Scorsone, S. Christie, K. Persaud, P. Simon, and F. Kvasnik, “Fibre-optic evanescent sensing of gaseous ammonia with two forms of a new near-infrared dye in comparison to phenol red”, Sens. Actuat. B. Chem., 90, 37 - 45 (2003).

39. R. Li, H.-P. Loock, and R. D. Oleschuk, “Capillary electrophoresis absorption detection using fiber-loop ring-down spectroscopy”, Anal. Chem., 78, 5685 - 5692 (2006).

40. J. A. Barnes, R. S. Brown, A. H. Cheung, M. A. Dreher, G. Mackey, and H.-P. Loock, “Chemical sensing using a polymer coated long-period fiber grating interrogated by ring-down spectroscopy”, Sens. Actuat. B Chem., 148, 221 - 226 (2010).

41. K. Atherton, G. Stewart, and B. Culshaw, “Gas detection by cavity ringdown absorption with a fiber optic amplifier loop”, Proc. SPIE, 4577, 25 - 31 (2002).

42. H-P. Loock, “Chemical sensor based on a long period fibre grating modified by a functionalized polydimethylsiloxane coating”, Analyst, 133, 1541 - 1549 (2008).

43. M. Iga, A. Seki, Y. Kubota, and K. Watanabe, “Acidity measurements based on a hetero-core structured fiber optic sensor”, Sens. Actuat. B. Chem., 96, 234 - 238 (2003).

44. J. R. Epstein and D. R. Walt, “Fluorescence-based fibre optic arrays: A universal platform for sensing”, Chem. Soc. Rev., 32, 203 - 214 (2003).

45. Z. Zhang, K. T. V. Grattan, and A. W. Palmer, “Fiber-optic high temperature sensor based on the fluorescence lifetime of alexandrite”, Rev. Sci. Instrum., 63, 3869 - 3873 (1992).

46. C. Wang and A. Mbi, “An alternative method to develop fibre grating temperature sensors using the fibre loop ringdown scheme”, Meas. Sci. Technol., 17, 1741 - 1745 (2006).

47. F. Shen, W. Peng, K. L. Cooper, G. Pickrell, and A. Wang, “UV-induced intrinsic Fabry-Perot interferometric fiber sensors”, Proc. SPIE, 5590, 47 - 56 (2004).

48. Y. Zhu, K. L. Cooper, G. R. Pickrell, and A. Wang, “High-temperature fiber-tip pressure sensor”, J. Lightwave Tech., 24, 861 - 869 (2006).

49. Z. Huang, X. Chen, Y. Zhu, and A. Wang, “Wavefront splitting intrinsic Fabry-Perot fiber optic sensor”, Opt. Eng. Lett., 44, 070501/1-3 (2005).

50. Y. Zhao, C. Yu, and Y. Liao, “Differential FBG sensor for temperature-compensated high-pressure (or displacement) measurement”, Opt. Laser Technol., 36, 39-42 (2004).

51. N. Ni, C. C. Chan, X. Y. Dong, J. Sun, and P. Shum, “Cavity ring-down long-period fibre grating strain sensor”, Meas. Sic. Technol., 18, 3135 - 3138 (2007).

52. K. Fidanboylu and H. S. Efendioglu, Fiber optic sensors and their applications, IATS, May 2009, pp 1-6.

53. F. Luo, J. Liu, N. Ma, and T. F. Morse, “A fiber optic microbend sensor for distributed sensing application in the structural strain monitoring”, Sens. Actuat. A: Phys., 75, 41 - 44 (1999).

54. S. Sekimoto, H. Nakagawa, S. Okazaki, K. Fukuda, S. Asakura, T. Shigemori, and S. Takahashi, “A fiber-optic evanescent-wave hydrogen gas sensor using palladium-supported tungsten oxide”, Sens. Actuat. B: Chem., 66, 142 - 145 (2000).

55. B. A. Flusberg, E. D. Cocker, W. Piyawattanametha, J. C. Jung, E. L. M. Cheung, and M. J. Schnitzer, “Fiber-optic fluorescence imaging”, Nat. Methods, 2, 941 - 950 (2005).

56. M. Shortreed, R. Kopelman, M. Kuhn, and B. Hoyland, “Fluorescent fiber-optic calcium sensor for physiological measurements”, Anal. Chem., 68, 1414 - 1418 (1996).

57. B. D. MacCraith, C. M. McDonagh, G. O'Keeffe, E. T. Keyes, J. G. Vos, B. O'Kelly and J. F. McGilp, “Fibre optic oxygen sensor based on fluorescence quenching of evanescent-wave excited ruthenium complexes in sol–gel derived porous coatings”, Analyst, 118, 385 - 388 (1993).

58. A. P. Demchenko, Introduction to fluorescence sensing, Springer Netherlands, Springder Science + Business Media B. V. 2009.

59. E. Udd, W. Schulz, J. Seim, J. Corones, and H. M. Laylor, Fiber optic sensors for infrastructure applications, Oregon Department of Transportation, Washington D.C., 1998.

60. A. D. Kersey, T. A. Berkoff, and W. W. Morey, “Multiplexed fiber Bragg grating strain-sensor system with a fiber Fabry-Perot wavelength filter”, Opt. Lett., 18, 1370 - 1372 (1993).

61. B. Zhang and M. Kahrizi, “High-temperature resistance fiber Bragg grating temperature sensor fabrication”, IEEE Sensors, 7, 586 - 591 (2007).

62. K. O. Hill and G. Meltz, “Fiber Bragg grating technology fundamentals and overview”, J. Lightw. Technol., 15, 1263 - 1276 (1997).

63. L. Ping, M. Liqiu, S. Kevin, and C. Qiying, “Tapered fiber Mach–Zehnder interferometer for simultaneous measurement of refractive index and temperature”, App. Phys. Lett., 94, 131110/1 - 3 (2009).

64. C. R. Liao, D. N. Wang, M. Wang, and M. Yang, “Fiber in-line Michelson interferometer tip sensor fabricated by femtosecond laser”, IEEE Photonics Tech. Lett., 24, 2060 - 2063 (2012).

65. C. Ma and A. Wang, “Multimode excitation-induced phase shifts in intrinsic Fabry–Perot interferometric fiber sensor spectra”, Appl. Opt., 49, 4836 - 4845 (2010).

66. W. J. Bock, T. R. Wolinski, and A. Barwicz, “Development of a polarimetric optical fiber sensor for electronic measurement of high pressure”, IEEE T. Instrum. Meas., 39, 715 - 721 (1990).

67. J. Burck, J-P. Conzen, and H-J. Ache, “A fiber optic evanescent field absorption sensor for monitoring organic contaminants in water”, Anal. Chem., 342, 394 - 400 (1992).

68. X. Su, Y. Sun, G. B. Ren, P. Shum, N. Q. Ngo, and Y. C. Kwok, “Evanescent field absorption sensor using a pure-silica defected-core photonic crystal fiber”, Photon. Technol. Lett., 20, 336 - 338 (2008).

69. N. Lagakos, J. H. Cole, and J. A. Bucaro, “Microbend fiber-optic sensors”, Appl. Opt., 26, 2171 - 2180 (1987).

70. K. O. Hill and G. Meltz, “Fiber Bragg grating technology fundamentals and overview”, J. Lightw. Technol., 15, 1263 - 1276 (1997).

71. http://www.sacher-laser.com/home/laser-diodes/distributed_feedback_laser/dfb/single_mode.html

72. http://www.toptica.com/products/diode_lasers/research_grade_diode_lasers/tunable_diode_lasers/ diode_lasers_with_largest_mode_hop_free_tuning_range.html

73. http://www.corning.com/docs/opticalfiber/pi1463.pdf

74. http://www.opneti.com/uploadfile/20101127/20101127181202600.pdf

75. C. Herath, Fiber loop ringdown evanescent field sensors, Master Thesis, Mississippi State University, MS, December 2010.

76. http://www.thorlabs.us/NewGroupPage9.cfm?ObjectGroup_ID=947

77. http://www.tek.com/oscilloscope

78. http://www.newport.com/LDT-5900C-Series-Laser-Diode-Thermoelectric-Tempe/1009826/1033/info.aspx

79. http://www.newport.com/LDX-3200-Series-Precision-Laser-Diode-Drivers/1010347/1033/info.aspx

80. H. Waechter, J. Litman, A.H. Cheung, J.A. Barnes, and H.P. Loock, "Chemical sensing using fiber cavity ring-down spectroscopy", Sensors, 10, 1716 - 1742 (2010).

81. H. S. Jang, K. N. Park, J. P. Kim, S. J. Sim, O. J. Know, Y. G. Han, and K. S. Lee, S"ensitive DNA biosensor based on a long-period grating formed on the side-polished fiber surface", Opt. Express, 17, 3855 - 3850 (2009).

82. X. Chen, L. Zhang, K. Zhou, E. Davies, K. Sugden, I. Bennion, M. Hughes, and A. Hine, "Real time detection of DNA interactions with long period fiber grating based biosensor", Opt. Lett., 32, 2541 - 2543 (2007).

83. S. Walford, M. McB. Page, and S. P. Allison, "The influence of renal threshold on the interpretation of urine tests for glucose in diabetic patients", Diabetes Care, 3, 672 - 674 (1980).

84. S. B. Waters, B. G. Topp, S. Q. Siler, and C. M. Alexander, "Treatment with sitagliptin or metformin does not increase body weight despite predicted reductions in urinary glucose excretion", J. Diabetes Sci. Technol., 3, 68 - 82 (2009).

85. A. W. Snyder and J. D. Love, Optical Waveguide Theory, Kluwer Academic Publishers, Norwell, MA (2000).

86. C. Wang and C. Herath, "High sensitivity-fiber loop ringdown evanescent–field index sensors using single–mode fiber", Opt. Lett., 35, 1629 - 1631 (2010).

87. P. Polynkin, A. Polynkin, N. Peyghambarian, and M. Mansuriphur, "Evanescent field–based optical fiber sensing device for measuring the refractive index of liquids in microfluidic channels", Opt. Lett., 30, 1273 - 1275 (2005).

88. M. I. White and X. Fan, "On the performance quantification of resonant refractive index sensors", Opt. Express, 16, 1020 - 1028 (2008).

89. S. Binu, V. P. M. Pillai, V. Pradeepkumar, B. B. Padhy, C. S. Joseph, and N. Chandrasekaran, "Fiber optic glucose sensors", Mater. Sci. Eng. C, 29, 183 - 186 (2009).

90. T. Q. Lin, Y. L. Lu, and C. C. Hsu, "Fabrication of glucose fiber sensor based on immobilized GOD technique for rapid measurement", Opt. Express, 18, 27560 - 27566 (2010).

91. D. Jiang, E. Liu, X. Chen and J. Huang, “Design and properties study of fiber optic glucose biosensor”, Chin. Opt. Lett., 1, 108 - 110 (2003).

92. A. B. Ganesh and T. K. Radhakrishnan, “Employment of fluorescence quenching for the determination of oxygen and glucose”, Sensors & Transducers, 60, 439 - 445 (2005).

93. M. Portaccio, M. Lepre, B. D. Ventura, O. Stoilova, N. Manolova, I. Rashkov and D. G. Mita, “Fiber-optic glucose biosensor based on glucose oxidase immobilized in a silica gel matrix”, Sol-Gel Sci. Technol., 50, 437 - 448 (2009).

94. R. D. Lawrence, “Renal threshold for glucose: Normal and in diabetics”, Br. Med. J., 1**,** 766 - 768 (1940).

95. “Relationship between salt solution and sugar concentration (brix) and reflective index at 20 ºC.” www.topac.com

96. K. Kadoya, N. Matsunaga and A. Nagashima, “Viscosity and thermal conductivity of dry air in the gaseous phase”, J. Phys. Chem. Ref. Data, 14, 947 - 970 (1985).

97. G. Stewart, K. Atherton, H Yu, and B. Culshaw, “An investigation of an optical fibre amplifier loop for intra-cavity and ring-down cavity loss measurements”. Meas. Sci. Technol., 12, 843 - 849 (2001).

98. P. B. Tarsa, A. D. Wist, P. Rabinowitz, and K. K. Lehmann, “Evanescent field absorption in a passive optical fiber Evanescent field absorption in a passive optical fiber spectroscopy”, Appl. Phys. Lett., 85**,** 4523 - 4525 (2004).

99. R. S. Brown, I. Kozin, Z. Tong, R. D. Oleschuk, and H. P. Loock, “Fiber-loop ring-down spectroscopy”, J. Chem. Phys., 117, 10444 - 10447 (2002).

100. Z. Tong, A. Wright, T. McCormick, R. Li, R. D. Oleschuk, and H. P. Loock, “Phase-shift fiber-loop ring-down spectroscopy”, Anal. Chem., 76, 6594 - 6599 (2004).

101. Heavy water reactors I. International Atomic Energy Agency. II. Series: Technical reports series (International Atomic Energy Agency); 407, VICL, 2002.

102. A. M. Armani and K. J. Vahala, “Heavy water detection using ultra-high-Q microcavities”, Opt. Lett., 31, 1896 - 1898 (2006).

103. Y. Oki, E. Tashiro, and M. Maeda, C. Honda, Y. Hasegawa, H. Futami, J. Izumi, and K. Matsuda, “Sensitive detection of trace elements in pure water by laser-induced atomic fluorescence spectroscopy in microwave discharge atomization”, Anal. Chem., 65, 2096 - 2101 (1993).

104. H. Sobral, R. Sanginés, and A. T. Vázquez, “Detection of trace elements in ice and water by laser-induced breakdown spectroscopy”, Spectrochim. Acta B, 78, 62 - 66 (2012).

105. J. Bublitz, A. Knaack, M. Dickenhausen, M. Gratz, W. Schade, T. Baumgartl, and R. Horn, “Fiber optic LIF-sensors for the trace analysis of environmental pollutants in water and in the soil”, Adv. Remote Sens., 3, 179 - 187 (1995).

106. R. Orghici, U. Willer, M. Gierzewska, S. R. Waldvogel, and W. Schade, “Fiber optic evanescent field sensor for detection of explosives and CO_2 dissolved in water”, Appl. Phys. B, 90, 355 - 360 (2008).

107. J. B. Jensen, L. H. Pedersen, P. E. Hoiby, L. B. Nielsen, Hansen T P, Folkenberg J R, J. Riishede, D. Noordegraaf, K. Nielsen, A. Carlsen, and A. Bjarklev, “Photonic crystal fiber based evanescent-wave sensor for detection of biomolecules in aqueous solutions”, Opt. Lett., 29, 1974 - 1976 (2004).

108. L. Xu, J.C. Fanguy, K. Soni, and S. Tao, “Optical fiber humidity sensor based on evanescent-wave scattering”, Opt. Lett., 29, 1191 - 1193 (2004).

109. M. Jiang, W. Zhang, Q. Zhang, Y. Liu, and B. Liu, “Investigation on an evanescent wave fiber-optic absorption sensor based on fiber loop cavity ring-down spectroscopy”, Opt. Commun., 283, 249 - 253 (2010).

110. P. D. Wilson, The nuclear fuel cycle: from Ore to Wastes, New York, NY: Oxford University Press, 1996. ISBN: 9780198565406.

111. D. Ahuja and N. Ahuja, “Nuclear power plant”, J. Automation Power Eng., 1, 97 - 100 (2012).

112. International Atomic Energy Agency, Code on the Safety of Nuclear Power Plants Sitting, IAEA-SS-50-C (Rev-1), Vienna 1988.

113. L. Lee, H. Park, T. S. Kim, K. H. Ko, and D. Y. Jeong, “A new sensor for detection of coolant leakage in nuclear power plants using off-axis integrated cavity output spectroscopy”, Nucl. Instrum. Meth. A, 678, 8 - 12 (2012).

114. Regulatory Guide 1.45, Reactor Coolant Pressure Boundary Leakage Detection Systems, U.S. Nuclear Regulatory Commission, May 2008, Washington, DC.

115. Refractive index database, refractiveindex.info

116. J. M. Harnly, “The future of atomic absorption spectrometry: a continuum source with a charge coupled array detector”, Anal. At. Spectrom., 14, 137 - 146 (1999).

117. K. Sutton, R. M. C. Sutton, and J. A. Caruso, “Inductively-coupled plasma mass-spectrometric detection for chromatography and capillary electrophoresis”, J. Chromatogr. A, 789, 85 - 126 (1997).

118. R. Klockenkamper and A. Bohlen, “Elemental analysis of environmental samples by total reflection *X-ray* fluorescence: A review”, X-Ray Spectrom., 25, 156 - 162 (1996).

119. P. J. S. Barbeira and N. R. Stradiotto, “Anodie stripping voltammetric determination of Zn, Pb and Cu traces in whisky samples”, Frensenius J. Anal. Chem., 361, 507 - 509 (1998).

120. X. Xie, D. Stuben, Z. Berner, J. Albers, R. Hintsche, and E. Jantzen, “Development of an ultra-microelectrode arrays (UMEAs) sensor for trace heavy metal measurement in water”, Sens. Actuat. B: Chem., 97, 168 - 173 (2004).

121. S. Wang, E. S. Forzani, and N. Tao, “Detection of heavy metal ions in water by high-resolution surface plasmon resonance spectroscopy combined with anodic stripping voltammetry”, Anal. Chem., 79, 4427 - 4432 (2007).

122. E. Forzani, H. Zhang, W. Chen, and N. Tao, “Detection of heavy metal ions in drinking water using a high-resolution differential surface plasmon resonance sensor”, Environ. Sci. Technol., 39, 1257 - 1262 (2005).

123. N. Verma, S. Kumar, and H. Kaur, “Fiber optic biosensor for detection of Cd in milk”, Biosens. Bioelectron., 1, 1000102/1 - 3 (2010).

124. H. Prestel, A. Gahr, and R. Niesser, “Detection of heavy metals in water by fluorescence spectroscopy: On the way to a suitable sensor system”, Fresenius J. Anal. Chem., 368, 182 - 191 (2000).

125. A. Mendez and T. F. Morse, “Overview of optical fibre sensors embedded in concrete”, Fibre Opt. Smart Struct. Skins, 1798, 205 - 216 (1992).

126. B. Glisic and D. Inaudi, “Development of method in service crack detection based on distributed fiber optic sensors”, Struct. Health Mon., 11, 161 - 171 (2011).

127. W. Xie, T. Sun, K. T. V. Grattan, D. McPolin, P. A. M. Basheer, and A. E. Long, “Fiber optic chemical sensor systems for internal concrete condition monitoring”, Proc. SPIE, 5502, 334 - 338 (2004).

128. D. O. McPolin, M. P. A. Basheer, A. E. Long, X. Weiguo, T. Sun, and K.T. V. Grattan, “Development and longer term in situ evaluation of Fiber-optic sensors for monitoring of structural concrete”, IEEE Sensors, 9, 1537 - 1545 (2009).

129. H. Kanare, Why are still having problems with moisture and concrete floor slabs?, Concrete Construction Magazine November 15, 2007 pp 1-4.

130. E. Samson, J. Marchand, K. A. Snyder, and J. J. Beaudoin, “Modeling ion and fluid transport in unsaturated cement systems in isothermal conditions”, Cement Concrete Research, 35, 141 - 153 (2005).

131. L. Basheer, J. Kropp, and D. J. Cleland, “Assessment of the durability of concrete from its permeation properties: a review”, Construct. Building Materials, 15, 93 - 103 (2001).

132. T. L. Yeo, M. A. C. Cox, L. F. Boswell, T. Sun, and K. T. V. Grattan, “Monitoring ingress of moisture in structural concrete using a novel optical-based sensor approach”, J. Phys. Conf., 45, 186 - 192 (2006).

133. K. Wang and J. Hu, “Use of moisture sensor for monitoring the effect of mixing procedure on uniformity of concrete mixtures”, J. Adv. Concrete Tech., 3, 371 - 384 (2005).

134. H-N. Li, D-S. Li, and G-B. Song, “Recent applications of fiber optic sensors to health monitoring in civil engineering”, Eng. Struct., 26, 1647 - 1657 (2004).

135. C. I. Merzbacher, A. D. Kersey, and E. J. Friebele, “Fiber optic sensors in concrete structures: a review”, Smart Mater. Struct., 5, 196 - 208 (1996).

136. A. Mendez, T. F. Morse, and F. Mendez, Applications of embedded optical fiber sensors in reinforced concrete buildings and structures, Fiber Opt. Smart Struct. Skins II, Washington, 1989, pp. 60-69.

137. P. L. Swart, R. Naude, and B. M. Lacquet, “Determining the moisture content in concrete with a fiber optic Mach-Zehnder interferometer: a feasibility study”, Meas. Sci. Technol., 12, 927 - 931 (2001).

138. T. L. Yeo, D. Eckstein, B. MCKinley, L. F. Boswell, T. Sun, and K. T. V. Grattan, “Demonstration of a fibre-optic sensing technique for the measurement of moisture absorption in concrete”, Smart Mater. Struct., 15, 40 - 45 (2006).

139. T. L. Yeo, Y. Yuan, L. F. Boswell, T. Sun, and K. T. V. Grattan, “Optical fibre sensors for the measurement of concrete sample properties following exposure to freeze/thaw tests”, Sens. Actuat. A: Phys., 153, 166 - 170 (2009).

140. W. M. Healy, S. Luo, M. Evans, A. Sucheta, and Y. Liu, Development of an optical fiber-based moisture sensor for building envelopes, 24th AIVC Conf. & BETEC Conf., Washington, DC, Oct. 14, 2003.

141. M. N. Alam, R. H. Bhuiyan, R. A. Dougal, and M. Ali, “Concrete moisture content measurement using interdigitated near-field sensors”, IEEE Sensors, 10, 1243 - 1248 (2010).

142. M. Ghandehari, C. S. Vimer, I. Ioannou, A. Sidelev, W. Jin, and P. Spellane, "In-situ measurement of liquid phase moisture in cement mortar", NDT&E Int., 45, 162 - 168 (2011).

143. B. D. Gupta and Ratnanjali, "A novel probe for a fiber optic humidity sensor", Sens. Actuat. B: Chem., 80, 132 - 135 (2001).

144. S. K. Khijwania, K. L. Srinivasan, and J. P. Singh, "An evanescent-wave optical fiber relative humidity sensor with enhanced sensitivity", Sens. Actuat. B: Chem., 104, 217 - 222 (2005).

145. T. L. Yeo, T. Sun, K. T. V. Grattan, D. Parry, R. Lade, and B. D. Powell, "Characterization of a polymer-coated fiber Bragg grating sensor for relative humidity sensing", Sens. Actuat. B: Chem., 110, 148 - 155 (2005).

146. S. Akita, H. Sasaki, K. Watanabe, and A. Seki, "A humidity sensor based on a hetero-core optical fiber", Sens. Actuat. B: Chem., 147, 385 - 391 (2010).

147. Z. Zhao and Y. Duan, "A low cost fiber optic humidity sensor based on silica sol-gel film", Sens. Actuat. B: Chem., 160, 1340 - 1345 (2011).

148. R. Aneesh and S. K. Khijwania, "Zinc oxide nanoparticle based optical fiber humidity sensor having linear response throughout a large dynamic range", Appl. Opt., 50, 5310 - 5314 (2011).

149. M. Rajesh, K. Geetha, M. Sheeba, P. Radhakrishnan, C. P. G. Vallabhan, and V. P. N. Nampoori, "A fiber optic smart sensor for studying the setting characteristics of various grades of cement", Opt. Lasers Eng., 44, 486 - 493 (2006).

150. P. Kronenberg, P. K. Rastogi, P. Giaccari, and H. G. Limberger, "Relative humidity sensor with optical fiber Bragg gratings", Opt. Lett., 27, 1385 - 1387 (2002).

151. T. L. Yeo, M. A. C. Cox, L. F. Boswell, T. Sun, and K. T. V. Grattan, "Optical fiber sensors for monitoring ingress of moisture in structural concrete", Rev. Sci. Inst., 77, 055108/1 - 7 (2006).

152. M. B. Reid and M. Ozcan, "Temperature dependence of fiber optic Bragg gratings at low temperatures", Opt. Eng., 37, 237 - 240 (1998).

153. K. P. Chong, N. J. Carino, and G. Washer, "Health monitoring of civil infrastructures", Smart Mater. Struct., 12, 483 - 493 (2003).

154. *Concrete Cracking.* Available online: http://www.cfawalls.org/foundations/cracking.htm (accessed on 5 March 2012).

155. D. J. Daniels, “Surface-penetrating radar”, Electron. Commun. Eng., 8, 165 - 182 (1996).

156. N. J. Carino, The impact-echo method: an overview. In *Proceedings of Structures Congress & Exposition*, Washington, DC, USA, 21–23 May 2001; pp. 1–18.

157. M. Clark, D. McCann, and M. Forde, “Application of infrared thermography to the non-destructive testing of concrete and masonry bridges”, NDT & E Int., 36, 265 - 275 (2003).

158. M. Ohtsu, “The history and development of acoustic emission in concrete engineering”, Mag. Concrete Res., 48, 312 - 330 (1996).

159. G. Song, Y. L. Mo, K. Otero, and H. Gu, “Health monitoring and rehabilitation of a concrete structure using intelligent materials”, Smart Mater. Struct., 15, 309 - 314 (2006).

160. G. Song, H. Gu, Y. L. Mo, T. T. C. Hsu, and H. Dhonde, “Concrete structural health monitoring using embedded piezoceramic transducers”, Smart Mater. Struct., 16, 959 - 968 (2007).

161. S. Yan, W. Sun, G. Song, H. Gu, L. S. Huo, B. Liu, and Y. G. Zhang, “Health monitoring of reinforced concrete shear walls using smart aggregates”, Smart Mater. Struct., 18, 047001/1 - 6 (2009).

162. H. Gu, Y. Moslehy, D. Sanders, G. Song, and Y. L. Mo, “Multi-functional smart aggregate-based structural health monitoring of circular reinforced concrete columns subjected to seismic excitations”, Smart Mater. Struct., 19, 06506/1 - 7 (2010).

163. P.C. Chang, A. Flatau, and S. Liu, “Review paper: Health monitoring of civil infrastructure”, Struct. Health Monit., 2, 257 - 267 (2003).

164. G. Song, H. C. Gu, and Y. L. Mo, “Smart aggregates: multi-functional sensors for concrete structures: A tutorial and a review”, Smart Mater. Struct., 17, 033001/1 - 17 (2008).

165. K. T. V. Grattan and T. Sun, “Fiber optic sensor technology: An overview”, Sens. Actuat. A: Phys., 82, 40 - 61 (2000).

166. C. K. Y. Leung, “Fiber optic sensors in concrete: the future?” NDT & E Int., 34, 85 - 94 (2001).

167. G. Zhou and L. M. Sim, “Damage detection and assessment in fibre-reinforced composite structures with embedded fibre optic sensors-review”, Smart Mater. Struct., 5, 925 - 940 (2002).

168. F. Ansari, Theory and applications of integrated fiber optic sensors. In *Intelligent Civil Engineering Materials and Structures*; F. Ansari, A. Maji, C. Leung, Eds.; American Society of Civil Engineers: New York, NY, USA, 1997; pp. 2–28.

169. P. Moyo, J. M. W. Brownjohn, R. Suresh, and S. J. Tjin, "Development of fiber Bragg grating sensors for monitoring civil infrastructure", Eng. Struct., 27, 1828 - 1834 (2005).

170. J. Leng and A. Asundi, "Structural health monitoring of smart composite materials by using EFPI and FBG sensors", Sens. Actuat. A, 103, 330 - 340 (2003).

171. B. Lee, "Review of the present status of optical fiber sensors", Opt. Fiber Technol., 9, 57 - 79 (2003).

172. M. Majumder, T. K. Gangopadhyay, A. K. Chakraborty, K. Dasgupta, and D. Bhattacharya, "Fibre Bragg gratings in structural health monitoring—present status and applications", Sens. Actuat. A, 147, 150 - 164 (2008).

173. B. Glišić and D. Inaudi, Chapter 2: In *Fibre Optic Methods for Structural Health Monitoring*; John Wiley & Sons: New York, NY**,** USA, 2008; pp. 20-40.

174. T. K. Gangopadhyay, M. Majumder, A. K. Chakraborty, A. K. Dikshit, and D. K. Bhattacharya, "Fibre Bragg grating strain sensor and study of its packaging material for use in critical analysis on steel structure", Sens. Actuat. A, 150, 78 - 86 (2009).

175. S. Villalba and J. R. Casas, Application of optical fiber distributed sensing to health monitoring of concrete structures, Mech. Syst. Signal Process., 2012, doi: 10.1016/j.ymssp.2012.01.027.

176. P. Rossi and F. Le Maou, "New method for detecting cracks in concrete using fibre optics", Mater. Struct., 22, 437 - 442 (1989).

177. F. Ansari and R. K. Navalurkar, "Kinematics of crack formation in cementitious composites by fiber optics", Eng. Mech., 112, 1048 - 1061 (1993).

178. C. K. Y. Leung, N. Elvin, N. Olson, T. F. Morse, and Y. F. He, "A novel distributed optical crack sensor for concrete structures", Eng. Fracture Mech., 65, 133 - 148 (2000).

179. W. R. Habel, I. Feddersen, and C. Fitschen, "Embedded quasi-distributed fiber-optic sensors for the long-term monitoring of the grouting area of rock anchors in a large gravity dam", Intelligent Mater. Syst. Struct., 10, 330 - 339 (1999).

180. D. Lee, J. Lee, I. Kwon, and D. Seo, “Monitoring of fatigue damage of composite structures by using embedded intensity-based optical fiber sensors”, Smart Mater. Struct., 10, 285 - 292 (2001).

181. K. K. K. Annamdas and V. G. M. Annamdas, “Review on developments in fiber optical sensors and applications”, Proc. SPIE, 76770, 76770R/1 - 12 (2010).

182. A. O’Keefe and D. A. G. Deacon, “Cavity ring-down optical spectrometer for absorption measurements using pulsed laser sources”, Rev. Sci. Instrum., 59, 2544 - 2551 (1988).

183. *Cavity-Ringdown Spectroscopy: An Ultratrace-Absorption Measurement Technique*; Busch, K. W., Busch, M. A., Eds.; American Chemical Society: Washington, DC, USA, 1999; Volume 720.

184. G. Berden, R. Peeters, and G. Meijer, “Cavity ring-down spectroscopy: Experimental schemes and applications”, Int. Rev. Phys. Chem., 19, 565 - 607 (2000).

185. P. B. Tarsa, P. Rabinowitz, and K. K. Lehmann, “Evanescent field absorption in a passive optical fiber resonator using continuous-wave cavity ring-down spectroscopy”, Chem. Phys. Lett., 383, 297 - 303 (2004).

186. C. Vallance, “Innovations in cavity ringdown spectroscopy”, New J. Chem., 29, 867 - 874 (2005).

187. H. Qiu, Y. Qiu, Z. Chen, B. Fu, X. Chen, and G. Li, “Multimode fiber ring-down pressure sensor”, Microw. Opt. Techn. Let., 49, 1698 - 1700 (2007).

188. N. Ni, C. Chan, W. Wong, L. Shao, X. Dong, and P. Shum, “Cavity ring-down long period grating pressure sensor”, Sens. Actuat. A, 158, 207 - 211 (2010).

189. L. Bo, L. Jianhua, and K. Guiyun, “Temperature and strain sensor based on weak LPG and fiber ring down”, Microw. Opt. Techn. Lett., 50, 111 - 114 (2007).

190. H. Qiu, Y. Qiu, Z. Chen, B. Fu, and G. Li, “Strain measurement by fiber-loop ring-down spectroscopy and fiber mode converter”, IEEE Sensors, 8, 1180 - 1183 (2008).

191. F. Ravet, F. Briffod, B. Glisic, M. Niklès, and D. Inaudi, “Submillimeter crack detection with Brillouin-based fiber-optic sensors”, Sensors, 9, 1391 - 1396 (2009).

192. P. B. Tarsa, D. M. Brzozowski, P. Rabinowitz, and K. K. Lehmann, “Cavity ringdown strain gauge”, Opt. Lett., 29, 1339 - 1341 (2004).

193. K. Kesavan, K. Ravisankar, S. Parivallal, P. Sreeshylam, and S. Sridhar, "Experimental studies on fiber optic sensors embedded in concrete", Measurement, 43, 157 - 163 (2010).

194. M. F. Vallejo and M. L. Amo, "Optical fiber networks for remote fiber optic sensors", Sensors, 12, 3929 - 3951 (2012).

195. K. Nakamura, "Applications of optical fiber sensing networks", Lasers Elect. Opt., 1, 498 - 499 (2001).

196. A. Dandridge and C. Kirkendall, Passive fiber optic sensor networks. In optical Fibre Sensing Technology, Lopez-Higuera, J.M., Ed.; Wiley&Son: Berlin, Germany, 2002, pp. 433-338.

197. P. Urquhart, H. Palezi, and P. Jardin, "Optical fiber bus protection network to multiplex sensors: Self-diagnostic operation", J. Lightw. Technol., 29, 1427 - 1436 (2011).

198. N. Mohamed, I. Jawhar, J. Al-Jaroodi, and L. Zhang, "Sensor network architectures for monitoring underwater pipelines", Sensors, 11, 10738 - 10764 (2011).

199. Q. Huang, C. Zhang, Q. Liu, N. Yan, and Y. Cao, New type of sensor network for smart grid interface of transmission system, IEEE Power and Energy Society General Meeting, July 2010, pp. 1-5.

200. C. Meunier, J. J. Guerin, M. Lequime, M. Rioual, E. Noel, D. Eguiazabal, D. Fleury, J. Maurin, and R. Mongin, "Industrial prototype of a fiber-optic sensor network for the thermal monitoring of the turbogenerator of a nuclear power plant-design, qualification, and settlement", J. Lightw. Technol., 13, 1354 - 1361 (1995).

201. R. A. Livingston, Fiber optic sensor networks for monitoring existing bridges, Rehabilitating and repairing the buildings and bridges of the Americas Conference 2001, published in 2002, Am. Soc. Civil Eng., pp. 65-75.

202. L. A. Riberio, J. B. Rosolem, D. C. Dini, C. Floridia, C. A. Hortencio, E. F. Costa, E. W. Bezerra, R. B. De Oliveira, M. D. Loichate, and A. S. Durelli, Fiber optic bending loss sensor for application on monitoring of embankment dams, IEEE Microwave & Optoelectronics Conference 2011, International, pp. 637-641.

203. E. Mehrani, A. Ayoub, and A. Ayoub, "Evaluation of fiber optic sensors for remote health monitoring of bridge structures", Mater. Struct./ Mater. Construct., 42, 183 - 199 (2009).

204. T. Saitho, K. Nakamura, Y. Takahashi, H. Iida, Y. Iki, and K. Miyagi, "Ultra-long-distance (230 km) FBG sensor system", Proc. SPIE, 7004, 70046/1 - 4 (2008).

205. M. K. Barnoski, and S. M. Jensen, "A novel technique for investigating attenuation characteristics", Appl. Opt., 15, 2112 - 2115 (1976).

206. Harold P.E. Stern and Samy A. Mahmoud, Communication Systems: Analysis and Design, Prentice-Hall Inc., Upper Saddle River, NJ. Sep 27, 2003, pp. 552.

207. M. D. Frederickson, B. Thaler, and P. Bratt, Fiber optic wavelength-division multiplexing, November 2010, ISO 9001:2008 Certified, ACI Technol. Inc., pp. 1-8.

208. J. P. Dakin, "Multiplexed and distributed optical fibre sensors systems", J. Phys. E: Sci. Instrum., 20, 954 - 967 (1987).

209. I. P. Giles, D. Uttam, B. Culshaw, and D. E. N. Davies, "Coherent optical fiber sensors with modulated laser sources", Elect. Lett. 20, 14 - 19 (1983).

210. D. Inaudi, "Coherence multiplexing of in-line displacement and temperature sensors", Opt. Eng., 34, 1912 - 1915 (1995).

211. J. L. Brooks, R. H. Wentworth, R. C. Youngquist, M. Tur, B. Y. Kim, and H. J. Shaw, "Coherence multiplexing of fiber-optic interferometric sensors", J. Lightw. Technol., 3, 1062 - 1072 (1985).

212. A. H. Gnauck, P.J. Winzer, S. Chandrasekhar, X. Liu, B. Zhu, D.W. Peckham, "10x224-Gb/s WDM transmission of 28-Gband PDM 16-QAM on a 50-GHz grid over 1200 km of fiber", OFC 2010, Post-deadline paper PDPB8, 2010.

213. A. Yi, L. Yan, B. Luo, W. Pan, and J. Ye, "All-optical regeneration of polarization division multiplexing signals in polarization nonlinear loop mirror", Opt. Commun., 284, 3619 - 3621 (2011).

214. M. Sjodin, E. Argel, P. Johanisson, G-W. Lu, P. A. Andrekson, and M. Karlsson, "Filter optimization for self-homodyne coherent wdm systems using interleaved polarization division multiplexing", J. Lightw. Technol., 29, 1219 - 1226 (2011).

APPENDIX A

PERMISSIONS FOR FIGURES USED IN THIS DISSERTATION

A.1 Permissions for figures from 2.2 (b) to 2.12

Feb 13 (4 days ago)

Malik Kaya <mk400@msstate.edu>
to reprint_permis.

Dear Sir/Madam,

I would like to get permission to use my following articles in my dessertation:

1. Fiber loop ringdown DNA and bacteria sensor,
Chamini Herath, Chuji Wang, Malik Kaya, David Chevalier
Published in Volume 16, Issue 05, May 2011 • 4 page

2. Evanescent field-fiber loop ringdown glucose sensor
Chuji Wang, Malik Kaya, Charlotte Wang
Published in Volume 17, Issue 03
March 2012 • 11 pages

Best Regards

Feb 15 (2 days ago)

Karen Thomas <karent@spie.org>
to me

Dear Malik,

Thank you for seeking permission from SPIE to reprint material from our publications. As author, SPIE shares the copyright with you, so you retain the right to reproduce your paper in part or in whole.

Publisher's permission is hereby granted under the following conditions:

(1) the material to be used has appeared in our publication without credit or acknowledgment to another source; and

(2) you credit the original SPIE publication. Include the authors' names, title of paper, volume title, SPIE volume number, and year of publication in your credit statement.

Sincerely,

Karen Thomas for
Eric Pepper, Director of Publications
SPIE
P.O. Box 10, Bellingham WA 98227-0010 USA
360/676-3290 (Pacific Time) eric@spie.org

From: Malik Kaya [mailto:mk400@msstate.edu]
Sent: Wednesday, February 13, 2013 3:55 PM
To: reprint_permission
Subject: Permission

Permissions for figures 3.4 and 3.5

Malik Kaya <mk400@msstate.edu> Mar 26 (10 days ago)

to wna

Dear Sir/Madam,

I have been writing my dissertation on fiber loop ringdown sensors.
I have used following link for nuclear reactor information:

http://www.world-nuclear.org/info/Nuclear-Fuel-Cycle/Power-Reactors/Nuclear-Power-Reactors/#.UVH1pxxg-So

I would like to have a copyright permission for pressurized water reactor figure and boiling water reactor figure.
Could you please help me with that?

Regards

Mar 27 (9 days ago)

Warwick Pipe <pipe@world-nuclear.org>
to me

Hello,

Thank you for your enquiry requesting permission to reproduce the PWR and BWR images from the WNA website.

You are welcome to do so, but please include an acknowledgement that the WNA was the source of the images.

Regards,

Warwick Pipe
Web Content Manager

Carlton House, 22a St. James's Square, London SW1Y 4JH, UK
t: +44 (0) 20 7451 1526 | f: +44 (0) 20 7839 1501
www.world-nuclear.org | www.world-nuclear-news.org | www.world-nuclear-university.org

A.2 Permissions for figures from 4.1 to 4.13 and tables 4.1 and 4.2

ELSEVIER LICENSE
TERMS AND CONDITIONS

Feb 13, 2013

This is a License Agreement between Malik Kaya ("You") and Elsevier ("Elsevier") provided by Copyright Clearance Center ("CCC"). The license consists of your order details, the terms and conditions provided by Elsevier, and the payment terms and conditions.

All payments must be made in full to CCC. For payment instructions, please see information listed at the bottom of this form.

Supplier	Elsevier Limited The Boulevard,Langford Lane Kidlington,Oxford,OX5 1GB,UK
Registered Company Number	1982084
Customer name	Malik Kaya
Customer address	400 E Gillespie St Apt 146 Starkville, MS 39759
License number	3087310062838
License date	Feb 13, 2013
Licensed content publisher	Elsevier
Licensed content publication	Sensors and Actuators B: Chemical
Licensed content title	Reproducibly reversible fiber loop ringdown water sensor embedded in concrete and grout for water monitoring
Licensed content author	Malik Kaya,Peeyush Sahay,Chuji Wang
Licensed content date	January 2013
Licensed content volume	176

number	
Licensed content issue number	
Number of pages	8
Start Page	803
End Page	810
Type of Use	reuse in a thesis/dissertation
Portion	full article
Format	both print and electronic
Are you the author of this Elsevier article?	Yes
Will you be translating?	No
Order reference number	
Title of your thesis/dissertation	Time-domain fiber loop ringdown sensors and sensor network
Expected completion date	Aug 2013
Estimated size (number of pages)	300
Elsevier VAT number	GB 494 6272 12
Permissions price	0.00 USD
VAT/Local Sales Tax	0.0 USD / 0.0 GBP
Total	0.00 USD
Terms and Conditions	

INTRODUCTION

1. The publisher for this copyrighted material is Elsevier. By clicking "accept" in connection with completing this licensing transaction, you agree that the following terms and conditions apply to this transaction (along with the Billing and Payment terms and conditions established by Copyright Clearance Center, Inc. ("CCC"), at the time that you opened your Rightslink account and that are available at any time at http://myaccount.copyright.com).

GENERAL TERMS

2. Elsevier hereby grants you permission to reproduce the aforementioned material subject to the terms and conditions indicated.

3. Acknowledgement: If any part of the material to be used (for example, figures) has appeared in our publication with credit or acknowledgement to another source, permission must also be sought from that source. If such permission is not obtained then

that material may not be included in your publication/copies. Suitable acknowledgement to the source must be made, either as a footnote or in a reference list at the end of your publication, as follows:

"Reprinted from Publication title, Vol /edition number, Author(s), Title of article / title of chapter, Pages No., Copyright (Year), with permission from Elsevier [OR APPLICABLE SOCIETY COPYRIGHT OWNER]." Also Lancet special credit - "Reprinted from The Lancet, Vol. number, Author(s), Title of article, Pages No., Copyright (Year), with permission from Elsevier."

4. Reproduction of this material is confined to the purpose and/or media for which permission is hereby given.

5. Altering/Modifying Material: Not Permitted. However figures and illustrations may be altered/adapted minimally to serve your work. Any other abbreviations, additions, deletions and/or any other alterations shall be made only with prior written authorization of Elsevier Ltd. (Please contact Elsevier at permissions@elsevier.com)

6. If the permission fee for the requested use of our material is waived in this instance, please be advised that your future requests for Elsevier materials may attract a fee.

7. Reservation of Rights: Publisher reserves all rights not specifically granted in the combination of (i) the license details provided by you and accepted in the course of this licensing transaction, (ii) these terms and conditions and (iii) CCC's Billing and Payment terms and conditions.

8. License Contingent Upon Payment: While you may exercise the rights licensed immediately upon issuance of the license at the end of the licensing process for the transaction, provided that you have disclosed complete and accurate details of your proposed use, no license is finally effective unless and until full payment is received from you (either by publisher or by CCC) as provided in CCC's Billing and Payment terms and conditions. If full payment is not received on a timely basis, then any license preliminarily granted shall be deemed automatically revoked and shall be void as if never granted. Further, in the event that you breach any of these terms and conditions or any of CCC's Billing and Payment terms and conditions, the license is automatically revoked and shall be void as if never granted. Use of materials as described in a revoked license, as well as any use of the materials beyond the scope of an unrevoked license, may constitute copyright infringement and publisher reserves the right to take any and all action to protect its copyright in the materials.

9. Warranties: Publisher makes no representations or warranties with respect to the licensed material.

10. Indemnity: You hereby indemnify and agree to hold harmless publisher and CCC, and their respective officers, directors, employees and agents, from and against any and all claims arising out of your use of the licensed material other than as specifically authorized pursuant to this license.

11. No Transfer of License: This license is personal to you and may not be sublicensed, assigned, or transferred by you to any other person without publisher's written permission.

12. No Amendment Except in Writing: This license may not be amended except in a writing signed by both parties (or, in the case of publisher, by CCC on publisher's

behalf).

13. Objection to Contrary Terms: Publisher hereby objects to any terms contained in any purchase order, acknowledgment, check endorsement or other writing prepared by you, which terms are inconsistent with these terms and conditions or CCC's Billing and Payment terms and conditions. These terms and conditions, together with CCC's Billing and Payment terms and conditions (which are incorporated herein), comprise the entire agreement between you and publisher (and CCC) concerning this licensing transaction. In the event of any conflict between your obligations established by these terms and conditions and those established by CCC's Billing and Payment terms and conditions, these terms and conditions shall control.

14. Revocation: Elsevier or Copyright Clearance Center may deny the permissions described in this License at their sole discretion, for any reason or no reason, with a full refund payable to you. Notice of such denial will be made using the contact information provided by you. Failure to receive such notice will not alter or invalidate the denial. In no event will Elsevier or Copyright Clearance Center be responsible or liable for any costs, expenses or damage incurred by you as a result of a denial of your permission request, other than a refund of the amount(s) paid by you to Elsevier and/or Copyright Clearance Center for denied permissions.

LIMITED LICENSE

The following terms and conditions apply only to specific license types:

15. **Translation**: This permission is granted for non-exclusive world **English** rights only unless your license was granted for translation rights. If you licensed translation rights you may only translate this content into the languages you requested. A professional translator must perform all translations and reproduce the content word for word preserving the integrity of the article. If this license is to re-use 1 or 2 figures then permission is granted for non-exclusive world rights in all languages.

16. **Website**: The following terms and conditions apply to electronic reserve and author websites:

Electronic reserve: If licensed material is to be posted to website, the web site is to be password-protected and made available only to bona fide students registered on a relevant course if:

This license was made in connection with a course,

This permission is granted for 1 year only. You may obtain a license for future website posting,

All content posted to the web site must maintain the copyright information line on the bottom of each image,

A hyper-text must be included to the Homepage of the journal from which you are licensing at http://www.sciencedirect.com/science/journal/xxxxx or the Elsevier homepage for books at http://www.elsevier.com , and

Central Storage: This license does not include permission for a scanned version of the material to be stored in a central repository such as that provided by Heron/XanEdu.

17. **Author website** for journals with the following additional clauses:

All content posted to the web site must maintain the copyright information line on the bottom of each image, and the permission granted is limited to the personal version of your paper. You are not allowed to download and post the published electronic version of

your article (whether PDF or HTML, proof or final version), nor may you scan the printed edition to create an electronic version. A hyper-text must be included to the Homepage of the journal from which you are licensing athttp://www.sciencedirect.com/science/journal/xxxxx . As part of our normal production process, you will receive an e-mail notice when your article appears on Elsevier's online service ScienceDirect (www.sciencedirect.com). That e-mail will include the article's Digital Object Identifier (DOI). This number provides the electronic link to the published article and should be included in the posting of your personal version. We ask that you wait until you receive this e-mail and have the DOI to do any posting.

Central Storage: This license does not include permission for a scanned version of the material to be stored in a central repository such as that provided by Heron/XanEdu.

18. **Author website** for books with the following additional clauses:
Authors are permitted to place a brief summary of their work online only.
A hyper-text must be included to the Elsevier homepage at http://www.elsevier.com . All content posted to the web site must maintain the copyright information line on the bottom of each image. You are not allowed to download and post the published electronic version of your chapter, nor may you scan the printed edition to create an electronic version.

Central Storage: This license does not include permission for a scanned version of the material to be stored in a central repository such as that provided by Heron/XanEdu.

19. **Website** (regular and for author): A hyper-text must be included to the Homepage of the journal from which you are licensing at http://www.sciencedirect.com/science/journal/xxxxx. or for books to the Elsevier homepage at http://www.elsevier.com

20. **Thesis/Dissertation**: If your license is for use in a thesis/dissertation your thesis may be submitted to your institution in either print or electronic form. Should your thesis be published commercially, please reapply for permission. These requirements include permission for the Library and Archives of Canada to supply single copies, on demand, of the complete thesis and include permission for UMI to supply single copies, on demand, of the complete thesis. Should your thesis be published commercially, please reapply for permission.

21. **Other Conditions**:

v1.6

If you would like to pay for this license now, please remit this license along with your payment made payable to "COPYRIGHT CLEARANCE CENTER" otherwise you will be invoiced within 48 hours of the license date. Payment should be in the form of a check or money order referencing your account number and this invoice number RLNK500956406.
Once you receive your invoice for this order, you may pay your invoice by credit card. Please follow instructions provided at that time.

Make Payment To:
Copyright Clearance Center
Dept 001
P.O. Box 843006
Boston, MA 02284-3006

For suggestions or comments regarding this order, contact RightsLink Customer Support:customercare@copyright.com or +1-877-622-5543 (toll free in the US) or +1-978-646-2777.

Gratis licenses (referencing $0 in the Total field) are free. Please retain this printable license for your reference. No payment is required.

Malik Kaya <mk400@msstate.edu> Apr 5 (4 days ago)

to Support

Dear Sir/Madam,

I would like to get permission for my following article to use in my desertation:

* Fiber Loop Ringdown Sensor for Potential Real-Time Monitoring of Cracks in
Concrete Structures: An Exploratory Study
Peeyush Sahay, Malik Kaya and Chuji Wang*
Sensors 2013, 13, 39-57; doi:10.3390/s130100039

Department of Physics and Astronomy, Mississippi State University, Starkville,
MS 39762, USA

Could you please help me to get permission?

Regards

Support – MDPI Apr 7 (2 days ago)

to me

Dear Malik,

Please note that the premission is herewith guaranteed.
The citation information can be find below the article.

Kind regards,
MDPI Support
Maria